

MAGNETOELASTIC INTERACTIONS AND SPIN-
TRANSFER TORQUE DRIVEN DYNAMICS IN
ULTRATHIN FERROMAGNETIC NANOSTRUCTURES

A Dissertation

Presented to the Faculty of the Graduate School

of Cornell University

in Partial Fulfillment of the Requirements for the Degree of

Doctor of Philosophy

by

Praveen G. Gowtham

January 2015

© 2015 Praveen G Gowtham

ALL RIGHTS RESERVED

MAGNETOELASTIC INTERACTIONS AND SPIN-TRANSFER TORQUE
DRIVEN DYNAMICS IN ULTRATHIN FERROMAGNETIC
NANOSTRUCTURES

Praveen G. Gowtham, Ph.D.

Cornell University 2015

This dissertation can be divided into two separate sections. Chapters 2-5 constitute the first section and reflect my general interest in magnetoelastic interactions in ultra-thin film structures. I became interested in both the fundamental structure and origin of magnetoelastic interactions in ultra-thin films as well as the various applications that this interaction can be used in. Chapters 2 and 3 focus on the fundamentals of the magnetoelastic interaction and how magnetoelastic interactions can be affected by surfaces. In particular, we conduct experiments in Chapter 3 that demonstrate the presence of strong surface magnetoelastic coupling in the technologically relevant Ta|CoFeB|MgO interface. While the subject of surface magnetoelasticity is not new, we argue for its relevance in certain quandaries that are currently riddling the community – in particular: a) the origin/behavior of the surface anisotropy in the CoFeB|MgO system and the optimization of the perpendicular magnetic anisotropy in this technologically relevant system. b) the modification of the anisotropy by electric field.

Chapter 4 focuses on using magnetoelastic interactions to drive spin wave resonance in ultra-thin film ferromagnetic films. We use surface acoustic waves

(SAWs) in combination with the magnetoelastic interaction to drive these resonances in Ni|Pt bilayers and use a combination of acoustical loss measurements (via Vector Network Analyzer) and spin pumping + inverse spin-Hall measurements to characterize the properties of the spin wave resonance and the SAW-generated magnetoelastic pump field. We argue that GHz-frequency SAWs in tandem with the magnetoelastic interaction can be used as a truly novel tool for studying spin-wave physics and manipulating nano-scale ferromagnets.

Chapter 5 describes modeling work that we conducted in order to understand the various limitations involved in using the magnetoelastic interaction in giant magnetostrictive materials to switch nanomagnets for ultra-low power memory applications. We discuss a variety of switching modes, geometries, and materials and conclude that implementation of giant magnetostrictive memories for ultra-high density, ultra-low power consumption data storage is not as straightforward as it would seem at first glance. We propose a few schemes that have not been considered that are better than others (e.g. giant magnetostrictive nanomagnets with perpendicular anisotropy) and discuss the limitations of the other schemes.

The second section of our work is concerned with Spin-Transfer Torque (STT) Driven Dynamics in MgO-based Magnetic Tunnel Junctions (MTJs). We have observed that upon high voltage stressing of the junction and subsequent partial breakdown of the barrier, the time-coherence of STT-induced auto-oscillations are vastly improved. We discuss the origin of this effect both from the point of view of a generalized nonlinear auto-oscillator dynamical system in the presence of Langevin

noise (discussed and elucidated thoroughly by Andrei Slavin), but also from the point of view of spatial changes in the magnetic structure of the MTJ. Our conclusion is that the formation of magnetic nanocontacts between the polarizer and free layers during voltages stressing are crucial to all of the observed phenomena including the increase in the auto-oscillator time coherence.

BIOGRAPHICAL SKETCH

Praveen G. Gowtham was born on July 8, 1983 in St. Luke's Hospital located in the Upper West Side of Manhattan. He attended St. Hilda's and St. Hugh's School from Kindergarten through 8th grade. He then was fortunate enough to be accepted for high school to The Trinity School and receive a scholarship from an anonymous donor that made it possible for his family to afford the tuition there. He has nothing but the deepest feelings of gratitude towards this person. Praveen then attended Columbia University where he majored in Applied Physics and Applied Math. He then decided that it was time to leave New York City and go somewhere else. He accepted an offer for graduate school at Cornell University and shipped off to Ithaca, NY. He fell in love with Ithaca and thoroughly enjoyed his time spent inside the hallowed confines of Clark Hall and without. After his first year, he ended up joining Bob Buhrman's lab. He likes to think that he learned something about what it really means to be a decent experimental physicist during his time there. Along the way he learned a lot about condensed matter physics and magnetism in particular. But most importantly he learned a lot about himself, what physical limitations were falsely perceived and what were real, the various mental weaknesses that he possesses and what he can do to fight them. After eight years in Bob's lab he will graduate and he feels, all things considered, that the time was well worth it.

ACKNOWLEDGEMENTS

The existence of this thesis is a testament to a cataclysmic and yet character enhancing experience. What I refer to is the abrupt meeting of Bob Buhman's foot with my rear end. In this regard, I am extremely grateful to my advisor. It was the perfect antidote to one of my worst traits – my inability to focus on one thing and seeing it to its end before moving on to some other random thought or idea that interested me. That being said, I would like to thank him for a whole host of other things as well. This includes giving me a tremendous amount of freedom to pursue whatever set of projects I wanted. I know of few advisors who would have allowed his or her student to go off on a limb and into a subfield not ostensibly related to the research conducted by the rest of the group or directly mandated by funding. In addition, I would like to thank Bob for making me defend the relevance of my work at key moments. It got me to clarify in my own head what my project aims were and what they should be, and where my work fit in the general scope of the field. I would like to also comment on the fact that I have thoroughly enjoyed his dry cynicism, frankness, farm animal jokes, and his colorful story telling. Finally, I would like to note that Bob has shown me a great deal of compassion over the years when things were not going so well. I can only express my deepest gratitude to him.

I would next like to thank Dan Ralph. I have learned a great deal from watching his analytical approach to physics, the type of problems that he has chosen to attack, his razor sharp attention to detail, and his insistence on clarity. I have also been inspired by his work with the nanoconstriction technique. His use of a single technique

to attack and address a wide array of physical phenomena (inelastic electron-phonon scattering microscopy, 2-channel Kondo, single nanoparticle conduction electron spectroscopy, and last but not least the Spin Transfer Torque) is simply amazing. The lesson I have learned from this is that one should know what one has and constantly reimagine what it might become. What long-standing and important problems can be addressed and studied? What new and important physics can be studied in a simple manner with the techniques you currently have in hand? I would finally like to note that he is quite accomplished at sprinkling witty and often quite funny one-liners here and there.

I would like to thank Bruce van Dover for serving as my minor committee all these years. I always felt that his door was open to me and I have thoroughly enjoyed our conversations throughout the years. His expertise in magnetoelastic phenomena and materials proved to be extremely important in the development of my thought. He has pointed me towards important references and publications in the field which I used as a springboard for deepening my own understanding and thinking. In addition, I have enjoyed my conversations with him regarding thin film growth techniques and film structure, soft granular magnetic materials, combinatorial sputtering, and his collaboration with the Computer Science department for phase diagram boundary prediction and optimization of the combinatorial sputtering techniques using crowd sourcing techniques. Really cool stuff. He has also been incredibly encouraging to me during my time here and we thank him for it.

I would next like to thank Sunil Bhave for introducing me to the lingo and concepts of MEMs devices. He has pointed me to various references regarding electromechanical devices and offering on many occasions to help me by supplying me with various types of exotic substrates and materials for my experiments. Sunil has also been a source of constant encouragement throughout the years.

I would next like to thank the various people we worked directly with on various projects. First, I would like to thank Ozhan Ozhatay who was my first mentor in the group. We worked on the side-wall oxide project together for a time. He taught me the basics of lock-in measurements, basic cryostat techniques, shielding techniques, and ground loop hunting. This was at a time when I knew nothing about experiment. I thank him for showing me the ropes in the Buhrman group and also for the fun weekend lunches at the Ivy Room.

I would also like to thank John Read. Although I did not work directly with him on a project, I can safely say that he was instrumental in my education. He taught me that thin film growth and UHV work is as much an art as a science. I learned a great deal about growth methods and characterization techniques simply by listening to him. His insane work ethic was also quite inspirational and taught me that sometimes there is no substitute for putting your head down and plowing through it. Towards the end of his time here he also became a very good friend and I enjoyed our conversations about astronomy, art, and life in general.

Vlad Pribiag helped me a great deal in the MTJ dynamics project. He taught me about the basics of high frequency measurement, what to do, and absolutely what

not to do. We shared F20 for an extended period of time and it was extremely fruitful in terms of the experimental techniques I learned from Vlad but also in a much more important way. Vlad became a close friend of mine and we would discuss many things ranging from film to Greek/Roman History to political philosophy and beyond. I am honored that he chose me as a witness at his wedding and feel fortunate to have had the opportunity to meet such an amazing person.

I would next like to thank Giovanni Finnochio and Mario Carpentieri for working with me on the MTJ dynamics project, running an obscene number of micromagnetic simulations and for generally enjoyable discussions on oscillator physics. I appreciate their work on the project almost as much as I appreciate their zeal in showing me why pasta al-dente is really the only way to have pasta. In short, they are my friends and I have enjoyed eating food, drinking beer with them, watching Giovanni dance, etc. I am also very happy to hear the recent news that Giovanni is a father. I wish him and his family the best.

I worked with Takahiro Moriyama on a variety of projects regarding magnetoelasticity. He is a talented experimentalist and taught us a lot of neat little lab tricks. I mention the “Taka-style” wafer-scribing technique which combines economy of hand motion with the advantage of not dirtying the wafer top side. I spent a lot of time in lab with him, developing working shift routines, brain-storming, analyzing data, collectively beating our heads against the wall, shaking our heads in abject despair, and jumping wildly and ecstatically when things started to work. I am truly

fortunate to have worked with someone like him and I wish him the best in all his future endeavors.

Finally I have had the pleasure of working with Greg Stiehl. He is extremely diligent, excited about physics, asks good questions and with this set of qualities has kept me honest and made me think carefully about the assumptions that I was making and the work I was doing. He was also a great help to me while I was taking data on the surface magnetoelasticity project by performing the tedious task of wire bonding all my samples. That work would not have been possible without him. Also I would like to note that he has become a good friend of mine and that I think he has an excellent sense of taste.

I would next like to thank all the staff members that contributed to my education and the work I did in this thesis. Among these are Bob Snedeker, Nate Ellis, Rodney Bowman, Jon Shu, Mick Thomas, John Grazul, Maura Weathers, Rob Ilic, John Treichler, Jerry Drumheller and Garry Bordonaro. I would also like to thank the building support staff who helped me a great deal during the times when I assembled the Intlvac ion mill and did all the plumbing and gas lines. In particular, I would like to thank Bob Kenyon and Dan Sheerer.

I would also like to thank the past and present members of the Buhrman and Ralph group that I shared time with here. Many of you became good friends to me and enhanced my life in the basement and outside. You know who you are. The rest I thank for helping us lift heavy objects, maintaining equipment, and graciously sharing time, tools, and space with me. I would also like to thank the many friends that I made

at Cornell and in Ithaca. The list is long and so I will simply say that, again, you know who you are and I am very thankful for having you in my life. I would like to specially thank my mother, uncle, and brother for their love, patience, prayers and self-sacrifice. I would not be who I am and be where I am today without them.

Finally, I would like to thank Anja for existing, somehow finding her way to the US and in particular Cornell, attending a house party that she was invited to, being amused by a random person who started rambling to her about the harpy eagle and orange elephants on hovercraft, becoming that random person's friend, playing chess and trading books and taking long walks with that person, and eventually after some time letting that friendship blossom into affection and love. I love you, cutie.

TABLE OF CONTENTS

Biographical Sketch.....	iv
Acknowledgements	v
Table of Contents	xi
List of Tables	xv
List of Figures.....	xvi
CHAPTER 1 Magnetoelectronics, Spin Torques, and Magnetization Dynamics: An Introduction	1
1.1 Introduction.....	1
1.2 Magnetoresistance Effects	2
1.2.1 Anisotropic Magnetoresistance (AMR)	2
1.3 Current-Perpendicular-to-Plane (CPP) Giant Magnetoresistance (GMR).....	3
1.4 Magnetic Tunnel Junctions and the Tunneling Magnetoresistance	4
1.4.1 Coherent Tunneling and TMR in MgO-based MTJs	7
1.5 The Spin Transfer Torque.....	12
1.5.1 Spin Torques in FM NM FM Trilayers	15
1.5.2 Spin Torques in Magnetic Tunnel Junctions	17
1.6 STT-Induced Magnetization Switching.....	18
1.7 STT-Driven Magnetization Dynamics.....	21
1.8 Spin Pumping.....	30
1.9 The Spin Hall Effect (SHE) and Inverse Spin Hall Effect (ISHE).....	36
CHAPTER 2 An Introduction to Surface Anisotropies and Magnetoelastic Effects in Magnetic Thin Films	47

2.1	Motivation.....	47
2.2	Néel Pair Anisotropy Model: Surface Symmetry Breaking and Phenomenology	48
2.3	Strain Behavior in Thin Films, Magnetoelasticity and the Connection to Surface Anisotropy.....	57
2.3.1	Magnetoelastic Surface and Volume Anisotropy: The Kink Model	57
2.3.2	Surface Magnetoelasticity, Strain Relaxation and the $K_{\text{eff}}t_{\text{eff}}$ Curve	62
2.3.3	Surface Magnetoelasticity and Second Order Couplings	65
2.3.4	Strain Behavior in Thin Films	66
2.4	Microscopic Sources of Néel-type Surface Anisotropy and Surface Magnetoelasticity	69
2.4.1	A Quick Review of Recent Progress in Surface Anisotropy.....	76
2.4.2	Experimental Studies on Surface Magnetoelasticity	78
CHAPTER 3 Surface Anisotropy and Magnetoelastic Effects in the Ta CoFeB MgO system		91
3.1	Recent Developments in the NM CoFeB MgO System.....	91
3.1.1	Perpendicular Anisotropy in NM (Fe,CoFe,CoFeB) MgO.....	91
3.1.2	Voltage Controlled Magnetic Anisotropy (VCMA).....	109
3.2	Motivation For Our Experiment	113
3.3	Film Growth & Preparation	114
3.4	Sample Fabrication	115
3.5	The Four Point Bend Method	121
3.6	Machining and Assembly of the Four Point Bend Setup.....	128
3.6.1	Machining of the Extender Structure	129
3.6.2	Machining of the Teflon Guider.....	132
3.6.3	Support Base + Support Pins.....	133

3.6.4	Machining of the Loading Column	134
3.6.5	Machining/Assembly of the Pusher Plate.....	135
3.7	Magnetometry Results: $K_{\text{eff}}t_{\text{eff}}$ vs t_{eff} curves and M_s extraction.....	137
3.8	Magnetoelastic Coupling Measurement Scheme & Geometry.....	141
3.9	Analysis Method for the In-plane Magnetoelastic Constant B_{eff}	146
3.10	Results on Thickness Dependence of the Magnetoelastic Coupling	149
3.10.1	Mechanism for Nonlinear $K_{\text{eff}}t_{\text{eff}}$ vs t_{eff} behavior	153
3.11	Voltage Controlled Magnetoelasticity (VCME)	159
CHAPTER 4 Gigahertz Frequency Magnetization Dynamics Induced by Surface Acoustic Waves		167
4.1	Introduction/Motivation.....	167
4.2	Surface Acoustic Waves	168
4.3	A Introduction to Electrical Generation of SAWs.....	172
4.4	SAW-induced Magnetoelastic Spin-Wave Resonance: Theory	179
4.5	Sample Growth and Fabrication	187
4.6	Measurement Setup.....	189
4.7	Magnetoelastic Resonance Measurements	193
4.8	Resonance Quantification using the Inverse Spin Hall Effect.....	205
4.9	Conclusion	215
CHAPTER 5 Modeling of Strain-Induced Reversal Dynamics in Giant Magnetostrictive Nanomagnets.....		221
5.1	Introduction/Motivation.....	221
5.2	Toggle Mode Switching.....	223
5.2.1	In-Plane Magnetized Magnetostrictive Materials	225
5.2.2	Magneto-Elastic Materials with PMA: Toggle Mode Switching.....	235

5.3	Two State Non-Toggle Switching	242
5.3.1	The Case of Cubic Anisotropy	243
5.3.2	The Case of Uniaxial Anisotropy	248
5.4	Conclusion	254
CHAPTER 6 The Effect of Magnetic Nanocontact Formation on Spin-Transfer Dynamics in MgO MTJs		261
6.1	Introduction.....	261
6.2	Experimental Procedure.....	262
6.3	Quasistatics: Experiment and Simulations	264
6.4	Dynamical Properties.....	273
6.5	Micromagnetic Simulations: Dynamics.....	293
6.6	Future Directions and Conclusion	302
CHAPTER 7 Conclusion/Summary		307

LIST OF TABLES

Table 2.1. Experimental and theoretical surface anisotropy values for relevant systems.	78
Table 2.3. Tabulation of first and second order magnetoelastic couplings of epitaxial magnetic film/substrate pairs.	84
Table 3.1. Outline of our fabrication process flow for our VCME devices.	117
Table 4.1 Coefficients coupling acoustic wave amplitudes and potential wave amplitudes in LiNbO_3	174
Table 4.2 SAW IDT and Ni Pt mesa/microwire fabrication process flow.	189

LIST OF FIGURES

Figure 1.1 Julliere cartoon of spin-dependent tunneling in magnetic tunnel junctions..	6
Figure 1.2 Majority transmission for 12 layers of MgO sharply peaked about $\vec{k}_{\parallel} = 0$..	8
Figure 1.3 Tunneling density of states (TDOS) for majority and minority bands in Fe MgO Fe in P state.	11
Figure 1.4 Diagram of torques on the magnetization as expressed in the LLG equation with spin-torque.....	14
Figure 1.5 Schematic of electron transmission and reflection in FM NM FM systems and illustration of the spin torque under different current flow directions.....	16
Figure 1.6 Illustration of anti-damping switching trajectory for an in-plane magnetized free layer and R vs V_{bias} STT-switching curve	19
Figure 1.7 IPP clamshell and OPP type orbits as predicted by the macrospin model..	22
Figure 1.8 f vs. I_{dc} for different hard axis bias fields H_y in an in-plane free layer/in-plane reference layer FM NM FM device.....	24
Figure 1.9 FM NM bilayer and schematic of spin-pumping with precessing magnetization	35
Figure 1.10 a) Illustration of SHE and ISHE processes	37
Figure 1.11 Representation of the processes contributing to the spin hall conductivity	38
Figure 2.1 Coordinate scheme for pair bond-oriented spin coupling and illustration of coupling in the bulk and near surfaces	49
Figure 2.3 Cubic lattice under uniaxial strain e_{xx} . Strain changes the anisotropic spin-spin interaction energies and contributes to the anisotropy.....	54
Figure 2.4. Accommodation of epitaxial misfit strains by introduction of edge dislocations.	59
Figure 2.5 a) Biaxial strain field as a function of thickness and resultant $K_{\text{eff}}t_{\text{eff}}vSt_{\text{eff}}$ vs t_{eff} curve for a multilayer/sandwich sample assuming the kink model.....	60

Figure 2.6 Kt vs t curve for the Cu/Ni(001)/Cu epitaxial system. The solid line represents a fit to the data by the kink model.....	61
Figure 2.7 $K_{eff}t_{eff}$ vs t_{eff} curve for the Ni/Cu(001) system as measured by Bochi et al.	64
Figure 2.8 In plane effective magnetoelastic coupling B_{eff} and $B_{eff}t_{eff}$ vs t_{eff} plots for polycrystalline evaporated NiFe/Ag/Si, NiFe/Cu/Si, and Ni/SiO ₂ /Si systems.....	80
Figure 2.9 Effective biaxial magnetoelastic coupling extracted from laser deflection measurements of magnetostrictive plate deformations on Fe/W(001) system in-situ.	81
Figure 2.10. Effective magnetoelastic coupling versus residual biaxial strain for various epitaxial systems	83
Figure 3.1 Minority d-band structure at optimally oxidized Fe-MgO interface decomposed into the various subbands	95
Figure 3.2 Red, green, and blue atoms correspond to the positions of O, Mg, and Fe in the optimally oxidized system. Energy levels/splitting and hybridization for the various Fe d bands and the O p _z bands at E _F near the Γ point.....	96
Figure 3.3 K_{ut} vs t without dead layer subtraction for Ta(2) Co ₆ Fe ₂ B ₂ MgO and Ru(2) Co ₆ Fe ₂ B ₂ MgO	98
Figure 3.4 $K_{eff}t_{eff}$ and M/A vs t_{eff} curves for Hf(5)/Co ₄₀ Fe ₄₀ B ₂₀ /MgO(2.2)/Ta(1) and Ta(5)/Co ₄₀ Fe ₄₀ B ₂₀ /MgO(2.2)/Ta(1) annealed at T = 300 °C for 1 hr.....	100
Figure 3.5 M/A and $K_{eff}t_{eff}$ vs CoFeB thickness shows no dead layering with either a β -W underlayer or a β -W underlayer with a Hf insert.....	101
Figure 3.6 $K_{eff}t_{eff}$ vs t_{eff} for Ta(1) Co ₂₀ Fe ₆₀ B ₂₀ MgO Ta(1) and TaN[1%](4) Co ₂₀ Fe ₆₀ B ₂₀ MgO Ta(1) and surface anisotropy and volume anisotropy vs N doping percentage into Ta buffer layer for annealed and as deposited samples	102
Figure 3.7 Dependence of M_s and dead layering as a function on N doping of the Ta layer for Ta Co ₂₀ Fe ₆₀ B ₂₀ MgO samples	104
Figure 3.8 R_{Hall} vs H loops for in-plane samples as a function of gate showing E-field induced changes in anisotropy.....	110
Figure 3.9 Photolith Mask Level 1 mage and optical microscope image of device after Photolith#1 and Ion Mill #1 for Gated Hall bars.....	118
Figure 3.10 Photolith Mask Level 2: Define gate stack/etch down to Ta bottom electrode. Optical microscope image after Ion Mill #2 etch.....	119

Figure 3.11 Photolith Mask Level 3: Etch through HfO ₂ to define Ta base electrodes. Optical microscope image of etch to Ta base electrode after Ion Mill #3.....	120
Figure 3.12 Photolith Mask Level 4: Define Gate and Hall and drain/source electrodes.	121
Figure 3.13 Sketch of four point bend test and loading pin positions.....	122
Figure 3.14. Diagram showing the neutral plane of a bowed beam and the relationship between the uniaxial strain in the direction of curvature and the distance from the neutral plane of the beam.	125
Figure 3.15 CAD drawing of entire extender/support structure without stepper motor, loading column, and pusher plate.....	129
Figure 3.16 CAD Drawing of M228.11S stepper motor.....	130
Figure 3.17 CAD Drawing of upper octagonal support.....	131
Figure 3.18 CAD Drawing of lower octagonal support.....	132
Figure 3.19 a) Top-down view of teflon guider. b) Perspective view of teflon guider.	133
Figure 3.20 a) Top-down image of support base with dimensions. b) perspective drawing of support base.....	134
Figure 3.21 Picture of final setup within the poles of the GMW Electromagnet. The entire extender structure was screwed into a modified Buhrman group probe/sample stage.....	136
Figure 3.22 Total magnetic moment/unit area vs nominal CoFeB thickness in as-deposited Ta(6) CoFeB(x) MgO(2.2) Hf(1) structures.....	137
Figure 3.23 Total magnetic moment/unit area vs. nominal CoFeB thickness for Ta(6) CoFeB(x) MgO(2.2) Hf(1) annealed at 300 °C for 1 hour.....	138
Figure 3.24 Room-temperature temperature SQUID in-plane field scans of annealed Ta(6) CoFeB(x) MgO(2.2) Hf(1) film stacks showing the transition from in-plane to out-of plane anisotropy at $t_{\text{CoFeB}}=1.2$ nm.....	139
Figure 3.25 $K_{\text{eff}}t_{\text{eff}}$ vs t_{eff} for as-deposited Ta(6) CoFeB(x) MgO(2.2) Hf(1) series. Solid line is fit to Neel Model.....	140

Figure 3.26 $K_{\text{eff}}t_{\text{eff}}$ data extracted from magnetometry and M-H anhysteretic curve data. The line fit of the data used to extract the surface and volume anisotropy is also shown.	141
Figure 3.27 a) Machined Delrin connector clamped to chip + wire-bonding geometry.	142
Figure 3.28 Device and lead geometry as well as coordinate system for our experiment and analysis	144
Figure 3.29 Home-built field annealing stage + chip holder for Lindbergh vacuum tube furnace	145
Figure 3.30 a) dV/dI vs H curve strain series for an annealed Ta(6) CoFeB(1.7) MgO(2.2) Hf(1) sample	146
Figure 3.31 a) Normalized AMR curves vs H_{app} along hard axis for annealed Ta(6) CoFeB(1.7) MgO(2.2) Hf(1) sample. The AMR curve and $H(m)$ vs m series goes from to $\varepsilon_{xx} = 0$ to $\varepsilon_{xx} \sim .1\%$	147
Figure 3.32 Integrated energy of $H(m)$ vs m between the normalized magnetization points $m_1=.4$ and $m_2=.8$ as a function of strain. Red dashed line corresponds to linear fit used to extract B_{eff}	149
Figure 3.33 Dependence of the effective magnetoelastic constant on thickness for as deposited (amorphous) CoFeB films.....	150
Figure 3.34 CoFeB thickness dependence of the magnetoelastic coupling for samples annealed in a 1.3 kOe in-plane field. The red line is a fit to the data using $B_{\text{eff}}=B_s/t+B_v$	151
Figure 3.35 Fit of the $K_{\text{eff}}t_{\text{eff}}$ vs t_{eff} data using a free energy that takes into account thickness dependent magnetoelastic coupling and thickness-dependent biaxial strain in the CoFeB film	156
Figure 4.1. Propagation of a Rayleigh-type SAW	169
Figure 4.2 Illustration of interdigitated electrodes launching a SAW	173
Figure 4.3 Plot of array factor $H(f)$ at the fundamental bandpass f_0 for $N = 40$ and $N = 120$ fingers. We have also plotted the response function for SAW launchers with $f_0 = 150$ MHz and $m = 0.4$ and 0.5 respectively.	177

Figure 4.4 $\zeta\eta\xi$ and xyz coordinate system for in-plane magnetized film and applied field.....	181
Figure 4.5 Completed Al(10)/AlO _x (2)/Ni(10)/Pt(15) microwire with Al(100 nm) SAW IDT transmitter and receiver.	189
Figure 4.6 Continuous wave and time-gated S_{21} measurement of a SAW delay line with $f_0 = 150$ MHz and an IDT metallization ratio $m = 0.5$	191
Figure 4.7 Time gated spectrum for a $f_0 = 300$ MHz SAW delay line with $m = 0.4$..	192
Figure 4.8 VNA $ S_{21} $ SAW absorption measurement at the center frequency of the bandpasses of a $f_0=300$ MHz SAW delay line with $m = 0.4$	194
Figure 4.9 AMR resistance curves for 0° (blue) and 90° (red) field angle with respect to the SAW propagation direction show that the Ni has a substantial in-plane anisotropy field H_k with 90° (i.e. the ζ axis) being the easy axis direction.	196
Figure 4.10 Out-of-plane field scan of Al(10)/AlO _x (2)/Ni(10)/Pt(15) bilayer on YZ-cut LiNbO ₃	198
Figure 4.11 Calculations of the field strength and field angle dependence of SAW power resonantly absorbed by a ferromagnetic film through the magnetoelastic interaction using the Damon-Eschbach theory.	199
Figure 4.12 Calculations of the absorbed power for dipole-exchange and exchange spin-wave resonance compared to S_{21} data	200
Figure 4.13 Pump frequency vs. applied field magnitude at which maximum absorption occurs at a field angle of 45 degrees off the η -axis.	201
Figure 4.14 Difference map $P_{\text{abs}}[\text{with dipolar correction}] - P_{\text{abs}}[\text{without dipolar correction}]$ of calculated absorption spectrum at 3.86 GHz. Purple is positive and red is negative in the difference map.....	203
Figure 4.15 Power absorption for SAW-induced resonance for Co ($M_s = 1420$ emu/cm ³) with $d = 10$ nm, $H_k = 0$ Oe, $f_{\text{saw}} = 3$ GHz with and without the dynamic dipolar field correction arising from the spin wave.....	204
Figure 4.16 Measurement of V_{ISHE} voltage vs. field and angle.....	211
Figure 4.17 Normalized V_{DC} curves plotted against the results of our spin wave calculation from Equation (4.38) at a few frequencies and field angles. The last plot shows the the V_{DC} vs. H_{app} data for these sweeps without normalization.....	212

Figure 5.1 Magnetoelastic elliptical memory element schematic, associated switching trajectories, and switching probability vs stress pulse amplitude and duration for in-plane magnetized $Tb_{3.3}Dy_{7.7}Fe_2$	226
Figure 5.2 Toggle mode magnetoelastic switching with a perpendicularly magnetized $TbFe_2$ element.....	238
Figure 5.3 Energy landscape for magnetoelastic $Fe_{81}Ga_{19}$ with biaxial magnetic anisotropy under various field bias conditions applied along 45 degrees and with stress field applied by [100].	245
Figure 5.4 a) Non-toggle mode magnetoelastic switching trajectories, stress pulse amplitude and duration switching probability phase diagram, and micromagnetic trajectories for $Fe_{81}Ga_{19}$	247
Figure 5.5 Non-toggle mode magnetoelastic switching trajectories, thermal stability considerations, stress pulse amplitude and duration switching probability phase diagram, and micromagnetic trajectories for $TbDyFe$	250
Figure 6.1 Changes of minor M.R. hysteresis loop as a function of the conditioning process and simulated hysteresis loops with magnetic nanocontacts.....	265
Figure 6.2 Micromagnetic configurations with magnetic nanocontacts and visualization of AP to P and P to AP switching	268
Figure 6.3 Annular dark-field (ADF) STEM and EELS spatial mapping for Co and Oxygen near a magnetic pinhole	271
Figure 6.4 Spatial mapping of the MCR fitting for metallic-type Co EELS signal ...	272
Figure 6.5 a) Power of first and second harmonics generated by an unstressed MTJ as a function of field and bias voltage. b) Power of first and second harmonic for conditioned MTJ. c) Typical Power spectral density (PSD) of unconditioned sample. d) Typical PSD after stressing procedure.....	274
Figure 6.6. a) Frequency and linewidth vs. V_{bias} and H_{app} behavior for different conditioned devices and with comparisons to unconditioned devices	277
Figure 6.7 a) 1f and 2f integrated power delivered to a 50 load as a function of DC voltage bias for a lower field $H = -600$ Oe and a higher field $H = -900$ Oe. b) Ratio of first to second harmonic integrated power at different fields.....	279

Figure 6.8 Average DC Resistance, average DC conductance with respect to the parallel conductance, and the parallel resistance as a function of V_{bias} across the MTJ for different field values	282
Figure 6.9 Conductance power spectral density of Sample 1 as a function of frequency for $H = -600$	284
Figure 6.10 Integrated conductance power for 1f and 2f peaks	285
Figure 6.11 Conductance oscillation amplitude at 1f and 2f for Sample 1 at $H = -900$ Oe.	286
Figure 6.12 FWHM of 1f peak vs V_{bias} at $H=-600$ Oe and $H=-900$ Oe.....	287
Figure 6.13 Frequency, 1f peak FWHM, and 1f and 2f conductance plotted as a function of V_{bias} at $H = -600$ Oe and $H = -900$ Oe	289
Figure 6.14 a) Micromagnetic results for frequency vs current density for unconditioned junctions b) Oscillator linewidth vs current density for unconditioned MTJ.....	295
Figure 6.15 a) 1 st Harmonic frequency dependence in the resistance signal vs. average current density with and without Oersted field for three pinhole case. b) Linewidth vs. current density for three pinhole case.....	298
Figure 6.16 a) f vs J (average current density) for first harmonic in the resistance oscillations of the three pinhole $A = 4 \text{ nm}^2$ scenario. b) Oscillation linewidth vs. current density of first harmonic. c) Spatially averaged m_z component time averaged over an oscillation cycle as a function of current density.	300
Figure 6.17 Snapshots of magnetization dynamics in three magnetic pinhole case ..	301

CHAPTER 1

MAGNETOELECTRONICS, SPIN TORQUES, AND MAGNETIZATION DYNAMICS: AN INTRODUCTION

1.1 Introduction

This thesis is organized into two parts. The first part reflects our most recent interest in magnetoelastic interactions in ultra-thin films. Chapter 2 is an introduction to magnetoelastic interactions and anisotropy with a specific eye towards surface effects in ultra-thin magnetic systems. Chapter 3 describes the current state of understanding of the surface anisotropy in NM|CoFeB|MgO systems and describes an experiment that we conducted to measure surface magnetoelastic interactions in these systems and how they might be important for understanding the behavior of the surface anisotropy. We also discuss how magnetoelastic interactions might play a role in electric-field based anisotropy control. Chapter 4 describes a study where we used GHz frequency surface acoustic waves (SAWs) to excite ferromagnetic resonance in Ni|Pt bilayers. We study the structure of such excitations and discuss the possibility of using SAWs for nano-scale to micron-scale magnetization control. Chapter 5 is a numerical study of various magnetoelastic switching modes and memory schemes in giant magnetostrictive magnets. Chapter 6 consists of work we did on spin-transfer torque driven dynamics of magnetic tunnel junctions. We observe that junctions that have been subject to high voltage stressing and subsequent degradation of the tunnel barrier exhibit spin-transfer induced magnetization dynamics that have a high degree

of spectral purity. Our study aimed to uncover what possible structural and magnetic changes occur during the stressing process and how this might affect the spin-torque dynamics of the system. The current chapter is devoted to providing a general introduction to key developments in spintronics and magnetization dynamics that are important for understanding what follows in the rest of the thesis.

1.2 Magnetoresistance Effects

Magnetoresistance is the change of the electrical resistance of a solid in the presence of a magnetic field. The effect does occur in all metals and is a consequence of the structure and evolution of k-space electronic states on the metal's Fermi surface. We, however, will focus on magnetoresistance effects in systems containing ferromagnets. Magnetoresistance in these systems provides a powerful way of electrically probing the magnetic state of the system as well as characterizing and quantifying spin-dependent processes in these systems. For these reasons, a discussion of the various classes of magnetoresistance in systems with ferromagnets is a good starting point for a general overview of magnetoelectronics.

1.2.1 Anisotropic Magnetoresistance (AMR)

The AMR is an effect that occurs in a conducting ferromagnet where the resistance depends on the relative orientation of the magnetization vector to the applied current direction flowing within the ferromagnet. The effect typically shows a resistance minimum when the magnetization is orthogonal to the current direction and has a

resistance maximum when the magnetization is parallel to the current direction. The angular dependence of this resistance for a single domain magnet is expressed as:

$$R(\varphi) = R_{\perp} + (R_{\parallel} - R_{\perp}) \sin^2 \varphi \quad (1.1)$$

Here φ is the angle between the current and the magnetization direction and $R_{\parallel} > R_{\perp}$.

The effect is on the order a few percent in permalloy and as low as a few tenths of a percent in an amorphous metalloid glass ferromagnet (like CoFeB). The effect cannot be interpreted in terms of classic galvanomagnetic effects in that a magnetic induction orthogonal to the current flow direction should retard electron motion. The AMR originates rather from s-d exchange scattering in the presence of spin orbit coupling. It can be shown that, in the presence of S.O. coupling, s-electrons are scattered less effectively via minority d-states when the electron flow is in the direction of the magnetization [1]. The effect is rather useful in characterizing magnetization processes in single ultra-thin magnetic films and so we will be employing it in many of the studies in this thesis.

1.3 Current-Perpendicular-to-Plane (CPP) Giant Magnetoresistance (GMR)

CPP-GMR was first discovered independently by Grunberg and Fert. The first studies were conducted on multilayer $[\text{Fe}|\text{Cr}]_n$ superlattices where the FMs were antiferromagnetically coupled at zero-field through NM conduction electron-mediated exchange [2], [3]. The percentage change in resistance $(R_{\text{AP}}-R_{\text{P}})/R_{\text{P}}$ for current flowing normal the film stack direction in these structures upon saturating them into the P state

could be quite high (~40%) compared to AMR effects. For non-superlattice systems (i.e. FM|NM|FM systems) the GMR is more modest with MRs on the order of 10%. The discovery of the GMR has had major impacts in terms of the understanding of spin transport physics in multilayer structures. The change in the electrical resistance of these devices is entirely due to spin-dependent scattering at the NM|FM interfaces and non-equilibrium spin-diffusive processes within the FM and NM layers. These non-equilibrium spin processes behind the CPP-GMR are described by the Valet-Fert model [4]. We will not discuss the GMR any further and refer readers to the many reviews articles on the subject for further details. The main reason we bringing it up is that the GMR was important in showing that the generation and manipulation of non-equilibrium spin currents could be used to make useful devices (e.g. GMR field sensors).

1.4 Magnetic Tunnel Junctions and the Tunneling Magnetoresistance

A similar magnetoresistance effect known as the Tunneling Magnetoresistance (TMR) is found in magnetic tunnel junctions (MTJs). MTJs are ferromagnet (FM)|ultra-thin insulator|ferromagnet heterostructures. Electrons tunneling through the insulator from one ferromagnet to the other will experience a resistance which depends on the relative orientation of the electrodes. The effect was first discovered by Julliere in an Fe|Ge-O|Co junction with a TMR $(R_{AP}-R_P)/R_P$ of ~14% at 4K. The discovery did not attract too much attention mainly due to the fact that the not particularly impressive MR could be observed only at cryogenic temperature. Interest in the TMR started to pick up with the discovery of room temperature TMRs of ~12% in CoFe|AlO_x|Co [5]

and ~18% in Fe|AlO_x|Fe [6] MTJs with amorphous aluminum oxide barriers. The highest R.T. TMR measured in these AlO_x barriers was ~70% in a Co₇₅Fe₂₅|AlO_x|Co₇₅Fe₂₅ junction [7]. The subsequent development of MgO barriers heralded a new age in MTJs with R.T. TMRs exceeding 100%. We will discuss the mechanisms in MgO barriers in some detail as we will be using CoFeB|MgO|CoFeB junctions in our dynamics study in Chapter 6.

One of the first descriptions of TMR was the Julliere model and it provides a simple picture for how spin dependent tunneling leads to a magnetoresistance. The model assumes that the spin-dependent tunnel current depends only on the majority band and minority band tunneling density of states (TDOS) in the left and right electrodes. Thus the model assumes that the tunneling matrix is independent of the magnetization orientation, wave-vector/electron state. Under these assumptions, the conductance in the P state will depend only on the TDOS for majority (minority) electrons in the left electrode tunneling and the TDOS for majority (minority) electrons in the right electrode. The conductance in the AP state then depends on the TDOS for majority (minority) in the left electrode and minority (majority) in the right electrode. The conductances in both states can be written as:

$$\begin{aligned}
 G_P &\propto n_{L\uparrow}n_{R\uparrow} + n_{L\downarrow}n_{R\downarrow} \\
 G_{AP} &\propto n_{L\uparrow}n_{R\downarrow} + n_{L\downarrow}n_{R\uparrow}
 \end{aligned}
 \tag{1.2}$$

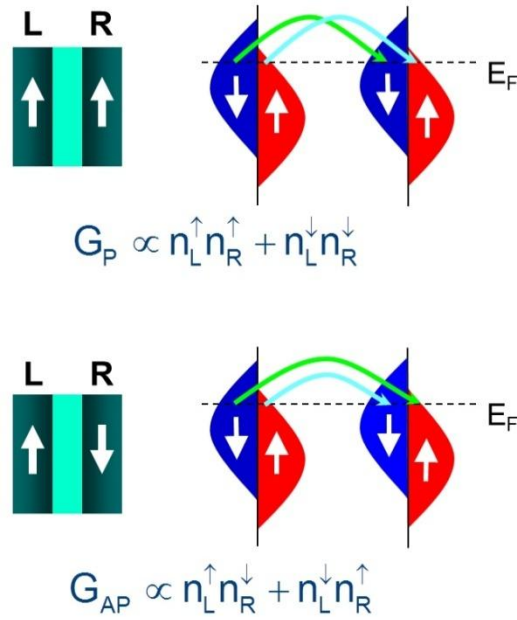


Figure 1.1 Julliere cartoon of spin-dependent tunneling in magnetic tunnel junctions.

Each electrode α has an effective tunneling spin polarization P_α :

$$P_\alpha = \frac{n_{\uparrow,\alpha} - n_{\downarrow,\alpha}}{n_{\uparrow,\alpha} + n_{\downarrow,\alpha}} \quad (1.3)$$

The TMR defined as the percentage change of resistance between the P and AP electrode configuration with respect to the P state resistance can then be recast in terms of the electrode tunneling spin polarizations

$$TMR|_{V=0} = \frac{G_P - G_{AP}}{G_{AP}} = \frac{R_{AP} - R_P}{R_P} = \frac{2P_L P_R}{1 - P_L P_R} \quad (1.4)$$

This model is phenomenological and is generally used as a way of making a very rough estimate on the magnitude of the TMR and the TSP factors. In reality, the tunneling comes from bands with different effective masses and so the TDOS is some weighted average over the states involved in the tunnel current. The general vagueness of this definition means that the TSP itself is not an entirely well-defined concept. The Julliere model also ignores the geometry and structure of the bands of the insulator. Even in the case of a free-electron model with a simple rectangular barrier the Julliere TDOS contains no information about states in the insulator. This has been shown to be inconsistent with a calculation of the TMR using a direct calculation of the wavefunctions and the resultant effective tunnel current [8]. Last and most importantly the assumption that the tunneling matrix is independent of the nature of the electronic states in the electrodes and the barriers can be a very bad one. We will see this in the next section.

1.4.1 Coherent Tunneling and TMR in MgO-based MTJs

The approximation made by Julliere is invalid in the case where there is an epitaxial lattice match between the ferromagnetic electrodes and barrier. Under these conditions, \vec{k}_{\parallel} is a conserved quantum number for the Bloch eigenstates in the system and wave-function matching considerations give considerable structure to the tunneling matrix. Calculations carried out independently by Butler [9] and Mathon [10] in the Fe|MgO|Fe system revealed that this conservation rule along with Bloch wave-function matching in the Fe electrodes and in the MgO are crucial in

determining the overall wave-functions/band structure and resultant conductance across the junction.

The symmetry-class of the Bloch wave-functions (which in general have complex \vec{k}) in the Fe and the MgO are crucial for determining the matching and subsequent transmission of electrons. First, we restrict the discussion of tunneling to areas in the 2D 1st B.Z. near the $\vec{k}_{\parallel}=0$ point (the $\bar{\Gamma}$ point). The reason for doing this is that majority transmission within the MgO barrier is strongly concentrated at $\vec{k}_{\parallel}=0$.

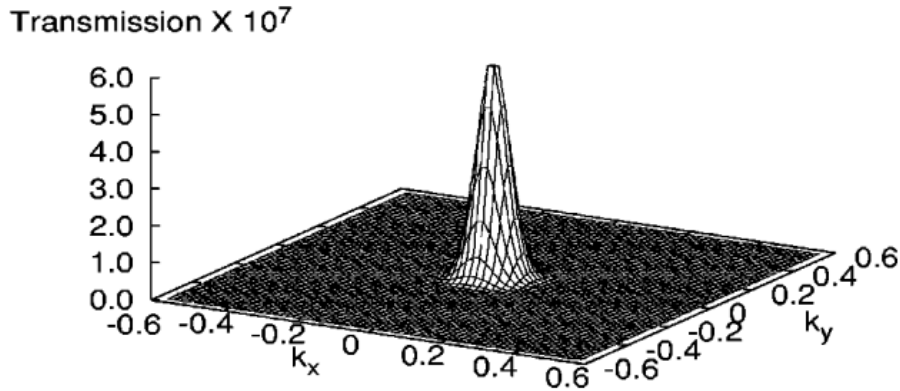


Figure 1.2 Majority transmission for 12 layers of MgO sharply peaked about $\vec{k}_{\parallel} = 0$. Taken from reference [9].

For simple rectangular barrier models the transmission is also strongly peaked near the $\bar{\Gamma}$ point (i.e. low \vec{k}_{\parallel}). Near the $\bar{\Gamma}$ point, the wave-functions can be classified by the symmetry group associated with the in-plane cubic epitaxial relationship between the Fe and the MgO. This group is denoted as C_{4v} (the tetragonal group) and contains five

irreducible representation of the group sometimes labeled as Δ_1 , Δ_1' , Δ_2 , Δ_2' , and Δ_5 . The first four are one-dimensional representations and the fifth is a two-dimensional representation of the group. Δ_1 is the trivial representation and represents states even with respect to C_4 rotations about the z-axis. The character of the wavefunctions associated with the Δ_1 representation are thus s, p_z , and d_{z^2} . The Δ_2 state is the 1D representation of the group associated with states that are odd with respect to the C_4 rotation but even with respect to the xz (or yz) plane. Thus the Δ_2 state correspond to $d_{x^2-y^2}$. The Δ_2' representation is the same as the Δ_2 except odd with respect to reflections about the xz mirror plane and thus corresponds to the d_{xy} state. The Δ_5 band is comprised of states of d_{xz} , d_{yz} , p_x and p_y character. The symmetry required for Δ_1' states require f electron systems and thus play no part in the Fe|MgO|Fe system. The crucial point is that Bloch wave-functions of the same symmetry character match at the Fe|MgO boundary and thus the bands extending through Fe|MgO|Fe and contributing to the tunnel current can be essentially labeled by the underlying symmetry of the wave-functions. Thus Δ_1 bands in the left Fe electrode match to Δ_1 band in the MgO and that to the Δ_1 band in the right Fe electrode – thus forming a band with a generally complex wave-vector in the Fe|MgO|Fe heterostructure. A similar argument applies to the Δ_5 band. The Δ_2 band in Fe connects to the Δ_2' band in MgO and vice-versa by noting that the BCC Fe and rock-salt structure MgO lattices are rotated by $\pi/4$ with respect to each other in the xy plane.

We now must consider that each of the symmetry classified bands are spin-split into minority and majority sub-bands. The conductance of the junction will then

depend on how the bands of various symmetry classes connect to each other when the electrodes are in the P and in the AP state. When the electrodes are in the P state, majority states will connect to majority states and minority states will couple to minority states (in absence of spin-flip scattering). Here the Δ_1 majority band dominates the tunnel current when the magnetization of both Fe electrodes are parallel [Figure 1.3]. The Δ_1 majority bands have a very low effective mass in the MgO in this Fe electrode configuration. Minority electron current dominated by the Δ_5 band is substantially smaller than the Δ_1 majority electron current. Therefore the tunnel current is highly spin polarized and this spin polarization derives entirely from in-plane wave-vector conservation, symmetry based selection rules, and the difference in effective masses between Bloch states of different symmetries.

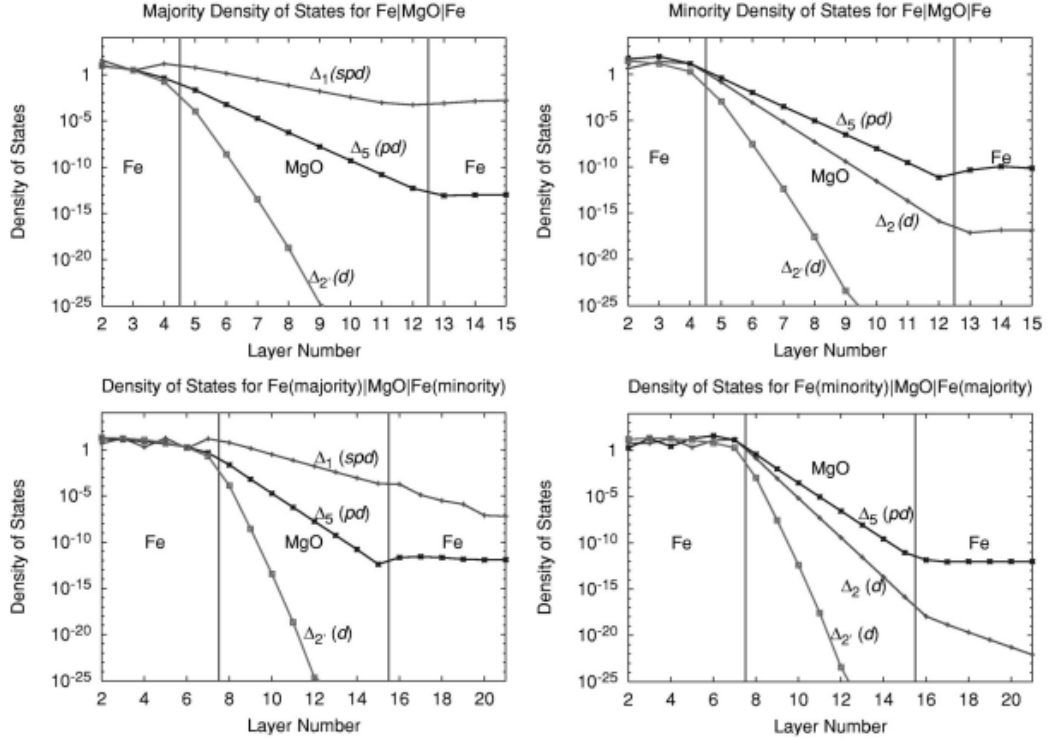


Figure 1.3 Tunneling density of states (TDOS) for majority and minority bands in Fe|MgO|Fe in P state. Bottom row corresponds to majority-minority and minority-majority tunneling in the AP state. States labeled by symmetry. Taken from reference [9].

When the Fe electrodes are in the AP configuration, majority to minority and minority to majority tunneling contributes to the conductance. However, there is a hole in the tunneling density of states for the Δ_1 minority band near the Fermi energy at $\vec{k}_{\parallel} = 0$. The Δ_1 wave-functions are still evanescent into the right Fe electrode and the tunnel current is highly suppressed. Other bands contribute to the tunnel current (e.g, the Δ_5 bands) but their contributions in total are considerably smaller than that of the Δ_1 bands. The main point is that in the AP state there is a very strong increase in the resistance when compared with the P state. This implies a very large TMR that is

entirely generated by symmetry-based selection rules. Ab-initio calculations (optimistic) have estimated the TMR in the Fe|MgO|Fe system to be on the order of ~1000%.

High room temperature TMRs (of ~180%) in epitaxial Fe|MgO|Fe junctions were subsequently demonstrated by Yuasa et al. In addition, they observed oscillations (not commensurate with the MgO lattice spacing) of the TMR with MgO thickness indicative of coherent tunneling and interpreted as interference between oscillatory decaying Δ_1 and Δ_5 states within the MgO barrier [11]. Even higher TMR (~220%) in sputtered and annealed polycrystalline $\text{Co}_{70}\text{Fe}_{30}$ |MgO| $\text{Co}_{70}\text{Fe}_{30}$ junctions was demonstrated by Parkin et al [12]. The replacement of CoFe with as-deposited amorphous CoFeB electrodes (allowing for a large degree of layer uniformity and smoothness) in MgO-MTJs constituted a significant advance [13]. Subsequent demonstrations of TMR in these junctions after post-deposition annealing showed TMR percentages around 600% at room temperature (1160% at T= 5 K) [14]. The low temperature values of the TMR in these junctions get close to the theoretical limits. The existence of such high TMRs in these MTJs and relative magnetic softness of these electrodes have obvious implications for their use in MRAM and sensor applications.

1.5 The Spin Transfer Torque

Spin currents impinging upon thin ferromagnetic layers (a few nanometers-thick) can exert a torque on the ferromagnet. This phenomenon, known as The Spin

Transfer Torque (STT), was first predicted by Slonczewski [15] and its effects first experimentally observed by Tsoi et al. [16]

The STT, at least in ferromagnets with low spin orbital coupling (e.g. Fe, Ni, Co and all their alloys), relies on conservation of the spin angular momentum and the fact that the spin quantization axis of the spin current tensor is not collinear with the magnetization of the ferromagnet. It can be shown that the component of the spin current transverse to the magnetization vector experiences a discontinuity at the FM interface [17]. This discontinuity implies a torque on the magnetization that can be represented in the Landau-Lifshitz-Gilbert (LLG) dynamics of the magnetization as:

$$\frac{d\vec{m}}{dt} = -\gamma\vec{m} \times \vec{H}_{eff} + \alpha\vec{m} \times \frac{d\vec{m}}{dt} + \vec{\tau}_{\parallel}^{STT} + \vec{\tau}_{\perp}^{STT} \quad (1.5)$$

The first STT vector is known as the Slonczewski spin-torque and has the form:

$$\vec{\tau}_{\parallel}^{STT} = \gamma \frac{\eta(\theta)\hbar J}{2edM_s} \vec{m} \times (\vec{p} \times \vec{m}) \quad (1.6)$$

The second STT vector is typically called the perpendicular or field-like torque term and has the form:

$$\vec{\tau}_{\perp}^{STT} = \beta\gamma \frac{\eta(\theta)\hbar J}{2edM_s} \vec{m} \times \vec{p} \quad (1.7)$$

The field-like torque is generally considered small in metallic systems due to rapid precessional spin dephasing from electrons coming from different parts of the Fermi surface of the FM. However, the field-like torque will be important for any system where the component of the spin accumulation transverse to the magnetization

vector does not dephase rapidly or where the thickness of the ferromagnet is on the order of the transverse spin coherence length (i.e. on the order of $\sim 1-2$ nm). For example, the field-like torque is non-negligible in MgO MTJs where the tunneling and the spin-torque come from specific pockets in the 2D B.Z. (i.e. $k_{\parallel}=0$ for majority electrons).

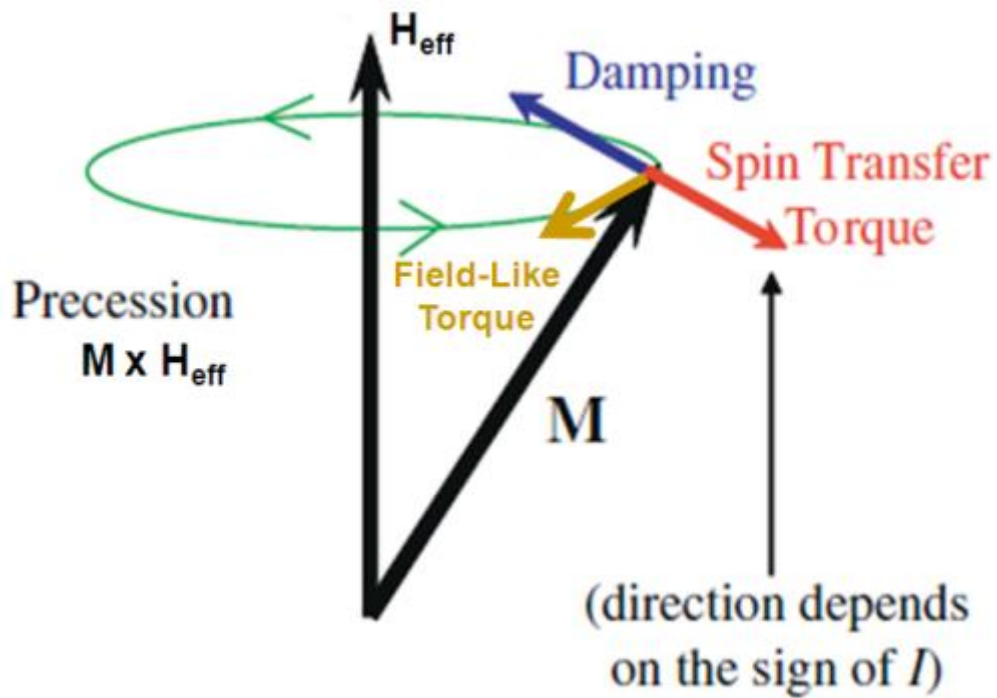


Figure 1.4 Diagram of torques on the magnetization as expressed in the LLG equation. When the polarization vector \vec{p} is near collinear with \vec{M} and \vec{H}_{eff} , the spin-torque acts either as a damping or anti-damping term and the field-like torque either adds to or subtracts the effective field (depending on whether \vec{p} is AP or P with respect to \vec{H}_{eff} and \vec{M}).

1.5.1 Spin Torques in FM|NM|FM Trilayers

Typically, FM|spacer|FM structures are used where one of the layers typically known as the fixed layer serves as a reference layer and an electron spin polarizer. The other layer is more readily influenced by field and the spin-torque and is known as the free layer. The spacer can be either a normal metal or a tunnel barrier. We will focus on the FM|NM|FM systems for the moment. In this geometry, electron current flow from the fixed to the free layer destabilizes the free layer when the electrode orientation is in the AP state and stabilizes the orientation when the layers are in the P state. When the electron current flows from the free to the fixed layer, the situation is a bit different. Electrons *reflected* from the reference layer and with spin polarization opposite to that of the fixed layer polarization exert a torque on the free layer magnetization. As the sign of the incident spin polarization is the opposite, the spin torque in this configuration will serve to destabilize the P state and stabilize the AP state. The basic schematic of this situation is illustrated in Figure 1.5.

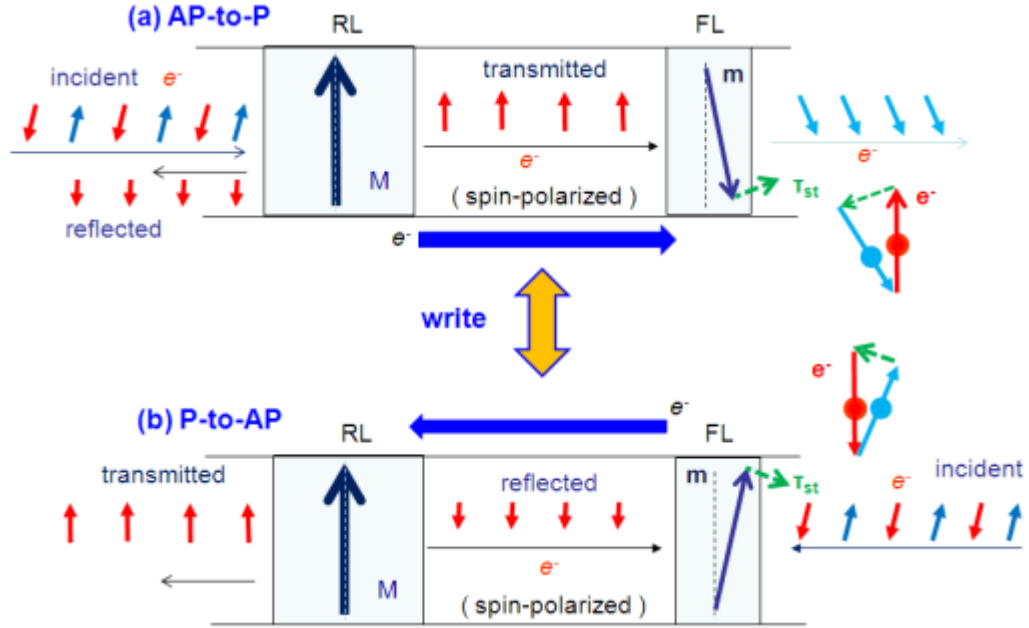


Figure 1.5 a) Shows spin-polarized electrons reflected and transmitted through reference layer (RL). Transmitted electrons will exert spin-torque that destabilizes AP state and acts as ant-damping torque on free layer. b) Reverse electron flow is required to destabilize the P case where the torque on the free layer comes from electrons reflected off the reference layer. Taken from reference [18].

This picture is actually a bit simplistic in an FM|NM|FM system, but serves as a good cartoon sketch. In reality there are multiple reflections between the free and fixed layers as well as spin diffusive process within the ferromagnetic electrodes and normal metal spacer that a self-consistent treatment of the actual magnitude of the torques should take into account. It has been shown that such spin-dependent reflections modify the spin-torque polarization function $\eta(\theta)$ [19]. For a general asymmetric electrode configuration $\eta(\theta)$ is given by [20]:

$$\eta(\theta) = \frac{q_+}{A + B \cos \theta} + \frac{q_-}{A - B \cos \theta} \quad (1.8)$$

1.5.2 Spin Torques in Magnetic Tunnel Junctions

The structure of the spin torque in magnetic tunnel junctions [21] differs from the spin-torque in all metallic nanostructures. First, it has been shown that the perpendicular torque is not negligible (as it is in metallic systems) and can be on the order of ~20-30% of the in-plane torque. The bias dependence of the spin-torque is also not as simple as in metallic structures where the torque is simply proportional to the current. Careful angle-dependent ST-FMR measurements have shown that the bias dependent part of the perpendicular torque $\tau_{\perp}(V) \propto V^2$ in a fairly large bias range $-.6V \leq V_{bias} \leq .6V$ (for a junction $RA=12\Omega\mu m^2$) [22]. The measured bias dependence of the perpendicular torque agrees with both ab-initio [23] and tight-binding calculations [24]. The measured in-plane torkance $\frac{d\tau_{\parallel}}{dV} = const. + f(V)$ exhibits a weak bias dependence in the experiment referenced [22]. In previous experiments it has been shown that in-plane torkance is bias independent (at least within the low voltage regime) [25]. This would imply that $\tau_{\parallel} \propto V$. Given this weak bias dependence of $\frac{d\tau_{\parallel}}{dV}$ in the low bias regime, the in-plane torkance can be expressed in terms of the angle between magnetization of the two ferromagnetic electrodes, the effective tunneling spin polarization factor, and the parallel conductance defined at $V = 0$ in the elastic coherent tunneling framework of Slonczewski [26]:

$$\frac{d\tau_{\parallel}}{dV}(V=0) = \frac{\hbar}{4e} \frac{2P_S}{1+P_S^2} \sin\theta \left(\frac{dI}{dV} \right)_P \Big|_{V=0} \quad (1.9)$$

Equation (1.9) reveals an important difference between FM|NM|FM and FM|I|FM systems. The theory predicts that the spin torque efficiency $\eta(\theta)$ has no angular dependence and that the only angular dependence of the torque comes from the cross product and thus varies as $\sin \theta$. This has to do with the fact that one does not need to consider multiple reflections and spin accumulation in the F|I|F system as one has to with the F|NM|F system. Lastly, we note that the torque per unit voltage is symmetric for the P and AP arrangement (for symmetric junctions). This implies that for MTJs where R_{AP} and R_P are very different, the torque per unit current can be very different for the P and AP states.

1.6 STT-Induced Magnetization Switching

Spin-torque driven switching of small nearly monodomain bodies was first demonstrated in CPP-GMR Co/Cu/Co nanopillars [27]. The discovery provided an unambiguous demonstration of the STT and that spin polarized currents could be used to manipulate magnetic bodies. STT-induced switching was eventually demonstrated in MTJs as well [28]. The free layer and fixed layers for these experiments were in the collinear geometry where the reversal is via anti-damping switching. When the current density (and in particular the spin-current density) is high enough and the sign of the current is such that the spin-torque cancels out the Gilbert damping, the magnetization starts to oscillate about its original equilibrium position ($\varphi = 0$). If the current density is high enough the magnetization amplitude will grow to the point where it tips over the anisotropy energy barrier and relaxes down to the new equilibrium position

at $\varphi = \pi$. During the relaxation process the spin torque acts as a damping torque to settle the magnetization. The entire switching process is illustrated in Figure 1.6a.

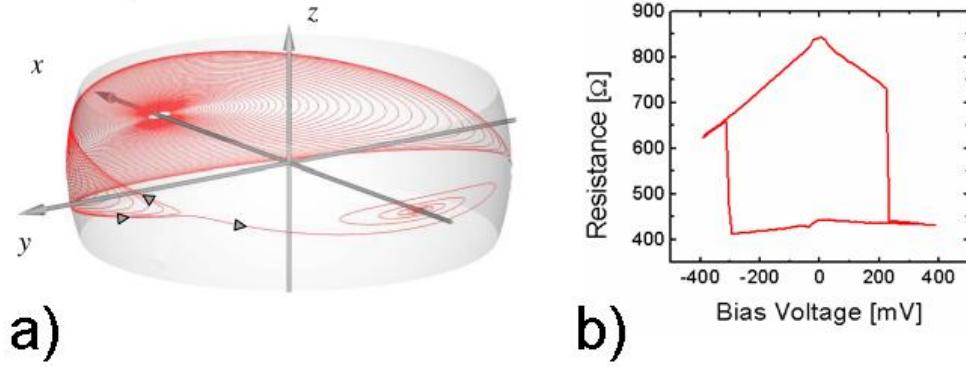


Figure 1.6 a) Anti-damping switching trajectory for an in-plane magnetized free layer. b) STT voltage switching curve for a CoFeB|MgO|CoFeB MTJ at $|H-H_{\text{dip}}|=0$.

The zero-temperature critical current instability for the anti-damping switching in the in-plane geometry is given by

$$J_{c0} \sim \frac{2ed\alpha M_s}{\hbar\eta(\theta)} \left(H_k + \frac{H_{\text{demag}}^{\text{eff}}}{2} \right) \quad (1.10)$$

When the free and fixed layers are both perpendicularly magnetized the critical current for anti-damping switching becomes

$$J_{c0} \sim \frac{2ed\alpha M_s}{\hbar\eta(\theta)} H_{k,eff}^\perp \quad (1.11)$$

In Equations (1.10) and (1.11), α is the Gilbert damping, d is the thickness of the free layer, $\eta(\theta)$ as the angular dependent spin-torque efficiency, H_k is the in-plane shape anisotropy of the free layer, $H_{demag}^{eff} = 4\pi M_s - H_k^\perp$ is the effective demagnetization field for an in-plane magnetized free layer that can be smaller than the full demagnetization due to a positive surface anisotropy contribution and $H_{k,eff}^\perp = H_k^\perp - 4\pi M_s$ is the effective perpendicular anisotropy field for an out-of-plane magnetized free layer. These expressions for the critical current are for $T = 0$ K and room temperature critical currents are generally substantially smaller due to the possibility of thermally activated reversal.

Switching in a geometry where the polarizer is magnetized out-of-plane with the free layer in plane has also been proposed [29], [30] and demonstrated experimentally [31], [32]. Here the magnetization reversal is precessional and ballistic in nature. The effect basically relies on the fact that the spin-torque acts to cant the magnetization slightly out-of-plane and that the free layer magnetization precesses about the effective demagnetization field. The simple picture is an idealization of the switching process and it has been shown that the effect of dipolar fields from the free and fixed layers, the spin-torque from additional layers (like an analyzer layer) and micromagnetic effects can be very important in understanding the nature of the switching.

1.7 STT-Driven Magnetization Dynamics

DC spin polarized current can also induce steady-state coherent microwave dynamics of the magnetization. This phenomenon essentially occurs when the spin torque anti-damping torque is large enough to balance out the Gilbert damping of the ferromagnet and the free energy landscape of the ferromagnet is such that the spin-torque stabilizes a limit cycle but where no other stable non-oscillatory states exist. For monodomain in-plane magnetized free layers with uniaxial anisotropy, this occurs when $H > H_k$ is applied along the easy axis. Under these conditions, a high enough anti-damping torque from the spin torque will cause in-plane precession. This oscillation of the free layer moment in a GMR or TMR stack structure will generate a microwave voltage. Magnetization dynamics of this kind was first observed by Kiselev et al. [33]. Since then DC-driven spin-torque dynamics have been studied in confined nanopillar FM|NM|FM structures, point-contacts [34], [35], and MTJs [36]–[38] with a whole host of magnetic layer structures and electrode configurations. More recent work has shown spin-transfer induced oscillations in SHE devices [39], [40]. Microwave emission induced by the spin-torque is attractive for a variety of reasons. These spin-torque driven oscillators being magnetic in nature have frequency tunability with field (1-10 MHz/Oe). They also can have considerable tunability with DC current bias (10-1000 MHz/mA). The essence of this frequency tunability comes from the fact that the frequency in these confined ferromagnets can depend heavily on the amplitude of the oscillations.

Perhaps the simplest case to consider is the DC spin-torque dynamics in the in-plane collinear electrode configuration. The dynamics in this configuration shows large red-shifting with I_{bias} . This red-shifting has been interpreted in terms of the theory of macro-spin orbits [41], [42] as being associated with the increasing amplitude of clam-shell type in-plane precessional (IPP) states. While the path-length of the orbit increases substantially as one increases the current density, the average orbital speed with which the magnetization traverses the path does not change significantly. This leads to a red-shifting of the oscillation frequency with I_{bias} and oscillation amplitude that can be substantial with $df/dI \sim -1 \text{ GHz/mA}$.

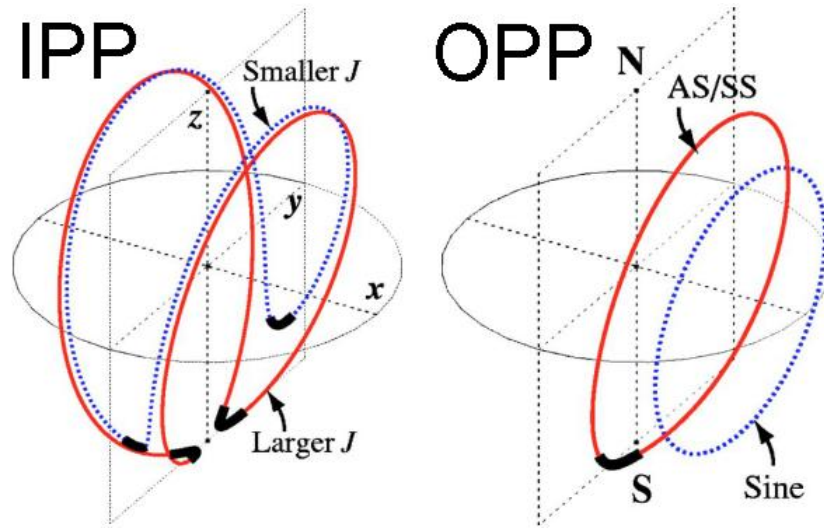


Figure 1.7 IPP clamshell and OPP type orbits as predicted by the macrosin model. The z-axis is the direction of the easy axis and the x-direction is normal to the magnetic film plane. Adapted from reference [41].

As the in-plane clamshell amplitude gets large enough with increasing current density, the macro-spin theory predicts that the orbits become unstable to a bifurcation and the orbits jump to a different trajectory where the precession axis is predominantly

out-of-plane. These out-of-plane precession (OPP) states are characterized by blue-shifting with increased current density. The predicted bifurcation of the macrospin model has been claimed to have been observed at high currents in the Py/Cu/Py system [43]. Blue-shifting with bias have also been observed in states where the magnetization has been saturated out of the plane or tilted out of plane by a large applied field [44] and is associated with the increase in the magnitude of the effective field as the oscillation amplitude increases. In general, however, the details of the dependence of frequency on bias can be quite subtle and will depend on the applied field direction and magnitude, the shape geometry and layer structure of the oscillator, magnetic moment orientation of the layers. For example, oscillators field-biased along the in-plane hard-axis can exhibit both weak blue-shifting and red-shifting and a cross-over regime where df/dI is relatively flat. We will, in fact, observe similar weak blue-shifting and red-shifting in our conditioned MTJ oscillators in Chapter 6. This weak blue-shifting observed in Figure 1.8 has nothing to do with out-of-plane precession as the trajectories of these hard-axis field bias oscillators are largely in-plane. The blue-shifting arises from the effect of the in-plane anisotropy as the oscillation power increases when the magnetization is hard-axis biased.

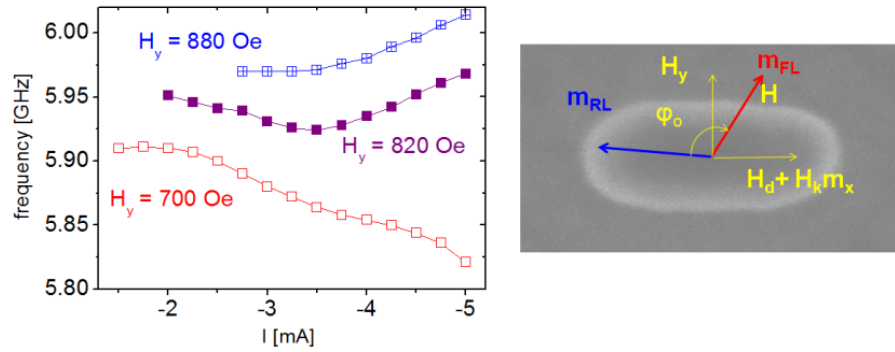


Figure 1.8 f vs. I_{dc} for different hard axis bias fields H_y in an in-plane free layer/in-plane reference layer FM|NM|FM device. Adapted from reference [18].

Besides the frequency behavior with current bias and field, another important characteristic of STNOs that needs to be understood and tailored is the oscillator linewidth. This is a direct measure of the coherence of the oscillator and it is often desirable to have a very low linewidth/phase noise for the oscillator. In general, there are many factors that can contribute to the linewidth. The first factor arises when there is either telegraphing between multiple competing modes or between metastable static states and dynamical modes. This telegraphing leads to a finite linewidth for each mode which is given as $\Delta f = \frac{1}{\pi\tau}$ where τ is the average dwell time in the state. In the case where the hopping out of a dynamical mode is well-described by thermally activation to another stable state (either dynamic or state) the expression for the linewidth becomes [45]:

$$\Delta f = \frac{1}{\pi} f_0 \exp[-E_b / k_B T] \quad (1.12)$$

This expression relies on the fact that the dynamic and static states of the oscillator can be characterized by an effective energy and are fully thermalized and described by the same temperature. A finite effective temperature, however, is not necessary to get this sort of line-width broadening. Chaotic dynamics associated with hopping between phase space attractors can yield similar effects even at $T = 0$ K as has been pointed out by K.J. Lee et al. [46]. Single-shot dynamics studies have shown that the simultaneous appearance of two broad peaks in spectrum analyzer measurements are actually hopping between the dynamical modes (on the scale of tens of nanoseconds) [47]. The linewidth broadening is then set by the dwell-times in each of the states. Spectrum analyzer measurements have also observed the presence of a broad dynamical peak with low frequency Lorentzian tails in the spectrum [48]. These line-width broadening and low frequency tails are associated with hopping between a dynamical and static state.

There are other contributions to linewidth that are not associated with mode hopping. At finite temperature a free running oscillator can exchange energy with the thermal bath. This exchange of energy leads to fluctuations in the amplitude and phase of the oscillator. In systems where the free-running oscillator frequency is independent of the amplitude, the phase fluctuations/diffusion gives rise to a broadening of the oscillator linewidth in the frequency domain. However, STNOs have frequency-amplitude nonlinear coupling and this adds an additional source of spectral broadening.

Slavin and Tiberkevitch have treated the problem of phase noise for STNOs where they have restricted the dynamics to a single oscillatory state with presumably an infinite dwell time. The basic starting point of the theory is a conversion of the LLG dynamics for a circular or elliptical precession to a first order ODE for a dimensional complex oscillation amplitude $c(t) = \sqrt{p(t)}e^{i\phi(t)}$.

$$\frac{dc(t)}{dt} + \left[i\omega(|c|^2) + \Gamma_+(|c|^2) - \Gamma_-(I, |c|^2) \right] c(t) = f(t) \quad (1.13)$$

Equation (1.13) is derived by recasting of the Cartesian magnetic coordinates into circular/elliptical coordinates associated with the oscillation and a Holstein-Primakoff transformation yielding the complex amplitude $c(t)$. In Equation (1.13), $\sqrt{p(t)}$ is the amplitude of the oscillator, $\phi(t)$ is the phase, $p = |c|^2$ is the dimensionless power of the oscillation, $\omega(|c|^2)$ is the power-dependent frequency of the auto-oscillation, $\Gamma_+(|c|^2) = \Gamma_G(1 + Q|c|^2 + Q'|c|^4 + \dots)$ is the nonlinear damping term, and $\Gamma_-(I, |c|^2) = \sigma I g(p)$ is the anti-damping term arising from the spin-torque. The terms Q, Q' and $g(p)$ depend on the polarizer and free layer geometry. In the collinear electrode case $g(p) = 1 - p$. $f(t)$ is a forcing term. The effects of thermal noise on the oscillator equation can be studied by making $f(t)$ be a Langevin-type forcing term. The statistics of $f(t)$ are uncorrelated white-noise distributed with an autocorrelation function $\langle f(t)f(t') \rangle = D\delta(t-t')$. D is an effective diffusion constant

associated with the noise and is defined as $D = \Gamma_+(p) \frac{k_B T}{\varepsilon(p)}$ where $\frac{k_B T}{\varepsilon(p)}$ is the effective noise power at oscillator power p and $\varepsilon(p)$ is the energy of the oscillation. Auto-oscillations begin when $\Gamma_+(0) = \Gamma_-(I_{th}, 0)$ which defines the threshold current for spin-torque driven oscillations. The oscillation power p increases with current and in steady state the nonlinear damping term must at some point balance out the anti-damping term to stabilize the limit cycle at a power p_0 . At this condition, $\Gamma_+(p_0) = \Gamma_-(I, p_0)$.

Equation (1.13) reduces to

$$\frac{dc(t)}{dt} + i\omega(p_0)c(t) = 0 \quad (1.14)$$

The solutions to Equation (1.14) have the steady-state form

$c(t) = \sqrt{p_0} \exp[i\omega(p_0)t + i\phi_0]$. This solution obviously does not hold when the

Langevin forcing term is included and the now the solution

becomes $c(t) = \left(\sqrt{p_0 + \delta p(t)}\right) \exp[i\omega(p_0)t + i\phi_0(t)]$ where $\delta p(t) \ll p_0$. Expanding

$c(t), \omega(p) = \omega(p_0) + \left. \frac{d\omega(p)}{dp} \right|_{p=p_0} \delta p$ and Equation (1.13) about the noise-free

unperturbed trajectory yields two equations for the power fluctuations and the phase

respectively. $N = \left. \frac{d\omega(p)}{dp} \right|_{p=p_0}$ Note that the equations are coupled.

$$\begin{aligned} & \left. \frac{d\delta p(t)}{dt} + 2 \left(\frac{\partial \Gamma_+(p)}{\partial p} - \frac{\partial \Gamma_-(p, I)}{\partial p} \right) \right|_{p=p_0} p_0 \delta p(t) \\ & = \frac{d\delta p(t)}{dt} + 2\Gamma_{\text{eff}}(p_0) \delta p(t) = 2\sqrt{p_0} \text{Re}[f(t)e^{-i\phi}] \end{aligned} \quad (1.15)$$

$$\frac{d\phi}{dt} + \omega_g = \frac{1}{\sqrt{p_0}} \text{Im}[f(t)e^{-i\phi(t)}] - N\delta p(t) \quad (1.16)$$

$$\Gamma_{\text{eff}}(p_0) = \left. \left(\frac{\partial \Gamma_+(p)}{\partial p} - \frac{\partial \Gamma_-(p, I)}{\partial p} \right) \right|_{p=p_0} p_0 \text{ in Equation (1.15). In the limit}$$

that $\Delta\omega \ll \Gamma_{\text{eff}}(p_0)$ which is a good approximation, $\frac{d\delta p(t)}{dt} \sim \Delta\omega \delta p(t)$ and is

negligible compared to the other terms in Equation (1.15). We can then solve for

$\delta p(t) = \frac{\sqrt{p_0}}{\Gamma_{\text{eff}}(p_0)} \text{Re}[f(t)e^{-i\phi}]$ and placing this into Equation (1.16) yields:

$$\frac{d\phi}{dt} + \omega_g = \frac{1}{\sqrt{p_0}} \left[\text{Im}[f(t)e^{-i\phi(t)}] - \frac{N}{\left(\frac{d\Gamma_+(p)}{dp} - \frac{d\Gamma_-(p)}{dp} \right)} \text{Re}[f(t)e^{-i\phi}] \right] \quad (1.17)$$

$$\frac{d\phi}{dt} + \omega_g = \frac{1}{\sqrt{p_0}} \sqrt{1+\nu^2} \text{Im}[f(t)e^{-i\alpha-i\phi}]$$

Where $\alpha = \arctan[N / \left(\frac{d\Gamma_+(p)}{dp} - \frac{d\Gamma_-(p)}{dp} \right)]$ and

$\nu = N / \left(\frac{d\Gamma_+(p)}{dp} - \frac{d\Gamma_-(p)}{dp} \right) \Big|_{p=p_0}$ is the dimensionless frequency shift

parameter. Equation (1.17) reveals a phase diffusion which contributes to the

linewidth of the oscillator. From these equations, it can be shown that the power spectrum of the oscillator is Lorentzian and the linewidth is:

$$\Delta\omega = (1 + \nu^2) \Gamma_+(p_0) \frac{k_B T}{\varepsilon(p_0)} \quad (1.18)$$

The linewidth is equivalent to the case of a linear oscillator but renormalized by the factor $\sqrt{1 + \nu^2}$ which includes effects arising from nonlinear power-frequency coupling. The conclusion is that the linewidth is highly dependent on the dimensionless nonlinear frequency shift. In order to have a small linewidth it is desirable to make $\nu \ll 1$. This can be accomplished by making N small (i.e. have very low frequency nonlinearity), or by making the denominator large. A large denominator for ν means an enhanced dynamic damping for any fluctuations in the oscillation amplitude caused by the Langevin noise. The source of this effective dynamic damping can, in principle, come from local spatial variations in the magnetization and the spin-torque which serve to self-limit the effect that thermal fluctuations have on the amplitude noise. In Chapter 6, we will investigate dynamics in conditioned magnetic tunnel junctions where spatial variations in the magnetization and in the spin-torque distribution can lead to a high degree of time-coherence and where it is possible that both the small N and large dynamic damping mechanisms are at work.

Besides reducing the linewidth of a single oscillator by tailoring the nonlinearities in the system via layer structure and field geometry, there have been many schemes used to externally reduce/manipulate the linewidth of these oscillators. Some of these include injection locking [49], [50], fractional locking and parametric

pumping [51], mutual oscillator phase-locking (via spin-wave coupling) [52], [53], etc. While much of the work has focused on mutual STNO coupling or injection locking to coherent electrical microwave signals, in Chapter 4 we will look at the possibility of coupling STNOs and magnetic thin films to GHz frequency acoustic phonons.

1.8 Spin Pumping

We have so far talked a great deal about the spin-transfer torque and the classes of dynamics that can be achieved by spin current injection into a ferromagnet. We now change tracks and discuss a reciprocal effect known as spin pumping.

The strong hybridization of the conduction electron fluid near the interface of a transition metal ferromagnetic|normal metal (FM|NM) bilayer with the d-bands of the ferromagnet give rise to a whole host of interesting phenomena. In equilibrium, the static part of this hybridization gives rise to a spatially decaying oscillatory spin polarization of the conduction electron fluid in the NM as one goes away from the interface. This oscillating spin density in the spacer gives rise to the interlayer exchange coupling (IEC) between two ferromagnets in an FM|NM|FM system. In the limit that the conduction electron-ferromagnet interactions are treated as a sheet-like s-d exchange interaction at the interface, the spin density oscillation follows the form of the sheet-RKKY range function. Spin pumping is precisely the phenomenon that describes what happens to this induced spin density in the conduction electron fluid of NM when the magnetization starts to precess. The process is thus related to the dynamic spin susceptibility of the conduction electron fluid.

Spin pumping is the production of a time-dependent oscillatory pure spin current pumped into NM by the precession of the magnetization in an FM|NM system. There are many ways to derive this phenomenon (scattering matrix theory [54], rotating frame analysis [55], etc.) but we like the linear response formalism [56], [57] due to the intuition it provides. The conduction electron fluid extending throughout the NM experiences an exchange field at the FM|NM interface. The Hamiltonian for this interfacial s-d exchange (with localized ferromagnets) can be written as:

$$H' = -\Delta \sum_i^{sheet} \int_V d^3 \vec{r} \left(\vec{s}(\vec{r}) \cdot \vec{S}(\vec{r}_i, t) \right) \delta(\vec{r} - \vec{r}_i) \quad (1.19)$$

The sheet-like localized s-d exchange Hamiltonian is a bit of an idealization particularly in transition-metal FM|NM systems. However, it serves to illustrate the main point we are trying to make. The s-d exchange Hamiltonian implies that the magnetization provides a torque on the spins of the conduction electrons. The spins of the conduction electrons therefore also provide a reaction torque on the ferromagnet.

The field that this reaction torque exerts on a local interfacial moment at a time t

is $\vec{H}_{eff,i}(0,t) = \frac{\Delta}{\gamma} \langle \vec{s}(z=0,t) \rangle$ where we have assumed that the torque of the conduction

electron fluid on the magnetization should be localized to the interface. This

assumption is justifiable in that any spin density transverse to the magnetization

decays away within the spin coherence length. The reaction field on the entire

ferromagnet can be shown to be $\vec{H}_{eff}(t) = \frac{\Delta a}{\gamma d} \langle \vec{s}(z=0,t) \rangle$. The average is an

expectation value and can be found by the linear response of the conduction electron spins to the magnetization. This is expressed as:

$$\begin{aligned}\langle s_\mu(\vec{r}, t) \rangle &= \Delta \sum_i^{sheet} \int_{-\infty}^{\infty} dt' \chi_{\mu\nu}(\vec{r}, \vec{r}_i, t') S(\vec{r}_i, t-t') \\ &= \frac{\Delta\Omega}{\gamma} \sum_i^{sheet} \int_{-\infty}^{\infty} dt' \chi_{\mu\nu}(\vec{r}, \vec{r}_i, t') \vec{M}(t-t')\end{aligned}\quad (1.20)$$

We use the relationship between the magnetization of the entire ferromagnet and the

local spins (assuming macrospin) $\vec{S}(\vec{r}_i, t) = \frac{\Omega}{\gamma} \vec{M}(t)$ where Ω is the volume of the

ferromagnet. We can expand Equation (1.20) under the assumption that the

magnetization motion is slow $M(t-t') = M(t) - t' \frac{dM(t)}{dt}$ and perform the sum over

the localized spins. We can express the average induced conduction electron spin

density depends (i.e. the coordinate normal to the FM|NM interface), we can integrate

Equation (1.20) over the interface

$$\begin{aligned}\langle s_\mu(z, t) \rangle &= \frac{\Delta\Omega}{\gamma} \lim_{\omega \rightarrow 0} \left[\text{Re} X_{\mu\nu}(z, \omega) M_\nu(t) - \frac{\partial \text{Im} X_{\mu\nu}(z, \omega)}{\partial \omega} \frac{dM_\nu(t)}{dt} \right] \\ X_{\mu\nu}(z, \omega) &= n_s \int_{-\infty}^{+\infty} \frac{dq_\perp}{2\pi} e^{iq_\perp z} \chi_{\mu\nu}(q_\perp, \omega)\end{aligned}\quad (1.21)$$

Here n_s is the sheet density of localized FM spins and Ω is the volume of the

ferromagnet. The component of this induced spin density at $z = 0$ transverse to the

magnetization generates the reaction torque $\vec{\tau} = \frac{\Delta a}{\gamma d} \vec{m} \times \langle \vec{s}(z=0, t) \rangle$ on the entire

ferromagnet. Evaluating Equation (1.21) at $z = 0$ and assuming all off diagonal terms

in the spin susceptibility are zero and that the response is isotropic yields a very simple expression for the torque:

$$\vec{\tau}_{sd} = -\gamma \vec{m} \times \vec{H}_{eff}(t) = \left\{ \frac{\Delta^2 \Omega a}{\gamma d} \frac{\partial}{\partial \omega} \int_{-\infty}^{\infty} \frac{dq}{2\pi} \text{Im}[\chi(q, \omega)] \right\} \vec{m} \times \frac{d\vec{m}}{dt} \quad (1.22)$$

The reaction torque is essentially due to the phase lag of the spin-response of the conduction electron sea with respect to the magnetization precession. This is clear from the fact that the reaction torque depends explicitly on the imaginary part of the susceptibility of the conduction electron sea in Equation (1.22). This out-of phase response of the electron sea generates an additional damping term on the magnetization. Note that the entire wave-vector structure of the conduction electrons at the interface (i.e. band structure, Fermi surface topography, interfacial hybridization, etc.) is built into the damping torque through the integral over the response function.

It can be shown, for general non-diagonal/anisotropic $\chi_{\mu\nu}$, that the form for the reaction torque on the entire FM is:

$$\vec{\tau}_{sd} = -\gamma \vec{m} \times \vec{H}_{eff}(t) = \Lambda_1 \frac{d\vec{m}}{dt} + \Lambda_2 \vec{m} \times \frac{d\vec{m}}{dt} \quad (1.23)$$

A derivation of this form is given by Mills [56]. The first torque term renormalizes the precession frequency. The second torque adds dissipation and serves to enhance the Gilbert damping. These two torques by conservation of spin angular momentum are

equivalent to spin currents emitted at the FM|NM interface and can be rewritten in the more familiar notation:

$$\vec{j}_s^{pump} = \frac{\hbar}{4\pi} \left(g_r^{\uparrow\downarrow} \bar{m} \times \frac{d\bar{m}}{dt} + g_i^{\uparrow\downarrow} \frac{d\bar{m}}{dt} \right) \quad (1.24)$$

Here $g_r^{\uparrow\downarrow}$ and $g_i^{\uparrow\downarrow}$ corresponds to the real part and imaginary part of mixing conductance respectively and clearly have the physics of the s-d hybridization, the interfacial band structure, and the conduction electron spin response tucked inside them. We have operated under the assumption that the NM is infinite and that pumped spin current never returns to the ferromagnet. For a finite NM there is also a backflow spin current associated with the $\vec{j}_s = 0$ boundary condition at the edge of the NM at $x = L$ (Figure 1.9).

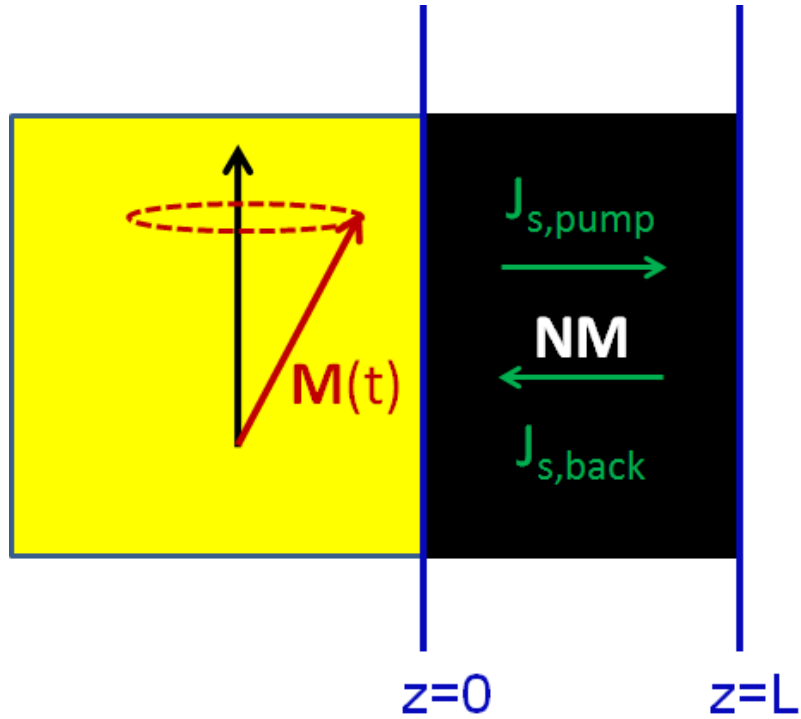


Figure 1.9 FM|NM bilayer and schematic of spin-pumping with precessing magnetization.

The backflow serves to reduce the effect of increased damping. In general, the measured spin current and the contribution to the magnetization damping from spin pumping in a FM|NM bilayer system has the details of the backflow and spin diffusion in the NM contained within it. This extracted quantity is the effective spin mixing conductance $g_{r,eff}^{\uparrow\downarrow}$ and is related to $g_r^{\uparrow\downarrow}$ by the following equation:

$$g_{r,eff}^{\uparrow\downarrow} = \frac{g_r^{\uparrow\downarrow}}{1 + \left[\sqrt{\varepsilon} \tanh(L / \lambda_{sd}) \right]^{-1}} \quad (1.25)$$

In the above equation, $\varepsilon = \tau / \tau_{sf}$ is the ratio of momentum to spin flip scattering time.

λ_{sd} is the spin diffusion length of the normal metal and L is the thickness of the

normal metal. The relation is derived by solving for the net emitted spin current at the FM|NM interface using the spin diffusion equation and relevant boundary conditions for the spin currents and spin accumulation. One way to extract the $g_r^{\uparrow\downarrow}$ for a FM|NM bilayer is to conduct an FMR experiment and measure the Gilbert damping using both an FM and NM thickness series. This allows one to extract $g_{r,eff}^{\uparrow\downarrow}$ for different values of NM thickness and then use Equation (1.25) to extract the true $g_r^{\uparrow\downarrow}$.

1.9 The Spin Hall Effect (SHE) and Inverse Spin Hall Effect (ISHE)

The Spin Hall Effect was first proposed by Dyakonov and Perel [58] and then re-proposed by Hirsch [59]. The basic idea is that a charge current flowing through a material with high spin-orbit coupling generates a pure spin current transverse to the direction of charge current flow. The spin orientation of the generated spin current points normal to the induced spin current propagation direction and the charge current direction. The situation is illustrated below in the first panel in Figure 1.10 a.

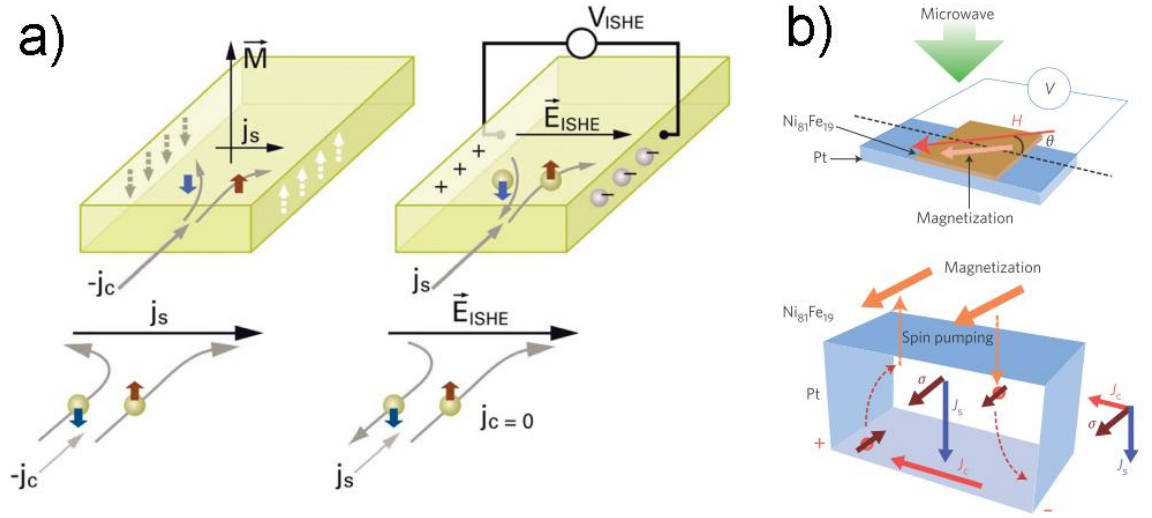


Figure 1.10 a) Illustration of SHE and ISHE processes. Adapted from reference [60] b) Pure spin currents injected into spin hall metal by resonant magnetization dynamics and spin pumping. Pure spin currents measured by charge voltage generated by ISHE. Adapted from reference [61].

By Onsager reciprocity, a pure spin current flowing in such a material will generate a charge current transverse to the spin flow direction. This reciprocal effect is known as the Inverse Spin Hall Effect (ISHE). The basic equations governing these two phenomena are given in Equation (1.26):

$$\begin{aligned}\vec{j}_s &= \frac{\theta_{SH}}{e} \frac{\hbar}{2} (\vec{j}_c \times \vec{\sigma}) \\ \vec{j}_c &= \theta_{SH} \frac{2e}{\hbar} (\vec{j}_s \times \vec{\sigma})\end{aligned}\tag{1.26}$$

θ_{SH} is the Spin Hall angle and is often defined as j_s/j_c (the ratio of the spin current to the charge current). It is also defined as the ratio of the off-diagonal spin to

longitudinal charge conductivity $\theta_{SH} = \frac{2e}{\hbar} \frac{\sigma_{xy}^s}{\sigma_{xx}}$. There are three mechanisms for this

charge current to spin current conversion. The first is intrinsic in nature and does not require scattering but is instead due to off-diagonal spin conductivities arising from the band structure in the presence of spin-orbit coupling. The last two mechanisms are known as skew-scattering and side-jump scattering and are associated with the opposite deflection that electrons of opposite spin experience upon scattering in the presence of large spin-orbit coupling. The processes are pictorially represented in Figure 1.11.

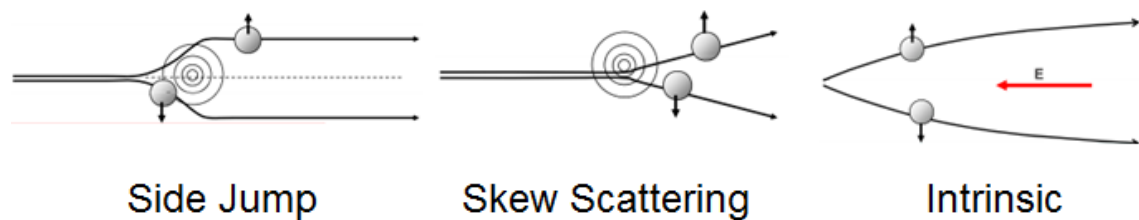


Figure 1.11 Representation of the processes contributing to the spin Hall conductivity. Adapted from [62].

The first demonstration of the SHE in a metallic system was in Al using a non-local voltage measurement [63]. Since then systematic and careful measurements demonstrated that very large spin Hall angles in heavy metals are possible.

Measurements of the SHE in Pt ($\theta_{SH} \sim .07$) [64], Ta ($\theta_{SH} \sim -.18$) [65],

W ($\theta_{SH} \sim -.30$) [66], Ir ($\theta_{SH} \sim .09$) and a few other elements and alloys have been carried out reporting large spin Hall angles. In Ta and W, in particular, the spin Hall angles are high enough to generate enough spin current to switch a nanomagnet in a three-terminal (3T) structure .

In systems where monodomain switching can be induced by SHE torques in a 3T device, θ_{SH} can be extracted from current ramp rate measurements. ST-FMR in bilayer systems has also proven to be a powerful technique for characterizing θ_{SH} although not without its artifacts and pitfalls. More recently, adiabatic lock-in techniques employing measurement of the first and second harmonic voltages of NM|FM in Hall bar devices have been used to measure current-induced torques (showing both Slonczewski and perpendicular torques) on the FM [67]–[69]. This method works well for devices with perpendicular anisotropy and the measurement of longitudinal and transverse torques has raised some interesting questions about the relationship between the torques and the nature of the spin-transport at these interfaces. θ_{SH} can be extracted by this method. Some have also used ferromagnetic resonance techniques using cavity FMR [70] and CPW geometries [71] in NM|FM bilayer systems in order to quantify θ_{SH} . Here spin pumping and ISHE voltage detection are used in tandem to extract the spin hall angle. We will use the spin pumping/ISHE combination to resonantly convert surface acoustic phonons into pure spin currents and as an aid in studying the structure of SAW-drive magnetization dynamics in Chapter 4.

REFERENCES

- [1] T. R. McGuire and R. I. Potter, “Anisotropic Magnetoresistance in Ferromagnetic 3d Alloys,” *IEEE Trans. Magn.*, vol. 11, pp. 1018–1038, 1975.
- [2] M. N. Baibich, J. M. Broto, A. Fert, F. N. van Dau, F. Petroff, P. Eitenne, G. Creuzet, A. Freiderich, and J. Chazelas, “Giant Magnetoresistance of (001)Fe/(001)Cr Magnetic Superlattices,” *Phys. Rev. Lett.*, vol. 61, p. 2473, 1988.
- [3] G. Binasch, P. Grunberg, F. Saurenbach, and W. Zinn, “Enhanced magnetoresistance in layered magnetic structures,” *Phys. Rev. B*, vol. 39, no. 7, pp. 4828–4830, 1989.
- [4] T. Valet and A. Fert, “Theory of perpendicular magnetoresistance in magnetic multilayers,” *Phys. Rev. B*, vol. 48, p. 7099, 1993.
- [5] J. Moodera, L. Kinder, T. Wong, and R. Meservey, “Large magnetoresistance at room temperature in ferromagnetic thin film tunnel junctions,” *Phys. Rev. Lett.*, vol. 74, no. 16, pp. 3273–3276, 1995.
- [6] T. Miyazaki and N. Tezuka, “Giant magnetic tunneling effect in Fe / Al₂O₃ / Fe junction,” vol. 139, pp. 94–97, 1995.
- [7] X.-F. Han, M. Oogane, H. Kubota, Y. Ando, and T. Miyazaki, “Fabrication of high-magnetoresistance tunnel junctions using Co₇₅Fe₂₅ ferromagnetic electrodes,” *Appl. Phys. Lett.*, vol. 77, no. 2, p. 283, 2000.
- [8] J. M. Maclaren and W. H. Butler, “Validity of the Julliere model of spin-dependent tunneling,” vol. 56, no. 18, pp. 827–832, 2008.
- [9] W. Butler, X.-G. Zhang, T. Schulthess, and J. MacLaren, “Spin-dependent tunneling conductance of Fe|MgO|Fe sandwiches,” *Phys. Rev. B*, vol. 63, no. 5, p. 054416, Jan. 2001.
- [10] J. Mathon and A. Umerski, “Theory of tunneling magnetoresistance of an epitaxial Fe/MgO/Fe(001) junction,” *Phys. Rev. B*, vol. 63, no. 22, p. 220403, May 2001.
- [11] S. Yuasa, T. Nagahama, A. Fukushima, Y. Suzuki, and K. Ando, “Giant room-temperature magnetoresistance in single-crystal Fe/MgO/Fe magnetic tunnel junctions,” *Nat. Mater.*, vol. 3, no. 12, pp. 868–71, Dec. 2004.

- [12] S. S. P. Parkin, C. Kaiser, A. Panchula, P. M. Rice, B. Hughes, M. Samant, and S.-H. Yang, “Giant tunnelling magnetoresistance at room temperature with MgO (100) tunnel barriers,” *Nat. Mater.*, vol. 3, no. 12, pp. 862–7, Dec. 2004.
- [13] D. D. Djayaprawira, K. Tsunekawa, M. Nagai, H. Maehara, S. Yamagata, N. Watanabe, S. Yuasa, Y. Suzuki, and K. Ando, “230% room-temperature magnetoresistance in CoFeB/MgO/CoFeB magnetic tunnel junctions,” *Appl. Phys. Lett.*, vol. 86, no. 9, p. 092502, 2005.
- [14] S. Ikeda, J. Hayakawa, Y. Ashizawa, Y. M. Lee, K. Miura, H. Hasegawa, M. Tsunoda, F. Matsukura, and H. Ohno, “Tunnel magnetoresistance of 604% at 300 K by suppression of Ta diffusion in CoFeB/MgO/CoFeB pseudo-spin-valves annealed at high temperature,” *Appl. Phys. Lett.*, vol. 93, no. 8, p. 082508, 2008.
- [15] J. C. Slonczewski, “Current-driven excitation of magnetic multilayers,” *J. Magn. Magn. Mater.*, vol. 159, no. 1–2, pp. L1–L7, Jun. 1996.
- [16] M. Tsoi, A. G. M. Jansen, J. Bass, W. Chiang, V. Tsoi, and P. Wyder, “Generation and detection of phase-coherent current-driven magnons in magnetic multilayers,” *Nature*, vol. 406, p. 46, 2000.
- [17] D. C. Ralph and M. D. Stiles, “Spin transfer torques,” *J. Magn. Magn. Mater.*, vol. 320, no. 7, pp. 1190–1216, Apr. 2008.
- [18] O. J. Lee, “Thesis: Non-Collinear Spin-Torque Driven Excitations in Nanomagnets,” Cornell University, 2013.
- [19] J. C. Slonczewski, “Currents and torques in metallic magnetic multilayers,” vol. 247, no. January, pp. 324–338, 2002.
- [20] J. Xiao, A. Zangwill, and M. Stiles, “Boltzmann test of Slonczewski’s theory of spin-transfer torque,” *Phys. Rev. B*, vol. 70, no. 17, p. 172405, Nov. 2004.
- [21] J. Z. Sun and D. C. Ralph, “Magnetoresistance and spin-transfer torque in magnetic tunnel junctions,” *J. Magn. Magn. Mater.*, vol. 320, no. 7, pp. 1227–1237, Apr. 2008.
- [22] C. Wang, Y.-T. Cui, J. Sun, J. Katine, R. Buhrman, and D. Ralph, “Bias and angular dependence of spin-transfer torque in magnetic tunnel junctions,” *Phys. Rev. B*, vol. 79, no. 22, p. 224416, Jun. 2009.
- [23] C. Heiliger and M. Stiles, “Ab Initio Studies of the Spin-Transfer Torque in Magnetic Tunnel Junctions,” *Phys. Rev. Lett.*, vol. 100, no. 18, p. 186805, May 2008.

- [24] I. Theodonis, N. Kioussis, A. Kalitsov, M. Chshiev, and W. Butler, “Anomalous Bias Dependence of Spin Torque in Magnetic Tunnel Junctions,” *Phys. Rev. Lett.*, vol. 97, no. 23, p. 237205, Dec. 2006.
- [25] J. C. Sankey, Y.-T. Cui, J. Z. Sun, J. C. Slonczewski, R. A. Buhrman, and D. C. Ralph, “Measurement of the spin-transfer-torque vector in magnetic tunnel junctions,” *Nat. Phys.*, vol. 4, no. 1, pp. 67–71, Nov. 2007.
- [26] J. Slonczewski, “Currents, torques, and polarization factors in magnetic tunnel junctions,” *Phys. Rev. B*, vol. 71, no. 2, p. 024411, Jan. 2005.
- [27] J. Katine, F. Albert, R. Buhrman, E. Myers, and D. Ralph, “Current-driven magnetization reversal and spin-wave excitations in Co /Cu /Co pillars,” *Phys. Rev. Lett.*, vol. 84, no. 14, pp. 3149–52, Apr. 2000.
- [28] G. D. Fuchs, N. C. Emley, I. N. Krivorotov, P. M. Braganca, E. M. Ryan, S. I. Kiselev, J. C. Sankey, D. C. Ralph, R. A. Buhrman, and J. A. Katine, “Spin-transfer effects in nanoscale magnetic tunnel junctions,” *Appl. Phys. Lett.*, vol. 85, no. 7, p. 1205, 2004.
- [29] A. D. Kent, B. Özyilmaz, and E. del Barco, “Spin-transfer-induced precessional magnetization reversal,” *Appl. Phys. Lett.*, vol. 84, no. 19, p. 3897, 2004.
- [30] K. J. Lee, O. Redon, and B. Dieny, “Analytical investigation of spin-transfer dynamics using a perpendicular-to-plane polarizer,” *Appl. Phys. Lett.*, vol. 86, no. 2, p. 022505, 2005.
- [31] O. J. Lee, V. S. Pribiag, P. M. Braganca, P. G. Gowtham, D. C. Ralph, and R. A. Buhrman, “Ultrafast switching of a nanomagnet by a combined out-of-plane and in-plane polarized spin current pulse,” *Appl. Phys. Lett.*, vol. 95, no. 1, p. 012506, 2009.
- [32] G. E. Rowlands, T. Rahman, J. A. Katine, J. Langer, A. Lyle, H. Zhao, J. G. Alzate, A. A. Kovalev, Y. Tserkovnyak, Z. M. Zeng, H. W. Jiang, K. Galatsis, Y. M. Huai, P. K. Amiri, K. L. Wang, I. N. Krivorotov, and J.-P. Wang, “Deep subnanosecond spin torque switching in magnetic tunnel junctions with combined in-plane and perpendicular polarizers,” *Appl. Phys. Lett.*, vol. 98, no. 10, p. 102509, 2011.
- [33] S. I. Kiselev, J. C. Sankey, I. N. Krivorotov, N. C. Emley, R. J. Schoelkopf, R. A. Buhrman, and D. C. Ralph, “Microwave oscillations of a nanomagnet driven by a spin-polarized current,” *Nature*, vol. 425, no. 6956, pp. 380–3, Sep. 2003.

- [34] W. Rippard, M. Pufall, S. Kaka, T. Silva, and S. Russek, “Current-driven microwave dynamics in magnetic point contacts as a function of applied field angle,” *Phys. Rev. B*, vol. 70, no. 10, p. 100406, Sep. 2004.
- [35] T. J. Silva and W. H. Rippard, “Developments in nano-oscillators based upon spin-transfer point-contact devices,” *J. Magn. Magn. Mater.*, vol. 320, no. 7, pp. 1260–1271, Apr. 2008.
- [36] A. M. Deac, A. Fukushima, H. Kubota, H. Maehara, Y. Suzuki, S. Yuasa, Y. Nagamine, K. Tsunekawa, D. D. Djayaprawira, and N. Watanabe, “Bias-driven high-power microwave emission from MgO-based tunnel magnetoresistance devices,” *Nat. Phys.*, vol. 4, no. 10, pp. 803–809, Aug. 2008.
- [37] D. Houssameddine, S. H. Florez, J. a. Katine, J.-P. Michel, U. Ebels, D. Mauri, O. Ozatay, B. Delaet, B. Viala, L. Folks, B. D. Terris, and M.-C. Cyrille, “Spin transfer induced coherent microwave emission with large power from nanoscale MgO tunnel junctions,” *Appl. Phys. Lett.*, vol. 93, no. 2, p. 022505, 2008.
- [38] D. Houssameddine, U. Ebels, B. Dieny, K. Garello, J.-P. Michel, B. Delaet, B. Viala, M.-C. Cyrille, J. Katine, and D. Mauri, “Temporal Coherence of MgO Based Magnetic Tunnel Junction Spin Torque Oscillators,” *Phys. Rev. Lett.*, vol. 102, no. 25, p. 257202, Jun. 2009.
- [39] R. Liu, W. Lim, and S. Urazhdin, “Spectral Characteristics of the Microwave Emission by the Spin Hall Nano-Oscillator,” *Phys. Rev. Lett.*, vol. 110, no. 14, p. 147601, Apr. 2013.
- [40] L. Liu, C.-F. Pai, D. C. Ralph, and R. A. Buhrman, “Magnetic Oscillations Driven by the Spin Hall Effect in 3-Terminal Magnetic Tunnel Junction Devices,” *Phys. Rev. Lett.*, vol. 109, no. 18, p. 186602, Oct. 2012.
- [41] J. Xiao, A. Zangwill, and M. Stiles, “Macrospin models of spin transfer dynamics,” *Phys. Rev. B*, vol. 72, no. 1, p. 014446, Jul. 2005.
- [42] S. Russek, S. Kaka, W. Rippard, M. Pufall, and T. Silva, “Finite-temperature modeling of nanoscale spin-transfer oscillators,” *Phys. Rev. B*, vol. 71, no. 10, p. 104425, Mar. 2005.
- [43] S. Kiselev, J. Sankey, I. Krivorotov, N. Emley, A. Garcia, R. Buhrman, and D. Ralph, “Spin-transfer excitations of permalloy nanopillars for large applied currents,” *Phys. Rev. B*, vol. 72, no. 6, p. 064430, Aug. 2005.
- [44] S. Kiselev, J. Sankey, I. Krivorotov, N. Emley, M. Rinkoski, C. Perez, R. Buhrman, and D. Ralph, “Current-Induced Nanomagnet Dynamics for

- Magnetic Fields Perpendicular to the Sample Plane,” *Phys. Rev. Lett.*, vol. 93, no. 3, p. 036601, Jul. 2004.
- [45] J. Sankey, I. Krivorotov, S. Kiselev, P. Braganca, N. Emley, R. Buhrman, and D. Ralph, “Mechanisms limiting the coherence time of spontaneous magnetic oscillations driven by dc spin-polarized currents,” *Phys. Rev. B*, vol. 72, no. 22, p. 224427, Dec. 2005.
- [46] K.-J. Lee, A. Deac, O. Redon, J.-P. Nozières, and B. Dieny, “Excitations of incoherent spin-waves due to spin-transfer torque,” *Nat. Mater.*, vol. 3, no. 12, pp. 877–81, Dec. 2004.
- [47] I. Krivorotov, N. Emley, R. Buhrman, and D. Ralph, “Time-domain studies of very-large-angle magnetization dynamics excited by spin transfer torques,” *Phys. Rev. B*, vol. 77, no. 5, p. 054440, Feb. 2008.
- [48] M. Pufall, W. Rippard, S. Kaka, S. Russek, T. Silva, J. Katine, and M. Carey, “Large-angle, gigahertz-rate random telegraph switching induced by spin-momentum transfer,” *Phys. Rev. B*, vol. 69, no. 21, p. 214409, Jun. 2004.
- [49] W. Rippard, M. Pufall, S. Kaka, T. Silva, S. Russek, and J. Katine, “Injection Locking and Phase Control of Spin Transfer Nano-oscillators,” *Phys. Rev. Lett.*, vol. 95, no. 6, p. 067203, Aug. 2005.
- [50] B. Georges, J. Grollier, M. Darques, V. Cros, C. Deranlot, B. Marcilhac, G. Faini, and A. Fert, “Coupling Efficiency for Phase Locking of a Spin Transfer Nano-Oscillator to a Microwave Current,” *Phys. Rev. Lett.*, vol. 101, no. 1, p. 017201, Jul. 2008.
- [51] S. Urazhdin, P. Tabor, V. Tiberkevich, and A. Slavin, “Fractional Synchronization of Spin-Torque Nano-Oscillators,” *Phys. Rev. Lett.*, vol. 105, no. 10, p. 104101, Aug. 2010.
- [52] S. Kaka, M. R. Pufall, W. H. Rippard, T. J. Silva, S. E. Russek, and J. A. Katine, “Mutual phase-locking of microwave spin torque nano-oscillators,” *Nature*, vol. 437, no. 7057, pp. 389–92, Sep. 2005.
- [53] F. B. Mancoff, N. D. Rizzo, B. N. Engel, and S. Tehrani, “Phase-locking in double-point-contact spin-transfer devices,” *Nature*, vol. 437, no. 7057, pp. 393–5, Sep. 2005.
- [54] Y. Tserkovnyak, A. Brataas, and G. Bauer, “Spin pumping and magnetization dynamics in metallic multilayers,” *Phys. Rev. B*, vol. 66, no. 22, p. 224403, Dec. 2002.

- [55] Y. Tserkovnyak, A. Brataas, and B. I. Halperin, “Nonlocal magnetization dynamics in ferromagnetic heterostructures,” vol. 77, no. October, 2005.
- [56] D. Mills, “Ferromagnetic resonance relaxation in ultrathin metal films: The role of the conduction electrons,” *Phys. Rev. B*, vol. 68, no. 1, p. 014419, Jul. 2003.
- [57] E. Šimánek and B. Heinrich, “Gilbert damping in magnetic multilayers,” *Phys. Rev. B*, vol. 67, no. 14, p. 144418, Apr. 2003.
- [58] M. I. D’yakonov and V. I. Perel’, “Possibility of Orienting Electron Spins with Current,” *ZheTF Pis. Red.*, vol. 13, no. 11, pp. 657–660, 1971.
- [59] J. Hirsch, “Spin Hall Effect,” *Phys. Rev. Lett.*, vol. 83, no. 9, pp. 1834–1837, Aug. 1999.
- [60] S. R. Boona, R. C. Myers, and J. P. Heremans, “Spin caloritronics,” *Energy Environ. Sci.*, vol. 7, no. 3, p. 885, 2014.
- [61] T. Jungwirth, J. Wunderlich, and K. Olejník, “Spin Hall effect devices,” *Nat. Mater.*, vol. 11, no. 5, pp. 382–90, May 2012.
- [62] N. Nagaosa, J. Sinova, S. Onoda, A. H. MacDonald, and N. P. Ong, “Anomalous Hall effect,” *Rev. Mod. Phys.*, vol. 82, no. 2, pp. 1539–1592, May 2010.
- [63] S. O. Valenzuela and M. Tinkham, “Direct electronic measurement of the spin Hall effect,” *Nature*, vol. 442, no. 7099, pp. 176–9, Jul. 2006.
- [64] L. Liu, T. Moriyama, D. C. Ralph, and R. A. Buhrman, “Spin-Torque Ferromagnetic Resonance Induced by the Spin Hall Effect,” *Phys. Rev. Lett.*, vol. 106, no. 3, p. 036601, Jan. 2011.
- [65] L. Liu, C.-F. Pai, Y. Li, H. W. Tseng, D. C. Ralph, and R. A. Buhrman, “Spin-torque switching with the giant spin Hall effect of tantalum,” *Science*, vol. 336, no. 6081, pp. 555–8, May 2012.
- [66] C.-F. Pai, L. Liu, Y. Li, H. W. Tseng, D. C. Ralph, and R. A. Buhrman, “Spin transfer torque devices utilizing the giant spin Hall effect of tungsten,” *Appl. Phys. Lett.*, vol. 101, no. 12, p. 122404, 2012.
- [67] M. Hayashi, J. Kim, M. Yamanouchi, and H. Ohno, “Quantitative characterization of the spin-orbit torque using harmonic Hall voltage measurements,” *Phys. Rev. B*, vol. 89, no. 14, p. 144425, Apr. 2014.

- [68] J. Kim, J. Sinha, M. Hayashi, M. Yamanouchi, S. Fukami, T. Suzuki, S. Mitani, and H. Ohno, “Layer thickness dependence of the current-induced effective field vector in Ta|CoFeB|MgO.,” *Nat. Mater.*, vol. 12, no. 3, pp. 240–5, Mar. 2013.
- [69] C.-F. Pai, M.-H. Nguyen, C. Belvin, L. H. Vilela-Leão, D. C. Ralph, and R. A. Buhrman, “Enhancement of perpendicular magnetic anisotropy and transmission of spin-Hall-effect-induced spin currents by a Hf spacer layer in W/Hf/CoFeB/MgO layer structures,” *Appl. Phys. Lett.*, vol. 104, no. 8, p. 082407, Feb. 2014.
- [70] A. Azevedo, L. H. Vilela-Leão, R. L. Rodríguez-Suárez, A. F. Lacerda Santos, and S. M. Rezende, “Spin pumping and anisotropic magnetoresistance voltages in magnetic bilayers: Theory and experiment,” *Phys. Rev. B*, vol. 83, no. 14, p. 144402, Apr. 2011.
- [71] O. Mosendz, J. E. Pearson, F. Y. Fradin, G. E. W. Bauer, S. D. Bader, and A. Hoffmann, “Quantifying Spin Hall Angles from Spin Pumping: Experiments and Theory,” *Phys. Rev. Lett.*, vol. 104, no. 4, p. 046601, Jan. 2010.

CHAPTER 2

AN INTRODUCTION TO SURFACE ANISOTROPIES AND MAGNETOELASTIC EFFECTS IN MAGNETIC THIN FILMS

2.1 Motivation

This chapter reviews both key theoretical insights and experimental findings in the study of perpendicular magnetic anisotropy (PMA) in ultra-thin magnetic films and provides the background which bears on our own studies in the subject matter that I will present in the following chapter. The past 30 years has seen much work done on magnetic surface anisotropy and PMA in 3d/4d and 3d/5d ferromagnetic/normal metal FM/NM transition metal multilayers. More recently there has been work on the perpendicular magnetic anisotropy of normal metal/ferromagnet/metal oxide (NM/FM/MO_x) trilayers. The discovery of PMA in these systems has reinvigorated research in the field in no small part due to the implication this has for all perpendicular magnetic tunnel junction structures (NM/FM/MO_x/FM/NM). Our main point of view in this chapter will be to derive and/or state some of the basic phenomenological models used in understanding the magnetic anisotropy and magnetoelastic interactions at surfaces and interfaces. We will show typical models assumed in quantifying and extracting the magnetic surface anisotropy, point out where these models need to be modified (or are wrong), and elucidate the role that magnetoelastic effects play in these systems. Then we will review some of the connections between the phenomenological models and microscopic theory and finally

review some experimental findings in magnetic surface anisotropy and magnetoelasticity that are relevant for our work.

2.2 Néel Pair Anisotropy Model: Surface Symmetry Breaking and Phenomenology

Néel posited that both magnetic anisotropy and magnetoelasticity could be derived from a common phenomenological framework known as the pair anisotropy model [1]. The model essentially assumes that there is a nearest neighbor spin-spin interaction energy that is dependent on the difference in the position vector of the two atoms. This interaction can be expressed in a multipole expansion and is written as:

$$E_{ij} = g_{ij}(r) + l_{ij}(r) \cdot \left(\cos^2(\theta) - \frac{1}{3} \right) + q_{ij}(r) \cdot \left(\cos^4(\theta) - \frac{6}{7} \cos^2(\theta) + \frac{3}{35} \right) + \dots \quad (2.1)$$

The angle θ is the angle between M and the vector between the atoms. This is pictorially represented in Figure 2.1a. The prefactors $\{l(r), q(r)\}$ represents the strength of dipolar and quadrupolar couplings.

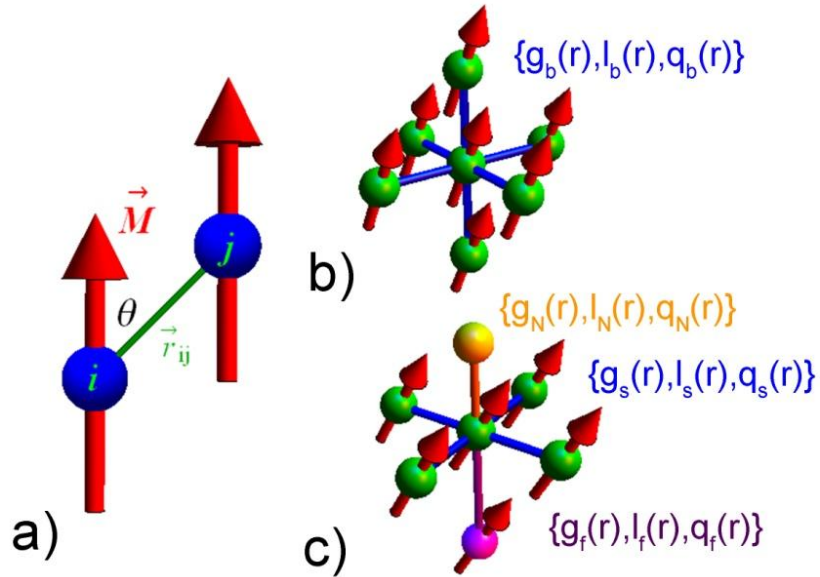


Figure 2.1 a) Shows coordinate scheme for pair bond-oriented spin coupling b) Spin-spin pair interactions are added for bulk cubic crystal. Coupling constants have full cubic lattice symmetry. c) Coupling situation at a surface with a nonmagnetic material N. Symmetry at a surface is reduced to tetragonal.

Van Vleck put the phenomenological model on firmer ground by arguing that anisotropic inter-site exchange interactions can arise by orbital valence considerations [2]. Wavefunction overlap and Coulomb repulsion energies will depend on the relative orientation of the orbital angular momentum on each site as well as the direction of the orbital angular momenta with respect to the bond directions. In transition metal ferromagnets the orbital angular momentum is generally quenched but the spin-orbit coupling allows for a partial recovery of the orbital angular momentum and also generates an effective spin Hamiltonian that is anisotropic (as it depends on the bond directions). This spin Hamiltonian is expanded to second and fourth order in spin variables and can be converted to the pseudo-dipolar and pseudo-quadrupolar terms in the free energy associated with the Néel model. Note that these are not true

dipolar and quadrupolar terms and therefore may be restricted to act over nearest neighbor sites. This restriction cannot be made with magnetic dipolar and quadrupolar interaction that are longer range by nature.

We apply the Néel pair anisotropy model to a bulk simple cubic material [Figure 2.1b]. The dipolar and quadrupolar contributions from an atom's six nearest neighbors can be added up. Here we assume that the g_{ij} , l_{ij} , and q_{ij} have the full cubic symmetry. The $\cos \theta_{ij}$ can be recast in terms of a dot product between the displacement vector and the magnetization in directional cosines where $\vec{m} = \{\alpha_1, \alpha_2, \alpha_3\}$ and $\hat{r}_{ij} = \{\beta_1, \beta_2, \beta_3\}$. For the simple cubic lattice and in fact all cubic Bravais lattices, it can be readily shown by summing over the lattice that the dipolar contribution produces terms that do not depend on the magnetization angle (although still important for the elastic energy). The first terms that depend on the magnetization direction arise from summing the quadrupolar term and using the trigonometric identity

$\alpha_1^2 + \alpha_2^2 + \alpha_3^2 = 1$ we find that:

$$\begin{aligned} E_{quad} &= q(r) \cdot (2\alpha_1^4 + 2\alpha_2^4 + 2\alpha_3^4) \\ &= q(r) \cdot (2(1 - \alpha_2^2 - \alpha_3^2)\alpha_1^2 + 2(1 - \alpha_1^2 - \alpha_3^2)\alpha_2^2 + 2(1 - \alpha_1^2 - \alpha_2^2)\alpha_3^2) \end{aligned} \quad (2.2)$$

After keeping terms that only have magnetization angular dependence we get:

$$E = 2N\Lambda q(r) \cdot [\alpha_1^2 \alpha_2^2 + \alpha_1^2 \alpha_3^2 + \alpha_3^2 \alpha_2^2] \quad (2.3)$$

where $\Lambda = -2, +16/9, +1$ for simple cubic, BCC, and FCC lattices respectively. Clearly, the dipolar terms have completely vanished due to the symmetry of the lattice and only quadrupolar terms remain. However, this is no longer true at surfaces and at interfaces as the symmetry that allowed for the cancellation of all dipolar terms is no longer applicable in the z-direction. First, the presence of non-magnetic atoms (or vacuum) breaks the cubic symmetry and indeed even the bond lengths in the z-direction into the solid will not be the same as in the bulk for the first few monolayers due to surface electronic effects. For a cubic crystal, the symmetry class at the surface then becomes reduced to a tetragonal symmetry ($a=b \neq c$). Different coupling constants are then required to describe the +z and -z couplings. Also of equal importance, the xy directional coupling at a surface can differ from bulk values. We will discuss the surface x-y couplings in more detail later as they have great import for surface magnetoelastic effects. For now, we simply label the x-y couplings as $\{g_s(r), l_s(r), q_s(r)\}$, the -z coupling into the ferromagnet as $\{g_f(r), l_f(r), q_f(r)\}$, and the +z coupling into the non-magnetic metal as $\{g_N(r), l_N(r), q_N(r)\}$. This last phenomenological coupling is not a true spin-spin coupling and could be viewed as a single-ion type term. We keep it here as an explicit reminder that surface electronic effects/surface spin-orbital coupling effects can modify spin anisotropy energies in ways that can be treated with single site spin energy terms. The situation at a surface described before is depicted in Figure 2.1c.

If we sum over the interactions about a site i at such an interface we get the following energy function to lowest order in the interaction strength:

$$E_i = const. + 2[(l_N(r_1) + l_F(r_2)) / 2 - l_s(r)]\alpha_3^2 + \dots \quad (2.4)$$

The symmetry breaking at the surface generates a surface anisotropy that depends on the angle with respect to the interface normal. Summing over a large 2D sheet we get a sheet anisotropy energy density:

$$\gamma_{sheet} = K_{\perp}^s \cos^2(\theta) \quad (2.5)$$

Assuming that these surface effects are really localized at the surface, we can express the contribution of the surface sheet to the anisotropy energy density as

$K_{\perp}^s \delta(t - t_{surface}) \cos^2 \theta$. Integrating the energy density anisotropy (including demagnetization and possible volume type terms) and normalizing with respect to the volume of the magnetic film yields the average anisotropy energy density f in Equation .

$$f = \left(K_V + \frac{K_s}{t} - 2\pi M_s^2 \right) \sin^2 \theta \quad (2.6)$$

The included volume type anisotropy term K_V may arise from either local bond-orientation (attained, for example, during magnetic annealing) or magnetoelastic interactions. The surface anisotropy contribution to the average energy density varies inversely with the film thickness as K_s/t . This surface anisotropy term will be modified $2K_s / t$ for sandwiches (e.g. Cu/Co/Cu) and multilayer stacks (e.g. [Co/Pd]_n)

where there are two identical interfaces per magnetic layer. Experimental fits to the Néel model involve multiplying the anisotropy energy density by the film thickness.

$$K_{eff}t = K_s + (K_v - 2\pi M_s^2)t \quad (2.7)$$

The surface anisotropy K_s is extracted by extrapolating the line and finding the y-intercept. Such a fit is depicted for the Co/Pd superlattice system [3]. The intercept is at 1.3 ergs/cm^2 and thus the extracted $K_s = 0.65 \text{ ergs/cm}^2$.

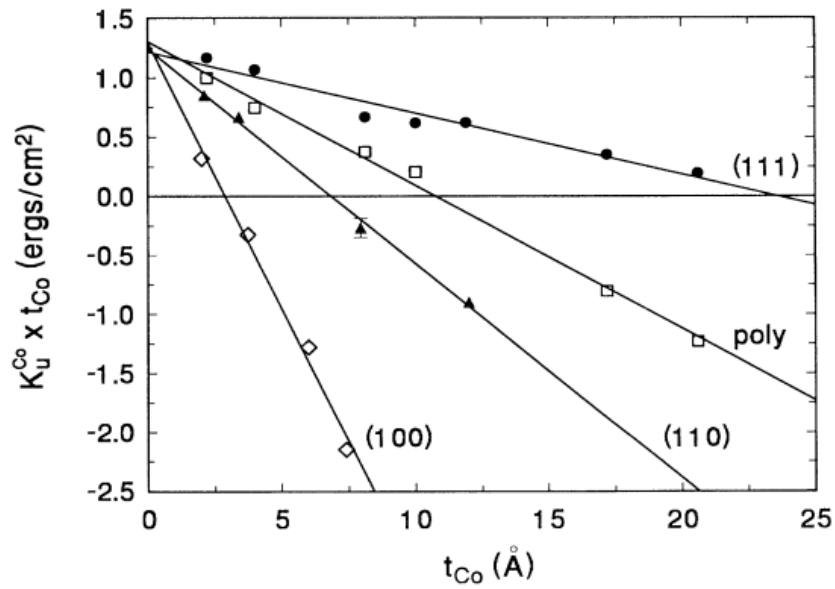


Figure 2.2: $K_{eff}t_{eff}$ vs t_{eff} curves for epitaxial $[\text{Co}(t)/\text{Pd}(10 \text{ \AA})]_{50}$ superlattices. The form fits well to the Néel model with a $K_s = 0.65 \text{ ergs/cm}^2$. Figure taken from [3].

The Néel model can also give a phenomenological description of magnetoelastic interactions as well. The magnetoelastic interaction is the change of the magnetic anisotropy energy density as a function of lattice strains. As we have

seen, the pair anisotropy model assumes that the anisotropy can be derived from a multipole expansion of anisotropic exchange interactions. Crystal strains will modify these effective spin interaction energies. We start with a bulk cubic crystal and we impose a strain in the x-direction. The new equilibrium bond lengths in the x-direction are $r = r_0(1+e_{xx})$. The interaction strengths are then changed from

$$\{g(r_0), l(r_0), q(r_0)\} \text{ to } \left\{ g(r) + \frac{dg(r)}{dr} r_0 e_{xx}, l(r) + \frac{dl(r)}{dr} r_0 e_{xx}, q(r) + \frac{dq(r)}{dr} r_0 e_{xx} \right\} \Bigg|_{r=r_0} \text{ to the}$$

lowest order in the strain. As crystal strains get larger (i.e. into the few percent), higher order terms in the crystal strain will be required to describe the change in the interaction strengths. An exaggerated representation of the situation can be seen below (Figure 2.3):

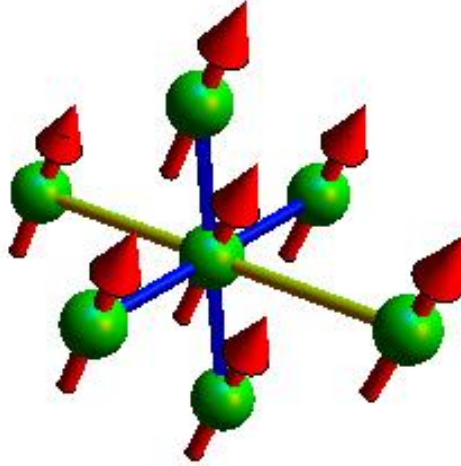


Figure 2.3 Cubic lattice under uniaxial strain e_{xx} . Strain changes the anisotropic spin-spin interaction energies and contributes to the anisotropy.

We sum over nearest neighbor interactions and this yields:

$$\begin{aligned}
 E &= g(r_0) + \frac{dg(r)}{dr} r_0 e_{xx} + \left(l(r) + \frac{dl(r)}{dr} r_0 e_{xx} \right) \Big|_{r=r_0} \alpha_1^2 + l(r) \cdot (\alpha_1^2 + \alpha_3^2) + \dots \\
 \Delta E_{strained} &= \left(\frac{dl(r)}{dr} r_0 e_{xx} \right) \Big|_{r=r_0} \alpha_1^2
 \end{aligned} \tag{2.8}$$

If we sum over lattice sites and include all other possible uniaxial strain components (and ignore the possibility of shear strains for the moment) we derive a magnetoelastic free energy that is:

$$f_{ME} = B_1 (e_{xx} \alpha_1^2 + e_{xx} \alpha_2^2 + e_{zz} \alpha_3^2) \tag{2.9}$$

where B_1 is the bulk magnetoelastic constant coupling the magnetization to uniaxial strains.

B_1 describes the way that the magnetic free energy changes under applied strain within the interior of a thicker film. However, the spin-spin coupling energies in ultra thin films may deviate substantially from the bulk and subsequently alter the behavior of the magnetic free energy under applied strain. The same Néel pair anisotropy model used to derive the surface anisotropy can be used to argue for the form and symmetry that magnetoelastic couplings have at interfaces and surfaces. We examine the case where the pair-pair interactions are coordinated as in Figure 2.1c. We look at the effect of in-plane strains as well as the effect of strains in the perpendicular direction at the surface. To lowest order for the surface atoms we get terms:

$$E_i = 2 \frac{dl_s(r)}{dr} r_0 (e_{xx} \alpha_1^2 + e_{yy} \alpha_2^2) + \left(\frac{dl_N(r)}{dr} + \frac{dl_f(r)}{dr} \right) r_0 \cdot e_{zz} \alpha_3^2 \quad (2.10)$$

The term $l_s(r)$ is used to explicitly denote that the in-plane spin-spin couplings will also be different at an interface or surface from the bulk, and in principle the z-direction spin couplings will also differ. A summation over the surface atoms and normalization by the volume then yields an addition to the magnetic anisotropy energy density:

$$f_{ME} = \left(\frac{B_{11}^s}{t} + B_1^{bulk} \right) (e_{xx} \alpha_1^2 + e_{yy} \alpha_2^2) + \left(\frac{B_{13}^s}{t} + B_1^{bulk} \right) e_{zz} \alpha_3^2 \quad (2.11)$$

The form we have derived is presented in O Handley et al. (we exclude shear terms) [4]. We note that there are two independent surface magnetoelastic couplings B_{11}^s and B_{13}^s for the simple cubic system and polycrystalline films that are z-axis textured (but oriented randomly in-plane). B_{11}^s is the magnetic coupling to in-plane non-shear strains (e_{xx}, e_{yy}) while B_{13}^s corresponds to magnetic coupling to dilatation/compression in the thickness direction (e_{zz}). In general these terms will both be important and can be measured independently. A complete symmetry-invariant form for the various surface and bulk magnetoelastic constants, anisotropy constants, and elastic constants have been derived by de Lachiesserie [5].

Equation 3.11 for the magnetoelastic energy only takes terms that are lowest order in the strain. We did this simply to show that the Néel model not only yields a

surface anisotropy term but also (to first order) yields a surface magnetoelastic term. However, first order approximations on the magnetoelastic coupling may not be appropriate for system under high strain ($>1\%$). Ultra-thin films are routinely under such high strains such that the volume magnetoelastic coupling will need to be expanded to the next order. Thus $B_{eff} = B + D\varepsilon$ where D is the second order magnetoelastic coupling. The relevance of second order magnetoelasticity and experimental evidence for it will be discussed in subsequent sections.

2.3 Strain Behavior in Thin Films, Magnetoelasticity and the Connection to Surface Anisotropy

2.3.1 Magnetoelastic Surface and Volume Anisotropy: The Kink Model

The Néel model for surface anisotropy, in its original form, assumes a sheet δ -function type term in the anisotropy energy that occurs at a surface or interface. However, this is only valid for perfectly flat interfaces and in situations where the changes to the anisotropy energy are confined to within an atomic layer or less (e.g. anisotropy changes induced by surface electronic effects in metals). There are effects however that can appear like Néel surface anisotropy terms in the energy density but whose origins lie in effects that penetrate deeper into the film. One such contribution

can arise from magnetoelastic interactions via biaxial strain fields that vary smoothly through the thickness of the film.

The first proposition of such a term was sketched out by Bruno and Chappert in the context of epitaxial Co/Au multilayers [6]. Epitaxial films grown on a substrate in heteroepitaxy will typically be under some degree of misfit strain. In the instances that the misfit is not too large and where Frank-van der Merwe growth is favorable, the film and substrate will grow in a state of strain and fully accommodate the misfit. This is known as the pseudomorphic growth phase and the biaxial strain will be $\varepsilon = -\eta$. However, at some critical thickness it will be energetically favorable to start relaxing the misfit strain by introducing dislocations. The critical thickness at which this occurs can be derived by comparing the elastic energy for introducing a sheet of edge dislocations and the elastic energy for keeping the film pseudomorphic. The energy analysis predicts a $t_c = \alpha\mu / (a_d C |\eta|)$ where α is factor of order unity, μ is the dislocation energy per unit length and is related to the shear modulus of the film and the Burgers vector associated with the dislocation, a_d is the in-plane lattice constant and C is the biaxial elastic modulus. The long-range strain field then starts to vary as $\varepsilon = -\frac{\eta t_c}{t}$ as the pseudomorphic strain relaxes via the introduction of dislocations. This phase of growth above the thermodynamic critical thickness is known as the incoherent growth mode.

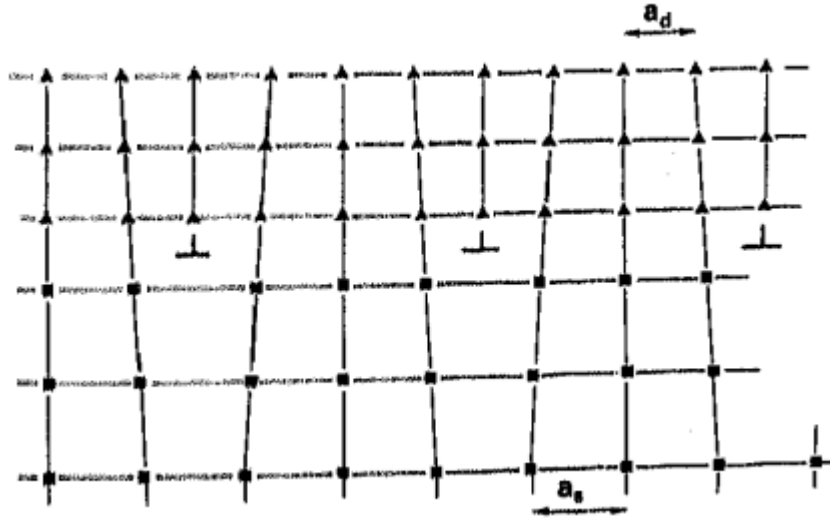


Figure 2.4. Accommodation of epitaxial misfit strains by introduction of edge dislocations. Taken from [6].

The functional form for the magnetoelastic anisotropy density within the coherent and the incoherent regime goes as:

$$f = \begin{cases} \left(\frac{K_N}{t} - B\eta \right) \sin^2 \theta & t < t_c \\ \frac{K_N}{t} - B\eta \frac{t_c}{t} \sin^2 \theta & t > t_c \end{cases} \quad (2.12)$$

K_N is used to denote a Néel-type interface anisotropy term. The magnetoelastic interaction appears as an effective surface in the incoherent regime. The magnitude of this effective surface anisotropy is not necessarily small. Assuming the magnetoelastic constant of bulk hcp Co, a misfit $\eta = -14\%$ between Co and Au(111) and $t_c = .2nm$,

Bruno estimated that the magnetoelastic contribution to K_s is ~ 0.7 ergs/cm². This is of the same order as the experimental value for the Co/Au system $K_s \sim 0.5$ ergs/cm² extracted by FMR experiments [7]. Thus magnetoelastic contributions can be an important contribution to the overall surface anisotropy.

If t_c is on the order of a few atomic layers the transition between coherent and incoherent growth will appear as a kink in the behavior of the $K_{eff}t_{eff}$ curve. This thickness dependence is depicted in Figure 2.5b.

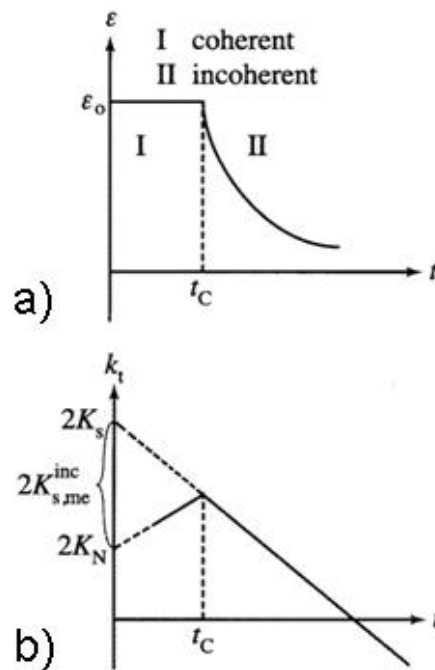


Figure 2.5 a) Biaxial strain field as a function of thickness. Region I corresponds to pseudomorphic growth and region II to incoherent growth modes. b) $K_{eff}t_{eff}$ vs t_{eff} for a multilayer/sandwich sample assuming a magnetoelastic interaction given by Equation (2.12). K_N is the “true” Néel surface anisotropy while K_s includes the magnetoelastic anisotropy.

The intercept made by extrapolating the $K_{eff}t_{eff}$ line to zero thickness in the incoherent regime is a measure of the combined Néel surface energy and magnetoelastic anisotropy contribution. In the coherent regime, the y-intercept constitutes a Néel type surface term. Such a kink model was used by Jungblut et al. to fit to data in the epitaxial Cu/Ni/Cu system where it is believed that magnetoelastic anisotropy is responsible for the emergence of PMA [8]. Their experimental $K_{eff}t_{eff}$ curve and fit are shown in Figure 2.6 .

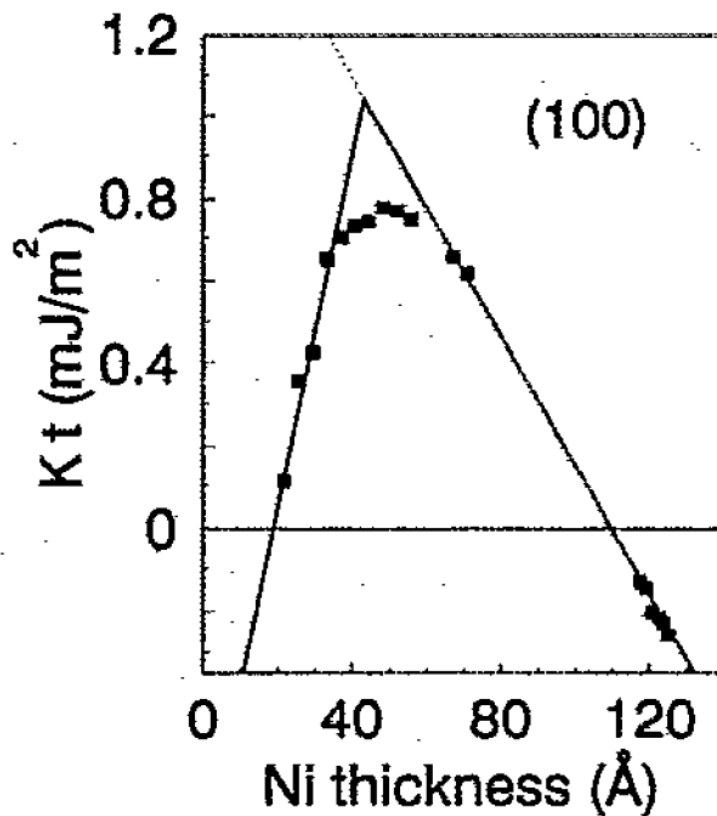


Figure 2.6 Kt vs t curve for the Cu/Ni(001)/Cu epitaxial system. The solid line represents a fit to the data by the kink model. Data taken from Jungblut et al. [8].

A quick examination of Figure 2.6 shows a region of approximately 3 nm (from 4-7 nm) in the Ni thickness that does not fit well to the kink model. In fact, the curve is anything but a kink and varies smoothly. This could be due to a large cross over region between the two strain regimes (i.e. coherent to incoherent). However, there is no evidence for such a large cross over region in the Ni/Cu (001) system. This raises the question as to whether there is an additional missing term.

2.3.2 Surface Magnetoelasticity, Strain Relaxation and the $K_{\text{eff}}t_{\text{eff}}$ Curve

The main problem with the energy term proposed by Bruno and used by Jungblut et al. is that the magnetoelastic coupling B is assumed to be the bulk value. As we have shown before, the magnetoelastic coupling itself need not be the same as the bulk value and may include a substantial surface term. If the system has a strong surface magnetoelasticity, the anisotropy energy given by Equation (2.12) is not reasonable and will lead to erroneous conclusions about the value of intrinsic Néel surface anisotropies. It may not even capture the functional form of the anisotropy energy with thickness. This was pointed out by Bochi et al. in the Co/Cu epitaxial superlattice [9] and Cu/Ni/Cu epitaxial system [10]. The analysis combines previous magnetometry/anisotropy data, and LEED measurements of the epitaxial strain in the magnetic layer to fit for the surface magnetoelastic and volume magnetoelastic coupling terms. In order to see the effects surface magnetoelasticity has on the anisotropy energy, we adopt Equation (2.11) to the case where the film is under

biaxial strain $\{\varepsilon_{xx}, \varepsilon_{yy}, \varepsilon_{zz}\} = \{\varepsilon_0(t), \varepsilon_0(t), \frac{-2\nu}{1-\nu} \varepsilon_0(t)\}$. Here we have ignored shear

strains and we assume that $\nu=1/3$ (which is reasonable for metals).

$$f = \left\{ \left[\frac{K^s}{t_{eff}} + \frac{B_s^{biaxial}}{t_{eff}} \varepsilon_0(t) \right] + \left(B_V^{biaxial} \varepsilon_0(t) - 2\pi M_s^2 \right) \right\} \sin^2 \theta \quad (2.13)$$

Here $B_s^{biaxial} = B_s^{11} + B_s^{13}$ and $B_V^{biaxial} = B_V^{11} + B_V^{13}$. The behavior of the anisotropy energy as

represented in Equation (2.13) depends heavily on the thickness dependence of the strain and the sign and magnitude of the volume and surface magnetoelastic couplings.

For a film in pseudomorphic growth (i.e. under constant biaxial strain), the

magnetoelastic energy will contribute both to the surface ($K_s^{ME} = -B_s \eta$) and volume

type ($K_V^{ME} = -B_V \eta$) magnetic anisotropy terms. In the incoherent growth regime the

magnetoelastic interaction will contribute a term $K_s^{ME} = -B_V \eta t_c$ to the surface

anisotropy, and a new term $-\frac{B_s}{t} \frac{\eta t_c}{t}$ to the anisotropy energy density. This new term

generates non-linearities in $K_{eff} t_{eff}$ vs t_{eff} as can be seen in Equation (2.14).

$$K_{eff} t_{eff} = -\frac{B_s^{biaxial} \eta t_c}{t_{eff}} + \left(K_s - B_V^{biaxial} \eta t_c \right) - 2\pi M_s^2 t_{eff} \quad (2.14)$$

Depending on the sign and magnitude of the surface and volume

magnetoelastic couplings and the strain relaxation profile, Equation (2.14) can fit the

crossover behavior seen in Jungblut et al and will appear as a sublinear deviation of

$K_{eff} t_{eff}$ in certain thickness regimes. An example from the Ni/Cu(001) system is

depicted in Figure 2.7. [10].

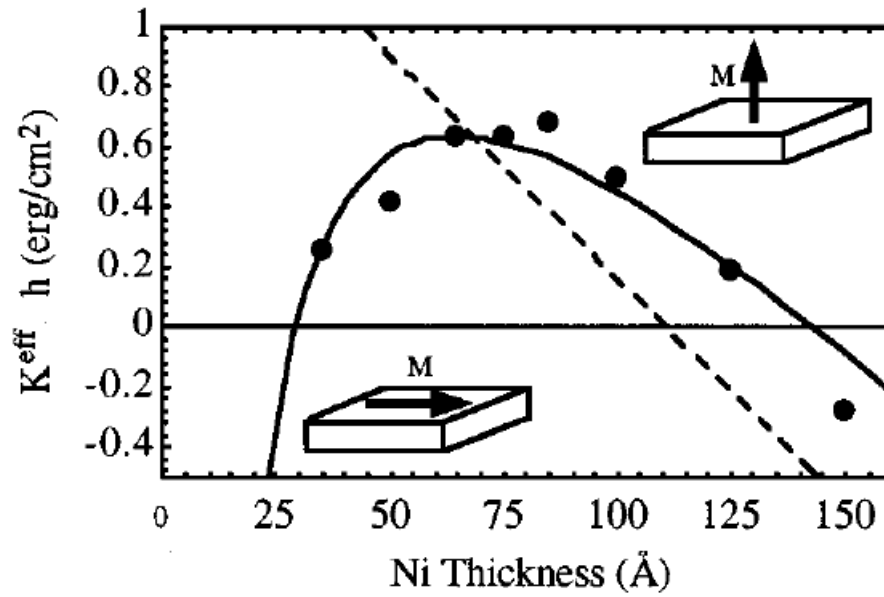


Figure 2.7 $K_{eff}t_{eff}$ vs t_{eff} curve for the Ni/Cu(001) system as measured by Bochi et al. The solid line represents a fit of the data using Equation (2.14) with extracted fit values of $B_s = -67$ ergs/cm² and $K_s = .98$ ergs/cm² and an assumed $\eta = 2.6\%$, $t_c = 1.8$ nm, and $B_V = -6.2 \times 10^7$ ergs/cm³. M_s was measured to be 488 emu/cm³.

The crossover/maximum in $K_{eff}t_{eff}$ vs t_{eff} in Jungblut et al. and Bochi et al. occur at a thickness well above the critical thermodynamic thickness for strain relaxation in the Ni/Cu(001) system. The presence of a Cu overlayer may change the value for the coherent-incoherent transition. However, the crossover in $K_{eff}t_{eff}$ does not necessarily need to arise from a coherent to incoherent transition and can have its origins in surface magnetoelastic effects coupled with strain relaxation.

2.3.3 Surface Magnetoelasticity and Second Order Couplings

The fitting by Bochi et al. is a phenomenological fit to the surface and volume magnetoelastic couplings. However, just as the surface anisotropy K_s can have its origin in Néel type terms or in strain relaxation effects, the same is true of the surface magnetoelastic coupling. As we mentioned before, the magnetoelastic coupling in systems under high strain will itself be strain dependent and will include second order terms. If one imagines a case where the strain is high and relaxes as $1/t$, then the effective magnetoelastic coupling can be expressed as:

$$B_{eff} = B_v^{eff} + D_{eff} \varepsilon(t) = B + D \cdot (\Gamma / t) \quad (2.15)$$

Thus the second order magnetoelastic term can look like a surface magnetoelastic coupling as well. Thus, in principle, surface magnetoelastic couplings in ultra-thin films under high strain will likely contain contributions from surface electronic effects as well as contributions from non-linear magnetoelastic energies. The importance of the latter has been determined by a series of experiments that will be discussed later. The most important point though is that a full understanding and characterization of the magnetoelasticity and strain must be carried out before one can understand and parse the behavior of the magnetic anisotropy of a film in the ultrathin regime.

2.3.4 Strain Behavior in Thin Films

The equilibrium theory (Matthews-Blakeslee) for strain relaxation from pseudomorphic growth considers the energy required to introduce a misfit dislocation and the elastic energy associated with pseudomorphic growth. [11] The equilibrium thickness t_c at which this relaxation occurs and associated interfacial dislocation density is found by minimizing the total elastic energy (from both dislocations and misfit). The resultant strain field in the plane of the interface will in general depend on the equilibrium dislocation density, the critical thickness and misfit strain. In a general form, the strain field can be expressed as:

$$\varepsilon(t) = \eta \frac{t_c}{t} \frac{\ln\left(\frac{4t}{b}\right)}{\ln\left(\frac{4t_c}{b}\right)} \approx \eta \frac{t_c}{t} \quad (2.16)$$

The approximation of a $1/t$ type strain dependence has been used by Bruno and Jungblut et al. as we have seen before. However, strain measurements on epitaxial films undergoing relaxation by dislocation generation do not always follow such a scaling law. For example, strain relaxation going as $t^{-0.70}$ has been measured for Ni films in epitaxial Cu/Ni(001)/Cu(001) sandwiches [12]. This type of deviation from a $1/t$ dependence may, in part, be due to the fact that the dislocation generation as a function of film thickness may be considerably lower than predicted by the equilibrium theory. Such an impedance to dislocation generation could arise from kinetic effects (i.e. energy barriers required for dislocation generation) and will depend

in detail on the elastic constants of material, the orientation of dislocation lines (i.e. whether the Burger's vector), and the thin film growth process.

Analysis and understanding of the stress in polycrystalline films where there is no epitaxial relationship between the film and the substrate can be even more complicated. Studies on magnetron sputtered films have shown films with strain thickness dependences $t^{-\alpha}$ with α ranging from 0.25 to 1. This scaling exponent in magnetron sputtered films is known to vary with Ar processing gas pressure and sputter power density [13].

The thickness dependence, and the sign and magnitude of strain in polycrystalline films are determined in detail by kinetic effects as well as morphological effects and atom-atom bonding energy considerations during the deposition. An obvious example of kinetics effects on film strain is seen in the case of magnetron sputtered films where the film is continually subject to high-energy (~tens of eV) bombardment by Ar neutrals and target atoms in the low Ar gas pressure regime (< a few mtorr). This continuous "peening" is known to put certain metallic films (Mo, Ta, W) under high compressive stress on the order of ~ 1 GPa even as the films grow thick (~ 1 μm) [14].

Morphological and kinetic effects in polycrystalline evaporated films are also of considerable importance. Depending on the wetting properties of the film to the substrate, well-separated islands may form in the initial phase of growth (e.g. Au on SiO_2). The stresses on each well-isolated island in this phase of growth can be highly compressive. However, as more atoms are deposited on the surface, the island density

will get higher and islands will get larger. Atom-atom interactions between closely spaced islands can either drive coalescence and/or cause the atoms in various islands or grains to be put under considerable tensile strain (on the order of several GPa for refractory/low adatom mobility metals). These types of tensile strains can relax as grains and islands coalesce [15]. The behavior of film stress with the nominal thickness is obviously not simple and various models have been proposed that relate the stress in the film to the average radius and height of each grain, the various surface interaction energies, ad-atom mobility, etc.

Clearly stress/strain evolution in thin films is not straightforward. We will not even pretend to review this subject matter any further. Our main point in this section is simply to point out that the strain magnitude in either epitaxial or polycrystalline ultra-thin films can be substantial and does not necessarily scale inversely with the film thickness. The dependence of strain field on the thickness will alter the thickness dependence of the magnetic anisotropy and the magnetoelastic couplings. A proper measurement of the strain field and its evolution is thus very important to characterize magnetoelastic effects in ultra-thin films and even more specifically to separate out what comes from strain effects and what comes from possible electronic effects that are closely confined to the interface.

2.4 Microscopic Sources of Néel-type Surface Anisotropy and Surface Magnetoelasticity

We have seen that the anisotropy can be viewed in terms of a combination of effects localized at the interface and effects emerging from longer-range behavior (e.g. residual strain fields). The Néel model, which captures the symmetries of effects localized at the surface, makes no statement on the microscopic origin of such couplings. What sort of electronic processes are responsible for the Néel-type surface anisotropy and what formalism is apt for describing these processes? The answer to these questions depends on the class of material involved (i.e. insulators with localized moments, rare earth metal f-electron systems, or transition metal d-electron ferromagnets). We focus on electronic processes in transition metal ferromagnets as our experiments will exclusively deal with these.

The Néel surface anisotropy derives from pseudodipolar and pseudoquadrupolar pair interaction terms. These terms have the effects of electron spin-orbit interaction, nearest-neighbor Coulomb interactions, and orbital hybridization tucked inside them. The last two contributions are commonly known as the crystal field potential in the literature. In ultra-thin transition metal ferromagnets, the way in which the magnetic anisotropy and magnetoelastic couplings depend on the spin-orbit interaction and the crystal fields will be informed by the structure of the d-bands, the chemical potential, and any surface electric field effects. Accounting for all of these requires a self-consistent treatment of the many electron problem in a metallic ferromagnet at a surface.

Some fairly general formalism has been laid down by Bruno [16] and Freeman [17] in order to calculate the magnetic surface anisotropy and magnetoelastic interaction in transition metal monolayers. The essential ingredient in all of these calculations is an accounting of the spin-orbit interaction in a 2D itinerant magnet with a proper calculation of the band structure in these systems. We sketch Bruno's scheme for calculating surface magnetic anisotropies as the method is intuitive and yields some fairly general relationships.

The anisotropy energy emerges from considering energy corrections of the ground state (i.e. the Fermi sea) in a 2D transition metal ferromagnet induced by the spin-orbital coupling. In transition metal ferromagnets, these spin orbit corrections can be treated perturbatively as the spin orbit energy scale in the 2D system is on the order of 10 meV/atom while the transition metal d-bandwidth (set by kinetic hopping terms and Coulomb repulsion) is on the order of eV/atom. The k-space diagonal part of the spin-orbit Hamiltonian can be expressed as:

$$H_{s.o.} = \xi \sum_{\mu_1, \sigma_1, \mu_2, \sigma_2} \langle \mu_1 \sigma_1 | \vec{L} \cdot \vec{S} | \mu_2 \sigma_2 \rangle \sum_{\vec{k}} c_{\mu_1, \sigma}^\dagger(\vec{k}) c_{\mu_2, \sigma}(\vec{k}) \quad (2.17)$$

The μ index ranges over 3d subbands of different orbital characters (xy, xz, yz, $3z^2-r^2$, x^2-y^2). Energy shifts can be computed by time-independent perturbation theory.

Any contributions of the spin-orbit matrix to energy shifts (diagonal terms) vanish in first order. This is easy to see by noting that the μ subbands denoting the orbitals in the cubic representation are actually equal admixtures of states of opposite orbital angular momentum. For example the angular part of the d_z^2 orbital can be

written as $(Y_2^2 + Y_2^{-2})/\sqrt{2}$. Naturally, the diagonal terms of the S.O. interaction will sum to zero. Therefore, any contribution to the energy must come as second order in the spin-orbit interaction strength. Using second order perturbation theory the energy correction is:

$$\Delta E = \sum_{exc} \frac{|\langle gr | H_{SO} | exc \rangle|^2}{\varepsilon_{gr} - \varepsilon_{exc}} \quad (2.18)$$

The ground state wavefunction can be written as:

$$|gr\rangle = \sum_{\substack{k < k_F \\ n, \sigma}} |k, n, \sigma\rangle = \sum_{\substack{k < k_F \\ n, \sigma}} \sum_{\mu_1} a_{n, \mu_1, \sigma}(\vec{k}) |k, \mu_1, \sigma\rangle \quad (2.19)$$

The virtual states excited by the spin orbit interaction can be expressed as $|exc\rangle = c_{n_2, \sigma_2}^\dagger(k) c_{n_1, \sigma_1}(k) |gr\rangle$ where the excited state energy is such that $\varepsilon_{n_1, \sigma_1}(k) < \varepsilon_F < \varepsilon_{n_2, \sigma_2}(k)$. Bruno showed that one can express (2.18) as

$$\Delta E = -\xi^2 \sum_{\mu_1, \mu_2, \mu_3, \mu_4} \frac{\langle \mu_1, \uparrow | \vec{L} \cdot \vec{S} | \mu_2, \uparrow \rangle \langle \mu_3, \uparrow | \vec{L} \cdot \vec{S} | \mu_4, \uparrow \rangle}{\varepsilon_{gr} - \varepsilon_{exc}} G(\mu_1, \mu_2, \mu_3, \mu_4) \quad (2.20)$$

where G is a factor associated with the spin-dependent density of states for the sub-bands above and below the Fermi level. The spin-orbit interaction can also lead to a substantial surface orbital moment. The expectation value of the orbital angular momentum along the spin quantization axis η to lowest order is:

$$\langle L_\eta \rangle = \sum_{exc} \frac{\langle gr | L_\eta | exc \rangle}{\varepsilon_{gr} - \varepsilon_{exc}} \langle exc | H_{SO} | gr \rangle + c.c. \quad (2.21)$$

Using the identity $\langle \mu_1 \sigma_1 | L_\eta | \mu_2 \sigma_2 \rangle = 2\delta_{\sigma_1 \sigma_2} \langle \mu_1 \uparrow | \vec{L} \cdot \vec{S} | \mu_2 \uparrow \rangle$, one can then express the average orbital angular momentum as:

$$\langle L_\eta \rangle = -4\xi \sum_{\mu_1, \mu_2, \mu_3, \mu_4} \frac{\langle \mu_1, \uparrow | \vec{L} \cdot \vec{S} | \mu_2, \uparrow \rangle \langle \mu_3, \uparrow | \vec{L} \cdot \vec{S} | \mu_4, \uparrow \rangle}{\mathcal{E}_{gr} - \mathcal{E}_{exc}} H(\mu_1, \mu_2, \mu_3, \mu_4) \quad (2.22)$$

H is also a factor associated with the density of states above and below the Fermi level (but distinct from G). The form in Equation 3.17 is identical to the energy shift apart from a prefactor of 4ξ and replacing G by H .

The matrix elements of $\vec{L} \cdot \vec{S}$ between the various subband states are not difficult to calculate but a reference is given here to the various matrix elements [18]. The orbital angular momentum is assumed to be quantized along the $0z$ axis, which corresponds to the film plane normal. The spin quantization axis is taken to lie along the 0η axis and makes a polar angle θ and azimuthal angle with the z axis. A summation over the various subbands with an explicit use of the matrix elements in terms of θ and φ yields $E = K_0 + K_s \sin^2 \theta$ and for (001) and (111) oriented films. A similar relationship must also hold for the orbital angular momentum about the spin quantization axis: $\langle L \rangle = L_0 + L_2 \sin^2 \theta$. The formulation by Bruno thus shows how surface anisotropy can emerge from interfacial electronic spin-orbit processes and how this surface anisotropy is connected to surface orbital moment anisotropy. This latter connection has been the subject of a few studies, the most recent of which has studied the relationship between the anisotropy in the g-factor $g_\perp - g_\parallel$ (which is an explicit measure of the orbital moment anisotropy) and the perpendicular anisotropy field H_k by FMR in Co/Ni multilayers [19].

Bruno's formalism, however, masks the details of the band structure in G and H type functions. A treatment by Wang, Wu and Freeman makes transparent the types of second order processes that are involved in determining the surface anisotropy and magnetoelasticity by explicitly looking at the role the exchange splitting of the d bands play. This treatment divides the spin-orbit electronic processes in two. The first comes from second order processes between occupied majority states and unoccupied minority states. The other comes from occupied minority states to unoccupied minority states. The large exchange splitting (~ 1 eV) of the d -bands is the main reason why there are no terms contributed from scattering through unoccupied majority states. The very large exchange splitting energy means that the majority states are nearly completely occupied and all lie below E_F .

$$E^{s.o.} = -\xi^2 \frac{|\langle o^+ | \sigma \cdot L | u^- \rangle|^2}{\delta \epsilon_{uo}} - \xi^2 \frac{|\langle o^- | \sigma \cdot L | u^- \rangle|^2}{\delta \epsilon_{uo}} \quad (2.23)$$

The first term (which they call the E^{ud}) can be treated by assuming that the energy gap between occupied majority states and unoccupied minority states are on the order of the exchange splitting ΔE_{ex} . We take terms of the spin-orbit interaction that involve spin-flip processes (with η as the spin-quantization axis). As we are summing over all the occupied majority states we are essentially summing over a complete orbital basis set. We then use the completeness relations to write the energy as:

$$E^{ud} = -\frac{\xi^2}{4\Delta E_{ex}} \sum_{u^-, o^+} \langle u^- | L_\eta^+ | o^+ \rangle \langle o^+ | L_\eta^- | u^- \rangle = -\frac{\xi^2}{4\Delta E_{ex}} \sum_{u^-} \langle u^- | L_\eta^+ L_\eta^- | u^- \rangle \quad (2.24)$$

A little manipulation and the completeness relation over the entire minority band yields:

$$E^{ud} = -\frac{\xi^2}{\Delta E_{ex}} \left\{ -\frac{2}{3} l(l+1)(2l+1) + \sum_{o^-} \langle o^- | L^2 - L_\eta^2 | o^- \rangle \right\} \quad (2.25)$$

The anisotropy ΔE^{ud} is simply the difference in energy between η being \hat{z} versus \hat{x} .

A little bit of algebraic manipulation shows that the contribution to the anisotropy energy from majority to minority processes is:

$$\Delta E^{ud} = E^{ud}(x) - E^{ud}(z) = \frac{\xi^2}{\Delta E_{ex}} \langle o^- | \frac{1}{2} (3L_z^2 - L^2) | o^- \rangle \quad (2.26)$$

Thus the spin-flip part of the second order spin-orbit processes yield a term that is directly proportional to the z-component of the orbital angular momentum. Thus it is really only this component of the surface anisotropy that is related to the surface orbital angular momentum in a way that is not very sensitive to fine changes in the band structure.

The second term in Equation (2.23) is the non-spin flip portion of the spin-orbit interaction and thus connects minority occupied to minority unoccupied states. The anisotropy associated with these processes is:

$$\Delta E^{dd} = -\xi^2 \left(\sum_{o^-, u^-} \frac{|\langle o^- | L_x | u^- \rangle|^2}{\epsilon_{u^-} - \epsilon_{o^-}} - \sum_{o^-, u^-} \frac{|\langle o^- | L_z | u^- \rangle|^2}{\epsilon_{u^-} - \epsilon_{o^-}} \right) \quad (2.27)$$

This component of the anisotropy energy density is very much more sensitive to the details of the minority band structure -- particularly in areas near band degeneracies. It is this component that will be sensitive to lifting of degeneracies induced by external stimuli (such as electric fields, etc.).

Accurate accounting of Néel-type surface anisotropies in TM ferromagnets thus requires a proper accounting of spin-orbit processes and the structure of the majority and minority bands. This is typically done by ab-initio (DFT) calculations where the bands and potentials are solved for self-consistently in some set of approximations on the way in which the potential depends on the electron density (the simplest being the LSDA). Calculations for the surface anisotropy in multilayered systems, sandwiches, and bilayers have been numerous and have met with reasonable success.

Fewer calculations have been done on the surface magnetoelasticity. Intrinsic surface magnetoelastic effects are also dependent on the band structure and spin-orbit processes. Ab-initio techniques allow determination of changes in the band structure under either uniaxial or biaxial strain that consequently alter the magnetic anisotropy energy. Calculations have been carried out for the magnetoelasticity/magnetostriction of Co monolayers on Cu(001) and Pd(001) [20]. These calculations show a strong dependence of the magnetostriction of fcc Co on the material with which it is

interfaced, $\lambda_{001} = -57$ ppm for Co/Cu(001) and $\lambda_{001} = +230$ ppm for Co/Pd(001). Calculations on Co/Pd(111) where PMA emerges shows $\lambda_{111} \sim 0$ [21]. Another calculation carried out on the Co/Cu(001) system reveal the presence of a surface magnetoelastic coupling $B_s = +5.51$ ergs/cm² opposing the sign of the bulk magnetoelastic coupling [22]. The magnitude of such surface magnetoelastic coupling terms can also be quite large (in the Co/Cu calculation B_s is nearly an order of magnitude larger than the interfacial anisotropy $K_s = 0.575$ ergs/cm²). These ab-initio calculations show that surface magnetoelastic effects can be very large at interfaces, have the opposite sign as the bulk, and are highly sensitive to the interface involved. Interfacial effects (including surface electronic processes, spin-orbit coupling) can be very important in determining the magnetoelastic response.

2.4.1 A Quick Review of Recent Progress in Surface Anisotropy

Experimental studies on surface anisotropy have been conducted in a wide variety of FM/NM bilayers, sandwiches, and multilayers. The sheer scope of the work in this field (extending back into the late 70's) prohibits a detailed discussion here. We refer the reader to a comprehensive review of the subject [23] and discuss some more recent results. It was widely believed that PMA driven by intrinsic surface electronic effects, as opposed to largely magnetoelastic driven PMA in epitaxial Ni systems, could only exist at highly spin-orbit coupled interfaces such as Co/Pt, Fe/Pt, Co/Pd, and Co/Au (although magnetoelastic interactions are probably very important in these systems as well). These interfaces exhibit high positive surface anisotropy even in sputtered or evaporated multilayers. However, the discovery of PMA in relatively low

S.O. coupling Co/Ni multilayers inspired by ab-initio predictions started to challenge the assumption that heavy metal/ferromagnet interfaces are required to drive perpendicular anisotropy [24]. More recent work in NM/FM/MO_x systems have shattered this notion altogether. The discovery of large enhancement of the PMA in Pt/Co/AlO_x over Pt/Co/Pt is one such example. The average surface anisotropy energy per interface in a 325 C post-annealed Pt|Co|AlO_x trilayer (deposited by sputtering) was reported to be 1.4 ergs/cm² [25]. This value is considerably larger than the largest interface anisotropy energy reported for sputtered Co|Pt(111) at K_s= 0.92 ergs/cm² [26]. Careful oxygen dose control of the AlO_x [27] combined with XAS and XPS measurements of the oxidation state [28] of the Co at the Co|AlO_x interface have determined that the interfacial anisotropy is highly sensitive to oxygen content. Similar results of exceptionally high positive surface anisotropy have been found in the sputtered and post-annealed (Ta,Hf)|CoFeB|MgO [29], [30] and in the epitaxial Fe|MgO system [31], [32]. The surface anisotropy at the Fe|MgO interface also appears to be very sensitive to the presence of oxygen with an optimal dose required to generate high surface anisotropy. A general consensus has emerged that oxygen at the CoFe|MgO or Fe|MgO interface is extremely important in driving the surface anisotropy in these systems.

These results in the Pt|Co|AlO_x and CoFeB|MgO system are surprising as MgO and AlO_x are comprised of light atoms and are systems in which the spin-orbit coupling is low. From where then does the large surface anisotropy arise? Ab initio studies have pointed out that that it can arise from charge transfer processes and hybridization effects between the interfacial d orbitals of Co and Fe and the p orbitals

of O. Energy splittings between the hybridized d bands of various characters can have a significant impact on energy dominators as well as the G and H functions in (2.20) (depending of course on where E_F lies). These factors in turn will be extremely important in determining the magnitude of the surface anisotropy. We will discuss experimental findings in the NM|CoFeB|MgO and Fe|MgO system in more detail in the next chapter. However, we list extracted surface anisotropy values for a select number of systems (both experiment and theory) for reference.

	$K_s(\text{ergs}/\text{cm}^2)$	Method
Co/Pt [26]	.92	DC Sputtering
Pt/Co/AlOx [25]	1.4	Magnetron Sputtering
Fe/MgO [31], [32]	1.18, 1	MBE
Ta/Co ₄₀ Fe ₄₀ B ₂₀ /MgO [29]	1.3	Magnetron Sputtering
Hf/Co ₄₀ Fe ₄₀ B ₂₀ /MgO [30]	2.3	Magnetron Sputtering
Fe MgO (optimal oxidation) [33]	2.93	Ab-initio
CoFe (MgO,MgB ₂ O ₆) [34]	(1.31, .679)	Ab-initio

Table 2.1. Experimental and theoretic surface anisotropy values for relevant systems.

2.4.2 Experimental Studies on Surface Magnetoelasticity

There has been a good deal of experimental evidence for the existence of surface magnetoelastic effects both in ultra-thin films, and at the surface of bulk samples. Study of the surface magnetoelastic coupling in bulk samples has been carried out in-situ by Sun et al [35] on CoCrB and FeCrB amorphous ferromagnetic

metalloid glass ribbons. A four-point bend strain method was used to exert either compressive or tensile strain on the sample surface and the surface magnetization was probed by analyzing the polarization of secondary electrons excited by a primary electron beam. Their results show that the average surface magnetoelastic coupling averaged over the estimated secondary electron volume was 6.0×10^6 and -1.6×10^6 ergs/cm³ for CoCrB and FeCrB respectively. These numbers deviate substantially from the measured bulk values of 1.8×10^6 (CoCrB) and -3.0×10^6 ergs/cm³ (FeCrB).

There is also strong evidence for surface magnetoelasticity/magnetostriction in ultrathin films, sandwiches, and multilayers. Surface magnetoelasticity has been shown to exist in polycrystalline e-beam evaporated magnetic films on different underlayers (Ni₈₁Fe₁₉/Ag/Si, Ni₈₁Fe₁₉/Cu/Si and Ni/SiO₂/Si) [36] as well as in Ni/Pb, Ni/C, Ni/Ti, Ni/Ag, and Fe/Gd multilayers [37]. Figure 2.8 shows that the thickness dependence of the surface magnetoelasticity can be fit well to a Néel model type dependence as $B_{\text{eff}}/(t-t_0)$ where t_0 is a magnetoelastic dead layer.

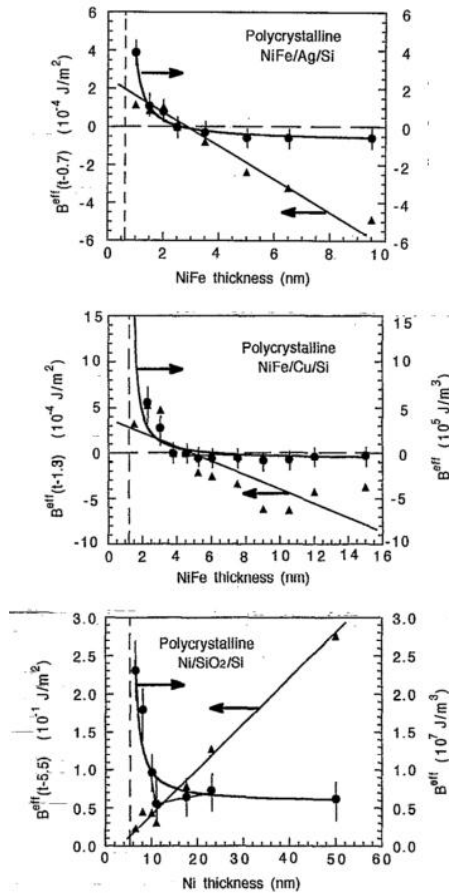


Figure 2.8 In plane effective magnetoelastic coupling B_{eff} and $B_{\text{eff}} t_{\text{eff}}$ vs t_{eff} plots for polycrystalline evaporated NiFe/Ag/Si, NiFe/Cu/Si, and Ni/SiO₂/Si systems.

It is clear that the surface magnetoelasticity is not necessarily a weak effect and that assuming bulk values in the ultrathin film regime is completely invalid. The magnetoelastic coupling of Py on Cu and Ag even reverses sign. We provide a table (Table 2.2) of measured (or fit) values for surface and volume magnetoelastic couplings in a few material systems in order to provide a quantitative feel for the numbers and scales that can be involved.

	B_V [ergs/cm ³]	B_s [ergs/cm ²]	Deposition Method
Cu/Ni/Cu(001)*	6.2×10^7 [for B_1^b]	-52 [for B_1^s]	MBE
FCC Co(111)/Cu*	$+2.6 \times 10^8$ [for B_2^b]	-23.4 [for B_2^s]	MBE
Py/Ag/SiO2/Si	-7.8×10^5	.14	Evaporation
Py/Cu/SiO2/Si	-7.6×10^5	.3	Evaporation
Ni/SiO2/Si	$+6 \times 10^7$	20	Evaporation

Table 2.2. Volume and surface magnetoelastoelastic couplings for select systems.
*Magnetoelastic values extracted from fit of anisotropy data and strain field.

The underlying cause of surface magnetoelasticity, as has been mentioned before, can be due to either intrinsic Néel-type surface effects (which include contributions from surface electronic structure) or to nonlinear magnetoelastic effects.

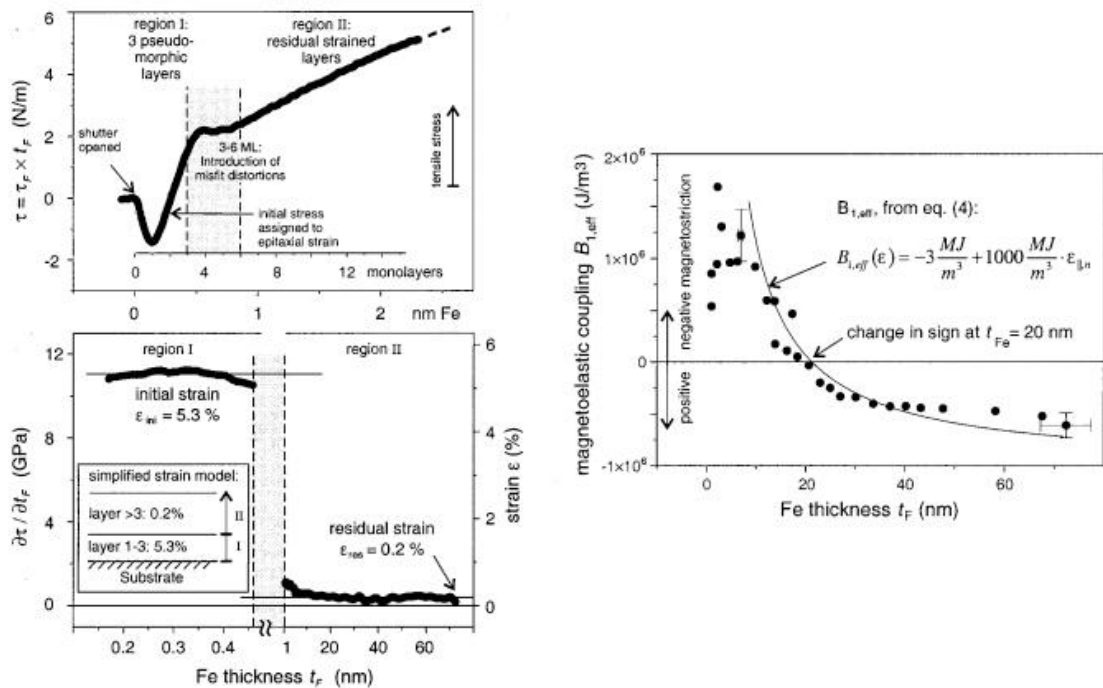


Figure 2.9 Effective biaxial magnetoelastic coupling extracted from laser deflection measurements of magnetostrictive plate deformations on Fe/W(001) system in-situ.

Growth stresses and strains also monitored by laser deflection techniques. Magnetoelastic coupling in Fe/W seems to be heavily dependent on residual strain state. Figures taken from [38].

A careful set of experiments by Sanders and Kirschner have shown that second order magnetoelastic effects cannot be ignored in describing the surface magnetoelasticity in systems under high strain. The first sets of experiments were conducted on Fe grown epitaxially on W(100) substrates [38], [39]. Both growth induced stress and magnetostrictive stress were characterized by substrate curvature/cantilever deflection measurement techniques. The magnetoelastic couplings were found to vary linearly with the average film stress in a broad stress range. Subsequent work using similar techniques was done on Co/W(001) [40], Fe/W(110) [41], Ni/W(110) [42], Co/Ir(001) [43], the epitaxial Cu/Ni/Cu systems [44], [45], and in the epitaxial Fe(001)/MgO(001) and Fe/Cr/MgO(001) system [46], [47]. An excellent review of these experiments on non-linear magnetoelastic effects in ultrathin films has appeared fairly recently [48]. Values for the first order coupling B and the second order coupling D can be extracted from fitting the effective magnetoelastic coupling strain dependence as shown in Figure 2.10.

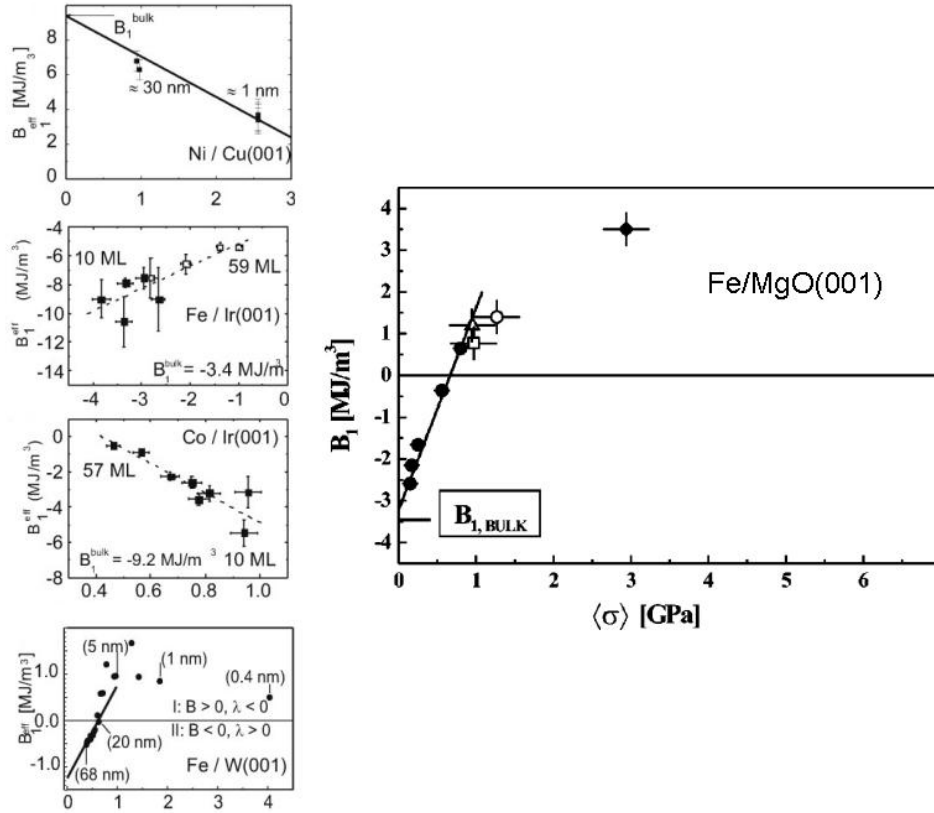


Figure 2.10. Effective magnetoelastic coupling versus residual biaxial strain for various epitaxial systems. Also shows dependence of the magnetoelastic coupling in epitaxial Fe/MgO(001) on residual stress. The solid circles for thick Fe films ($t > 50$ nm). Different average stresses were obtained by deposition at different temperatures and by using different thicknesses.

Extracted values for a few epitaxial systems are shown in Table 2.3. B_2 and D_2 are the first and second order shear magnetoelastic couplings respectively.

	B_1 (Mergs/cm ³)	D_1 (Mergs/cm ³)	B_2 (Mergs/cm ³)	$2D_2$ (Mergs/cm ³)
Fe/W(001)	-12	+2000	-	-
Fe/MgO(001)	-34	+11000	+78	-3650
Fe/Ir(001)	-36	+1550	-	-
Co/Ir(001)	+35	-8420	+18	+9300
Ni/Cu(001)	+94	-2340	100	-

Table 2.3. Tabulation of first and second order magnetoelastic couplings of epitaxial magnetic film/substrate pairs.

The extracted values for B and D across many of these epitaxial systems reveal that the effective magnetoelastic constant can deviate substantially on the scale of the first order magnetoelastic constant even with a few tenths of a percent of strain. Residual strains on the order of a percent are enough to either completely reverse the sign of the magnetoelastic constant as occurs in the Fe/W system or in the Fe/MgO system.

Clearly strain dependence of the magnetoelastic effect can not *a priori* be neglected and appeals to bulk magnetoelastic couplings even in thicker films under strain is not appropriate. The importance of second order magnetoelastic couplings in describing the magnetoelasticity of films under high strain has also been corroborated by *ab-initio* calculations [49].

Deviation from linearity of the magnetoelastic coupling in the residual stress does occur in certain systems (e.g. Fe/W(001), and Fe/MgO(001)) at higher residual stresses. Usually the higher residual stress states occur when the film starts to get very thin (i.e. on the order of 2 nm or less). Deviations from linearity of the magnetoelastic coupling with stress in the ultra-thin film regime could be due to higher order magnetoelastic terms and/or complicated changes in the film morphology (i.e. coincidence structures, pyramids, etc.), but it may also have its origins in true Néel-type surface effects induced by spin-orbit interactions. No experiments up to date have been conducted to try and separate non-linear magnetoelastic effects from surface spin orbit effects or to try and directly quantify the surface electronic contribution to the magnetoelasticity in the ultra-thin film regime. Likely both contributions will be important in these ultra-thin systems. Regardless, the thickness dependence of the magnetoelasticity coupled to large strains will have very important implications for the magnetic anisotropy in ultra-thin film structures. A quantification of such interactions and strains thus is of some importance if one is to attempt to understand the origin of the magnetic anisotropy in a particular system and optimize it for a specific application.

REFERENCES

- [1] L. Neel, "L'approche a la saturation de la magnetostriction," *J. Phys. Rad.*, vol. 15, p. 376, 1954.
- [2] J. H. Van Vleck, "On the Anisotropy of Cubic Ferromagnetic Crystals," *Phys. Rev.*, vol. 52, pp. 1178–1198, 1937.
- [3] B. Engel, C. England, Van Leeuwen RA, M. Wiedmann, and C. Falco, "Interface magnetic anisotropy in epitaxial superlattices," *Phys. Rev. Lett.*, vol. 67, no. 14, pp. 1910–1913, Sep. 1991.
- [4] R. C. O'Handley, O.-S. Song, and C. A. Ballentine, "Determining thin-film magnetoelastic constants," *J. Appl. Phys.*, vol. 74, no. 10, p. 6302, 1993.
- [5] E. T. De Lacheisserie, "Definition and measurement of the surface magnetoelastic coupling coefficients in thin films and multilayers," vol. 51, no. 22, 1995.
- [6] C. Chappert and P. Bruno, "Magnetic anisotropy in metallic ultrathin films and related experiments on cobalt films (invited)," *J. Appl. Phys.*, vol. 64, pp. 5736–5741, 1988.
- [7] C. Chappert, K. Le Dang, P. Beauvillain, H. Hurdequint, and D. Renard, "Ferromagnetic resonance studies of very thin cobalt films on a gold substrate," *Phys. Rev. B*, vol. 34, no. 5, p. 3192, 1986.
- [8] R. Jungblut, M. T. Johnson, J. aan de Stegge, A. Reinders, and F. J. A. den Broeder, "Orientational and structural dependence of magnetic anisotropy of Cu/Ni/Cu sandwiches: Misfit interface anisotropy," *J. Appl. Phys.*, vol. 75, no. 10, p. 6424, 1994.
- [9] G. Bochi, O. Song, and R. O'Handley, "Surface magnetoelastic coupling coefficients of single-crystal fcc Co thin films," *Phys. Rev. B*, vol. 50, no. 3, pp. 2043–2046, 1994.
- [10] G. Bochi, C. Ballentine, H. Inglefield, C. Thompson, and R. O'Handley, "Evidence for strong surface magnetoelastic anisotropy in epitaxial Cu/Ni/Cu(001) sandwiches," *Phys. Rev. B. Condens. Matter*, vol. 53, no. 4, pp. R1729–R1732, Jan. 1996.
- [11] J. W. Matthews, "Defects associated with the accommodation of misfit between crystals," *J. Vac. Sci. Technol.*, vol. 12, no. 1, p. 126, Jan. 1975.
- [12] H. Inglefield, "Ph.D Thesis," MIT, 1995.

- [13] G. C. A. M. Janssen, "Stress and strain in polycrystalline thin films," *Thin Solid Films*, vol. 515, no. 17, pp. 6654–6664, Jun. 2007.
- [14] J. Thornton and D. Hoffman, "Stress-related effects in thin films," *Thin Solid Films*, vol. 171, pp. 5–31, 1989.
- [15] W. Nix and B. Clemens, "Crystallite coalescence: A mechanism for intrinsic tensile stresses in thin films," *J. Mater. Res.*, pp. 3467–3473, 1999.
- [16] P. Bruno, "Tight-binding approach to the orbital magnetic moment and magnetocrystalline anisotropy of transition-metal monolayers.," *Phys. Rev. B. Condens. Matter*, vol. 39, no. 1, pp. 865–868, Jan. 1989.
- [17] D. Wang, R. Wu, and A. Freeman, "First-principles theory of surface magnetocrystalline anisotropy and the diatomic-pair model.," *Phys. Rev. B. Condens. Matter*, vol. 47, no. 22, pp. 14932–14947, Jun. 1993.
- [18] K. P. Takayama, H. Bohnen and P. Fulde, "Magnetic surface anisotropy of transition metals," *Phys. Rev. B*, vol. 14, no. 6, p. 2287, 1976.
- [19] J. M. Shaw, H. T. Nembach, and T. J. Silva, "Measurement of orbital asymmetry and strain in Co₉₀Fe₁₀/Ni multilayers and alloys," *Phys. Rev. B*, vol. 87, no. 5, p. 054416, Feb. 2013.
- [20] R. Wu and A. J. Freeman, "First principles determinations of magnetostriction in transition metals (invited)," *J. Appl. Phys.*, vol. 79, no. 8, p. 6209, 1996.
- [21] R. Q. Wu, L. J. Chen, and A. Shick, "First-principles determinations of magneto-crystalline anisotropy and magnetostriction in bulk and thin-film transition metals," *J. Magn. Magn. Mater.*, vol. 181, pp. 1216–1219, 1998.
- [22] A. Shick, D. Novikov, and A. Freeman, "Relativistic spin-polarized theory of magnetoelastic coupling and magnetic anisotropy strain dependence: Application to Co/Cu(001)," *Phys. Rev. B*, vol. 56, no. 22, pp. R14259–R14262, Dec. 1997.
- [23] M. T. Johnson, P. J. H. Bloemen, F. J. . den Broeder, and J. J. de Vries, "Magnetic anisotropy in metallic multilayers," *Rep. Prog. Phys*, vol. 59, pp. 1409–1458, 1996.
- [24] G. H. . Daalderop, P. J. Kelly, and F. J. A. den Broeder, "Prediction and Confirmation of Perpendicular Magnetic Anisotropy in Co/Ni Multilayers," *Phys. Rev. Lett.*, vol. 68, p. 682, 1991.

- [25] Y. Dahmane, S. Auffret, U. Ebels, B. Rodmacq, B. Dieny, I. Spintec, and G. Cedex, "Perpendicular Magnetic Anisotropy at Co / AlO_x Interface," *IEEE Trans. Magn.*, vol. 44, no. 11, pp. 2865–2867, 2008.
- [26] D. Weller, R. C. Farrow, R. F. Marks, G. R. Harp, H. Notarys, and G. Gorman, "Anisotropy in Co/Pt," *Proc. Mater. Res. Soc. Conf.*, vol. 313, pp. 791–797, Feb. 1993.
- [27] S. Monso, B. Rodmacq, S. Auffret, G. Casali, F. Fettar, B. Gilles, B. Dieny, and P. Boyer, "Crossover from in-plane to perpendicular anisotropy in Pt/CoFe/AlO_x sandwiches as a function of Al oxidation: A very accurate control of the oxidation of tunnel barriers," *Appl. Phys. Lett.*, vol. 80, no. 22, p. 4157, 2002.
- [28] A. Manchon, C. Ducruet, L. Lombard, S. Auffret, B. Rodmacq, B. Dieny, S. Pizzini, J. Vogel, V. Uhlř, M. Hochstrasser, and G. Panaccione, "Analysis of oxygen induced anisotropy crossover in Pt/Co/MO_x trilayers," *J. Appl. Phys.*, vol. 104, no. 4, p. 043914, 2008.
- [29] S. Ikeda, K. Miura, H. Yamamoto, K. Mizunuma, H. D. Gan, M. Endo, S. Kanai, J. Hayakawa, F. Matsukura, and H. Ohno, "A perpendicular-anisotropy CoFeB-MgO magnetic tunnel junction," *Nat. Mater.*, vol. 9, no. 9, pp. 721–4, Sep. 2010.
- [30] T. Liu, J. W. Cai, and L. Sun, "Large enhanced perpendicular magnetic anisotropy in CoFeB/MgO system with the typical Ta buffer replaced by an Hf layer," *AIP Adv.*, vol. 2, no. 3, p. 032151, 2012.
- [31] M. Klaua, D. Ullmann, J. Barthel, W. Wulfhekel, J. Kirschner, R. Urban, T. Monchesky, A. Enders, J. Cochran, and B. Heinrich, "Growth, structure, electronic, and magnetic properties of MgO/Fe(001) bilayers and Fe/MgO/Fe(001) trilayers," *Phys. Rev. B*, vol. 64, no. 13, p. 134411, Sep. 2001.
- [32] C.-H. Lambert, A. Rajanikanth, T. Hauet, S. Mangin, E. E. Fullerton, and S. Andrieu, "Quantifying perpendicular magnetic anisotropy at the Fe-MgO(001) interface," *Appl. Phys. Lett.*, vol. 102, no. 12, p. 122410, 2013.
- [33] H. X. Yang, M. Chshiev, B. Dieny, J. H. Lee, A. Manchon, and K. H. Shin, "First-principles investigation of the very large perpendicular magnetic anisotropy at Fe|MgO and Co|MgO interfaces," *Phys. Rev. B*, vol. 84, no. 5, p. 054401, Aug. 2011.
- [34] K. H. Khoo, G. Wu, M. H. Jhon, M. Tran, F. Ernult, K. Eason, H. J. Choi, and C. K. Gan, "First-principles study of perpendicular magnetic anisotropy in

- CoFe/MgO and CoFe/Mg₃B₂O₆ interfaces,” *Phys. Rev. B*, vol. 87, no. 17, p. 174403, May 2013.
- [35] S. Sun and R. O’Handley, “Surface magnetoelastic coupling,” *Phys. Rev. Lett.*, vol. 66, no. 21, pp. 2798–2801, May 1991.
- [36] O. Song, C. A. Ballentine, and R. C. O’Handley, “Giant surface magnetostriction in polycrystalline Ni and NiFe films,” *Appl. Phys. Lett.*, vol. 64, no. 19, p. 2593, 1994.
- [37] H. Szymczak, “Surface magnetoelastic behavior of magnetic multilayers (invited) Magneto-Elastic and Magneto-Optic Materials I Nitin Samarth, Chairman,” vol. 5411, no. 1997, pp. 8–13, 2013.
- [38] A. Enders, D. Sander, and J. Kirschner, “Strain dependence of the magnetic properties of nm Fe films on W(100),” *J. Appl. Phys.*, vol. 85, no. 8, p. 5279, 1999.
- [39] D. Sander, A. Enders, and J. Kirschner, “Magnetoelastic coupling and epitaxial misfit stress in ultrathin Fe (1 0 0) films on W (1 0 0),” *J. Magn. Magn. Mater.*, vol. 199, pp. 519–521, 1999.
- [40] T. Gutjahr-loser, D. Sander, and J. Kirschner, “Magnetoelastic coupling in Co thin films on W (0 0 1),” *J. Magn. Magn. Mater.*, vol. 220, pp. L1–L7, 2000.
- [41] D. Sander, A. Enders, and J. Kirschner, “Anisotropic surface stress on W(110),” *Europhys. Lett.*, vol. 45, no. 2, pp. 208–214, Jan. 1999.
- [42] D. Sander, C. Schmidthals, A. Enders, and J. Kirschner, “Stress and structure of Ni monolayers on W(110): The importance of lattice mismatch,” *Phys. Rev. B*, vol. 57, no. 3, pp. 1406–1409, Jan. 1998.
- [43] Z. Tian, D. Sander, and J. Kirschner, “Nonlinear magnetoelastic coupling of epitaxial layers of Fe, Co, and Ni on Ir(100),” *Phys. Rev. B*, vol. 79, no. 2, p. 024432, Jan. 2009.
- [44] M. Ciria, K. Ha, D. Bono, and R. C. O’Handley, “Magnetoelastic coupling in epitaxial Cu/Ni₉₀Fe₁₀/Cu/Si(001) thin films,” *J. Appl. Phys.*, vol. 91, no. 10, p. 8150, 2002.
- [45] K. Ha and R. C. O’Handley, “Nonlinear magnetoelastic anisotropy in Cu/Ni/Cu/Si(001) films,” *J. Appl. Phys.*, vol. 85, no. 8, p. 5282, 1999.

- [46] R. Koch, M. Weber, K. Thirmer, and K. H. Rieder, “Magnetoelastic coupling of Fe at high stress investigated by means of epitaxial Fe (001) films,” vol. 159, p. L11, 1996.
- [47] G. Wedler, J. Walz, A. Greuer, and R. Koch, “Stress dependence of the magnetoelastic coupling constants B1 and B2 of epitaxial Fe(001),” *Phys. Rev. B*, vol. 60, no. 16, pp. 313–316, 1999.
- [48] D. Sander and J. Kirschner, “Non-linear magnetoelastic coupling in monolayers: Experimental challenges and theoretical insights,” *Phys. Status Solidi*, vol. 248, no. 10, pp. 2389–2397, Oct. 2011.
- [49] M. Komelj and M. Fähnle, “Ab-initio modeling of nonlinear magnetoelastic coupling in epitaxial films,” *J. Magn. Magn. Mater.*, vol. 272–276, pp. E1587–E1588, May 2004.

CHAPTER 3

SURFACE ANISOTROPY AND MAGNETOELASTIC EFFECTS IN THE Ta/CoFeB/MgO SYSTEM

3.1 Recent Developments in the NM|CoFeB|MgO System

3.1.1 Perpendicular Anisotropy in NM|(Fe,CoFe,CoFeB)|MgO

The discovery of PMA in the Ta/CoFeB/MgO system was both fortuitous, of great technological importance, and somewhat perplexing. The Ta|CoFeB|MgO sequence was already an integral component of the stack structure in high TMR CoFeB/MgO/CoFeB based MTJs. It was observed that the CoFeB layers when not much thinner than ~ 2 nm would start to exhibit PMA after standard MTJ post anneals (used typically to enhance the TMR ratio). The effective perpendicular anisotropy energies in these CoFeB layers could become quite high (i.e. $K_u^{eff} \geq 4 \times 10^6 \text{ ergs} / \text{cm}^3$) and thus allowed for the engineering of small (< 50 nm) diameter, reasonable TMR ($> 100\%$) CoFeB|MgO|CoFeB junctions employing very thin CoFeB electrodes that were all perpendicular. These all perpendicular-MTJs (p-MTJs) exhibit some major advantages over in-plane polarizer/in-plane free layer type CoFeB|MgO|CoFeB MTJ spin-torque based switching such as enhanced thermal stability at smaller dimensions and lower write critical currents. These two facts lie at the heart of what makes the discovery of perpendicular anisotropy in the CoFeB|MgO of great technological interest. Results both by the IBM Watson group [1] and the Ohno group [2] in Japan

showed switching currents in p-MTJs as low as $I_c \sim 50\mu A$ for a 40 nm diameter MTJ and a $T = 300$ °K thermal stability factor $\Delta \sim 43$ respectively.

What makes the discovery one of fundamental interest is that the magnitude of the surface anisotropy energy in the annealed Ta|CoFeB|MgO system is quite large with values quoted as high as $K_s = 1.6$ ergs/cm² (we have ignored higher values which do not actively take into account dead layering). The origin of such high surface anisotropy is not immediately clear. Polycrystalline Ta|Co, Ta|Fe, and Ta|CoFe multilayers do not exhibit strong surface anisotropies. This would suggest that the CoFeB|MgO interface is extremely important in determining the magnitude of the surface anisotropy. However, MgO is composed of light elements where the spin-orbit coupling is presumably fairly weak. As is known from the case of Co|Ni multilayers, the spin-orbit coupling strength alone does not determine the surface anisotropy and the details of the band structure can also be important in determining the PMA. However, the scale of surface anisotropy ($K_s \sim 0.4$ ergs/cm²) in the model weak-S.O. Co|Ni PMA system is considerably smaller than what has been observed in the CoFeB|MgO system. Thus it would be quite interesting to understand the key ingredients which allow for the generation of high surface anisotropy at the CoFeB|MgO interface.

The surface anisotropy in the Ta|CoFeB|MgO system is heavily dependent on post-deposition annealing treatment. Annealing studies on Ta|CoFeB(x)|MgO structures tend to show a sharp increase in the PMA and the CoFeB thickness range over which PMA is exhibited as these systems are annealed at $T_a > 250$ °C (for a fixed

anneal time of 1 hour) [3]. Increasing the annealing temperature further results in a maximum of the PMA (typically at $T_a \sim 300$ °C) until at approximately $T_a > 350$ °C the PMA starts to drop sharply. Another study shows, using Rapid Thermal Annealing (RTA), that the effective TMR drops at longer anneal times when $T_a > 300$ °C but that this drop in the effective TMR is associated with the destruction of PMA rather than the interdiffusion of Ta into the CoFeB|MgO interface (which would destroy the TMR) [4]. The increase/decrease in the PMA and presumably the surface anisotropy upon annealing could be interpreted in terms of changes in the state of oxidation of surface Fe and Co atoms at the CoFeB|MgO interface. Careful XPS studies conducted by John Read have shown that RF-sputtered MgO on CoFeB has a tendency of oxidizing the CoFeB interface. Post-deposition annealing serves to reduce these ferromagnetic surface oxides via the oxygen reacting with any free Mg ions and by boron reduction [5]. Annealing at higher temperatures or for longer times can either re-oxidize the surface and/or allow for Ta diffusion to the CoFeB|MgO interface which also presumably reduces the surface anisotropy [6]. The presence of the oxygen anions at the CoFeB|MgO interface would seem then to be crucial in determining the overall strength of the surface anisotropy. Over-oxidation tends to destroy the PMA while there seems to be an optimal surface oxidation which yields the highest PMA. These conclusions are supported by experimental studies on the dependence of the PMA of CoFe|MgO and CoFeB|MgO interfaces as a function of Mg thickness under natural oxidation [7] and studies of XMCD spectra of Fe L edge absorption in Si|SiO₂|MgO|CoFeB(1.5)|Pt(2) as a function of plasma oxidation time on a 2 nm Mg buffer layer [8].

Crystallization kinetics and post-annealed crystal structure could also be important in determining the PMA magnitude at the CoFeB|MgO interface. As-deposited, amorphous CoFeB starts crystallizing typically at annealing temperatures of $\sim T > 300$ °C. At this temperature B starts diffusing out of the CoFeB and into the MgO barrier [9] and Ta seed layer [10]. As a consequence of the removal of the B glass former, the CoFeB starts to undergo a grain-by-grain pseudo-epitaxial crystallization off of the MgO (001)-oriented polycrystalline texture [11]. This interfacial grain-by-grain epitaxy/atomic coherence is considered responsible for the increase in the TMR of CoFeB|MgO|CoFeB MTJs (a la Butler-Mathon). It stands to reason that increased interfacial coherence at a CoFeB|MgO system might be the cause of the observed post-annealing increase of the PMA in these systems.

Ab-initio studies have pointed out that the hybridization of O $2p_z$ orbitals and Fe $3d_{z^2}$ orbitals at a coherent Fe|MgO interface and the associated changes in the band structure could be largely responsible for the enhanced surface anisotropy in this system [12]–[15]. Reference [16] interprets their results from the point of view that the S.O. coupling between occupied and unoccupied minority band states are primarily responsible for the magnetocrystalline anisotropy (MCA) as majority band states are presumed to be typically below E_F on the order of a few eV associated with the Stoner splitting. S.O. couplings connecting minority d_{z^2} bands to minority d_{xz} , d_{yz} bands about the $\bar{\Gamma}$ point in a free-standing Fe monolayer generate negative contributions to the overall surface MCA energy. These negative contributions are removed by the hybridization of d_{z^2} bands with the O p_z orbitals which raises the minority d_{z^2} bands

above E_F . Nakamura et al. argue that this removal of the negative contribution about the $\bar{\Gamma}$ point generates the positive enhancement of the PMA in the pure epitaxial Fe|MgO interface. Contributions to the MCA at other k-points in the first B.Z. are similar to the case of the free-standing Fe monolayer.

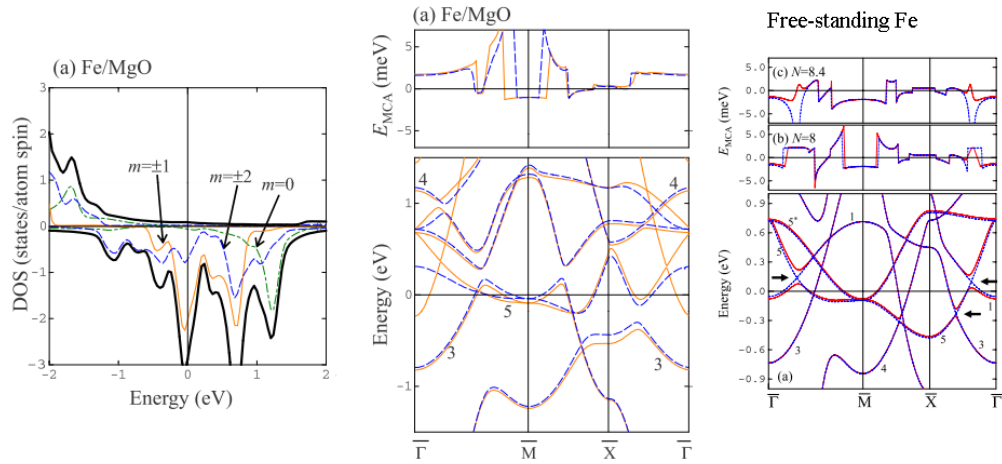


Figure 3.1 Minority d-band structure at optimally oxidized Fe-MgO interface decomposed into the various subbands. Note d_{z^2} band ($m=0$) pulled ~ 1 eV above E_F . Next we have a side-by-side comparison of the band structure of Fe at the Fe|MgO interface ($N=8$) and for a free standing Fe monolayer at $N=8$.

Yang et al., on the other hand, argues that the energy level structure at the $\bar{\Gamma}$ point in the majority band is also important for determining the MCA.

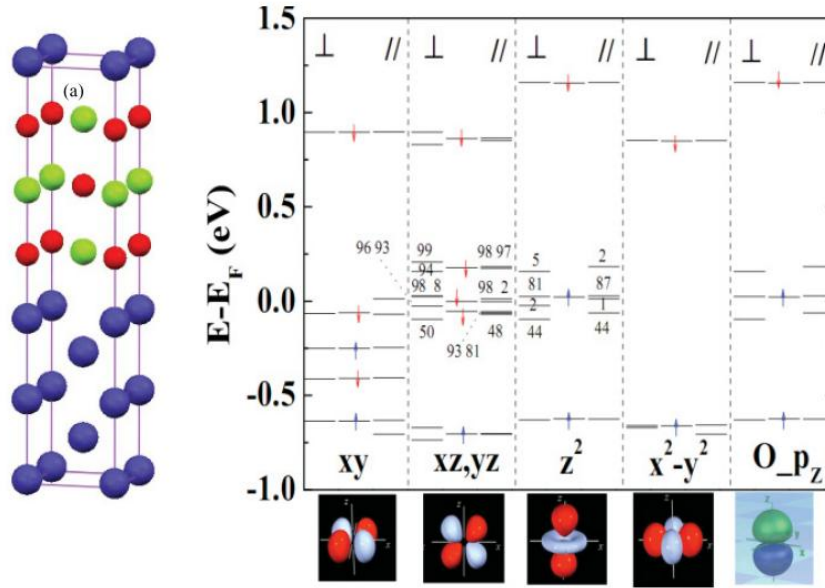


Figure 3.2 Red, green, and blue atoms correspond to the positions of O, Mg, and Fe in the optimally oxidized system. Energy levels/splitting and hybridization for the various Fe d bands and the O p_z bands at E_F near the Γ point. Taken from reference [12].

Figure 3.2 shows that the majority hybridized Fe $d_{z^2} - O p_z$ bands get close to the Fermi level. When the spin-orbit interaction is turned on these previously hybridized $p_z/3 d_{z^2}$ bands become admixed with minority d_{xz} and d_{yz} bands. In addition, degenerate d_{xz} and d_{yz} bands admix amongst themselves and are split. Thus the spin-orbit interaction and majority O $p_z - d_{z^2}$ and $p_z - d_{xz}, d_{yz}$ hybridization also seem to be an important component of the MCA near the $\bar{\Gamma}$ point. Yang et. al do not mention the behavior of the MCA at any other point in the BZ. It is unclear why they exclusively use the $\bar{\Gamma}$ point to explain the MCA. We say this because the problem of MCA is not the same as the Fe|MgO|Fe tunneling problem where in the thick MgO limit it is clear

that the $\bar{\Gamma}$ point should dominate. We can only surmise that they too find that the major difference in the MCA energy between freestanding Fe and Fe|MgO lies near the $\bar{\Gamma}$ point.

All of the ab-initio studies show that the surface anisotropy is extremely sensitive to the state of oxidation at the Fe|MgO interface. Yang et al. show that they get interfacial anisotropy energies of $K_s = 2.93$ ergs/cm² for an optimally oxidized, structurally relaxed interface, $K_s = 2.27$ ergs/cm² for an under-oxidized interface, and $K_s = 0.98$ ergs/cm² for an over-oxidized interface. The calculations by Nakamura et al. yield interfacial anisotropy energies of 1.28 meV/atom for optimal oxidation and -0.18 meV/atom for an over-oxidized interface (only layer of interfacial FeO). While there are considerable quantitative differences in predicted PMA values between [12] and [13], the general prediction that over-oxidation seems to destroy PMA is one shared amongst all the theoretical works (and corroborated by experiment).

The content of Fe in BCC CoFe alloys/MgO or NM/CoFeB/MgO annealed systems also seems to be important. Experimental results by IBM have demonstrated that Fe dusting at the CoFeB|MgO interface is effective at enhancing the PMA. [17] In addition works by other groups have shown that changing the ratio x towards higher Fe concentration in $[\text{Fe}_x\text{Co}_{1-x}]_8\text{B}_2$ tends to increase the induced surface anisotropy at the CoFeB|MgO interface [18]–[21]. Some have taken this as evidence for the importance of specific Fe site 3d orbital-O 2p_z hybridization. Others have taken this to be a sign of the importance of where the chemical potential sits in the band structure (assuming that the rigid band model is valid for the d-bands in the FeCo alloy system).

The addition of Co into the system effectively increases the number of valence electrons/unit cell. The idea is that the PMA decreases with increasing electron number N in the vicinity of $N = 8$.

Lastly the surface anisotropy in the CoFeB|MgO system seems to be heavily dependent on the underlayer. This dependence is by and far the most confusing aspect of the surface anisotropy at CoFeB|MgO interfaces and raises many questions about the basic mechanisms involved. The first NM|CoFeB|MgO to exhibit strong PMA/surface anisotropy was the Ta|CoFeB|MgO system ($K_s=1.8$ ergs/cm² without dead layer corrections), Figure 3.3 shows the $K_u t$ vs t curve for the Ru underlayer and the Ta underlayer case.

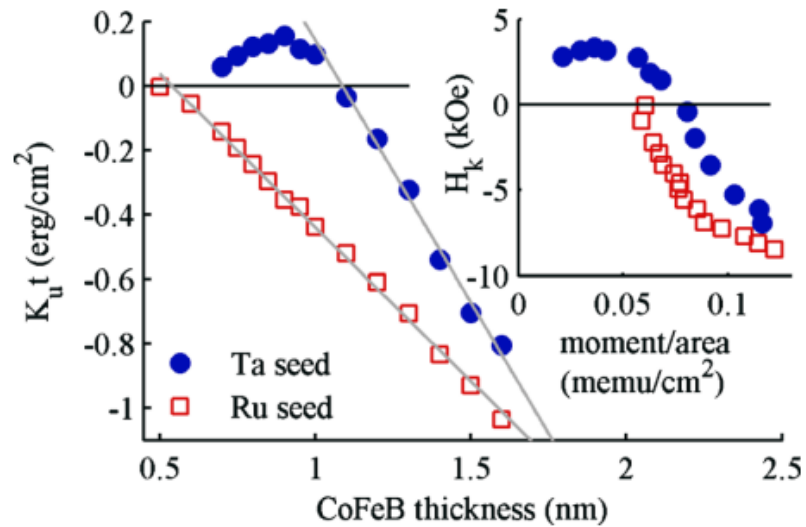


Figure 3.3 $K_u t$ vs t without dead layer subtraction for Ta(2)|Co₆Fe₂B₂|MgO and Ru(2)|Co₆Fe₂B₂|MgO taken from reference [1].

Clearly, the underlayer has bearing on the magnitude and behavior of the anisotropy in these NM|CoFeB|MgO systems. However, it is generally not possible to express the impact that the underlayer has on the total surface anisotropy in terms of a sum of interfacial anisotropies $K_s^{tot} = K_s^{CFB|Underlayer} + K_s^{CFB|MgO}$. We actually find this general practice to be a highly suspect as it assumes the interfaces are uncorrelated. This assumption is very hard to justify when dealing with ferromagnets that are a few atomic layers thick and whose structure will in general depend heavily on the underlayer and capping layer. It is clear that the Ta|CoFeB interface by itself generates no surface anisotropy. Ta|CoFeB|Ta (both annealed and as deposited) has been shown to generate no surface anisotropy [22]. It is for these reasons that the CoFeB|MgO interface in the Ta|CoFeB|MgO system is widely held to be solely responsible for the large surface anisotropy. However, the Ta underlayer clearly serves to greatly enhance the PMA at the CoFeB|MgO interface during the post-deposition anneal (as compared to underlayers such as Ru).

The reason why Ta serves to promote the surface anisotropy at CoFeB|MgO interface may have a great deal to do with its reactivity with B. It is well known that Ta is an effective boron sink (certainly much more effective than Ru). Hindmarch et al. [23] have pointed out that the enthalpy for boride formation is considerably lower for Ta than for Ru. Thus boron diffusion out of the CoFeB electrodes and into the buffer layer is much more effective when NM = Ta than when NM = Ru. It has been argued that better crystallization and coherence at the CoFeB|MgO interface (associated with buffer layers having lower enthalpy for boride formation) could be

the reason why the surface anisotropy in annealed Ta|CoFeB|MgO is much higher than in Ru|CoFeB|MgO. Guided by this general line of thinking, Hf (with a considerably lower enthalpy than Ta for boride formation) was next tried to see what its effects on K_s in at CoFeB|MgO interface might be.

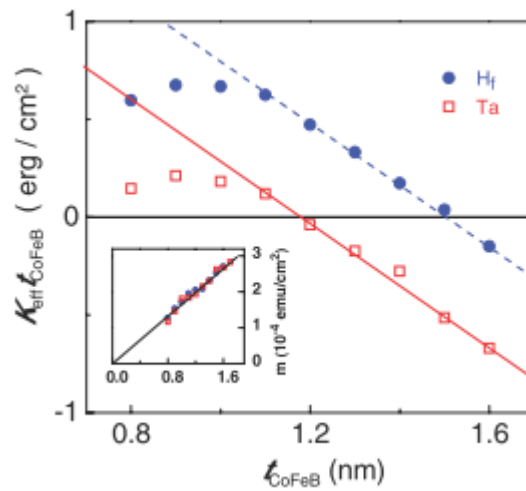


Figure 3.4 $K_{\text{eff}}^{\text{CoFeB}}$ vs t_{eff} curve for Hf(5)/Co₄₀Fe₄₀B₂₀/MgO(2.2)/Ta(1) and Ta(5)/Co₄₀Fe₄₀B₂₀/MgO(2.2)/Ta(1) annealed at $T = 300$ °C for 1 hr. The inset shows M/A vs t_{CFB} for both the Hf and the Ta series and reveals that neither series has a magnetic dead layer.

It was found that the use of Hf as either an underlayer or even as a sub-monolayer insert greatly enhances the PMA over the Ta|CoFeB|MgO system. A study by Liu et al [22] showed that $K_s=2.2$ ergs/cm² in the Hf|Co₄Fe₄B₂|MgO system (extracted from fits to the Néel model) as compared to $K_s=1.7$ ergs/cm² in the Ta|Co₄Fe₄B₂|MgO system. A second study showed that a thin 1 nm Hf insert has the effect of enhancing

the PMA considerably in the W/CoFeB/MgO system from $K_s \sim 0.02 \text{ ergs/cm}^2$ to $K_s \sim 1.9 \text{ ergs/cm}^2$.

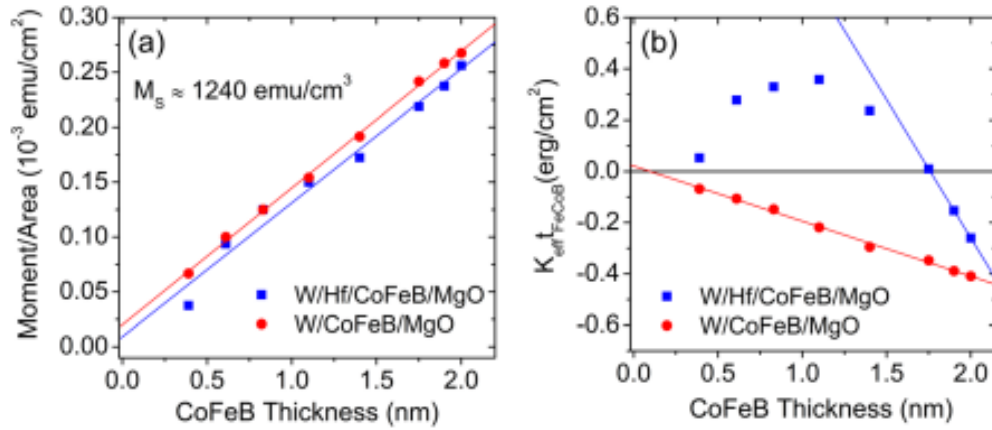


Figure 3.5 a) M/A vs CoFeB thickness shows no dead layering with either a β -W underlayer or a β -W underlayer with a Hf insert. Interestingly, the $M_s \sim 1240 \text{ emu/cm}^3$ is low and is the same with and without the Hf insert. b) $K_{\text{eff}} t_{\text{eff}}$ vs t_{eff} for both cases. Note that K_s increases substantially with the Hf(1) insert whereas $K_s \sim 0$ with the pure β -W underlayer. Taken from reference [24].

Thus there seems to be a strong positive correlation between the reactivity of the underlayer with B and the strength of K_s induced in the NM|CoFeB|MgO system.

However, there are other factors that are important in increasing K_s . Diffusion of the buffer layer to the CoFeB|MgO interface during annealing likely has deleterious consequences for the surface anisotropy. One study has focused on the use of nitrogen doping of the Ta buffer layer in order to block Ta diffusion into the CoFeB layer during the high temperature anneal. The study reports $K_s = 1.4 \text{ ergs/cm}^2$ for Ta(1)/Co₂Fe₆B₂/MgO. K_s rises to 1.8 ergs/cm^2 with a 1% N doping into the Ta layer during sputtering (note that for the N-doped layers they use Ta_{1-x}N_x (4 nm) underlayers

to compare with their Ta (1 nm) underlayer). Further increase of the N content in the Ta underlayer causes a substantial reduction in K_s . K_s drops to 1.1 ergs/cm² at 2% N doping and drops further with increased N doping. The study also reports anomalously high positive volume anisotropy in their Ta(1)/CoFeB/MgO stacks ($K_v \sim 8 \times 10^6$ ergs/cm³). This volume anisotropy decreases with the introduction of N doping (Figure 3.6). The reason that such high volume anisotropies arise in these systems (particularly in the Ta underlayer case) is not clear at all.

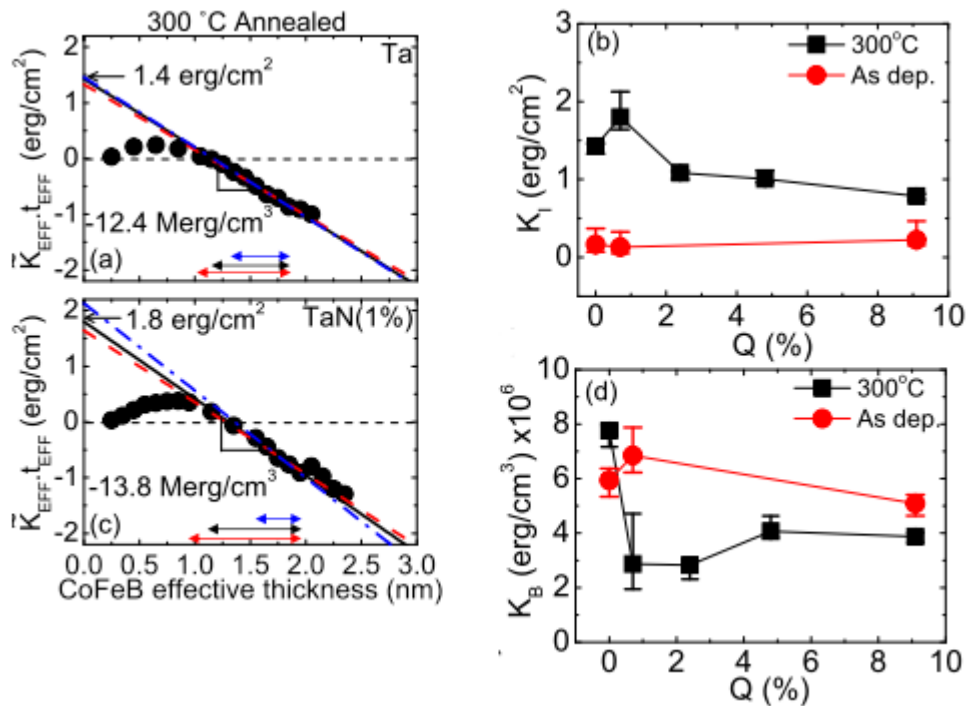


Figure 3.6 $K_{\text{eff}}t_{\text{eff}}$ vs t_{eff} for Ta(1)|Co₂₀Fe₆₀B₂₀|MgO|Ta(1) and TaN[1%](4)|Co₂₀Fe₆₀B₂₀|MgO|Ta(1) and surface anisotropy and volume anisotropy vs N doping percentage into Ta buffer layer for annealed and as deposited samples. Adapted from reference [25].

The nitrogen doping helps to suppress magnetic dead layer formation that could arise from Ta diffusion into the CoFeB during annealing. With only a Ta (1 nm) buffer layer they observe magnetic dead layers as high as 6 Å (seen in Figure 3.7 below). When 1% Nitrogen is doped into Ta it reduces the dead layer down to 3 Å. This suppression of Ta diffusion (associated with the general notion that TaN forms a good diffusion barrier), probably enhances K_s at the CoFeB|MgO interface. The diffusion of Ta can substantially hamper CoFeB crystallization (via amorphous Ta_xB_{1-x} formation throughout the magnetic layer) as well as suppress K_s at CoFeB|MgO interface by allowing for TaO_x formation instead of encouraging Fe-O hybridization. Thus the suppression of Ta diffusion for 1% N doped Ta underlayer is likely the reason for the enhancement of K_s at the CoFeB|MgO interface.

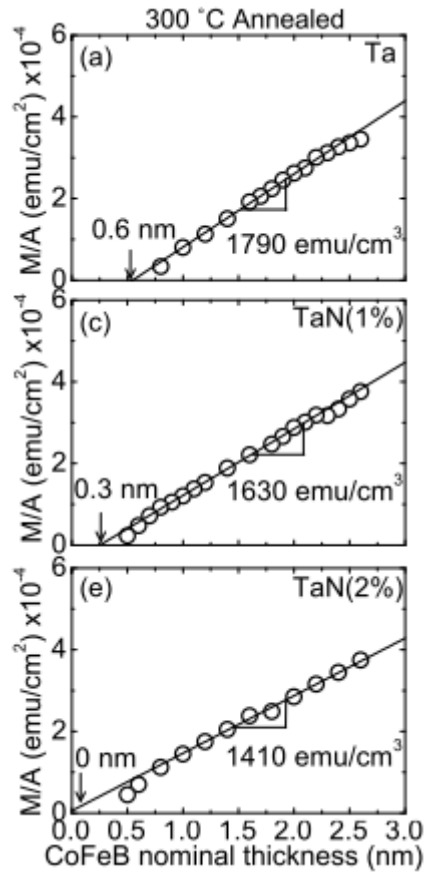


Figure 3.7 Dependence of M_s and dead layering as a function on N doping of the Ta layer for Ta|Co₂₀Fe₆₀B₂₀|MgO samples. Taken from supplementary of reference [25].

Increased nitrogen content past 1% starts to reduce K_s substantially. This is probably the regime of nitrogen doping where the TaN acts as a very good diffusion barrier not just against large atoms like Ta but also against smaller atoms like B. Nitridization at this level also probably suppresses the boron gettering properties of the Ta underlayer. This is consistent with the general observation that buffer layers which suck up B tend to lead to higher induced K_s at the CoFeB|MgO interface.

A more recent study has shown that high $K_s = 2 \text{ ergs/cm}^2$ can be achieved in the Mo|CoFeB|MgO system with a 1 hour long $T = 300 \text{ }^\circ\text{C}$ anneal [26]. It was demonstrated that Mo is an underlayer which does not diffuse into the CoFeB even during higher temperature ($T > 350 \text{ }^\circ\text{C}$) annealing and is well-crystallized in a way that can aid the CoFeB|MgO grain-by-grain templating effect. From the point of view of diffusion into CoFeB and allowing the CoFeB at the CoFeB|MgO interface to crystallize well, Mo seems to fit some of the statements made on what is required for the emergence of high surface anisotropy at the CoFeB|MgO interface. Of course, one of the main questions is: how does Mo allow for high crystallinity at the CoFeB|MgO interface? Is it also effective at B sinking? Bulk data seems to suggest it is much worse as a B sink than Ta or Hf. However, Mo in ultra-thin film form (which could be under potentially high stresses), might have a low enthalpy for boride formation. Since no spectroscopy was done in [26], it is difficult to know where the B has actually gone. If very little B is found in the Mo underlayer and most of it is found in the MgO, it would certainly be quite interesting as the physics of CoFeB|MgB_xO_y is probably a little different than CoFeB|MgO. Frankly, at this point, Mo as an underlayer poses some interesting questions – which in the absence of more data cannot be answered.

We have discussed some general correlations in NM|CoFeB|MgO systems. However, we would like to point out that there are, even with a given buffer layer, things that are clearly not universal. Magnetic dead layer formation in the Ta|CoFeB|MgO system seems to be one of these non-universal things. Certain experiments show dead layering at the Ta|CoFeB interface before and after annealing with Ta directly deposited on SiO₂. [1], [17], [25]. Figure 3.7 above shows that

substantial dead layers can develop (i.e. on the order of $t_{DL} = .6$ nm or more). Other studies (including our own study) show no such dead layer formation [22]. One study claims that dead layering on the order of .5 nm in their p-MTJ structures occurs in the top CoFeB electrode (MgO|CoFeB|Ta(5) cap) but not in the bottom CoFeB electrode (Ta(5)|Ru(10)|Ta(5)|CoFeB|MgO) [2]. Clearly, dead layer formation at the Ta|CoFeB interface (and probably at many other NM|CoFeB interfaces) is sensitive to deposition conditions and annealing procedure. For example, we firmly believe that deposition rate, deposition voltage, gun-to-substrate distance, and gas working pressure will all critically affect the degree of intermixing between layers and thermal stability of these interfaces under subsequent annealing. The saturation magnetization M_s (with dead layer corrections) also show a wide degree of variability for nominally identical systems and similar annealing treatment.

We have discussed the general empirical trends, deviations from universal behavior and quandaries that data taken across many NM underlayer systems expose about surface anisotropy generation in the NM|CoFeB|MgO system. We have yet to attack the more difficult question of what the mechanism(s) of surface anisotropy generation in the NM|CoFeB|MgO are. For example, in what ways do B diffusion out of CoFeB actually affect the surface anisotropy? B diffusion out of CoFeB could entail crystallization of the CoFeB|MgO interface. Is this interfacial crystallization a pre-requisite for high K_s ? Perhaps the diffusion of B during annealing has another effect. The B diffuses away from the CoFeB|MgO interface and O anions rearrange themselves to bond/hybridize effectively with Co and/or Fe atoms (instead of with B). The difference between the two scenarios is whether 2D interfacial long-range order at

the CoFeB|MgO interface is required in order to generate/maximize the surface anisotropy at the CoFeB|MgO interface or whether short range Fe-O and Co-O correlations alone can drive very high surface anisotropies. We believe that crystallization is not a prerequisite to achieving significant positive surface anisotropy although we think that crystallization will certainly have significant effects on the magnitude of K_s and the thickness dependence of the PMA. We back this statement up with the observation that, at least at some point, in the AJA Orion sputtering system we observed in-plane to out-of plane transitions for CoFeB films as thick as $t_{\text{CoFeB}} = 1.4$ nm in as-deposited Ta|CoFeB|MgO samples. Unfortunately we did not, at that time, do a full thickness series to extract the surface anisotropy or dead layers induced in these as-deposited Ta|CoFeB|MgO structures. The surface anisotropy induced in as-deposited samples seems to be highly sensitive to the MgO target used and can change after a vent. Recent TEMs of the W/Hf(1)/CoFeB(x)|MgO structures used in Reference [24] show that the CoFeB is also amorphous. Despite the lack of crystallization of the CoFeB at the CoFeB|MgO interface, the surface anisotropy in this system is large with $K_s = 1.9$ ergs/cm². Regardless, it is extremely unclear what kind of oxygen anion ordering and Fe ordering is required to drive high surface anisotropy at the CoFeB|MgO interface and how the surface anisotropy changes if the 2D interface becomes more ordered due to CoFeB crystallization. We think that systematic work along these lines would be very interesting indeed.

B diffusion, subsequent B gradients in the CoFeB, and/or CoFeB crystallization can also have other effects. The strain present in the CoFeB film associated with B diffusion might have also have a significant impact on the surface

anisotropy. Varying degrees of strain in the CoFeB film and/or strain relaxation behavior could arise from differences in the crystal structure and residual strain of the underlayer as well as the underlayer's ability to soak up B. In addition the underlayer and its ability to diffuse and react with B could affect the morphology of the partially crystallized CoFeB grains. Changes in the state of strain and morphology at the CoFeB|MgO interface and deeper into the "bulk" of the CoFeB film may have very important implications for the surface anisotropy. As has been pointed out by Yang et al., differences in the surface anisotropy between relaxed and unrelaxed Fe|MgO and structure can be quite significant. The calculated surface anisotropy for a relaxed structure is ~ 3 ergs/cm² and for an unrelaxed structure is ~ 1.3 ergs/cm². Lee et al. [27] have also pointed out that the distance between the oxygen anions and Fe atoms can have substantial effects on the surface anisotropy. They found that K_s could be increased by a factor of 3 by increasing the Fe-O plane distance by 8%. This is, admittedly, a very large strain. In a smaller strain regime, the calculation shows that an increase of $\sim 2\%$ in the Fe-O plane distance leads to a surface anisotropy decrease of $\Delta K_s \sim -0.2$ ergs/cm². Strain changes in the magnetic film induced by B diffusion and CoFeB crystallization could thus contribute to the increases/decreases in the surface anisotropy. Clearly, there is room for studying strain effects in these systems and, in general, for more systematic and careful work in parsing the structure of the interactions leading to high surface anisotropy in the CoFeB|MgO system.

3.1.2 Voltage Controlled Magnetic Anisotropy (VCMA)

The CoFeB|MgO interface exhibits another effect related to the PMA known as the VCMA. The CoFeB|MgO interface is fundamentally a junction between a magnetic metal and an insulator. This fact suggested the possibility of modifying the PMA at the CoFeB|MgO interface by application of an electric field through the insulator. A number of experiments have confirmed that one can modify the PMA anisotropy in ultrathin CoFe alloy|MgO systems and that the effect, at least in terms of absolute field, can be quite sizeable (~several hundreds of Oe). The typical scales involved in terms of the anisotropy energy change and in particular the surface anisotropy change are around $\Delta K_i \sim 20\text{-}30$ mergs/cm² in $\Delta E_g \sim 6$ MV/cm at the CoFeB|MgO interface. In other words dK_i/dE_g is on the order of ~ 5 (mergs/cm²)/(MV/cm) or 50 mergs/cm²/(V/nm). E_g is the electric field within the MgO. This scale seems to be the same both in patterned nanopillar CoFeB|MgO|CoFeB MTJs and in micron-sized Ta|CoFeB|MgO|(HfO₂/ZrO₂) gated Hall structures [28]. In studies of the VCMA in the Ta|CoFeB|MgO, Fe|MgO [29], and CoFe|MgO system [30], the anisotropy increases (decreases) as electrons are removed (added). Data showing the typical sign and magnitude of the effect is shown below in Figure 3.8 below.

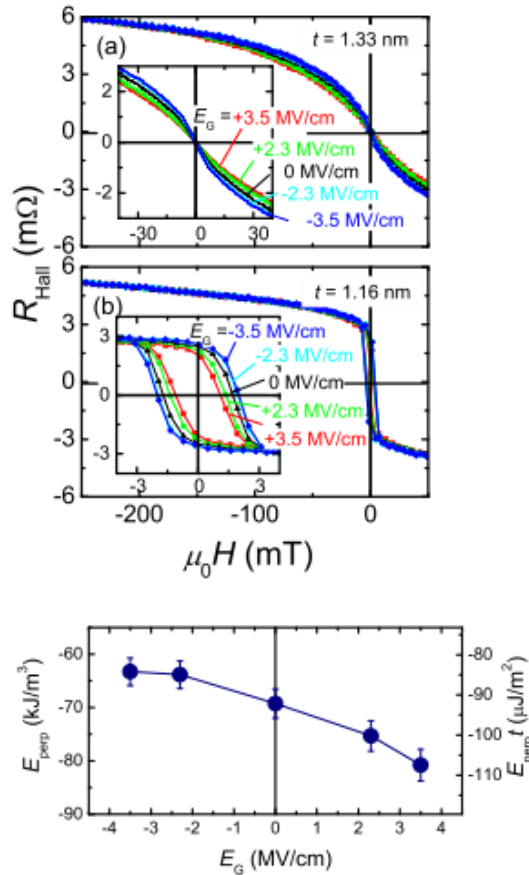


Figure 3.8 R_{Hall} vs H loops for in-plane samples as a function of gate showing E-field induced changes in anisotropy as well as easy axis loops for perpendicular sample as a function of E-field (showing modulation of H_c). The increase in H_c is thought to arise primarily from increases in H_k . Lastly the change in the surface anisotropy energy as a function of gate electric field is shown. Data taken from [28].

The consequence of being able to modify the perpendicular magnetic anisotropy by gate voltage has been explored extensively. Among these works are gate-voltage induced ferromagnetic resonance in Fe|MgO|Fe micron size epitaxial junctions [31], VCMA-assisted magnetic field switching [32], VCMA tuning of the operational frequency of a spin-Hall spin torque oscillator [33] as well as gate modulation of switching currents, simultaneous probing of the VCMA and STT torques via STT-

FMR and the consequences that VCMA has for spin torque resonant detectors [34].

Despite the research that has already been poured into the VCMA, the origin(s) of the VCMA and its behavior are still quite open to debate. One possibility is that the electric field modifies the chemical potential via introduction of surface charge onto the metallic ferromagnet. This E-field induced change in the chemical potential would modify the surface anisotropy energy as the interfacial density of states (and the G and H functions of Bruno's theory [35]) would now be different from $E_g = 0$ case. This assumes that the interfacial bands themselves do not deform or change under an external E-field. A few ab-initio papers have shown that the electric field might (along with changing the chemical potential) induce splittings in the bands structure near certain band degeneracies. Band modification can emerge from the fact that a z -directional E-field can alter the matrix elements between O p_z orbitals and Fe d_{z^2} bands via selection rule physics [13], [16]. Another reason is that the electric field could induce structural changes local to the Fe-O interface (i.e. E-field induced lattice breathing) that then alters the interfacial band structure and the surface anisotropy [13].

There are other propositions as to what mechanisms drive the VCMA at the CoFeB|MgO or Fe|MgO interface and what factors are important for determining the magnitude and sign of dK_s/dE_g . One study conducted in the Pt|Co|GdO_x system has concluded that the VCMA effect is dominated by oxygen anion motion induced by the electric-field [36]. As we have noted in Section 3.1.1, the surface anisotropy is highly dependent on the oxygenation level. Thus by modifying the oxygen anion density at

the surface by gate voltage, one effectively tunes the surface anisotropy. This certainly may be going on in the NM|CoFeB|MgO system although we do point out that E-field induced ionic motion is much more likely in a thicker amorphous sub-oxide like GdO_x than it is in a thin fully crystallized MgO barrier. Another paper has claimed that strain-mediated effects associated with deformation of the MgO dielectric under an applied E-field is largely responsible. Their claim is that magnetoelastic effects are largely responsible for the VCMA [37].

Another experimental finding has served only to complicate the picture. This study has shown that dK_s/dE_g reverses sign in the annealed NM|CoFeB|MgO system when the standard Ta seed layer is replaced by a Ru underlayer [38]. The experiment shows that $dK_s/dE_g = -29 \text{ fJ/Vm}$ with Ta underlayer to $dK_s/dE_g = +18 \text{ fJ/Vm}$ with Ru underlayer. While it is surmised that replacing Ta with Ru affects changes at the CoFeB|MgO interface, it is not clear at all what these changes might be. Does the sign of dK_s/dE_g change due to the fact that the boron and/or oxygen content at the CoFeB|MgO interface differ when a Ru or Ta underlayer is used? Perhaps it is a primary function of relative levels of crystallinity of the CoFeB at the CoFeB|MgO interface. Or maybe different underlayers put the CoFeB at the CoFeB|MgO interface under different degrees of strain – which in turn might change the sign/magnitude of the VCMA.

3.2 Motivation For Our Experiment

There are many open questions with regards to what factors shape the PMA and the VCMA sensitivity and how they may be tuned. Strain (both bulk and interfacial) and magnetoelastic interactions in the CoFeB|MgO system, as we have discussed, may be important in determining the behavior of the PMA and the VCMA (i.e. thickness dependence, magnitude, and sign). However, no study yet has undertaken a systematic characterization of strain-dependent effects in the NM|CoFeB|MgO system or rigorously discussed what impact magnetoelastic effects might have on the PMA or the VCMA in these systems. The studies that have discussed magnetoelastic effects (in a rather ad-hoc fashion) use bulk values of magnetostriction for amorphous CoFeB alloys to count or discount the importance of magnetoelastic couplings. However, there is no assurance that the magnetoelastic coupling in ultrathin amorphous CoFeB films is the same as the bulk value for amorphous CoFeB or that it is even the same sign. The use of the bulk amorphous CoFeB magnetostriction values is even more unjustified when discussing annealed/partially crystallized CoFeB layers. Partial crystallization off of the MgO, material and strain gradients in the CoFeB, second-order magnetoelastic effects, and intrinsic surface magnetoelastic effects at the CoFeB|MgO interface could generate strong thickness dependence of the magnetoelastic coupling, the PMA, and potentially be important in understanding the VCMA in NM|CoFeB|MgO systems.

Our experiment thus endeavors to systematically characterize magnetoelastic couplings in the Ta|CoFeB|MgO stack – both for annealed and as deposited samples.

We conduct a study of the thickness dependence of the magnetoelasticity for both types of samples. Knowledge of the thickness dependence of magnetoelastic effects in both annealed and as-deposited samples may shed light into the magnitude and thickness dependence of the perpendicular anisotropy in NM|CoFeB|MgO systems. A quantification of the thickness dependence of the magnetoelastic coupling would also be a prerequisite for parsing and separating out strain-mediated contributions to the VCMA. Finally, we perform an experiment to see whether the VCMA is sensitive to changes in strain. To first order in strain and voltage this measurement is equivalent to probing the voltage dependence of the magnetoelastic coupling B_{eff} . A quantification of this effect would be useful for understanding what sorts of processes play a role in the VCMA at the CoFeB|MgO interface. For convenience we call this effect Voltage Controlled Magnetoelasticity (VCME).

3.3 Film Growth & Preparation

The film stacks used in this study were grown in the AJA ATC-2200 Orion 7 gun Magnetron Sputtering System. All films were grown at a base pressure $P_0 < 1 \times 10^{-8}$ torr. We grew Ta(6 nm)/Co₄Fe₄B_{2(x)}/MgO (2.2 nm)/Hf (1 nm) stacks with a range $x = 0.7-2.0$ nm onto a thermally oxidized 375 μm thick Si[001] wafer. All metallic films were grown at low power $P = 30$ W and at relatively low sputter pressure of $P_{\text{sputt}} = 2$ mtorr. The MgO was grown at 100 W RF Forward power at 2 mtorr. The deposition rates for our metallic films were low at typical rates of ~ 0.1 A/s. Our CoFeB was deposited at an average rate of ~ 0.08 A/sec. The MgO deposition rate at the conditions we sputtered at was ~ 0.04 A/s. All films were grown with stage

rotation on and with the normal stage so that there was no deposition magnetic field. We diced a set of the wafers we grew into $3.5 \times 3.5 \text{ mm}^2$ chips for magnetometry using the KS7100 Wafer Saw in CNF. Accurate knowledge of the chip size is required for accurate magnetization measurements. The other set of wafers were used to make Hall bar structures used for measurement of the magnetoelastic constants. The annealed samples were annealed at $T = 300 \text{ }^\circ\text{C}$ (which corresponds to $T = 200 \text{ }^\circ\text{C}$ on the temperature controller) for 1 hour in the Lindbergh Vacuum Furnace in CCMR in an in-plane field of 1.3 kOe for SQUID magnetometry.

3.4 Sample Fabrication

The wafers for magnetoelastic characterization were transferred to CNF in an evacuated dessicator for patterning. We fabricated un-gated and gated Hall-bar devices. The un-gated devices were used to measure the thickness dependence of the magnetoelastic coupling. For these un-gated devices, we fabricated the entire thickness series range Ta(6)/CoFeB(x)/MgO(2.2)/Hf(1) with x ranging from 0.7-2.0 nm. The gated devices were used for our VCME idea and, as we wanted to probe the in-plane magnetoelastic coupling, we wished to keep the magnetization in-plane (albeit with strongly reduced effective demagnetization field). For these we only fabricated samples close to the crossover from in-plane to out of plane anisotropy at $x = 1.3 \text{ nm}$ and $x = 1.4 \text{ nm}$. We outline the gated device process in detail (the un-gated process is a subset of this). Table 3.1 gives an outline of my process flow.

1.	<p>Photolith 1: Isolate Devices/Define Alignment Marks</p> <p>S1813: Spin Speed 2000 RPM for 60 secs</p> <p>115 C Pre-Bake for 1 min + 20 secs on chill block</p> <p>Karl Suss MA6/BA6 Contact Aligner, Mode: Soft Contact, Exposure Time: 4 s</p> <p>Alignment Gap: 30 μm</p>
2.	<p>Ion Mill 1: Etch to isolate device.</p> <p>Etch Angle at 165 degrees until endpoint detection on SiO_x. 1 min etch after that at 110 degrees to clean sidewalls.</p>
3.	<p>Photolith 2: Define mesas.</p> <p>Same parameters for resist spin and exposure as Photolith 1.</p>
4.	<p>Ion Mill 2: Etch to Ta base electrode to define mesa.</p> <p>Etch Angle at 165 degrees until endpoint detection on Ta. 1 min etch after that at 110 degrees to clean sidewalls.</p>
5.	<p>Deposition 1: ALD HfO_2 Gate oxide deposition.</p> <p>Thermal ALD at 200 °C. 208 loops = 26.5 nm thickness as measured by Woolam ellipsometer.</p>
6.	<p>Photolith 3: Define etch windows for oxide above contact.</p> <p>Option 1: For W, Ta underlayers we use ion milling with endpoint detection</p> <p>Option 2: Can use Oxford 81/82 RIE @ 150 W RF, CF_4 10 mtorr if base</p>

	electrode is Pt.
7.	Ion Mill 3: Etch HfO ₂ down to Ta base electrode. Same etch parameters as IM #2
8.	Photolith 4: Define Contacts and Gate Electrode.
9.	Deposition 2: Contacts/Gate Electrode Metallization CNF AJA: Back sputter clean for 120 secs. Then deposit Ti(8 nm)/Cu (225 nm)/Pt (10 nm). P=200 W, 4 mtorr
10.	KS7100 Dicing Saw: S1235 Si blade only. Do NOT use the general purpose blade. Samples are diced into .53 mm x 4.5 cm chips.

Table 3.1. Outline of our fabrication process flow for our VCME devices.

Mask Levels:

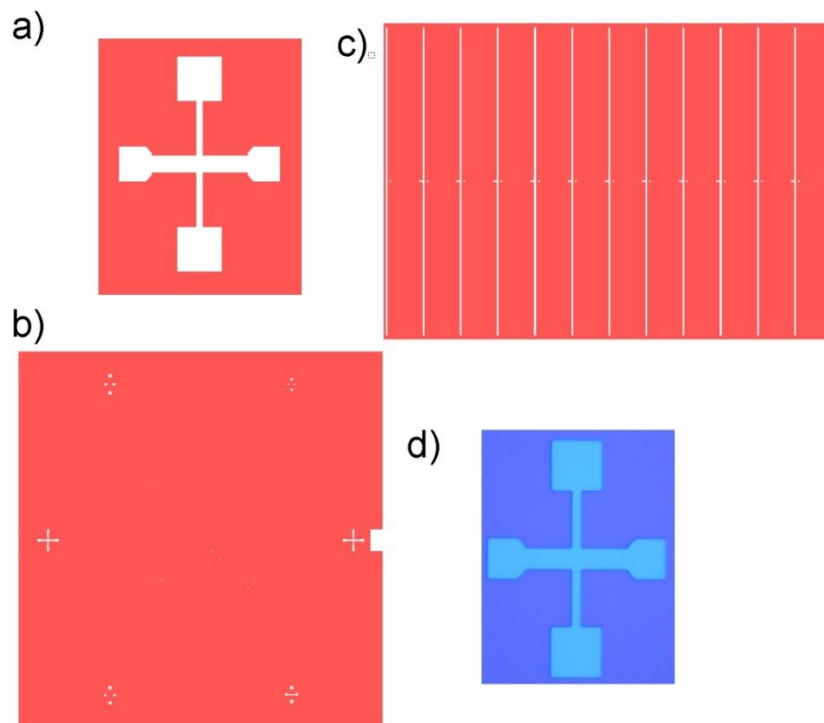


Figure 3.9 Photolith Mask Level 1. a) Close-up of an individual Hall bar device. b) Zoom out showing the four devices on the die as well as the contact aligner marks. c) Shows wafer scale die structure. There are 12 die per wafer. d) Optical microscope image of device after Photolith#1 and Ion Mill #1.

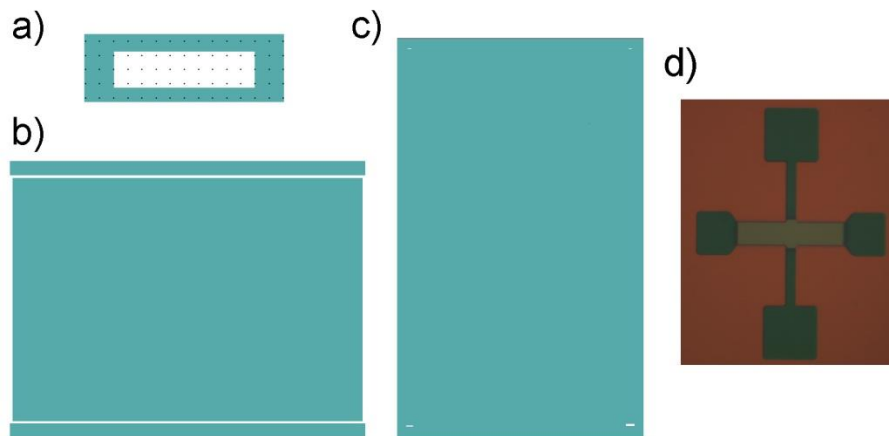


Figure 3.10 Mask Level 2: Define gate stack/etch down to Ta bottom electrode. a) close-up of masked-off area which will define the gate stack. Etch-stop at Ta underlayer using Hiden SIMS Endpoint detector. b) Etched area (solid teal) across the wafer. Top and bottom bars are used for endpoint detection signal. c) Mask image of single die. d) Optical microscope image after etch. Dark green is Ta base electrodes and light brown is gate stack defined by Ion Mill #2.

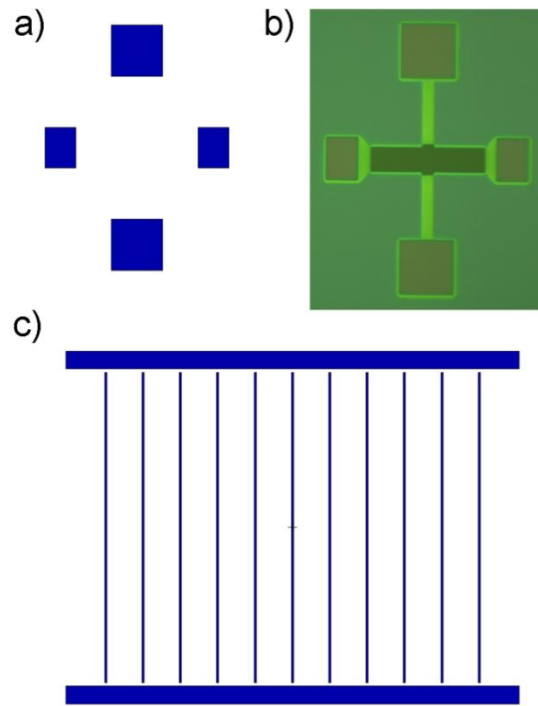


Figure 3.11 Mask Level 3: Etch through HfO_2 to define Ta base electrodes. b) Optical microscope image of etch to Ta base electrode after IM#3. c) Bars between dies and on top and bottom used for endpoint detection.

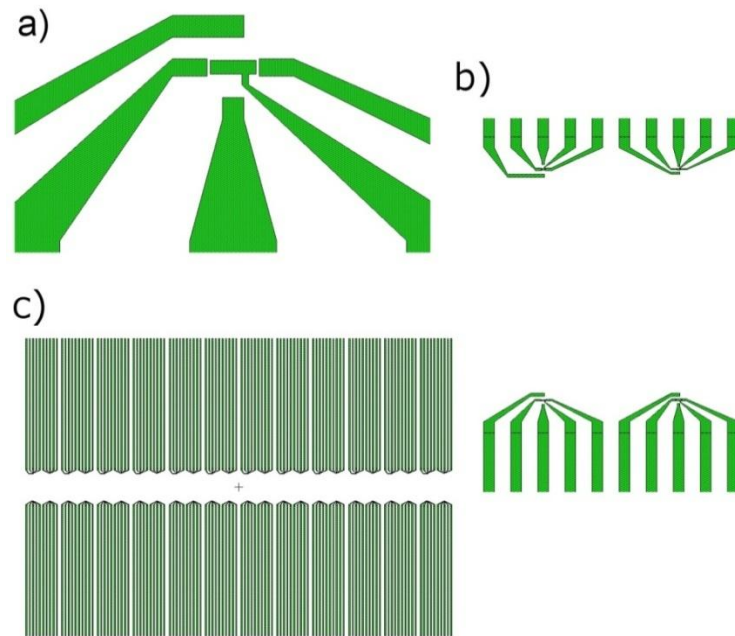


Figure 3.12 Mask Level 4: Define Gate and Hall and drain/source electrodes.

The fabrication process is simpler for ungated devices. The process consists only of the isolate devices step (Photolith 1 and Ion Mill 1) and the top contact step with the added step of a 4 min RF backsputter in the CNF AJA before depositing top contacts. The relatively long backsputter is used to help clear any oxidized cap layer and MgO where the pads will be deposited. The gate contact pad is removed in the Photolith 4 mask.

3.5 The Four Point Bend Method

We extract magnetoelastic constants by applying a uniform uniaxial strain to the device and measuring changes in the in-plane anisotropy energy. We used a four-point bending (4PB) bend test method in order to apply this uniaxial strain. The 4-PB test uses four loading points to bend a beam which in our case is our diced chip. The

bending will cause a uniaxial strain to develop along the direction of the bending. A sketch of the four-point method is shown in Figure 3.13.

The nice thing about the 4PB test is that the stress and strain (along the direction of curvature) between the two inner loading pins is uniform. We will derive the basic equations governing the four-point bend method and show why the strain is uniform between the inner loading pins. We have assumed that classical beam theory is applicable to our experiment which is true when the thickness of the beam is much smaller than its length.

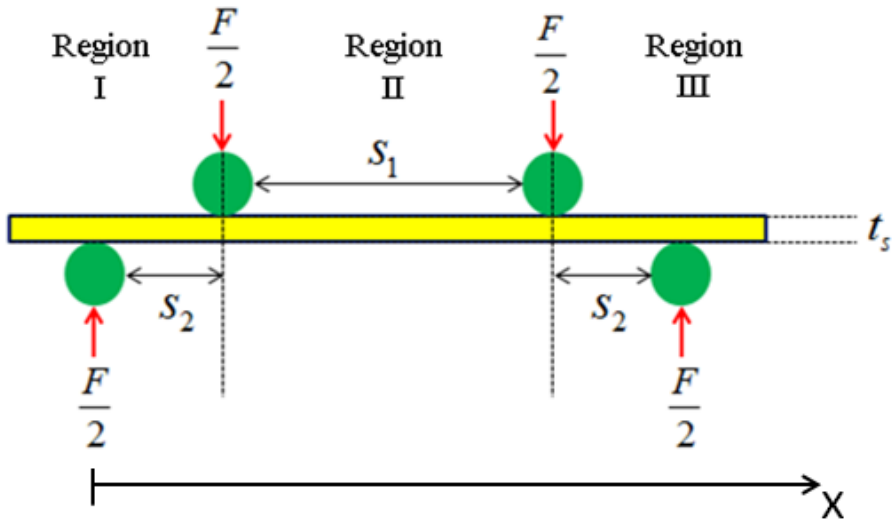


Figure 3.13 Sketch of four point bend test and loading pin positions. The distance s_1 corresponds to the distance between the inner loading points on the pusher plate while the distance s_2 is the distance (in x) between the inner loading point and the outer support pins.

The basic scheme is that the chip lies on the support pins and the loading pins apply a force to the chip that bends it. The curvature in the x-direction produced by the loading can create a x-component stress/strain that is highly uniform in between the loading pins. In order to ensure static equilibrium we require that all linear forces, shear forces, and torques add up to zero at any position on the beam. The first condition is easily met by the fact that the normal forces applied by the two top loading pins are cancelled exactly by the two support pins on the bottom. If the total force exerted by the loading pins on the beam is F , then each loading pin exerts a force $+F/2$ and each support pin must apply a normal force $-F/2$. The shear and torques should be considered separately in the three regions (I, II, and III). We analyze only regions I and II as region III is essentially the same as I.

Region I:

In this region, the torque at a position x from the action of the left-most support pin is

$\frac{-F}{2} x$ (where we use the position of the left-most support pin as our origin for

calculating torques). The condition of static equilibrium enforce that there is a restoring torque from the solid as it bends. At each position x the torque must be such

that $\tau_x = \frac{F}{2} x$ to cancel the torque coming from the force applied at the left-most

support pin position. In addition, the force applied by the left-most pin will also exert a shear force on the solid beam. In static equilibrium, a constant z-x restoring shear force of $-F/2$ from the lattice must cancel out the shear force created by the support pin.

Region II:

The torque at a position x from the action of the left-most support pin is again $\frac{-F}{2}x$.

However, there is another torque coming from the left loading pin of $\frac{-F}{2}(s_2 - x)$. Torque

balance thus requires that for the central region $\tau_x = \frac{F}{2}s_2$. In addition it is easy to see

that the shear force contributions from the left support-pin and left loading pin cancel each other out. The facts that the bending moment is a constant and that the shear forces sum to zero in this region have direct implications for the stress/strain distribution in this region.

In our experimental setup, the position of the loading pins is the quantity that is controlled. Whatever force that is needed to attain that position is generated by the stepper motor. Therefore it is much more useful for our experiment to know what the strain distribution is given a loading pin z -position and beam deflection. We proceed to calculate this now following the derivation given by Hollenberg et al. [39]. The loading and subsequent bending of a thin beam can be expressed in terms of the local radius of curvature ρ . The radius of curvature defines the bend of the neutral plane of the beam (i.e. the plane where the deformation strain ε_{xx} coming from the bending is zero). The following figure shows a section of a bent beam.

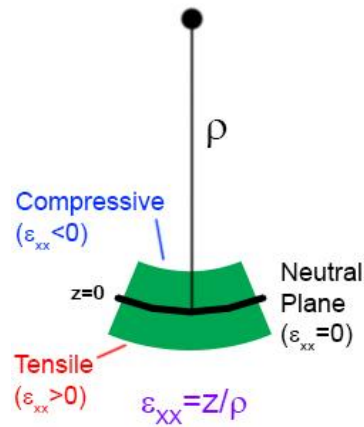


Figure 3.14. Diagram showing the neutral plane of a bowed beam and the relationship between the uniaxial strain in the direction of curvature and the distance from the neutral plane of the beam.

Positions that are closer to the center of the radius of curvature than the neutral plane are under compressive strain. Those that are farther are under tensile strain. The precise mathematical formulation of the strain is given by:

$$\epsilon_{xx} = z / \rho \quad (3.1)$$

The beam deflection is given by $\delta h(x)$ and is defined as the vertical position of the top surface of the deflected beam with respect to its position if it were un-deflected. For small deflections the beam profile and the curvature can be related by:

$$\frac{1}{\rho} = \frac{d^2 \delta h(x)}{dx^2} \quad (3.2)$$

In order to solve for the deflection profile we need to have an expression for the radius of curvature which relates to the bending moment about the neutral axis. The neutral axis of the beam is the x-y plane within the deformed beam for which the length is the same as the original undeformed beam (i.e. for which $\varepsilon_x = 0$). The stress profile can be calculated by recognizing that the bending torque, also known as the bending moment $M(x)$, about the neutral plane is generated by an internal stress distribution governed by:

$$M(x) = W \int_{-t_s/2}^{t_s/2} z' \sigma(x, z') dz' = W \int_{-t_s/2}^{t_s/2} z' \left(\frac{Y z'}{\rho(x)} \right) dz' \quad (3.3)$$

where z is the distance normal away from the neutral plane of the beam, W is the width of the beam, Y is the Young's modulus of the beam and $\sigma(x, z)$ is the stress distribution in the beam. This yields a final result for the torque/bending moment $M(x)$:

$$M(x) = \frac{YI}{\rho(x)} = \frac{I\sigma(x, z)}{z} = \frac{YI\varepsilon(x, z)}{z} \quad (3.4)$$

I is the moment of inertia and we have used the strain relationship to the radius of curvature. The fact that M is independent of x within the central loading pins thus immediately implies that ε and σ are independent of the x position along the beam in this region. Using our previous formula, we then get:

$$\frac{d^2 \delta h(x)}{dx^2} = \frac{M(x)}{YI} \quad (3.5)$$

This equation must be solved in three different regions where the bending torque profile is different. A final set of differential equations must be solved with the boundary conditions that the strain and stress is continuous between the three regions, $\delta h(x) = 0$ at the positions of the supports and that $d\delta h(x)/dx = 0$ at the center of the beam:

$$\frac{d^2 \delta h(x)}{dx^2} = \frac{1}{YI} \begin{cases} \frac{F}{2} x \\ \frac{F}{2} s_1 \\ \frac{F}{2} (s_1 + 2s_2 - x) \end{cases} \quad (3.6)$$

The result of matching boundary conditions and solving for the strain at the top surface between the two loading pins yields a constant strain:

$$\varepsilon_{top}^{xx} = \frac{t_s \delta h_{load}}{\frac{2}{3} s_2^2 + s_1 s_2} \quad (3.7)$$

For a film that is very thin compared to the substrate and in a regime where the induced strain is not so high in the film (i.e. the deformation is not plastic and/or not in the creep regime), we equate the strain due to bending at the top surface to the induced uniaxial strain in the film $\varepsilon_f^{xx} = \varepsilon_{top}^{xx}$. Thus the imposed uniaxial strain in the film is completely determined by the spacing between the loading pins, the spacing between the support pins and the loading pins, and the height of the loading pins relative to when they just touch down on the chip and the beam is undeflected.

3.6 Machining and Assembly of the Four Point Bend Setup

We now give some details on the machining of the four-point bend setup. The setup is designed to apply a four-point bend strain while at the same time fitting between the poles of a GMW 5403 Electromagnet at a pole gap of 5 cm. In addition, the setup is designed (after admittedly, many iterations) to allow relatively easy access to electrically and mechanically mounting the chip. The loading pins are driven by a Physik Instrument M228-11S Stepper Linear Actuator. The linear actuator has a fairly small backlash of $\sim 10 \mu m$ and a uni-directional repeatability of $2 \mu m$. The maximum load that the stepper motor can supply is 50 N which is certainly adequate for bending $.375 \mu m$ thick Si chips. It is important that the stepper motor is put well outside of the magnetic field generated by the GMW Electromagnet. Therefore an extender structure was required to raise the height of the stepper motor. We measured a 10 G field at the position of the stepper motor when the field between the poles is at 2 kG. Since the setup is designed to be in high fields up to 5 kG we have made all parts out of non-magnetic materials. All parts are machined out of aluminum except for the support pins, loading pins, and loading column guider. The setup is pictured below and labeled:

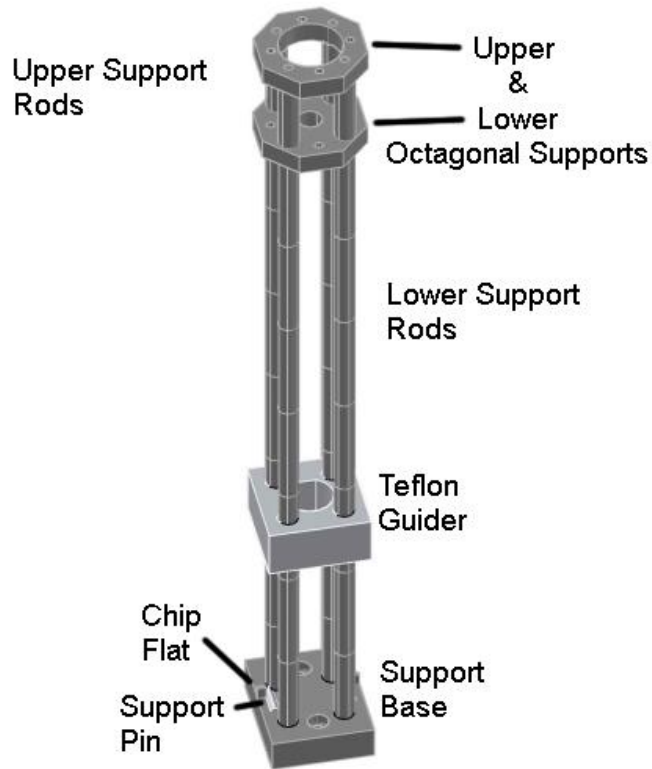


Figure 3.15 CAD drawing of entire extender/support structure without stepper motor, loading column, and pusher plate.

3.6.1 Machining of the Extender Structure

The stepper motor needs to be attached to the entire setup and fixed so that it does not move while it applies a force to the loading columns and the chip. This was achieved by machining a support with a through hole for the end of the stepper motor.

A CAD diagram of the stepper motor is shown below:

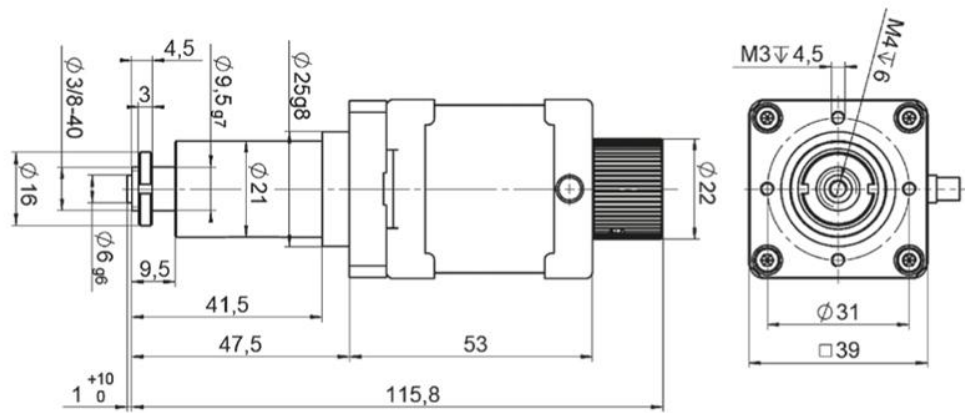


Figure 3.16 CAD Drawing of M228.11S stepper motor.

An octagonal support was machined with a through-hole of 1" diameter which corresponds to the widest diameter before the base of the stepper motor. The octagon is cut out by taking a 1.75" diameter cylinder and using a dividing head to define the octagonal profile. The piece was then bandsawed and endmilled until its thickness was 0.3125". Eight through holes (only four are necessary) for M3 screws were drilled into the octagonal support structure with a size 30 drill.

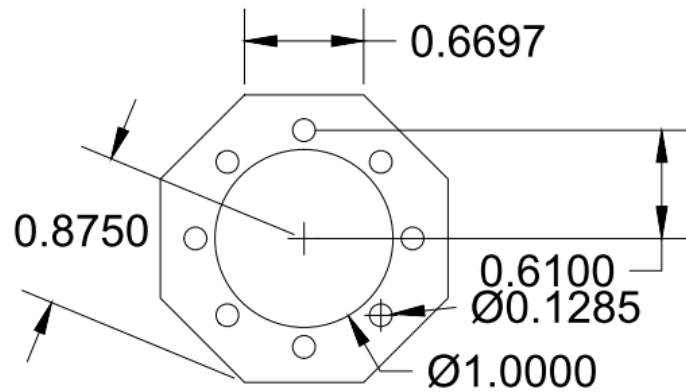


Figure 3.17 CAD Drawing of upper octagonal support.

Four aluminum rods of 0.3125" diameter were then machined to make the upper extender rods. The rods were all turned down to an identical length of 1.187 ±.002 inches on the lathe. Both ends of the rods were then tap-drilled (at the center of the rod) with a size 41 drill, countersunk, and then tapped with an M3 tap. Then M3 threaded rod was screwed into the four M3-threaded holes in the bottom of the stepper motor. The octagonal support was then put on aligning four of the holes to threaded rod. Then the four aluminum rods were screwed onto the threaded rod that extends beyond the thickness of the support and thus fastens the support to the stepper motor. Next we machine the lower octagonal support. This serves to provide extra stability to the extender and prevents all the stress being placed directly on the upper extender rods. The lower octagonal support has a through-hole at the center which has diameter of 3/8". This can then be fit over the end of the stepper motor and fastened tightly on to the end of the stepper motor with a 3/8"-40 nut.

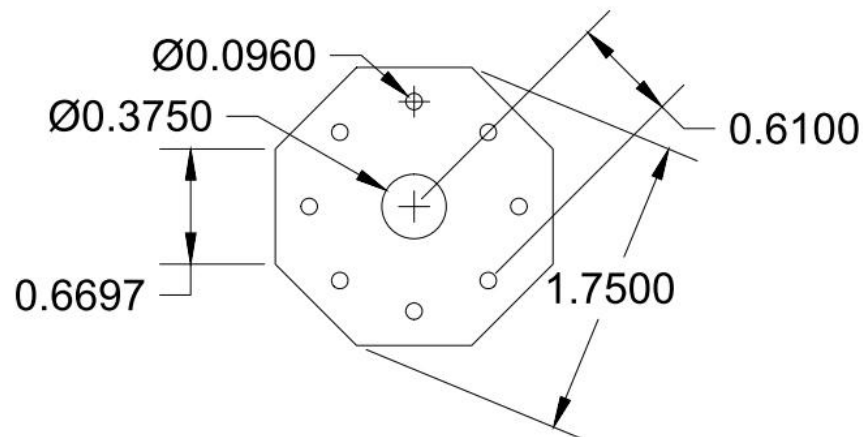


Figure 3.18 CAD Drawing of lower octagonal support.

The next step is to machine the four lower extender rods. The lower extender rods are machined to 11.75" long. It is not possible to hold these pieces in the standard lathe as they are too long so the four rods were machined to the same length on the mill by holding the rod in a vice and fixing one of the ends of the rod on a mill flat. Both sides of the rods were then drilled with a size 41 drill, countersunk, and then tapped with an M3 tap. The four rods can then be attached to the bottom octagonal support with M3 threaded rods.

3.6.2 Machining of the Teflon Guider

The Teflon Guider has the dual role of both stabilizing the long bottom support rods and making them completely rigid as well as providing a guide for the loading column so that it (and the attaching pusher plate) remain flush with the base of the four point bend setup. The dimensions can be seen in the diagram below. The slot for the loading column was machined on the CNC mill in the student shop using a 1/4" mill cutter.

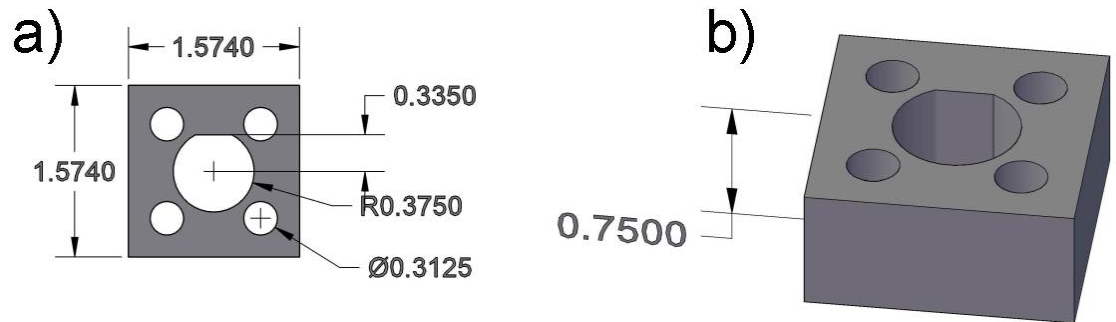


Figure 3.19 a) Top-down view of teflon guider. b) Perspective view of teflon guider.

3.6.3 Support Base + Support Pins

The aluminum support base is the base of the entire structure and has the support pins on which the chip rests. Two slots were machined on the top of the support base for the cylindrical support pins using a 1/8" ball end-mill and cutting to a depth of 1/16". The locations for these slots are diagrammed in Figure 3.20 below and were spaced apart by 30 mm. 1/8" diameter MACOR rods were cut and machined to fit into the ball-milled grooves (~3/4" long) and then epoxied in using a two part epoxy that is readily available in the LASSP stockroom. These MACOR rods are the support pins that provide part of the bending strain in the 4PB test.

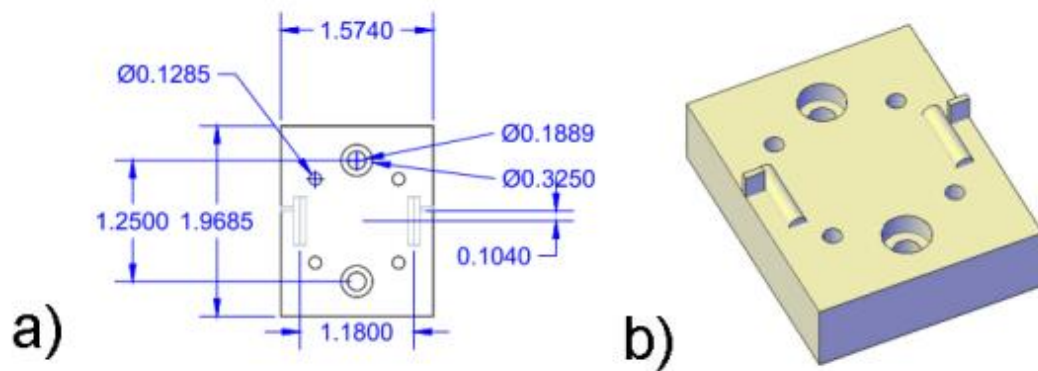


Figure 3.20 a) Top-down image of support base with dimensions. b) perspective drawing of support base.

Four through-holes for M3 socket head screws were machined on the backside of the support base using a size 31 clearance drill and counterbored to a depth of 3 mm as to sink the socket head. M3 socket head screws were then used to screw the support base into the four lower extender rods. On the top side two clearance holes were drilled with size 17 drills for M4 Socket Head screws and the top was counterbored to a depth of 4 mm. The M4 socket heads were used to screw the support base into a standard Buhrman group probe/sample stand. We finally machined two slots with a 1/16" mill cutter at the edges of the base and epoxied aluminum shims into these slots. The shims were used as chip flats. The chip was pressed up flat against both shims to ensure that the chip lies parallel with respect to the applied field direction.

3.6.4 Machining of the Loading Column

The loading column is the long solid shaft to which the loading pin pusher plate is screwed into. The shaft length was machined on the lathe to a length of 10.75".

Then a cut was made on the mill lengthwise along the cylindrical shaft that was .040" deep in order to define a flat for the loading column. This allows the entire loading column to slide through the teflon guider. An M4 tapped hole was machined onto either side of the loading column. One side is fastened with M4 threaded rod to the stepper motor. The other side is used to thread the pusher plate onto. A 3/64" hole was drilled and tapped for a 0-80 set screw situated 1/2" from the edge of the loading column on the pusher plate end. This set screw is used to attach the pusher plate assembly rigidly to the loading column and keep the M4 threaded rod attached to the pusher plate from rotating in the loading column.

3.6.5 Machining/Assembly of the Pusher Plate

The pusher plate was machined out of aluminum. A 3/8" aluminum cylinder was machined down to a length of .2" using a lathe collet. The cylinder was then drilled all the way through on the lathe with a drill, countersunk, and then tapped with an M4 tap. The piece was then taken to the mill and slots for the loading pins were cut with a 1/8" ball endmill. The slots were space 14 mm apart from each other. Two 1/8" MACOR rods were cut and machined down to a length of 1/2". These were bonded to the ball end-milled slots in the pusher plate by the same two-part epoxy used for the support pins. An M4 threaded rod was screwed into the pusher plate and then was locked in place by applying LOCTITE in between the threads of the rod and the threaded hole in the pusher plate. The whole pusher plate can then be threaded onto the loading column and secured by the 0-80 set screw. We measured and marked the

position on the M4 threaded rod to which the pusher assembly is supposed to be screwed into the loading column (before being fastened by the set screw) so as to have little angular (< 1 degree) misalignment between the support pins and the loading pins.

For our experiment, the relevant quantities that govern the strain generated in the CoFeB film are the spacings between the support and loading pins. Referring to Figure 3.13 and Equation (3.7) our setup has $s_1=14$ mm, $s_2 = 8$ mm while $t_{\text{substrate}} = 0.375$ mm. A 0.5 mm stepper-motor initiated displacement of the loading pins thus corresponds to a 0.12% x-directional compressive strain increase in the film. The final setup within the poles of the GMW electromagnet is shown in Figure 3.21:

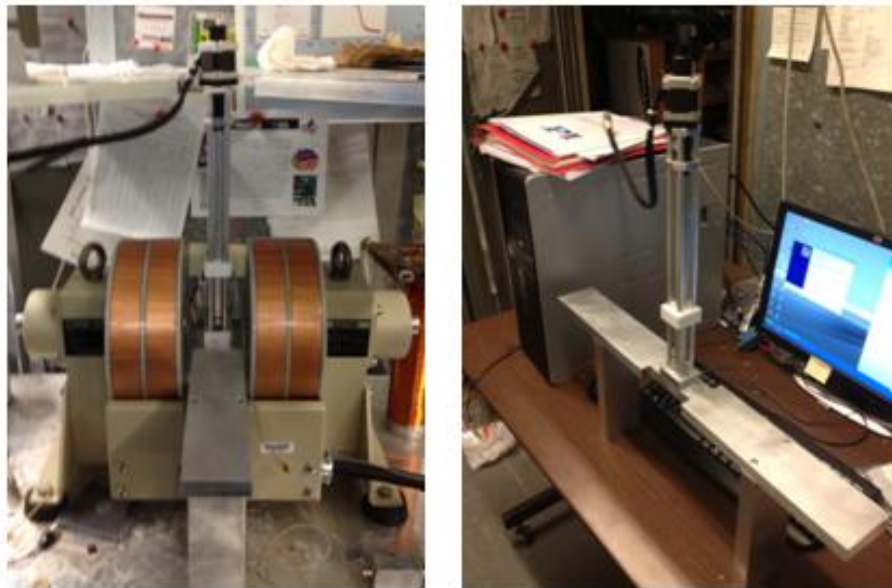


Figure 3.21 Picture of final setup within the poles of the GMW Electromagnet. The entire extender structure was screwed into a modified Buhrman group probe/sample stage.

This design has the benefit that different pusher plates and support bases can be put on to the setup with relative ease. Thus one can easily change to a 3-point bend test configuration by changing the pusher plate or to a biaxial ring-on-ring test by changing the pusher plate and the support base.

3.7 Magnetometry Results: $K_{\text{eff}}t_{\text{eff}}$ vs t_{eff} curves and M_s extraction

We conducted SQUID magnetometry on our as-deposited and annealed films in order to extract the magnetization and magnetic anisotropy for both types of samples. Figure 3.22 shows the results of our saturation magnetization measurements as a function of the nominal CoFeB thickness for our as-deposited samples.

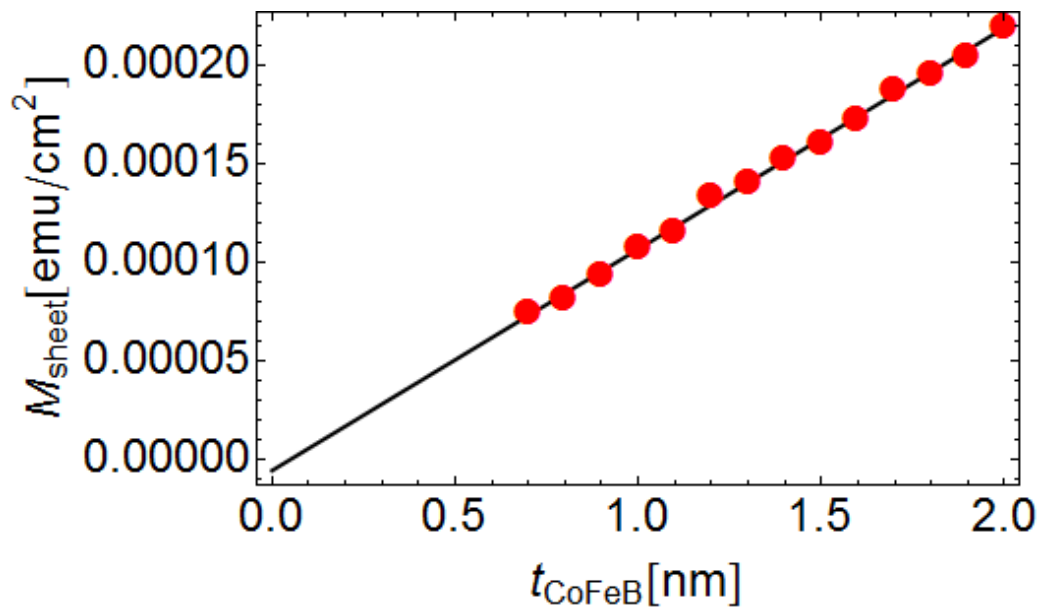


Figure 3.22 Total magnetic moment/unit area vs nominal CoFeB thickness in as-deposited Ta(6)|CoFeB(x)|MgO(2.2)|Hf(1) structures. The slope of the fit yields an $M_s \sim 1120 \text{ emu}/\text{cm}^3$. The dead layer thickness is negligible.

We plot the magnetic moment per unit area as a function of the nominal CoFeB film thickness. From the slope we extract an $M_s \sim 1120 \text{ emu/cm}^3$. Our data also shows that we have a negligible magnetic dead layer. In addition, there is no evidence of a faster than linear decrease of magnetic moment/unit area as the CoFeB film is made ultrathin. We conclude for our samples that no intermixing occurs at the Ta|CoFeB interface during the sputtering process. We then did the same thing for our annealed samples and plotted the magnetic moment per unit area vs nominal CoFeB thickness (Figure 3.23). An $M_s \sim 1380 \text{ emu/cm}^3$ and a dead layer thickness $t_{dl}=0 \text{ nm}$ were found after annealing. Thus, in our samples, we observe a rise in the saturation magnetization indicating CoFeB crystallization and B diffusion out of the CoFeB but with no associated dead layer formation.

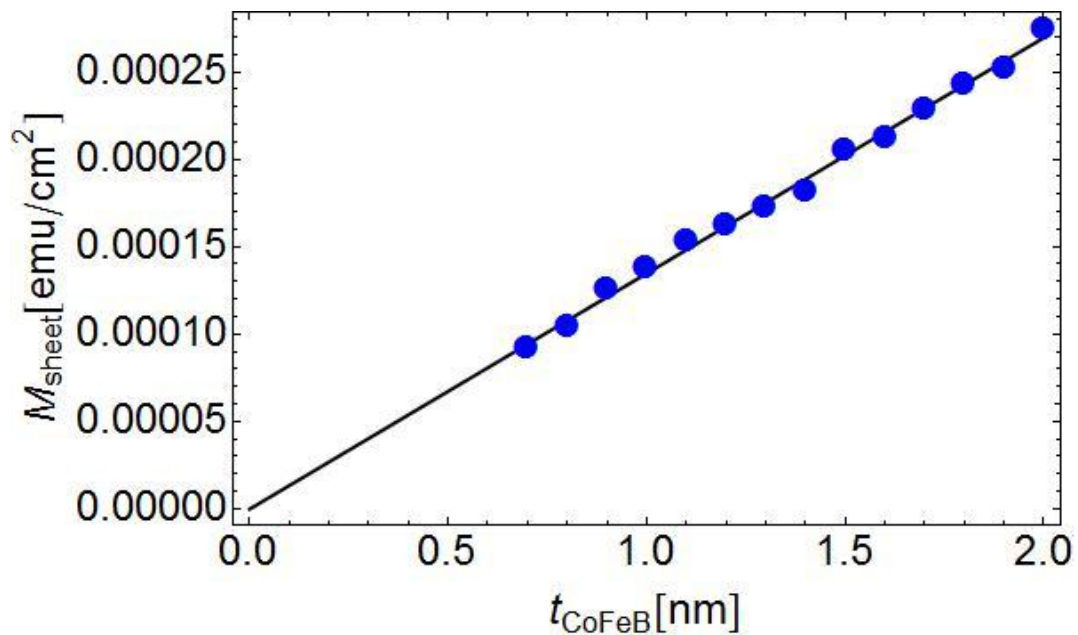


Figure 3.23 Total magnetic moment/unit area vs. nominal CoFeB thickness for Ta(6)|CoFeB(x)|MgO(2.2)|Hf(1) annealed at 300 °C for 1 hour. The slope of the linear fit corresponds to $M_s \sim 1380 \text{ emu/cm}^3$ and the x-intercept corresponds to $t_{DL} \sim 0 \text{ nm}$.

In order to extract the thickness dependence of the perpendicular magnetic anisotropy energy density, we conducted field scans parallel and perpendicular to the film plane. The anisotropy energy density can be extracted by the following equation:

$$K_{eff} = M_s \left(\int_0^1 H_{\perp}(m_{\perp}) dm_{\perp} - \int_0^1 H_{\parallel}(m_{\parallel}) dm_{\parallel} \right) \quad (3.8)$$

Employing this integral method for various thicknesses, we can extract K_{eff} as a function of t_{eff} and build up the $K_{eff}t_{eff}$ vs t_{eff} curve. The annealed samples have strong surface anisotropy as can be seen in the rapid decrease of the effective demagnetization field with film thickness. The magnetization easy axis goes out of plane at $t_{eff}=1.2$ nm as seen in Figure 3.24.

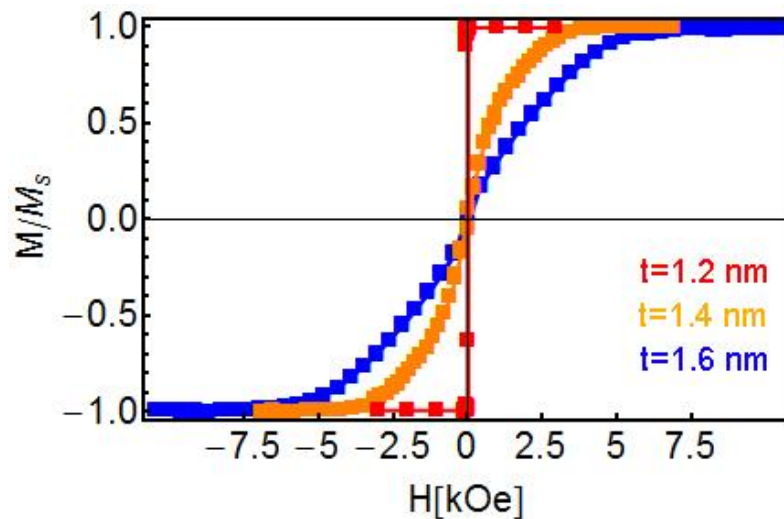


Figure 3.24 Room-temperature temperature SQUID in-plane field scans of annealed Ta(6)|CoFeB(x)|MgO(2.2)|Hf(1) film stacks showing the transition from in-plane to

out-of plane anisotropy at $t_{\text{CoFeB}}=1.2$ nm. Magnetization in these plots is normalized to M_s .

$K_{\text{eff}}t_{\text{eff}}$ vs t_{eff} is plotted both for as-deposited (Figure 3.25) and annealed samples (Figure 3.26). We used a linear Neel-model fit to extract surface and volume anisotropies for both series. The as-deposited series exhibits a $K_{\text{eff}}t_{\text{eff}}$ vs t_{eff} curve that is quite linear through the thickness range studied. A small surface anisotropy of $K_s \sim 0.31$ ergs/cm² and a volume anisotropy of $K_v \sim 1.6 \times 10^6$ ergs/cm³ were extracted from the Neel model. The $K_{\text{eff}}t_{\text{eff}}$ vs t_{eff} curve for the annealed samples is linear up until $t_{\text{eff}} = 1.1$ nm at which point the curve starts to deviate strongly from this linear behavior. From a linear fit to the region between $t_{\text{eff}} = 1.1$ nm-2.0 nm, we extracted a surface anisotropy $K_s = 1.5$ ergs/cm² and a volume anisotropy of $K_v \sim 7 \times 10^5$ ergs/cm³.

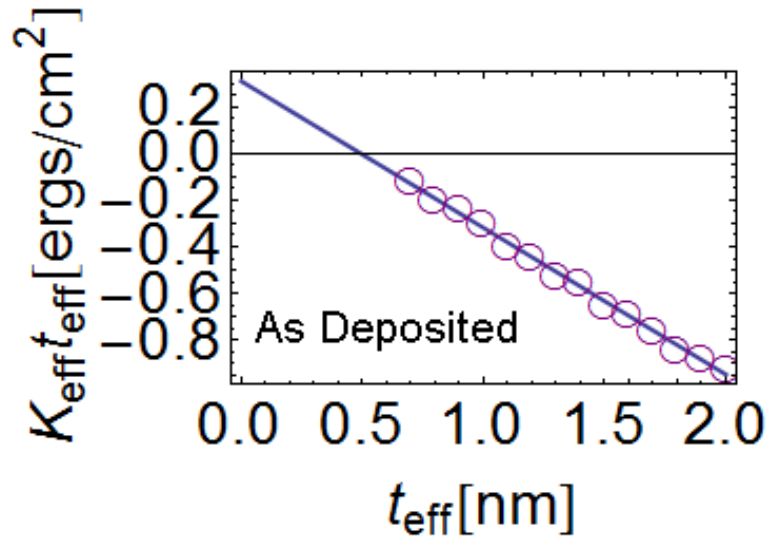


Figure 3.25 $K_{\text{eff}}t_{\text{eff}}$ vs t_{eff} for as-deposited Ta(6)|CoFeB(x)|MgO(2.2)|Hf(1) series. Solid line is fit to Neel Model.

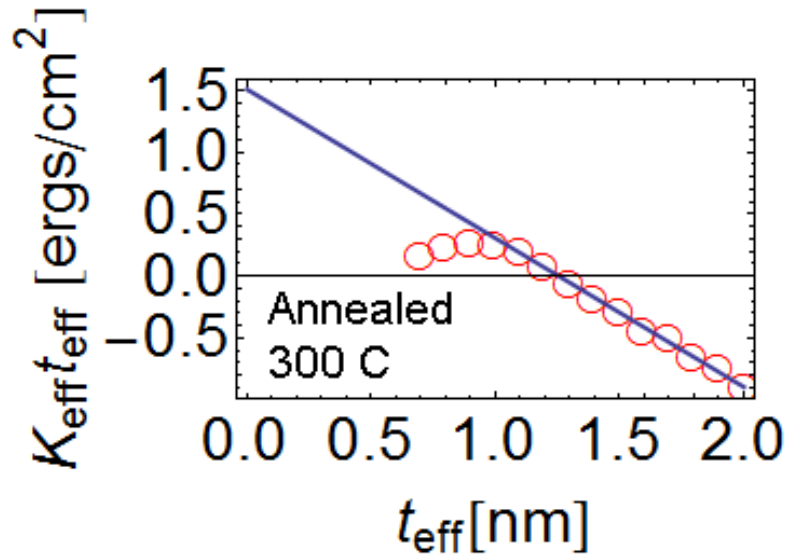
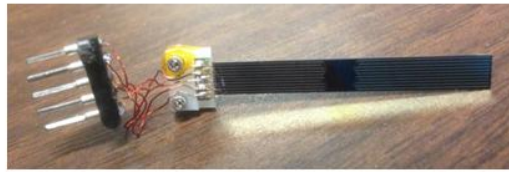


Figure 3.26 $K_{\text{eff}}t_{\text{eff}}$ data extracted from magnetometry and M-H an hysteretic curve data. The line fit of the data used to extract the surface and volume anisotropy is also shown.

3.8 Magnetoelastic Coupling Measurement Scheme & Geometry

We then employed our 4PB strain setup to measure the magnetoelastic coupling thickness dependence of CoFeB. We performed dV/dI and Hall vs H measurements while applying uniaxial strain to the entire device. The leads of our devices are wire bonded to a home built connector. The pad/connector geometry and wire bonding pattern are displayed in Figure 3.27 below. The chip was placed on to the support pins and the pusher plate so that the loading pins were touching flush with the chip. This ensured that the chip did not move. The connector was then plugged into a ribbon cable leading to a custom-built breakout box.

a)



b)

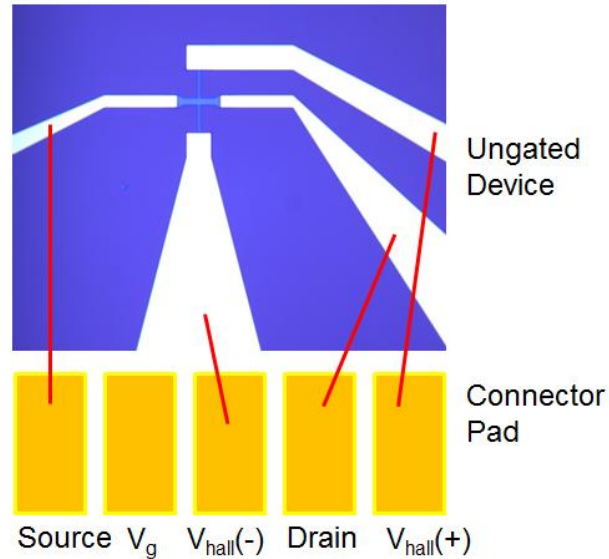


Figure 3.27 a) Machined Delrin connector clamped to chip. Long sample leads are wire-bonded to gold pads on connector. b) Connector + wire-bonding geometry.

We used two lock-ins (Lock-in #1 and Lock-in #2) simultaneously to measure the longitudinal dV/dI of the channel as well as the Hall voltage. Lock-in#1 was hooked up to the sample through a standard Buhrman group Wheatstone-Bridge circuit and the oscillator output on Lockin #1 was used as the excitation source. The oscillator frequency was set to 500 Hz with a 5V RMS amplitude and a 20 ms time constant. In our configuration we used 100 k Ω branch resistors (2 of them in parallel) and a resistance decade box for balancing the device resistance. Therefore, the sense

current is $I_{ac} \sim 100 \mu\text{A}$. Lockin #2 uses the oscillator output of Lock-in #1 as reference and was used to measure the Planar Hall and/or Anomalous Hall contributions off of the transverse leads.

We use the changes in the longitudinal resistance via the Anisotropic Magnetoresistance (AMR) to measure changes in the magnetization. The AMR resistance can be mapped to magnetization (θ, φ) coordinates as follows:

$$R(\theta, \varphi) = R_0 + \Delta R \sin^2 \theta \sin^2 \varphi \quad (3.9)$$

Here θ represent the polar angle made with the z-axis (normal to the film-plane) and φ represents the angle the magnetization with respect to the axis that is normal to the current direction and in the film plane. In our experimental geometry this axis is our field sweep direction which is the x-axis. The field, current flow and strain geometry and angle φ is shown in Figure 3.28.

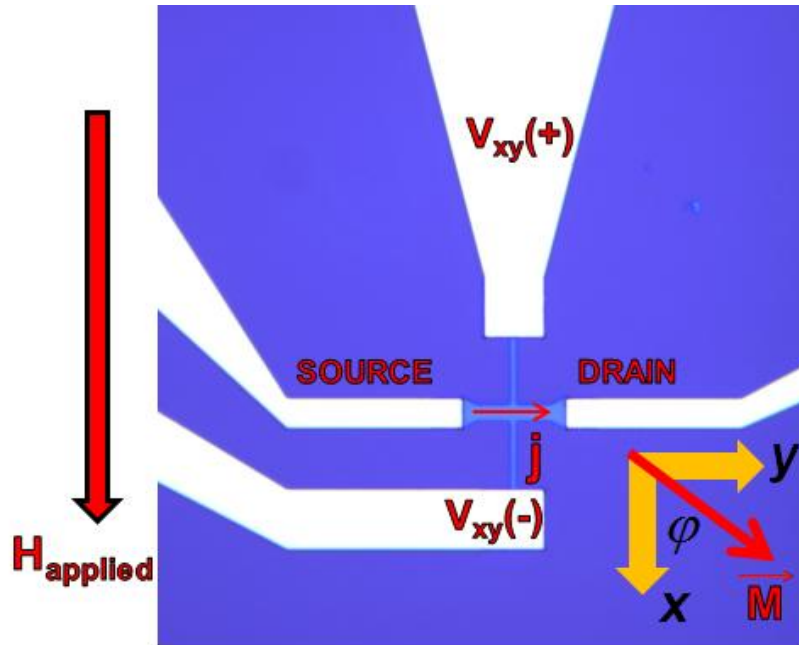


Figure 3.28 Device and lead geometry as well as coordinate system for our experiment and analysis. H_{applied} is along the long axis of the chip (the x-axis). The current for sensing the AMR flows along the y-axis. The uniaxial compressive bending stress is generated along the x-axis.

The AMR serves as a good representation of the magnetization when easy and hard directions are clearly defined and when the field is swept along a hard axis. If the field is swept along an easy axis, the magnetization process proceeds through 180 degree wall motion which shows a very small signal in an AMR trace. We ensure that our field sweep direction is along a hard axis by field-annealing chips at 300 °C for 1 hour in our home-made set-up annealing stage in the geometry shown in Figure 3.29.

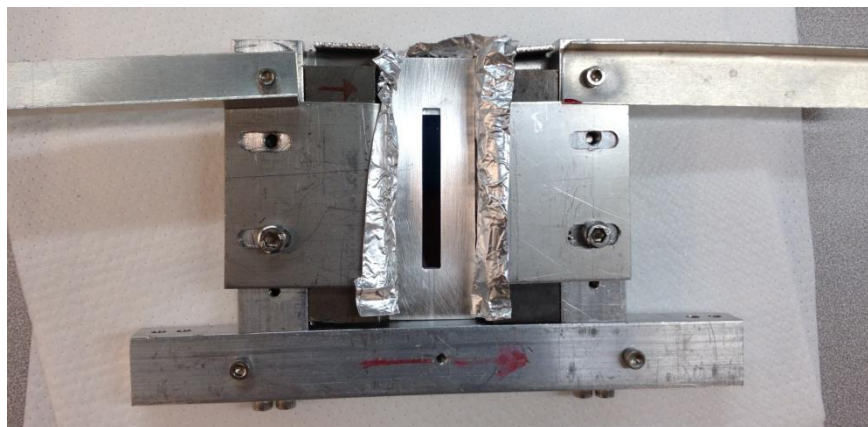


Figure 3.29 Home-built field annealing stage + chip holder for Lindbergh vacuum tube furnace. The in-plane field measured at the center of the chip is 1.3 kOe

The field anneal direction is thus along the current path direction (which we label the y-axis). This sets up the long-axis of the chip to be the magnetic hard-axis (which we call the x-axis). This is the direction of our field sweep and is also the axis that we apply our compressive bend strain on. For as-deposited samples it was necessary to define the hard axis by starting the scan with $\sim 0.05\%$ compressive strain already on. This was sufficient in making the y-axis a clearly defined easy axis.

We first conducted a full dV/dI vs H hysteresis loop going to saturation in $-x$ and $+x$ directions, then we increased the strain on the chip, then did another dV/dI vs H loop, increased the strain and iterated these steps until we had enough AMR curves at different strain values to extract B_{eff} reliably. Typically the strain increment was to a maximum compressive strain of $\sim .1\%$. This procedure generates a series of AMR curves (Figure 3.30) as a function of uniaxial strain which can then be used to extract the magnetoelastic coupling.

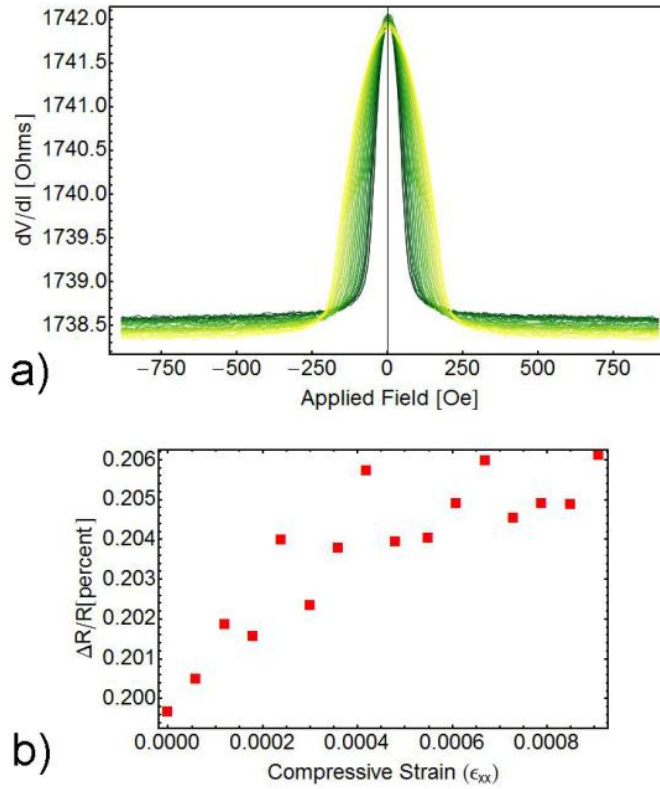


Figure 3.30 a) dV/dI vs H curve series for an annealed Ta(6)|CoFeB(1.7)|MgO(2.2)|Hf(1) sample. We used a full compressive strain range ϵ_{xx} of .095% in increments of $\epsilon_{xx}=6.1 \times 10^{-5}$. b) The change in the effective AMR with strain. The reason for this dependence is not clear but could arise from piezo-resistance in the Ta underlayer, changes in contact resistance associated with the wire-bonds, as well as changes in the actual AMR percentage in the CoFeB as a function of strain.

3.9 Analysis Method for the In-plane Magnetoelastic Constant B_{eff}

We first normalized the AMR curve as the device resistance and effective AMR % were dependent on the strain. We make the assumption that the maximum of the AMR curve corresponds to $\varphi = \pi/2$ (or $3\pi/2$) and that the magnetization at saturation corresponds to $\varphi = 0$ (or π). The AMR curve is then normalized to lie between 0 and 1 where 0 corresponds to $\varphi = 0$ (or π) and $\varphi = \pi/2$ (or $3\pi/2$).

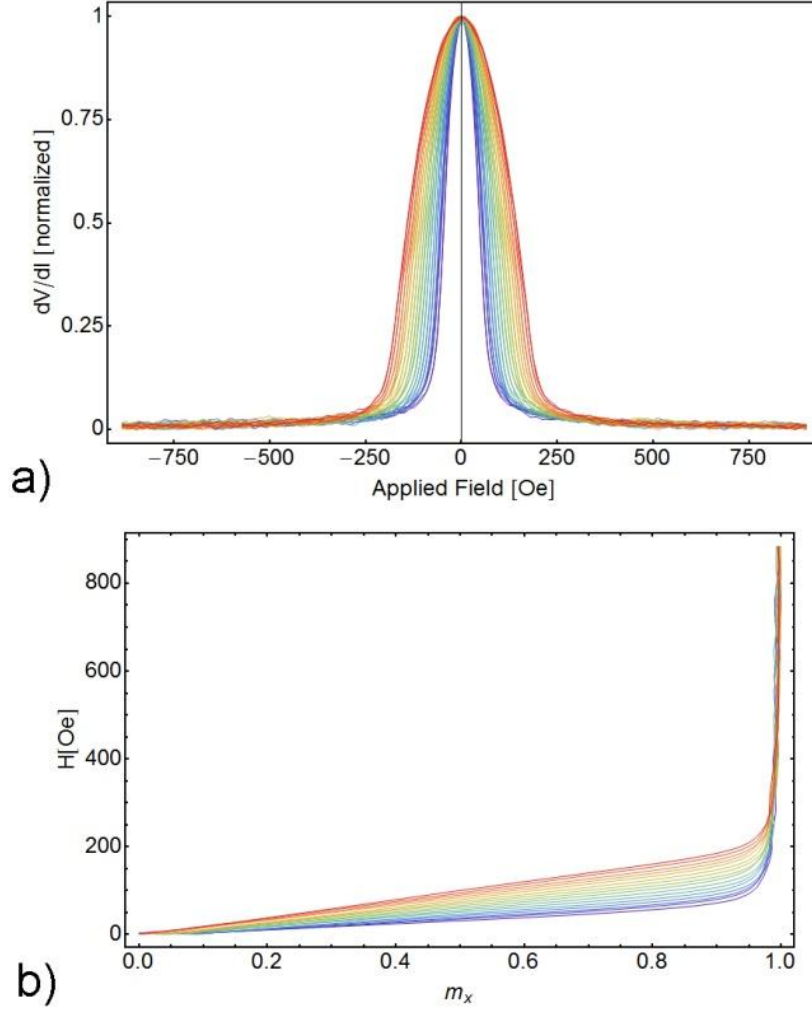


Figure 3.31 a) Normalized AMR curves vs H_{app} along hard axis for annealed Ta(6)|CoFeB(1.7)|MgO(2.2)|Hf(1) sample. The AMR curve series goes from to $\varepsilon_{xx} = 0$ to $\varepsilon_{xx} \sim .1\%$ b) conversion of the AMR vs H signal into an $H(m_x)$ vs. m_x curve used for integration.

The normalized AMR curves in turn can be transformed to $H(m_x)$ vs m_x curves (Figure 3.31b) by using the relation $m_x = \cos[\arcsin[\sqrt{R_{norm}}]]$. This form can be derived by inverting the normalized form of Equation (3.9 and solving for φ and

recognizing that $m_x = \cos[\varphi]$. The $H(m_x)$ vs m_x curve series is used to extract the in-plane magnetoelastic constant. We use a curve integration technique to do this. The work done by the field on the magnetic system going from a magnetization m_1 to m_2 can be written as $\Delta E = M_s \int_{m_1}^{m_2} H(m) dm$. The change in the internal energy of the

magnetic system during the magnetization process is given by

$$\Delta E = \left[K_u + \frac{4}{3} B_{eff} \delta e_{xx} \right] (m_2^2 - m_1^2). \text{ This assumes that the change in the internal energy}$$

from rotating the magnetization from m_1 to m_2 is governed by the uniaxial anisotropy energy density and magnetoelastic anisotropy arising from the bend strain. Equating the two sides we get:

$$\frac{4}{3} B_{eff} \delta e_{xx} (m_2^2 - m_1^2) = M_s \left(\int_{m_1}^{m_2} H(m, \delta e_{xx}) dm - \int_{m_1}^{m_2} H(m, 0) dm \right) \quad (3.10)$$

Rearranging this equation yields the final expression that we use for extracting the magnetoelastic coupling B_{eff} :

$$B_{eff} = \frac{\frac{3}{4} M_s \left(\int_{m_1}^{m_2} H(m, \delta \varepsilon) dm - \int_{m_1}^{m_2} H(m, 0) dm \right)}{\delta \varepsilon \cdot (m_2^2 - m_1^2)} \quad (3.11)$$

To extract magnetoelastic coefficients we plotted the quantity $\frac{\frac{3}{4} M_s \left(\int_{m_1}^{m_2} H(m, \varepsilon) dm \right)}{(m_2^2 - m_1^2)}$

vs. strain and performed a linear fit. The slope is simply B_{eff} . The relationship is

general for anhysteretic magnetization curves of any shape. In addition, m_1 and m_2 can be chosen arbitrarily or as is convenient. One does not need to use $m_1=0$ and $m_2=1$. In cases where one is measuring the actual magnetization (and not the AMR) it is not even necessary to saturate the sample. For our experiment we evaluated the integrals from $m_1=.4$ to $m_2=.8$. Figure 3.32 shows an example of a plot of

$$\frac{\frac{3}{4} M_s \left(\int_{m_1}^{m_2} H(m, \varepsilon) dm \right)}{(m_2^2 - m_1^2)}$$

as a function of strain that was used to extract B_{eff} .

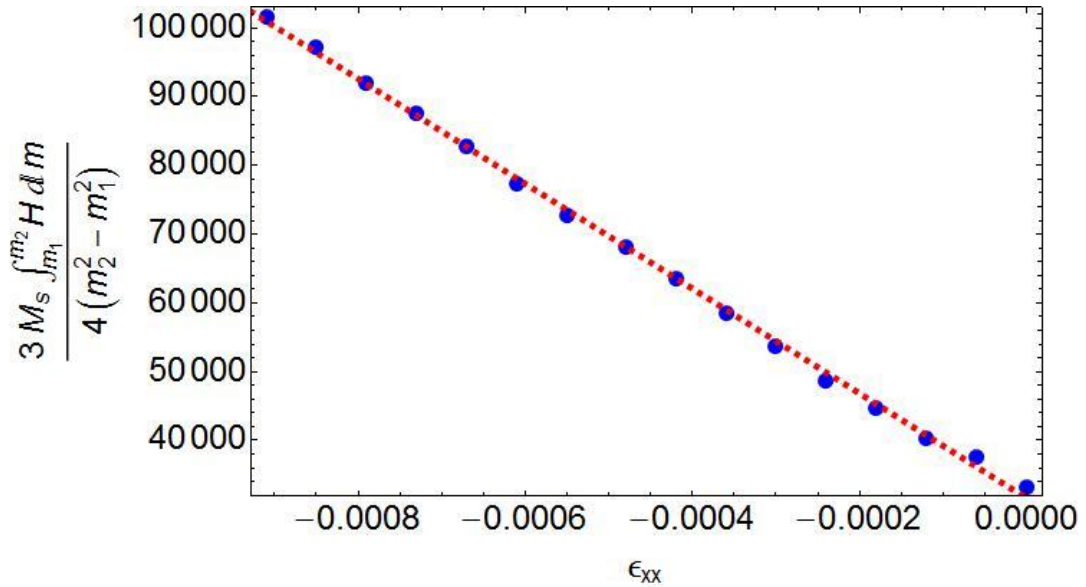


Figure 3.32 Integrated energy of $H(m)$ vs m between the normalized magnetization points $m_1=.4$ and $m_2=.8$ as a function of strain. Red dashed line corresponds to linear fit used to extract $B_{\text{eff}} \sim -7.6 \times 10^7$ ergs/cm³ for $t_{\text{CoFeB}}=1.7$ nm.

3.10 Results on Thickness Dependence of the Magnetoelastic Coupling

We carried out strain bending measurements for the as-deposited and annealed series as a function of CoFeB thickness ranging from $t_{\text{CoFeB}}=1.3$ nm to 2.0 nm. The samples are in a thickness regime where the magnetization still lies in the film plane.

Figure 3.33 and Figure 3.34 shows the dependence of the magnetoelastic coupling for the as deposited and annealed series respectively.

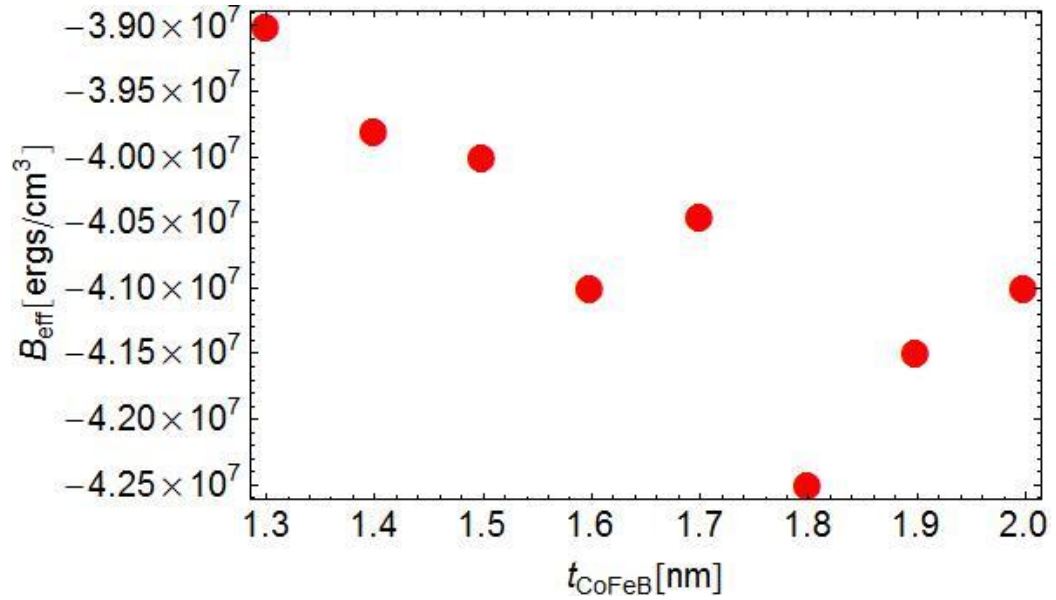


Figure 3.33 Dependence of the effective magnetoelastic constant on thickness for as deposited (amorphous) CoFeB films.

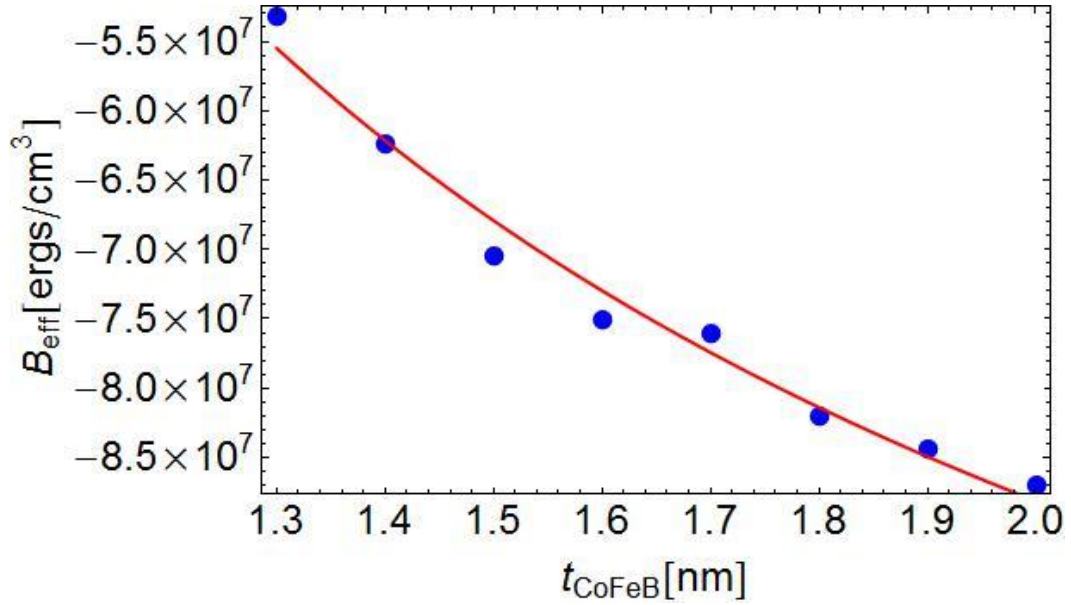


Figure 3.34 CoFeB thickness dependence of the magnetoelastic coupling for samples annealed in a 1.3 kOe in-plane field. The red line is a fit to the data using $B_{\text{eff}} = B_s/t + B_v$.

The magnetoelastic coupling in as-deposited samples has weak thickness dependence and ranges from $\sim -3.9 \times 10^7$ to -4.3×10^7 ergs/cm³. The dependence does not exhibit any clear functional form and an extraction of the surface and volume type magnetoelastic contributions is not possible. We find that after annealing the magnetoelastic coupling B_{eff} becomes considerably larger (e.g. from -4.1×10^7 to -8.7×10^7 ergs/cm³ at $t_{\text{CoFeB}} = 2.0$ nm). In addition the thickness dependence of B_{eff} becomes quite pronounced and changes on the order of 30% within a thickness range of 0.7 nm. This thickness dependence also fits well to the functional form $B_{\text{eff}} = B_s/t + B_v$ dependence. The fit yields an effective surface magnetoelastic coupling $B_s = +12.1$ ergs/cm² and a volume magnetoelastic coupling $B_v = -1.5 \times 10^8$ ergs/cm².

The emergence of a substantial effective surface and volume magnetoelastic coupling in the CoFeB after the annealing may have several root causes. The development of surface magnetoelastic coupling could, in theory, be due to intrinsic surface electronic effects at the annealed and partially crystallized CoFeB|MgO interface (i.e. Fe-3d/O 2p hybridization). This scenario would be interesting as it would mean that the surface electronic processes generating the PMA could be simultaneously altering the effective magnetoelasticity of the CoFeB film. The $B_{\text{eff}} = B_s/t + B_V$ behavior of the magnetoelastic coupling could also be due to effects that are second-order in the residual film strain [40]. Second order corrections to the magnetoelastic coupling $B_{\text{eff}} = B_V + D\varepsilon$ (with D being second order magnetoelastic coupling) can become significant when larger residual biaxial strains (typically > 0.5%) are present in the film. These second order effects can produce thickness dependence in the magnetoelastic interaction when the average residual biaxial strain varies with the film thickness. The second order magnetoelastic coupling would appear as an effective surface magnetoelastic coupling when the average biaxial strain field relaxes as $1/t$.

It is plausible that large strains develop in ultra-thin CoFeB films as grain-on-grain crystallization [11] off of the MgO commences. One study measured that CoFeB layers were already under high compressive biaxial strains (~ 1%) in an annealed CoFeB(6 nm)|MgO (2 nm) superlattice [41]. Strains in ultra-thin CoFeB films ($t < 2$ nm) have the potential to be even higher. CoFeB films in this thickness regime show evidence of being highly granular. Granularity and the presence of islanding in

ultrathin crystallized CoFeB films are supported by TEM observation [25] and by the onset of superparamagnetism in annealed Ta|CoFeB|MgO stacks as the CoFeB is made thin [42]. It is well known that ultra-thin granular films can be under very high strains that are in general dependent on the thickness of the film. These strains would lead to a thickness dependence of B_{eff} in CoFeB due to second order magnetoelastic effects. Such phenomena have been observed in studies on sputtered, polycrystalline $\text{Ni}_{81}\text{Fe}_{19}$ films where surface roughening and granularity in the films have been shown to be correlated with thickness dependent magnetoelastic coupling [43].

3.10.1 Mechanism for Nonlinear $K_{\text{eff}}t_{\text{eff}}$ vs t_{eff} behavior

Strong effective surface magnetoelasticity, regardless of its origins, can have important implications for anisotropy behavior in the ultra-thin film limit. The presence of large thickness dependent strains in this limit along with surface magnetoelastic coupling can cause the observed nonlinearities in the $K_{\text{eff}}t_{\text{eff}}$ curve. In order to see this we introduce an anisotropy energy function multiplied by the effective thickness in Equation (3.12 which extends beyond the simplistic Néel model. This energy function was introduced in Chapter 2 and was first explicated by Bochi et al. to explain anisotropy behavior in epitaxial Cu/Ni/Cu sandwiches [44].

$$K_{\text{eff}}t_{\text{eff}} = \left\{ K_s + \left(B_V^{\text{biaxial}} + \frac{B_s^{\text{biaxial}}}{t_{\text{eff}}} \right) \cdot \left(\frac{\gamma}{t_{\text{eff}}} + \varepsilon_0 \right) t_{\text{eff}} - (2\pi M_s^2) t_{\text{eff}} \right\} \quad (3.12)$$

The expression is comprised of three separate terms. The first term K_s is the interfacial

magnetic anisotropy energy assuming that all the strain in the Ta|CoFeB|MgO system is completely relaxed. The next term comes from the magnetoelastic interaction. We have assumed that the average biaxial strain field follows the relation:

$$\varepsilon_{biax} = \frac{\gamma}{t} + \varepsilon_0 \quad (3.13)$$

The biaxial strain fields couple to the magnetic free energy by the biaxial magnetoelastic couplings. We emphasize that our measurements have only extracted the in-plane magnetoelastic couplings only. The in-plane magnetoelastic coupling is one part of the biaxial coupling. The biaxial coupling constant is composed of the in-plane magnetoelastic coupling and a coupling B_{eff}^{13} that connects the magnetic free energy to strains in the film thickness direction (z-direction).

$$\begin{aligned} E &= B_{eff} (\alpha_1^2 e_{xx} + \alpha_2^2 e_{yy}) + B_{eff}^{13} \alpha_3^2 e_{zz} \\ \vec{m} &= \{\alpha_1, \alpha_2, \alpha_3\} \\ \varepsilon_{xx} &= \varepsilon_{yy} = \varepsilon_0 \\ \varepsilon_{zz} &= -\frac{2\nu}{1-\nu} \varepsilon_0 \\ E_{M.E.}^{biaxial} &= B_{eff} \varepsilon_0 (\alpha_1^2 + \alpha_2^2) - B_{eff}^{13} \varepsilon_0 \alpha_3^2 = -(B_{eff} + B_{eff}^{13}) \varepsilon_0 \cos^2 \theta \end{aligned} \quad (3.14)$$

The last relation of Equation (3.14) is true for metallic films where $\nu \sim 1/3$. One thus sees that the biaxial magnetoelastic coupling $B_{eff}^{biax} = B_{eff} + B_{13}^{eff}$. We unfortunately could

not measure B_{13}^{eff} or B_{eff}^{biax} in this experiment. Thus we must make some reasonable guesses on both the surface and volume B_{13}^{eff} terms. We make the assumption that $B_V^{eff} \sim B_{13}^{V,eff}$ which makes sense if the crystal structure has full cubic symmetry. As a crystallized CoFeB film next to MgO is oriented body-centered tetragonal this cannot be strictly true. However, we do not think that the assumption is a terrible one. The surface term magnetoelastic coupling $B_{13}^{s,eff}$ is a completely unknown quantity. It can depend heavily on the nature of the Fe-O hybridization at the surface. It can and should depend heavily on strain relaxation mechanisms via the second-order magnetoelastic couplings. However, we provide a guess for the lower bound coming from the electronic contribution based on a calculation by Lee et al. [27]. They show an approximately linear decrease in the surface anisotropy as the Fe-O plane distance is increased (in other words z-directional tensile strain of the entire structure) up until the strain reaches about 5%. From their calculation, we eyeball a lower bound on $B_{13}^{s,eff} \sim +7$ ergs/cm². Of course, it is entirely possible that the ab-initio calculation is off by a factor of 2 or so from whatever the real electronic contribution to surface magnetoelasticity is in our system. In addition, any second order magnetoelastic effects can create very large effective surface magnetoelastic terms. For example, in Ni films deposited on SiO₂ surface magnetoelastic coupling likely arising from second order magnetoelastic effects can be as large as + 20 ergs/cm² [45]. Given the uncertainty, we have just arbitrarily chosen a value of $B_s^{eff} = B_{13}^{s,eff} = +12.1$ ergs/cm² to do our fitting but we note that larger positive values of $B_{13}^{s,eff}$ are possible.

The last term arises in Equation (3.12) comes from the out of plane demagnetization energy. Using the set of assumptions we have listed such that $B_{s,eff}^{biax} = +24.2$ ergs/cm² and $B_{V,eff}^{biax} = -3 \times 10^8$ ergs/cm³, we fit the data using the surface magneto-elastic model and use it to extract the parameters $\gamma = -.53$ nm⁻¹, $\varepsilon_0 = .019$, and $K_s = 1.2$ ergs/cm². Figure 3.35 shows the fit to our $K_{eff}t_{eff}$ vs t_{eff} data from magnetometry.

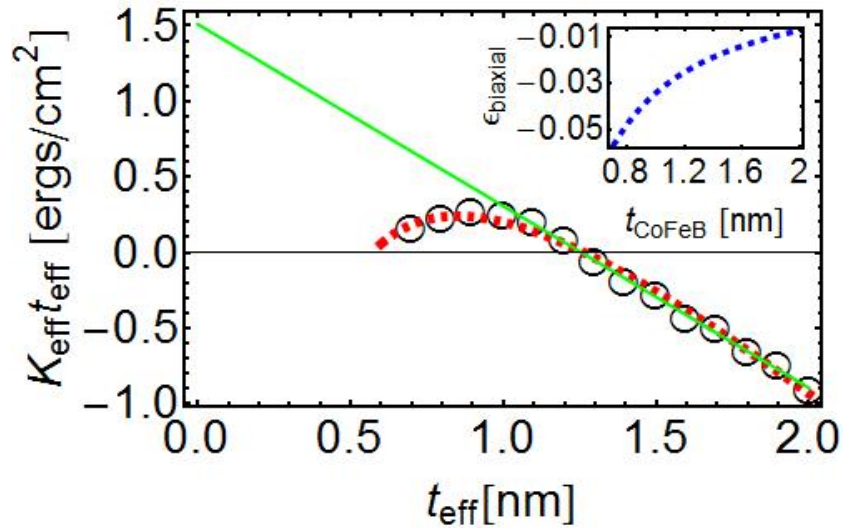


Figure 3.35 Fit of the $K_{eff}t_{eff}$ vs t_{eff} data using a free energy that takes into account thickness dependent magnetoelastic coupling and thickness-dependent biaxial strain in the CoFeB film. [Inset: In-plane biaxial strain as a function of film thickness required to fit $K_{eff}t_{eff}$ vs t_{eff} data.]

We have also plotted the thickness-averaged biaxial strain field as a function of CoFeB thickness in the region that we are fitting the magnetometry data in the inset of Figure 3.35 above. The magnetometry data can be fit well if the film is under thickness dependent compressive strains particularly as the films get to be a few monolayers thick. The main point is that thickness dependent magnetoelastic effects

have the same form as the observed deviation from the linear Néel model. As we have measured, the volume and surface magnetoelastic couplings are not small in the annealed Ta|CoFeB|MgO system. It is also quite plausible that the strains in the partially crystallized CoFeB are large (on the order of 1% or more) and thickness dependent. Thus thickness dependent strain and magnetoelastic effects may be essential in understanding the behavior of the perpendicular anisotropy. We of course do not discount other non-magnetoelastic effects on the anisotropy associated with roughness and islanding. In addition, Ta diffusion to the CoFeB|MgO interface in systems exhibiting Ta/CoFeB intermixing and magnetic dead layering will likely reduce the PMA – particularly as the CoFeB is made thin. A simultaneous quantification of the thickness dependence of the biaxial magnetoelastic coupling and strain is thus required in order to evaluate the contribution of magnetoelastic effects to the overall perpendicular anisotropy. Greg Stiehl (in the Ralph group) and I have been discussing methods and trying to design a simple experiment to directly quantify the biaxial magnetoelastic coupling and residual strain throughout the entire thickness range (i.e. when the film is out-of-plane as well as when it is in-plane). In short, the setup would involve depositing the NM|CoFeB|MgO structures on kapton substrates and machining a contraption to apply biaxial tensile strains to the kapton substrate via stretching. We refer interested parties to Greg's A exam paper for further details [46].

The strong thickness dependent magnetoelasticity in the Ta|CoFeB|MgO system opens up new salient avenues for tuning the perpendicular magnetic anisotropy. The engineering of a homogenous biaxial strain in the magnetic layer is generally thought

to modify only the volume anisotropy as $B_V \varepsilon_0 t_{eff}$ in $K_{eff} t_{eff}$. However, the magnetoelastic term $B_s^{biaxial} \varepsilon_0 + B_V \gamma$ in $K_{eff} t_{eff}$ modifies the surface anisotropy as well. An externally imposed constant tensile strain would enhance the surface anisotropy in a thin film system with a positive effective surface magnetoelastic coupling. For a system with $B_s^{biaxial} = +24 \text{ ergs/cm}^2$, an imposed tensile strain of 1% would yield a surface anisotropy increase of $\Delta K_s = +0.24 \text{ ergs/cm}^2$ to first order in the magnetoelastic interaction. Of course, the imposed tensile strain would also decrease the volume anisotropy which would serve to reduce the PMA as the film gets thicker. Therefore knowledge of both the surface and volume magnetoelastic couplings is required in order to tailor the PMA of the CoFeB layer within a specified thickness range by imposed uniform biaxial strain. The experiment proposed by Greg does have the capability of applying large tensile biaxial strains. It would be very interesting to see how the application of large tensile biaxial strains can change both the volume anisotropy *and* the surface anisotropy. The engineering of strain gradients in the film could also be used to modify both the surface anisotropy via the term $B_V^{biaxial} \gamma$ as well as the nonlinearity in $K_{eff} t_{eff}$ via $\frac{B_s^{biaxial} \gamma}{t}$ in Equation (3.12). While it is not clear to us how to engineer strain gradients, the notion that one could in principal tune the nonlinearity in $K_{eff} t_{eff}$ is rather exciting. If one could engineer a sufficiently large tensile strain gradient, the $K_{eff} t_{eff}$ vs t_{eff} curve could bend upwards instead of downwards – assuming $B_s^{biaxial}$ is positive. We know it's a stretch (insert bad pun laughter here), but it is food for thought.

In summary, this part of our work has experimentally established the presence of strong thickness dependent magnetoelastic interactions in the Ta|CoFeB|MgO. We then introduced an analytical model for the anisotropy that includes these magnetoelastic interactions and showed that this model could be partly responsible for the nonlinear $K_{\text{eff}}t_{\text{eff}}$ behavior in the ultrathin CoFeB limit. We finally pointed out new routes for tuning the PMA in the NM|CoFeB|MgO system opened up by the presence of thickness dependent magnetoelastic effects.

3.11 Voltage Controlled Magnetoelasticity (VCME)

Unfortunately, this part of the project did not go so well. While our 300 °C annealed Ta(6)|CoFeB(1.4 nm)|MgO(2.2 nm)|HfO_x (26.5 nm)|Electrode gated Hall bars did exhibit reasonably large electric-field tuning of the perpendicular anisotropy (at $dK_s/dE_g = -17$ fJ/Vm), we could not detect any change in the magnetoelastic coupling as a function of gate electric field. We think the main reason for this is that the strains we could apply were not large enough to resolve whether the magnetoelastic coupling had been altered by the application of an electric field. In mathematical terms, the energy changes we needed to probe were second order in nature – precisely terms in the free energy function that go as $\frac{d^2 K_s}{dVd\varepsilon} \delta\varepsilon\delta V$. The field resolution of our setup ($\sim .5$ Oe) was probably not good enough to measure this energy difference from AMR curves for the maximum strains ($\sim .1\%$) and gate electric fields ($\sim \pm 3$ MV/cm) we could apply. Despite our failure in this regard, we still think that the idea behind the experiment was a good one. Looking at the strain dependence of the VCMA could reveal valuable information about the electronic processes that are

occurring at the CoFeB|MgO interface and might aid in putting a handle on the mechanism involved in both the PMA and VCMA in NM|CoFeB|MgO systems.

If we were to redo this part of the experiment, we would concentrate on testing the VCMA in a system where the strain imposed on the entire NM|CoFeB|MgO stack could be made much larger. We make a guess that the percentage change in the magnetoelastic coupling is of the same order as the interfacial anisotropy energy with respect to the electric field. Previous VCMA studies show ~ 1-2% change in the interfacial energy with respect to the full scale surface anisotropy over the electric field bias ranges used. If we have a surface biaxial magnetoelastic coupling of +24 ergs/cm² then we guess a full scale E-field induced change of the surface biaxial magnetoelastic coupling of ~ .48 ergs/cm² assuming a 2% percentage change over the accessible E-field range. For a 1.4 nm thick CoFeB film with a biaxial strain of 2%, the change in the anisotropy energy associate with the voltage-induced modification of the surface magnetoelastic coupling is ~ 7×10^4 ergs/cm³. Assuming a $M_s = 1380$ emu/cm³ yields a change in the anisotropy field of ~ 100 Oe. Given that the full scale anisotropy field change with voltage is typically around 300-400 Oe, it is quite plausible that changes due to E-field modification of the surface magnetoelastic coupling are detectable provided that the biaxial strain is of the order of at least 1–2%. We would ideally fabricate the structure on a stretchable substrate that can support and impose such high strains on the film stack and do something similar to what Greg has proposed with Kapton. By stretching the substrate, we would change the state of biaxial strain in the stack. We would also probably ditch the Hall bar geometry and use a sub-micron lateral area NM|CoFeB|MgO|CoFeB|NM|cap MTJ with one in-plane

magnetized electrode whose thickness is near the spin re-orientation transition and one-perpendicularly magnetized electrode. We would want to grow a reasonably thick MgO barrier ($\sim 2\text{-}2.5$ nm) to avoid any spin-torque effects. The perpendicularly magnetized electrode would effectively be the analyzer layer and the field would be swept out-of-plane. Thus one could effectively measure changes in the effective demagnetization energy of the in-plane magnetized layer as a function of bias voltage across the junction. The idea would then be to look at how dK_s/dE_g changes with and without the large biaxial strain.

REFERENCES

- [1] D. C. Worledge, G. Hu, D. W. Abraham, J. Z. Sun, P. L. Trouilloud, J. Nowak, S. Brown, M. C. Gaidis, E. J. O'Sullivan, and R. P. Robertazzi, "Spin torque switching of perpendicular Ta/CoFeB/MgO-based magnetic tunnel junctions," *Appl. Phys. Lett.*, vol. 98, no. 2, p. 022501, 2011.
- [2] S. Ikeda, K. Miura, H. Yamamoto, K. Mizunuma, H. D. Gan, M. Endo, S. Kanai, J. Hayakawa, F. Matsukura, and H. Ohno, "A perpendicular-anisotropy CoFeB-MgO magnetic tunnel junction," *Nat. Mater.*, vol. 9, no. 9, pp. 721–4, Sep. 2010.
- [3] M. Yamanouchi, R. Koizumi, S. Ikeda, H. Sato, K. Mizunuma, K. Miura, H. D. Gan, F. Matsukura, and H. Ohno, "Dependence of magnetic anisotropy on MgO thickness and buffer layer in Co₂₀Fe₆₀B₂₀-MgO structure," *J. Appl. Phys.*, vol. 109, no. 7, p. 07C712, 2011.
- [4] W.-G. Wang, S. Hageman, M. Li, S. Huang, X. Kou, X. Fan, J. Q. Xiao, and C. L. Chien, "Rapid thermal annealing study of magnetoresistance and perpendicular anisotropy in magnetic tunnel junctions based on MgO and CoFeB," *Appl. Phys. Lett.*, vol. 99, no. 10, p. 102502, 2011.
- [5] J. C. Read, P. G. Mather, and R. A. Buhrman, "X-ray photoemission study of CoFeB/MgO thin film bilayers," *Appl. Phys. Lett.*, vol. 90, no. 13, p. 132503, 2007.
- [6] N. Miyakawa, D. C. Worledge, and K. Kita, "Impact of Ta Diffusion on the Perpendicular Magnetic Anisotropy of Ta/CoFeB/MgO," *IEEE Magn. Lett.*, vol. 4, p. 1000104, 2013.
- [7] L. E. Nistor, B. Rodmacq, C. Ducruet, C. Portemont, I. L. Prejbeanu, and B. Dieny, "Correlation Between Perpendicular Anisotropy and Magnetoresistance in Magnetic Tunnel Junctions," *IEEE Trans. Magn.*, vol. 46, no. 6, pp. 1412–1415, Jun. 2010.
- [8] W. C. Tsai, S. C. Liao, H. C. Hou, C. T. Yen, Y. H. Wang, H. M. Tsai, F. H. Chang, H. J. Lin, and C.-H. Lai, "Investigation of perpendicular magnetic anisotropy of CoFeB by x-ray magnetic circular dichroism," *Appl. Phys. Lett.*, vol. 100, no. 17, p. 172414, 2012.
- [9] J. J. Cha, J. C. Read, W. F. Egelhoff, P. Y. Huang, H. W. Tseng, Y. Li, R. A. Buhrman, and D. A. Muller, "Atomic-scale spectroscopic imaging of CoFeB/Mg–B–O/CoFeB magnetic tunnel junctions," *Appl. Phys. Lett.*, vol. 95, no. 3, p. 032506, 2009.

- [10] S. V. Karthik, Y. K. Takahashi, T. Ohkubo, K. Hono, H. D. Gan, S. Ikeda, and H. Ohno, "Transmission electron microscopy study on the effect of various capping layers on CoFeB/MgO/CoFeB pseudo spin valves annealed at different temperatures," *J. Appl. Phys.*, vol. 111, no. 8, p. 083922, 2012.
- [11] Y. S. Choi, K. Tsunekawa, Y. Nagamine, and D. Djayaprawira, "Transmission electron microscopy study on the polycrystalline CoFeB/MgO/CoFeB based magnetic tunnel junction showing a high tunneling magnetoresistance, predicted in single crystal magnetic tunnel junction," *J. Appl. Phys.*, vol. 101, no. 1, p. 013907, 2007.
- [12] H. X. Yang, M. Chshiev, B. Dieny, J. H. Lee, A. Manchon, and K. H. Shin, "First-principles investigation of the very large perpendicular magnetic anisotropy at Fe|MgO and Co|MgO interfaces," *Phys. Rev. B*, vol. 84, no. 5, p. 054401, Aug. 2011.
- [13] K. Nakamura, T. Akiyama, T. Ito, M. Weinert, and A. J. Freeman, "Role of an interfacial FeO layer in the electric-field-driven switching of magnetocrystalline anisotropy at the Fe/MgO interface," *Phys. Rev. B*, vol. 81, no. 22, p. 220409, Jun. 2010.
- [14] M. K. Niranjana, C.-G. Duan, S. S. Jaswal, and E. Y. Tsybal, "Electric field effect on magnetization at the Fe/MgO(001) interface," *Appl. Phys. Lett.*, vol. 96, no. 22, p. 222504, 2010.
- [15] K. H. Khoo, G. Wu, M. H. Jhon, M. Tran, F. Ernult, K. Eason, H. J. Choi, and C. K. Gan, "First-principles study of perpendicular magnetic anisotropy in CoFe/MgO and CoFe/Mg₃B₂O₆ interfaces," *Phys. Rev. B*, vol. 87, no. 17, p. 174403, May 2013.
- [16] K. Nakamura, R. Shimabukuro, Y. Fujiwara, T. Akiyama, T. Ito, and A. Freeman, "Giant Modification of the Magnetocrystalline Anisotropy in Transition-Metal Monolayers by an External Electric Field," *Phys. Rev. Lett.*, vol. 102, no. 18, p. 187201, May 2009.
- [17] D. C. Worledge, G. Hu, D. W. Abraham, P. L. Trouilloud, and S. Brown, "Development of perpendicularly magnetized Ta|CoFeB|MgO-based tunnel junctions at IBM (invited)," *J. Appl. Phys.*, vol. 115, no. 17, p. 172601, May 2014.
- [18] V. Sokalski, M. T. Moneck, E. Yang, and J.-G. Zhu, "Optimization of Ta thickness for perpendicular magnetic tunnel junction applications in the MgO-FeCoB-Ta system," *Appl. Phys. Lett.*, vol. 101, no. 7, p. 072411, Aug. 2012.

- [19] S. Ahn and G. S. D. Beach, “Crossover between in-plane and perpendicular anisotropy in Ta / Co x Fe 100- x / MgO films as a function of Co composition,” *J. Appl. Phys.*, vol. 112, no. May 2014, pp. 2011–2014, 2013.
- [20] D. D. Lam, F. Bonell, S. Miwa, Y. Shiota, K. Yakushiji, and H. Kubota, “Composition Dependence of Perpendicular Magnetic Anisotropy in,” *J. Magn.*, vol. 18, no. 1, pp. 5–8, 2013.
- [21] S. Yakata, H. Kubota, Y. Suzuki, K. Yakushiji, A. Fukushima, S. Yuasa, and K. Ando, “Influence of perpendicular magnetic anisotropy on spin-transfer switching current in CoFeB/MgO/CoFeB magnetic tunnel junctions,” *J. Appl. Phys.*, vol. 105, no. 7, p. 07D131, 2009.
- [22] T. Liu, J. W. Cai, and L. Sun, “Large enhanced perpendicular magnetic anisotropy in CoFeB/MgO system with the typical Ta buffer replaced by an Hf layer,” *AIP Adv.*, vol. 2, no. 3, p. 032151, 2012.
- [23] A. T. Hindmarch, V. Harnchana, A. S. Walton, A. P. Brown, R. M. D. Brydson, and C. H. Marrows, “Zirconium as a Boron Sink in Crystalline CoFeB/MgO/CoFeB Magnetic Tunnel Junctions,” *Appl. Phys. Express*, vol. 4, no. 1, p. 013002, Jan. 2011.
- [24] C.-F. Pai, M.-H. Nguyen, C. Belvin, L. H. Vilela-Leão, D. C. Ralph, and R. A. Buhrman, “Enhancement of perpendicular magnetic anisotropy and transmission of spin-Hall-effect-induced spin currents by a Hf spacer layer in W/Hf/CoFeB/MgO layer structures,” *Appl. Phys. Lett.*, vol. 104, no. 8, p. 082407, Feb. 2014.
- [25] J. Sinha, M. Hayashi, A. J. Kellock, S. Fukami, M. Yamanouchi, H. Sato, S. Ikeda, S. Mitani, S. Yang, S. S. P. Parkin, and H. Ohno, “Enhanced interface perpendicular magnetic anisotropy in Ta|CoFeB|MgO using nitrogen doped Ta underlayers,” *Appl. Phys. Lett.*, vol. 102, no. 24, p. 242405, Jun. 2013.
- [26] T. Liu, Y. Zhang, J. W. Cai, and H. Y. Pan, “Thermally robust Mo/CoFeB/MgO trilayers with strong perpendicular magnetic anisotropy,” *Sci. Rep.*, vol. 4, no. 5, p. 5895, Jan. 2014.
- [27] S.-C. Lee, K.-S. Kim, S.-H. Lee, U.-H. Pi, K. Kim, Y. Jang, and U.-I. Chung, “Effect of Fe–O distance on magnetocrystalline anisotropy energy at the Fe/MgO(001) interface,” *J. Appl. Phys.*, vol. 113, no. 2, p. 023914, 2013.
- [28] M. Endo, S. Kanai, S. Ikeda, F. Matsukura, and H. Ohno, “Electric-field effects on thickness dependent magnetic anisotropy of sputtered MgO/Co₄₀Fe₄₀B₂₀/Ta structures,” *Appl. Phys. Lett.*, vol. 96, no. 21, p. 212503, 2010.

- [29] T. Maruyama, Y. Shiota, T. Nozaki, K. Ohta, N. Toda, M. Mizuguchi, A. A. Tulapurkar, T. Shinjo, M. Shiraishi, S. Mizukami, Y. Ando, and Y. Suzuki, “Large voltage-induced magnetic anisotropy change in a few atomic layers of iron,” *Nat. Nanotechnol.*, vol. 4, no. March, pp. 158–161, 2009.
- [30] Y. Shiota, S. Murakami, F. Bonell, T. Nozaki, T. Shinjo, and Y. Suzuki, “Quantitative Evaluation of Voltage-Induced Magnetic Anisotropy Change by Magnetoresistance Measurement,” *Appl. Phys. Express*, vol. 4, no. 4, p. 043005, Mar. 2011.
- [31] T. Nozaki, Y. Shiota, S. Miwa, S. Murakami, F. Bonell, S. Ishibashi, H. Kubota, K. Yakushiji, T. Saruya, A. Fukushima, S. Yuasa, T. Shinjo, and Y. Suzuki, “Electric-field-induced ferromagnetic resonance excitation in an ultrathin ferromagnetic metal layer,” *Nat. Phys.*, vol. 8, no. 6, pp. 492–497, Apr. 2012.
- [32] W.-G. Wang, M. Li, S. Hageman, and C. L. Chien, “Electric-field-assisted switching in magnetic tunnel junctions,” *Nat. Mater.*, vol. 11, no. 1, pp. 64–8, Jan. 2012.
- [33] L. Liu, C.-F. Pai, D. C. Ralph, and R. A. Buhrman, “Magnetic Oscillations Driven by the Spin Hall Effect in 3-Terminal Magnetic Tunnel Junction Devices,” *Phys. Rev. Lett.*, vol. 109, no. 18, p. 186602, Oct. 2012.
- [34] J. Zhu, J. A. Katine, G. E. Rowlands, Y.-J. Chen, Z. Duan, J. G. Alzate, P. Upadhyaya, J. Langer, P. K. Amiri, K. L. Wang, and I. N. Krivorotov, “Voltage-Induced Ferromagnetic Resonance in Magnetic Tunnel Junctions,” *Phys. Rev. Lett.*, vol. 108, no. 19, p. 197203, May 2012.
- [35] P. Bruno, “Tight-binding approach to the orbital magnetic moment and magnetocrystalline anisotropy of transition-metal monolayers,” *Phys. Rev. B. Condens. Matter*, vol. 39, no. 1, pp. 865–868, Jan. 1989.
- [36] U. Bauer, L. Yao, S. Emori, H. L. Tuller, S. Van Dijken, and G. S. D. Beach, “Magneto-ionic Control of Interfacial Magnetism,” pp. 1–24.
- [37] V. B. Naik, H. Meng, J. X. Xiao, R. S. Liu, A. Kumar, K. Y. Zeng, P. Luo, and S. Yap, “Electric-field-induced strain-mediated magnetoelectric effect in CoFeB-MgO magnetic tunnel junctions,” Nov. 2013.
- [38] Y. Shiota, F. Bonell, S. Miwa, N. Mizuochi, T. Shinjo, and Y. Suzuki, “Opposite signs of voltage-induced perpendicular magnetic anisotropy change in CoFeB/MgO junctions with different underlayers,” *Appl. Phys. Lett.*, vol. 103, no. 8, p. 082410, 2013.

- [39] G. W. Hollenberg, G. R. Terwilliger, and R. S. Gordon, "Calculation of Stresses and Strains in Four-Point Bending Creep Tests," *J. Am. Ceram. Soc.*, vol. 54, no. 4, pp. 196–199, 1970.
- [40] Z. Tian, D. Sander, and J. Kirschner, "Nonlinear magnetoelastic coupling of epitaxial layers of Fe, Co, and Ni on Ir(100)," *Phys. Rev. B*, vol. 79, no. 2, p. 024432, Jan. 2009.
- [41] S. S. Mukherjee, F. Bai, D. MacMahon, C.-L. Lee, S. K. Gupta, and S. K. Kurinec, "Crystallization and grain growth behavior of CoFeB and MgO layers in multilayer magnetic tunnel junctions," *J. Appl. Phys.*, vol. 106, no. 3, p. 033906, 2009.
- [42] C. C. Tsai, C.-W. Cheng, M.-C. Tsai, and G. Chern, "Superparamagnetic States and Perpendicular Magnetic Anisotropy in Ultrathin MgO/CoFeB/Ta Structures," *IEEE Trans. Magn.*, vol. 50, no. 1, pp. 1–4, Jan. 2014.
- [43] Y. K. Kim and T. J. Silva, "Magnetostriction characteristics of ultrathin permalloy films," *Appl. Phys. Lett.*, vol. 68, no. 20, p. 2885, 1996.
- [44] G. Bochi, C. Ballentine, H. Inglefield, C. Thompson, and R. O'Handley, "Evidence for strong surface magnetoelastic anisotropy in epitaxial Cu/Ni/Cu(001) sandwiches," *Phys. Rev. B. Condens. Matter*, vol. 53, no. 4, pp. R1729–R1732, Jan. 1996.
- [45] O. Song, C. A. Ballentine, and R. C. O'Handley, "Giant surface magnetostriction in polycrystalline Ni and NiFe films," *Appl. Phys. Lett.*, vol. 64, no. 19, p. 2593, 1994.
- [46] G. M. Stiehl, "A-Exam Write-up," 2014.

CHAPTER 4

GIGAHERTZ FREQUENCY MAGNETIZATION DYNAMICS INDUCED BY SURFACE ACOUSTIC WAVES

4.1 Introduction/Motivation

This chapter is devoted to the study of magnetization dynamics excited by surface acoustic waves (SAWs). We have conducted experimental studies on Ni|Pt bilayers and have succeeded in exciting ferromagnetic resonance by using a SAW as a pump and relying on the magnetoelastic interaction to couple the surface acoustic waves into the magnetic degrees of freedom. We have measured the acoustical absorption induced by the magnetoelastic resonance via Vector Network Analyzer transmission measurements on a SAW delay line and we have also measured the inverse spin Hall voltage generated by spin current pumped into the Pt from the SAW-induced magnetoelastic resonance in Ni. Our central finding of this chapter is that the SAW-induced resonance angular dependence and the resonance fields at which maximum absorption occur can only be quantitatively and qualitatively understood if the excitation is a dipolar Damon-Eschbach spin-wave where the wave-vector of the spin-wave is fixed by the traveling SAW. Previous experiments [1]–[3] and theoretical considerations [4] have completely neglected dynamic dipolar interactions associated with the spin-wave and consequently their theoretical description does not match their data nor does it have the power to qualitatively describe the nature of the spin wave excitations induced by SAWs. We derive the correct expression for the susceptibility of the SAW-induced resonance in the SAW wavelength regime employed. We then

show that our calculated susceptibility quantitatively matches our SAW absorption data with no free parameters except the spin wave damping. Next, we show that our measured DC voltages associated with magnetoelastic resonance derive almost entirely from the spin-pumping/ISHE mechanism and not from other rectification effects. We point out that a previous publication [2] took great pains to separate spin-pumping signals from AMR effects and that this separation was one of the central points of that paper. We show that the problem can be avoided by clever engineering of the film stack structure. We then use our ISHE voltage to quantify the effective RF magnetic field generated by the surface acoustic wave, the effective amplitude of the magnetoelastic excitation, and the magnetoelastic coupling of the Ni film. We conclude the chapter by arguing that ultrasonic excitation of ferromagnets could become a legitimately powerful and fundamentally new tool for studying different regimes and length-scales of magnetization dynamics from the micrometer-scale down into the nano-scale.

4.2 Surface Acoustic Waves

Surface acoustic waves are propagating waves that are localized close to the surface of a solid body. Lord Rayleigh first derived them by considering a semi-infinite isotropic solid and showed that one could have solutions to the elastic wave equation that were localized at the surface (i.e. whose amplitude decayed exponentially away from the surface). These waves are now formally known as Rayleigh waves both to honor their discoverer and to distinguish them from other

types of surface acoustic waves which can exist in anisotropic media (e.g. Love waves). Rayleigh SAWs have a longitudinal displacement component and a transverse coupled shear component that is in the direction normal to the surface. A propagating plane Rayleigh wave is pictured below:

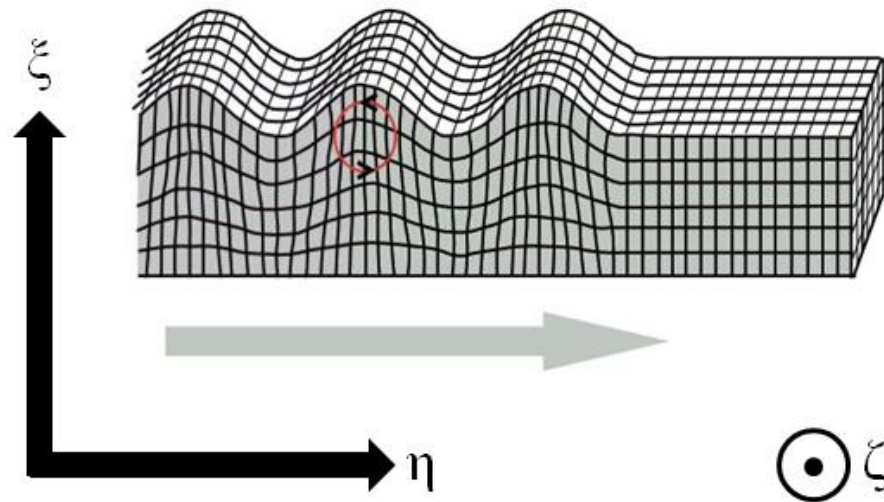


Figure 4.1. Propagation of a Rayleigh-type SAW. Red circle in the diagram is a cartoon of the mixed longitudinal and vertical shear wave motion associated with the Rayleigh SAW.

This “mixed” polarization wave occurs essentially due to boundary conditions at the surface. The elastic equation for an isotropic medium can be written as:

$$\rho \partial_t^2 \vec{u} = \nabla \cdot \sigma = c_T^2 \nabla^2 \vec{u} + (c_L^2 - c_T^2) \vec{\nabla} (\vec{\nabla} \cdot \vec{u}) \quad (4.1)$$

σ is the stress tensor, \vec{u} is the displacement field, and c_L and c_T are the longitudinal and transverse sound velocities respectively. The right hand side can be arrived at by

using the constitutive relations for an isotropic solid $\sigma_{ik} = \frac{E}{1+\nu} \left(u_{ik} + \frac{\nu}{1-2\nu} u_{ll} \delta_{ik} \right)$ and

by regrouping expressions involving the Young's modulus and Poisson ratio into the transverse and longitudinal sound velocities. The displacement field \vec{u} can be written as $\vec{u} = \vec{u}_T + \vec{u}_L$ where \vec{u}_T is the divergenceless component of the motion and \vec{u}_L is the curl-less component. Taking the curl and the divergence of the elastic equation yields two uncoupled wave equations for \vec{u}_T and \vec{u}_L :

$$\begin{aligned} \partial_t^2 \vec{u}_T &= c_T^2 \nabla^2 \vec{u}_T \\ \partial_t^2 \vec{u}_L &= c_L^2 \nabla^2 \vec{u}_L \end{aligned} \quad (4.2)$$

The free boundary conditions on the surface can be expressed as $\sigma_{ik} n_k = 0$ where n is the vector normal to the surface. We then assume that our solid is semi-infinite and that the surface normal is in the ξ -direction. Using the constitutive relations gives us three equations that are valid at $\xi = 0$ (i.e. the surface):

$$\begin{aligned} \partial_\xi u_\eta + \partial_\eta u_\xi &= 0 \\ \partial_\zeta u_\eta + \partial_\eta u_\zeta &= 0 \\ c_L^2 \partial_\xi u_\xi + (c_L^2 - 2c_T^2) \partial_\eta u_\eta &= 0 \end{aligned} \quad (4.3)$$

The boundary conditions couple motion in the ξ and η direction. Since we are at a surface we look for modes that are dependent on the coordinate normal to the surface. We assume plane wave propagation in the $+\eta$ direction and try for solutions of the wave equations that go as $u_T = f_T(\xi) \exp[i(q\eta - \omega t)]$ and $u_L = f_L(\xi) \exp[i(q\eta - \omega t)]$.

Each wave equation satisfies:

$$\begin{aligned}\frac{\partial^2 f_T(\xi)}{\partial \xi^2} &= \left(q^2 - \frac{\omega^2}{c_T^2}\right) f_T(\xi) \\ \frac{\partial^2 f_L(\xi)}{\partial \xi^2} &= \left(q^2 - \frac{\omega^2}{c_L^2}\right) f_L(\xi)\end{aligned}\tag{4.4}$$

We are looking for solutions for $f(\xi)$ that are decaying away from the surface which

occurs when $q^2 > \frac{\omega^2}{c^2}$. The solutions we seek are then of the

form $\vec{u}_T = \vec{u}_T^0 \exp[\kappa_T \xi] \exp[i(q\eta - \omega t)]$ and $\vec{u}_L = \vec{u}_L^0 \exp[\kappa_L \xi] \exp[i(q\eta - \omega t)]$. The

boundary conditions can be used to solve for the amplitudes. The first boundary

condition ensures that no transverse shear component of the wave (i.e. $u_{\zeta\eta}$ and $u_{\xi\eta}$)

can exist at the surface. The relationship between the ξ and η components of \vec{u}_T and

\vec{u}_L can be found then by using the condition that the divergence and curl of either

vanish respectively. The last two B.C.s can be used to solve for the dispersion

relationship for this wave and it is found that the resultant dispersion is $\omega = c_T \beta q$. β is

purely a function of the ratio $\left(\frac{c_T}{c_L}\right)$. For $0 \leq \nu \leq .5$ (i.e. from a fully compressible to an

incompressible solid) we get a range of $\beta \sim .84 - .95$. Thus Rayleigh waves are slower

than either bulk transverse or longitudinal sound waves. A final solution for the

displacement amplitude of the waves goes as:

$$\begin{aligned}u_\xi &= A \exp[i(q\eta - \omega t)] \cdot \left(-iq \exp[\kappa_T \xi] - i\kappa_L \frac{2\sqrt{1-\beta^2}}{2-\beta^2} \exp[\kappa_L \xi] \right) \\ u_\eta &= A \exp[i(q\eta - \omega t)] \cdot \left(\kappa_T \exp[\kappa_T \xi] - \frac{2\sqrt{1-\beta^2}}{2-\beta^2} q \exp[\kappa_L \xi] \right)\end{aligned}\tag{4.5}$$

This shows an exponentially decaying surface wave with a coupled longitudinal and z-directional transverse motion. The SAW decay length or penetration depth is on the order of $d \sim \kappa_T^{-1}, \kappa_L^{-1} \sim O(\lambda_{SAW})$. For readers interested in the details of the derivation we refer them to Landau and Lifshitz's treatise on elasticity theory. [5]

4.3 A Introduction to Electrical Generation of SAWs

SAWs can be generated electrically on the surface of a piezoelectric insulator. Typically the surface of the piezoelectric insulator is metallized by a pair of interlocked electrodes. The first electrode is the signal line and the other is the ground electrode. Such a configuration is shown in Figure 4.2. The electrodes are known as interdigitated transducers (IDT). When a voltage is applied to the electrodes it enforces that potential and an associated charge distribution on the piezoelectric. The potential also induces an acoustical response from the piezoelectric. An RF voltage will thus generate an RF acoustical response from the piezoelectric.

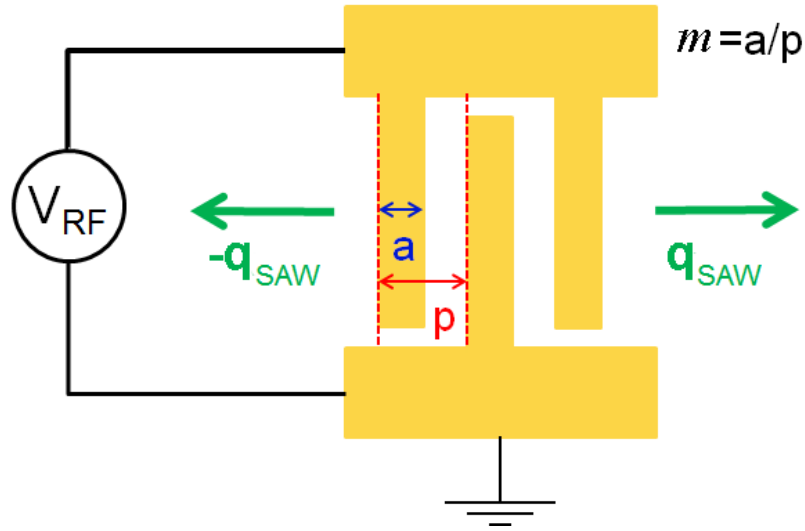


Figure 4.2 Illustration of interdigitated electrodes launching a SAW. $m = a / p$ is the metallization ratio where a is the IDT finger width and p is the electrode pitch.

In general, the acoustic response of the piezoelectric for an arbitrary RF frequency will be low. This is essentially due to the fact that each finger pumps a SAW with a certain amplitude and phase. When the acoustic waves pumped from each finger are not in-phase the IDT electrodes do not launch a coherent SAW. However, when they are all in phase the electrical signal is converted into a coherent forward (and backwards) traveling wave. The backwards traveling wave is due to the fact that the IDT has no directionality. The condition for phase constructive addition and SAW launching is that the pumped RF voltage has a frequency such that the associated wavelength of the SAW (given by $\lambda_{SAW} = c_{SAW} / f_{pump}$) is an integer multiple of the pitch of the IDT electrodes. It is important to note that IDTs cannot be oriented arbitrarily on the piezoelectric substrate as piezoelectric solids tend to be highly anisotropic. Only certain crystallographic directions/substrate cuts can support plane-

wave type propagating SAWs. For example, plane-wave SAWs can be launched on Y-cut LiNbO₃ only when the IDTs are aligned along the Z-axis (which is the long c-axis of the LiNbO₃ unit cell and corresponds to η axis in our coordinate system).

Propagation off this axis in the YZ plane can lead to beam-steering and diffraction effects. These effects can certainly be used to do some interesting things in real space but for our initial experiment we want to keep things simple and restrict our SAW to a plane wave with a well-defined wave-vector.

The SAW is generally characterized by the potential amplitude ϕ^+ and displacement amplitudes u_ζ , u_ξ , and u_η . The acoustic amplitudes are related to the potential amplitude and in some of the more well-known substrate materials and cuts are extremely well characterized. We will be using YZ-cut LiNbO₃ with propagation along the Z direction (η axis) for our experiment. The Y crystal axis in our coordinate system is the ξ axis. The SAW propagation velocity in YZ-cut LiNbO₃ is $v_{\text{SAW}} = 3488$ m/s. The coefficients relating the SAW acoustic amplitudes to the potential wave amplitude (i.e. $u_\alpha = c_\alpha \phi^+$) are given in Table 4.1.

Complex Amplitude Coefficient	Values for LiNbO ₃
c_ζ	0 \AA/V
c_ξ	$1.8i \text{ \AA/V}$
c_η	-1.2 \AA/V

Table 4.1 Coefficients coupling acoustic wave amplitudes and potential wave amplitudes in LiNbO₃.

The potential amplitude $\phi^+(f)$ of a SAW can be derived by assuming that the response of the entire IDT is a summation of the response function of one electrode (known as the single-tap response function) over the entire IDT array. This is usually expressed in terms of a decomposition of the response function into the single tap response function $\mu_s(f, m)$ and the array factor $H(f)$.

$$\phi^+(f) = \mu_s(f, m)H(f) \quad (4.6)$$

The single tap response has the information about the electrostatics of a single IDT pair built into it. It depends on the piezoelectric coupling constant K^2 , the electrode pitch, and the metallization ratio m (defined in Figure 4.2). K^2 is a measure of how much charge density a passing SAW induces on a metal sheet and vice-versa. It can be shown that it is also a measure of the change of the effective transmission line capacitance and the velocity of the SAW (in fact $K^2 = 2 \cdot \Delta v_{SAW} / v_{SAW}$). $K^2 = 4.6\%$ for YZ-cut LiNbO₃. For a light electrode (such as Al that is not too-thick), we can ignore mass-loading effects where the electrode itself provides enough inertia to hamper the generation of a SAW. When these effects are neglected, the single tap response is expressed as:

$$\mu_s^l(f, m) = .8K^2 \sin[\pi f / (2f_0)] \cdot P_l[\cos[m\pi]] \quad (4.7)$$

Equation (4.7) is defined between $0 < f < 2f_0$. The integer l is defined as

$l \equiv \text{Integer} \left[\frac{f}{2f_0} \right]$. The corresponding Legendre polynomial weights associated with

the bandpasses (1st, 3rd, etc.) come from approximate solutions to Poisson's equation for an IDT signal and ground pair. Another important point is that SAW bandpasses

can only exist centered about odd integers of f_0 . This is due to the fact that the amplitude at the ground electrodes must always be π out of phase with the amplitude at the signal electrodes.

The array factor is the spatial Fourier transform of the electrode voltage array with the assumption that each electrode can be approximated as a delta function. The array factor is then a sum over the voltage and the different phase factors at each electrode of a SAW of frequency f :

$$H(f) = \sum_n V_n e^{-i\left(\frac{2\pi f}{v_{SAW}}\right)z_n} \quad (4.8)$$

In our case, the electrodes are evenly spaced by the pitch p , $z_n = np$, $\lambda_{SAW} = 2p$ and the IDT voltages on alternating electrodes are $+V/2$ and $-V/2$. The array factor is then:

$$|H(f)| = \frac{V}{2} \left| \frac{\sin\left[\frac{N\pi(f-f_0)}{2f_0}\right]}{\sin\left[\frac{\pi(f-f_0)}{2f_0}\right]} \right| \quad (4.9)$$

The response function and the array factor is plotted. We also plot the response function for a different metallization ratio $m=0.4$.

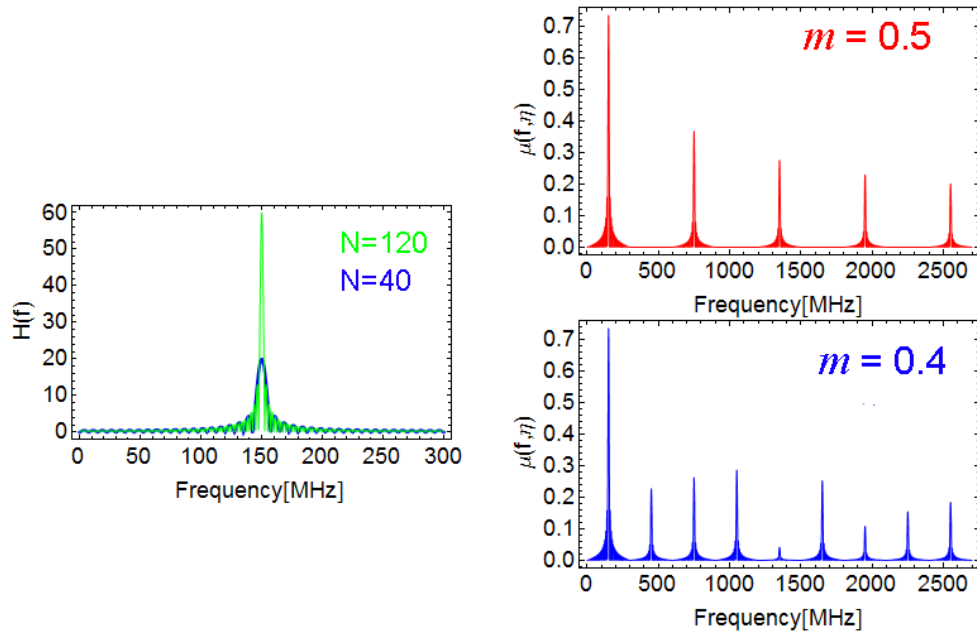


Figure 4.3 Plot of array factor $H(f)$ at the fundamental bandpass f_0 for $N = 40$ and $N = 120$ fingers. We have also plotted the response function for SAW launchers with $f_0 = 150$ MHz and $m = 0.4$ and 0.5 respectively.

Our experiment uses a SAW delay-line geometry. A delay line consists of two IDT electrodes – an IDT antenna and a receiver separated by some distance L . The delay line is essentially a 2-port reciprocal network and the surface of the piezoelectric substrate acts as an electromechanical transmission line. We measure the change in S_{21} of this delay line to measure the attenuation and power absorption of the SAW when the magnetization is being driven by magnetoelastic resonance. S_{11} measures the power reflected by the input IDT due to impedance mismatch. It thus provides a direct measure of the power flow into the electromechanical transmission line. Some of this power flow will not be in the form of SAWs and will be associated with bulk acoustic

waves, electromagnetic radiation, etc. We want the power flow associated with the SAW which can be expressed as:

$$P_{trans}^{SAW} = \frac{1}{2} \left(|S_{11}^{rest}|^2 - |S_{11}^{rest+SAW}|^2 \right) P_{RF} \quad (4.10)$$

The factor of $\frac{1}{2}$ comes from the bi-directionality of the SAW. Thus a launched SAW will appear as a dip in S_{11} and we can essentially subtract out the background S_{11} to get the transmitted SAW power. The potential amplitude is related to the SAW power flow:

$$P_{SAW} = \frac{1}{2} Y_0 |\phi|^2 = \frac{1}{2} y_0 \frac{W}{\lambda_{SAW}} |\phi|^2 \quad (4.11)$$

Y_0 is the effective electrical admittance of a SAW propagating on the substrate while y_0 is intrinsic and depends on the substrate material and cut and SAW propagation direction. For LiNbO_3 , $y_0 = 0.21$ mmhos and our IDT electrodes have a width $W = 500 \mu\text{m}$. We can use Equation (4.11) and the relations $|u_\eta|^2 = |c_\eta|^2 |\phi|^2$ and $|\varepsilon_{\eta\eta}|^2 = q^2 |u_\eta|^2$ we get an expression for the peak SAW strain amplitude:

$$|\varepsilon_{\eta\eta}| = |c_\eta| q \sqrt{\frac{2P_{SAW}}{y_0 \left(\frac{W}{\lambda_{SAW}} \right)}} \quad (4.12)$$

The coupling coefficient $|c_\eta| = 1.2 \times 10^{-10}$ m/V. The longitudinal strain wave amplitude can then be expressed as a function of RF input power and S_{11} reflection coefficients as:

$$|\varepsilon_{\eta\eta}| = |c_\eta| q \sqrt{\frac{\left(|S_{11}^{rest}|^2 - |S_{11}^{rest+SAW}|^2 \right) P_{RF}}{y_0 \left(\frac{W}{\lambda_{SAW}} \right)}} \quad (4.13)$$

We typically know everything except the S_{11} coefficients. Once these are measured we can use Equation (4.13) to directly solve for the strain wave amplitude. Our discussion of electrical SAW generation can be found in greater detail in books by Datta [6] and Campbell [7].

4.4 SAW-induced Magnetoelastic Spin-Wave Resonance: Theory

SAWs traveling on the surface of the LiNbO_3 will generate a time-dependent and spatially varying traveling strain wave on any film deposited on top of the LiNbO_3 . In the limit that the film thickness is much smaller than the decay length of the SAW (which is approximately the SAW wavelength) we can expect that the strain field can be approximated by the strain field on the LiNbO_3 surface. In a ferromagnetic film this induced strain can generate torques on the magnetization through the magnetoelastic interaction. We can express the SAW-induced torques on the magnetization as a spatially-varying, time dependent effective internal field on the magnetization. This

time dependent effective field can, in the appropriate field and magnetization orientation, act as a tickle field to excite resonant dynamics in the ferromagnetic film.

The tickle field, for a given SAW pump frequency, will have a wave-vector $\vec{q} = \frac{2\pi f_{SAW}}{c_{SAW}} \hat{\eta}$. The $\hat{\eta}$ direction is the SAW propagation direction corresponding in our case to the LiNbO₃ Z-axis. This immediately implies that the resonance we excite will be a spin-wave resonance where the spin wave also is enforced to have a wave-vector \vec{q} . We stress that the nature of this spin wave resonance here is different from spin wave resonances induced by a spatially homogenous r.f. magnetic field. In the latter case the spin wave resonance is associated with boundary conditions on the magnetic induction and magnetization whereas our spin wave is pumped locally at each point in the ferromagnetic film by the spatially varying acoustic wave.

The magnetization dynamics can be treated in the LLG framework. The LLG dynamics can be written as:

$$\frac{d\vec{m}(\vec{r})}{dt} = -\gamma \vec{m}(\vec{r}) \times \vec{H}_{eff} + \Gamma \vec{m}(\vec{r}) \times \frac{d\vec{m}(\vec{r})}{dt} \quad (4.14)$$

We have replaced α with Γ to explicitly acknowledge that we are discussing a spin-wave damping term and not the Gilbert damping of the uniform mode. We still assume that $\Gamma \ll 1$ so that the damping term can be treated as a perturbation.

The problem is treated in the case where the thin film magnet possesses a uniaxial anisotropy with easy axis along the ζ axis and hard axis along the η axis (our SAW propagation direction being $+\eta$), and an applied field H_{app} at an azimuthal

angle ϕ_H with respect to the ζ axis. The applied field is assumed to always be in the plane of the film. The axis ξ is normal to the film plane. The coordinate system is shown in Figure 4.4.

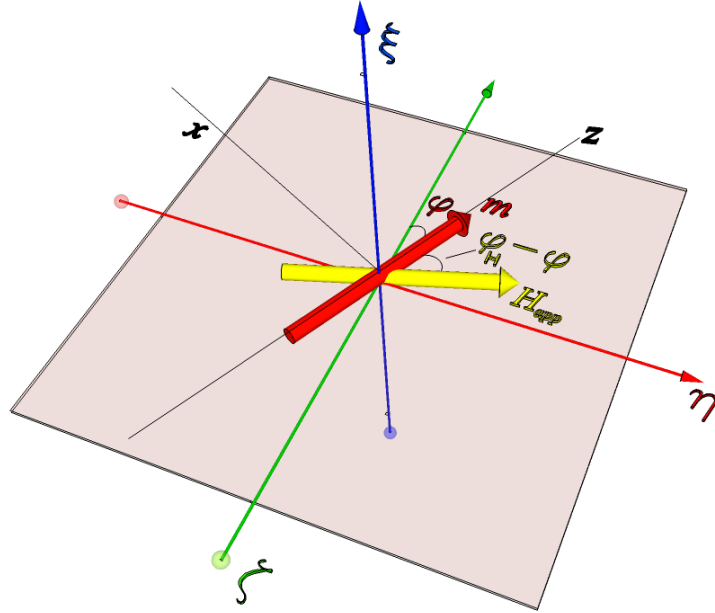


Figure 4.4 $\zeta\eta\xi$ and xyz coordinate system for in-plane magnetized film and applied field. The polar angle θ is not shown but is the angle the magnetization makes with the ξ axis.

Before the SAW comes in, we assume that the magnetization and the magnetic free energy are spatially and time-independent. The free energy density can be then expressed as:

$$\begin{aligned}
 f_s &= -K_u m_\zeta^2 - M_s H_{app} (\cos(\phi_H) m_\zeta + \sin(\phi_H) m_\eta) + 2\pi M_s^2 m_\zeta^2 \\
 f_s &= -K_u \cos^2 \phi - M_s H_{app} \cos(\phi - \phi_H) + 2\pi M_s^2 \cos^2 \theta
 \end{aligned} \tag{4.15}$$

The static part of the free energy is then used to find the equilibrium in-plane magnetization coordinate $\vec{m}_0 = \cos(\phi_0)\hat{\zeta} + \sin(\phi_0)\hat{\eta}$. The equilibrium magnetization can be found by the condition $\partial_\phi f_s = 0$ and $\partial_\phi^{(2)} f_s \geq 0$. This yields the equation for the equilibrium angle ϕ_0 :

$$-H_k \cos \phi_0 \sin \phi_0 = H_{app} \sin(\phi_0 - \phi_H) \quad (4.16)$$

The LLG spin wave dynamics are then linearized about the equilibrium magnetization defined by the applied field and the anisotropy. The magnetization is expressed as $\vec{m}(\vec{r}) = \vec{m}_0 + \delta\vec{m}(\vec{r})$ and we transform into a $\hat{x}, \hat{y}, \hat{z}$ coordinate system where the equilibrium magnetization unit vector is set as the \hat{z} axis. The film is in the xz plane in our coordinate system. Then $\vec{m}_0 \sim \hat{z}$ and $\delta\vec{m}(\vec{r}) = (\delta m_q^x(y)\hat{x} + \delta m_q^y(y)\hat{y})e^{i(\vec{q}\cdot\vec{r}-\omega t)}$ where in our experiment ω is the SAW pump frequency and where we have assumed a traveling spin wave with the same in-plane wave-vector as the SAW. We have thus ignored as a first approximation any reflections of the spin wave and the SAW at the boundaries of the film. Explicit y dependence of the magnetization was retained for reasons that will soon become clear. We then define a local free energy density:

$$f(\vec{r}, t) = -\vec{m}(\vec{r}, t) \cdot (\vec{H}_{app} + \vec{H}_{anis} + A\nabla^2 \vec{m}(\vec{r}, t) + \vec{h}_d(\vec{r}, t) + \vec{h}_{RF}(\vec{r}, t)) \quad (4.17)$$

The applied field and anisotropy field contributions are contained in the static and spatially homogenous free energy in Equation (4.17). The third term is the exchange

field associated with the non-uniform magnetization of the spin wave. This non-uniformity is also time-dependent and implies that there is a dynamic source term for dipolar fields (via $\vec{\nabla} \cdot \vec{m} \neq 0$) not just as the film surfaces but at all points throughout the film. This fluctuating and spatially varying dipolar field will also generate torques on the magnetization and so we have included these effects in the term $h_d(\vec{r}, t)$. This dipolar field will, in general, not be uniform through the thickness of the film. This non-uniformity in the y-direction from the dipolar fields makes it necessary to keep the y-dependence in the LLG dynamics. The last term is the effective field that the SAW produces through the magnetoelastic interaction. It is the only term in Equation (4.17) that is explicitly time dependent. The magnetoelastic free energy describing the interaction between the magnetization and the traveling SAW is:

$$f_{ME} = -B_1 \varepsilon_{\eta\eta} e^{i(\vec{q}\cdot\vec{r} - \omega t)} \sin^2 \theta \cos^2 \phi + B_2 \varepsilon_{\eta\xi} e^{i(\vec{q}\cdot\vec{r} - \omega t)} \cos \theta \sin \theta \sin \phi \quad (4.18)$$

The amplitudes $\varepsilon_{\eta\eta}$ and $\varepsilon_{\eta\xi}$ correspond to longitudinal and shear strains respectively.

We expect the shear strain component in ultra-thin films (i.e. $d_{\text{film}} \ll \lambda_{\text{SAW}}$) to be rather small. This is due to the fact that a SAW must obey the zero shear strain boundary condition at the surface. Thicker films (e.g. a 150 nm film with $\lambda_{\text{SAW}} = .7 \mu\text{m}$) may develop a substantial shear component. Therefore we keep the shear term in our equations although for our experiments (with $d_{\text{film}} = 10 \text{ nm}$) we argue that we can ignore shear effects. We have completely left out the magnetoelastic coupling between m_ξ and $\varepsilon_{\xi\xi}$ (the transverse strain amplitude) as the torque arising from this coupling is negligible for in-plane magnetized systems. In the x, y, z

coordinate system we can show that the effective field derived from the magnetoelastic interaction is:

$$\begin{aligned} h_{RF}(\vec{r}, t) &= + \frac{2B_1}{M_s} \varepsilon_{\eta\eta} \sin(\phi_0) \cos(\phi_0) e^{i(\vec{q}\cdot\vec{r}-\omega t)} \hat{x} - \frac{B_2}{M_s} \varepsilon_{\eta\xi} \sin(\phi_0) e^{i(\vec{q}\cdot\vec{r}-\omega t)} \hat{y} \\ &= \left(h_{rf}^x \hat{x} + h_{rf}^y \hat{y} \right) e^{i(\vec{q}\cdot\vec{r}-\omega t)} \end{aligned} \quad (4.19)$$

We will treat this field as a tickle field and it enters the LLG equations as a 1st order term in our linearization. It is not difficult to show that the linearized LLG equation in the x, y, z coordinate system is:

$$\begin{aligned} -i\omega \delta m_x(y) &= -\gamma \left(H_k \cos^2(\phi_0) + H_{app} \cos(\phi_0 - \phi_H) + \frac{2A}{M_s} \left[q^2 - \frac{\partial^2}{\partial y^2} \right] \right) \delta m_y(y) \\ &+ \gamma h_d^y(y) + \gamma h_{RF}^y + i\omega \Gamma \delta m_y(y) \end{aligned} \quad (4.20)$$

$$\begin{aligned} -i\omega \delta m_y(y) &= +\gamma \left(H_k \cos(2\phi_0) + H_{app} \cos(\phi_0 - \phi_H) + \frac{2A}{M_s} \left[q^2 - \frac{\partial^2}{\partial y^2} \right] \right) \delta m_x(y) \\ &- \gamma h_d^x(y) - \gamma h_{RF}^x - i\omega \Gamma \delta m_x(x) \end{aligned} \quad (4.21)$$

The dipolar fields must be solved for simultaneously with the LLG equation. The dipolar field follows the magnetostatic equations:

$$\begin{aligned} \vec{\nabla} \times \vec{h}_d &= 0 \\ \vec{\nabla} \cdot \vec{h}_d &= -4\pi \vec{\nabla} \cdot \delta \vec{m}(\vec{r}) \end{aligned} \quad (4.22)$$

For our case, the dipolar fields can be solved for by using a magnetostatic potential $\vec{h}_d = -\vec{\nabla}\psi$ and by solving for $\psi(y)$ and $\delta \vec{m}(y)$ using Rado-Weertman

boundary conditions. These are exchange/surface-anisotropy conditions that express how free or pinned the magnetization is at the boundary. The calculation turns out to be not too difficult to do and has been carried out by Stamps and Hillebrand [8] in a marginally simpler situation. As they did, we have restricted ourselves to the limit that $qd_{film} \ll 1$ which for our study is quite reasonable. In this regime, the corresponding excitation is known as a Damon-Eschbach surface spin-wave. The equations of motion for the magnetization averaged through the thickness of the film become:

$$\left\{ \begin{array}{l} \left(H_k \cos(2\phi_0) + H_{app} \cos(\phi_0 - \phi_H) + \right. \\ \left. \frac{2A}{M_s} q^2 + 2\pi M_s qd \cos^2 \phi_0 \right) - \frac{i\omega\Gamma}{\gamma} \end{array} \right\} \delta m_x + i \frac{\omega}{\gamma} \delta m_y = h_{RF}^x \quad (4.23)$$

$$-i \frac{\omega}{\gamma} \delta m_x + \left\{ \begin{array}{l} \left(H_k \cos^2 \phi_0 + H_{app} \cos(\phi_0 - \phi_H) + \frac{2A}{M_s} q^2 \right) - \frac{i\omega\Gamma}{\gamma} \\ \left(4\pi M_s - K_{\perp} \right) - 4\pi M_s \left(\frac{qd}{2} \right) \end{array} \right\} \delta m_y = h_{RF}^y \quad (4.24)$$

We have explicitly included an extra perpendicular anisotropy term that might arise either from volume or surface interactions that serves to reduce the effective out-of-plane demagnetization field. This system of equations can be inverted to find the dynamic susceptibility tensor.

$$\chi = \frac{AB - \left(\frac{\omega}{\gamma}\right)^2 + \frac{i\Gamma\omega}{\gamma}(A+B)}{\left(AB - \left(\frac{\omega}{\gamma}\right)^2\right)^2 + \left(\frac{\Gamma\omega(A+B)}{\gamma}\right)^2} \cdot \begin{pmatrix} B - \frac{i\omega\Gamma}{\gamma} & -\frac{i\omega}{\gamma} \\ +\frac{i\omega}{\gamma} & A - \frac{i\omega\Gamma}{\gamma} \end{pmatrix} \quad (4.25)$$

$$\begin{aligned}
A &= H_k \cos(2\phi_0) + H_{app} \cos(\phi_0 - \phi_H) + \frac{2A}{M_s} q^2 + 2\pi M_s q d \cos^2 \phi_0 \\
B &= H_k \cos^2 \phi_0 + H_{app} \cos(\phi_0 - \phi_H) + \frac{2A}{M_s} q^2 + (4\pi M_s - K_\perp) - 4\pi M_s \left(\frac{qd}{2}\right)
\end{aligned} \tag{4.26}$$

The resonance frequency is simply:

$$\omega_{res} = \gamma \sqrt{A \times B} \tag{4.27}$$

The power absorbed under conditions of magnetoelastic resonance is governed by the magnetization response out of phase with rf pump field. The absorption is thus related to the imaginary part of the dynamical susceptibility tensor:

$$P_{abs} = \frac{\omega}{2} \vec{h}_{RF}^\dagger \cdot \overline{\chi}'' \cdot \vec{h}_{RF} \tag{4.28}$$

We write down the absorbed power explicitly:

$$\begin{aligned}
P_{abs} &= \frac{\frac{\omega^2}{2\gamma} \Gamma \left(B^2 + \left(\frac{\omega}{\gamma} \right)^2 \right)}{\left(\left(\frac{\omega_{res}}{\gamma} \right)^2 - \left(\frac{\omega}{\gamma} \right)^2 \right)^2 + \left(\frac{\omega \Gamma (A+B)}{\gamma} \right)^2} \left(\frac{2B_1}{M_s} \varepsilon_{\eta\eta} \right)^2 \sin^2 \phi_0 \cos^2 \phi_0 \\
&+ \frac{\frac{\omega^2}{2\gamma} \Gamma \left(A^2 + \left(\frac{\omega}{\gamma} \right)^2 \right)}{\left(\left(\frac{\omega_{res}}{\gamma} \right)^2 - \left(\frac{\omega}{\gamma} \right)^2 \right)^2 + \left(\frac{\omega \Gamma (A+B)}{\gamma} \right)^2} \left(\frac{B_2}{M_s} \varepsilon_{\eta\xi} \right)^2 \sin^2 \phi_0
\end{aligned} \tag{4.29}$$

When $H_k = 0$, $\phi_0 = \phi_H$ and it is easy to see that the ϕ_H angular dependence of the power absorbed by the spin-wave resonance comes from the magnetoelastic field and

the angular dependence in $A = H_{app} + \frac{2A}{M_s} q^2 + 2\pi M_s qd \cos^2 \phi_0$ in ω_{res} arising from dipolar interactions. We note that the dipolar corrections are not small. For a 10 nm-thick Ni film with $M_s=485 \text{ emu/cm}^3$, a SAW pump frequency of 3.86 GHz and a corresponding $q = 6.95 \times 10^4 \text{ cm}^{-1}$, the factor $2\pi M_s qd = 212 \text{ Oe}$. The dipolar interactions thus can add a substantial internal magnetic field and produce an additional angular dependence in the magnetic response. When an in-plane anisotropy field is included, $\phi_0 \neq \phi_H$ in general and the (ϕ_H, H_{app}) dependence of the absorption gains some additional features. We will discuss these features more fully while comparing this formulation with our experimental data in Section 4.7.

4.5 Sample Growth and Fabrication

All of our samples were grown on .5 mm thick Y-Z cut LiNbO₃ wafers procured from MTI Corp. All wafers were single-side polished as surface roughness on the wafer backside will ensure that bulk waves destructively interfere (as IDTs do not just excite SAWs but a whole variety of BAWs as well). The wafers have flats which are perpendicular to the crystal Z direction for ease of IDT receiver and transmitter alignment along the z-axis. All of our film growth was done in the Kurt Lesker 6 gun sputter system with a base pressure $P_0 < 4 \times 10^{-9}$ torr. All metallic films (except the SAW metallization) were sputtered at 50 W, $P_{\text{Argon}} = 2 \text{ mtorr}$. The Al deposited for SAW metallization was sputtered at 100 W, $P_{\text{Argon}} = 2 \text{ mtorr}$. The first step in the process involved defining Al(10)|AlO_x(2)|Ni(10)|Pt(15) mesas and micron wide wires

by lift-off. Then we deposit Al(100 nm) for SAW IDT metallization and define the IDTs by lift-off. All our SAW IDTs used for our delay lines have $N = 40$ fingers. We designed IDTs with $f_0 = 300$ MHz and $m = 0.4$, $f_0 = 150$ MHz and $m = 0.5$ and $f_0 = 400$ MHz and $m = 0.5$. All of our S_{21} transmission measurements and V_{ISHE} measurements that we present in this chapter come from $60 \mu\text{m} \times 500 \mu\text{m}$ wires. The fabrication process flow is detailed in Table 4.2.

Spin Resist Bilayer	<ul style="list-style-type: none"> -Spin LOR3A @ 3000 RPM for 60 secs -Bake 115 C for 1 min, 20 sec on chill block -Spin S1813 @ 2000 RPM for 60 secs -Bake 115 C for 1 min, 20 sec on chill block
2. SAW FMR Photolith #1	<ul style="list-style-type: none"> - Use Mask Level #1: SAW_FMR Mesas/Wires - Make sure stepper mode is on transparent. -Exposure Time ~ .5 secs - Hamatech Develop for 60 secs in MIF 721.
Stack Deposition + Liftoff : Kurt Lesker 6-Gun Sputter System	<ul style="list-style-type: none"> - Deposit Al(12 nm) and transfer back to load-lock for oxidation. Native oxide ~ 1 - 2 nm - Transfer sample back into main chamber, lift magnet and deposit Ni(10 nm)/Pt(10) [or Ni(10 nm)/Cu(15) for ISHE control sample.] -Liftoff: PG Remover for 2 hours @ 70 C in hotplate, Ultrasonicate for 5 mins. Transfer to IPA bath and ultrasonicate for 10 mins. N₂ blow dry.
SAW FMR Photolith #2: 5X Stepper	<ul style="list-style-type: none"> Define IDT Delay Line Metallization. -Use either Mask Level #2: IDT Delay Line with $m = 0.4$ or $m = 0.5$. - Make sure stepper mode is on transparent.

	-Exposure Time ~ .5 secs (optimize focus test) - Hamatech Develop for 60 secs in MIF 726.
SAW Metallization/Lead Definition: Kurt Lesker 6-Gun Sputter System	-Deposit Al(100 nm). - Liftoff: PG Remover for 2 hours @ 65 C in hotplate, Ultrasonicate for 5 mins. Transfer to IPA bath and ultrasonicate for 10 mins. N ₂ blow dry.

Table 4.2 SAW IDT and Ni|Pt mesa/microwire fabrication process flow.

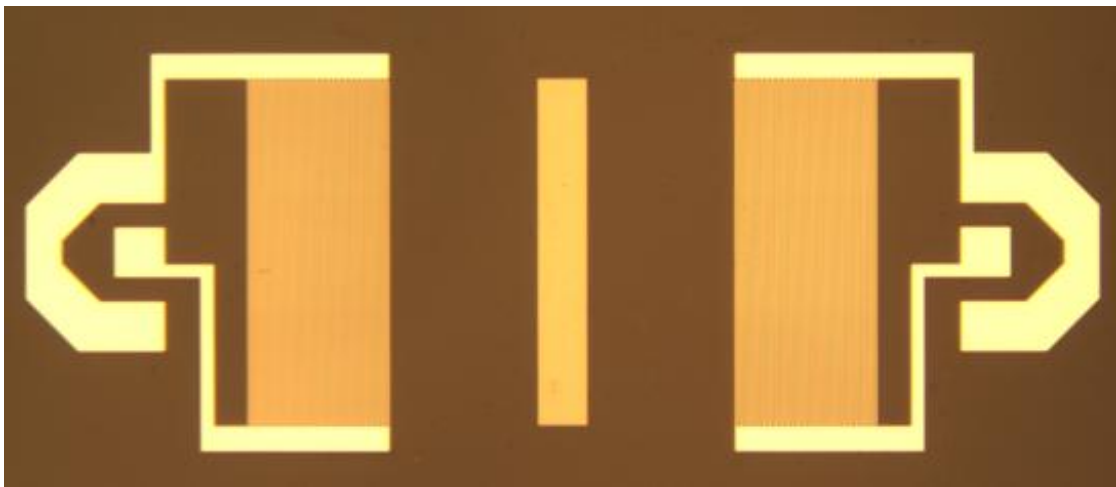


Figure 4.5 Completed Al(10)/AlO_x(2)/Ni(10)/Pt(15) microwire with Al(100 nm) SAW IDT transmitter and receiver.

4.6 Measurement Setup

Our measurements were conducted on a probe station setup equipped with a GMW Projected Field Magnet. The Projected Field station enabled us to change the in-plane angle of the magnetic field. We used an Agilent 8722ES Vector Network Analyzer

(VNA) to perform the transmission measurements on our SAW IDT Delay lines. Contact was made to the IDT transmitter and receiver with RF probes. S_{21} transmission measurements were first conducted on the SAW delay line as a function of frequency in order to characterize the bandpasses of the SAW. We performed a time-gated measurement of the transmission in order to reject signals associated with interference from triple-transit SAW reflections between the receiver and emitter as well any interference from electromagnetic waves generated by the transmitter. Time-gating, in our case, involves finding the maximum in S_{21} associated with the single-transit time of the SAW. We set where this maximum occurs to be our center time for our gating window and set the window width so it rejects the transmission peaks associated with triple transit. The 8722ES VNA has an in-built time domain gating option where one can view the time-domain response, fix the time window and center time and then automatically apply the windowing to the swept frequency domain measurements. We set the gate center to $\sim 0.2 \mu\text{s}$ corresponding to our single transit signal. The gate span was set to $\sim 0.1 \mu\text{s}$. The S_{21} spectrum for a SAW with an IDT pitch of $11.6 \mu\text{m}$, $N = 40$ fingers, and a metallization ratio $m = 0.5$ is shown in Figure 4.6, with and without the time-domain gating. The delay line shows sharp SAW bandpasses at $f_0, 5f_0, 7f_0, 9f_0, 11f_0$, etc. We suspect that the reason our experimental S_{21} bandpasses do not match the SAW spectrum for $m = 0.5$ (Figure 4.3) is that the higher order bandpasses are very sensitive to the metallization ratio. Deviations of the electrode width from its expected value due to overexposure in the photolithography might account for a different effective metallization ratio. We have also included the time-gated S_{21} spectrum for a SAW delay line with $f_0 = 300 \text{ MHz}$, $m = 0.4$, and an

IDT pitch of $5.8 \mu\text{m}$ (Figure 4.7). All our subsequent magnetoelastic resonance measurements use a SAW delay line with this set of specifications. The gate center time for the spectrum in Figure 4.7 was set at $\sim 0.2 \mu\text{s}$ and we used a span of $0.05 \mu\text{s}$.

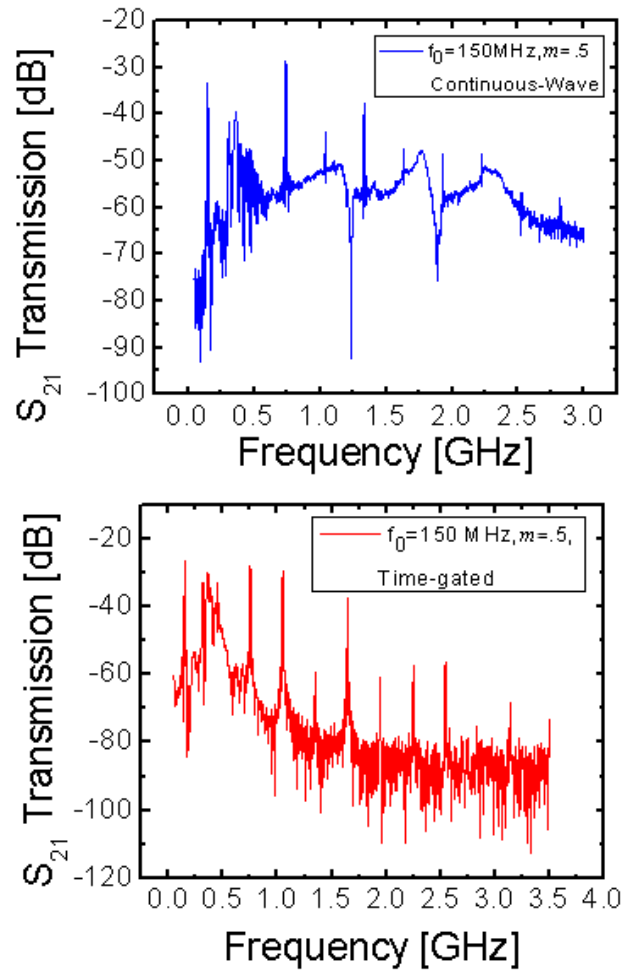


Figure 4.6 Continuous wave and time-gated S_{21} measurement of a SAW delay line with $f_0 = 150 \text{ MHz}$ and an IDT metallization ratio $m = 0.5$.

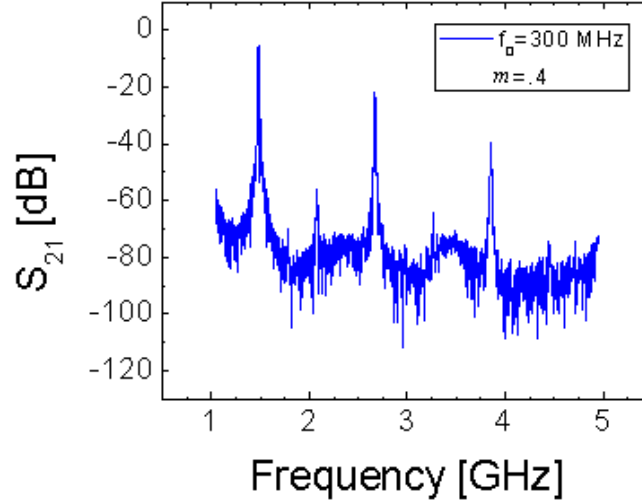


Figure 4.7 Time gated spectrum for a $f_0 = 300$ MHz SAW delay line with $m = 0.4$. We have plotted the bandpasses at $f = 1.48$ GHz, 2.08 GHz, 2.67 GHz, 3.26 GHz, 3.86 GHz, and 4.45 GHz.

Our measurement of DC voltages arising from spin pumping/ISHE due to magnetoelastic resonance was measured by two DC needle probes placed directly (and very gently) on either side of the Al|AlO_x(2)|Ni(10)|Pt(15) micro-wire. The voltage was measured directly with a Keithley 2000 Multimeter. In order to get an appreciable signal during our V_{ISHE} measurements, we hooked up two Picosecond Pulse Lab Model 5867 amplifiers to amplify the output of the 8722ES (which has a max power output at +5 dBm) and thus increase the input power into the SAW delay line.

4.7 Magnetoelastic Resonance Measurements

We measured the SAW delay line transmission and ISHE voltage of the Al|AlO_x|Ni|Pt microwires as a function of applied field H_{app} and in-plane field angle at different bandpasses of the SAW. When the field and angle configuration meets the resonance configuration for the given SAW pump frequency, we expect that there is absorption of the surface acoustic wave and simultaneously a voltage associated with the ISHE from spin pumping into the Pt induced by the resonant dynamics of the Ni. The SAW absorption is measured through the quantity $|S_{21}^{loss}| = |S_{21}(H, \alpha_H)| - |S_{21}(H = 0, \alpha_H)|$. When $H_{app} = 0$ we are far in (H_{app}, φ_H) -space from any magnetic resonance and the loss is determined by changes in the transmission line impedance due to mass-loading and capacitive coupling to the magnetic metallic film. We show SAW absorption data as a function of field and field angle (defined as the azimuthal angle with respect to the SAW propagation direction $+\hat{\eta}$) for a SAW transmitter/receiver of $f_0 = 300$ MHz and metallization ratio of 0.4.

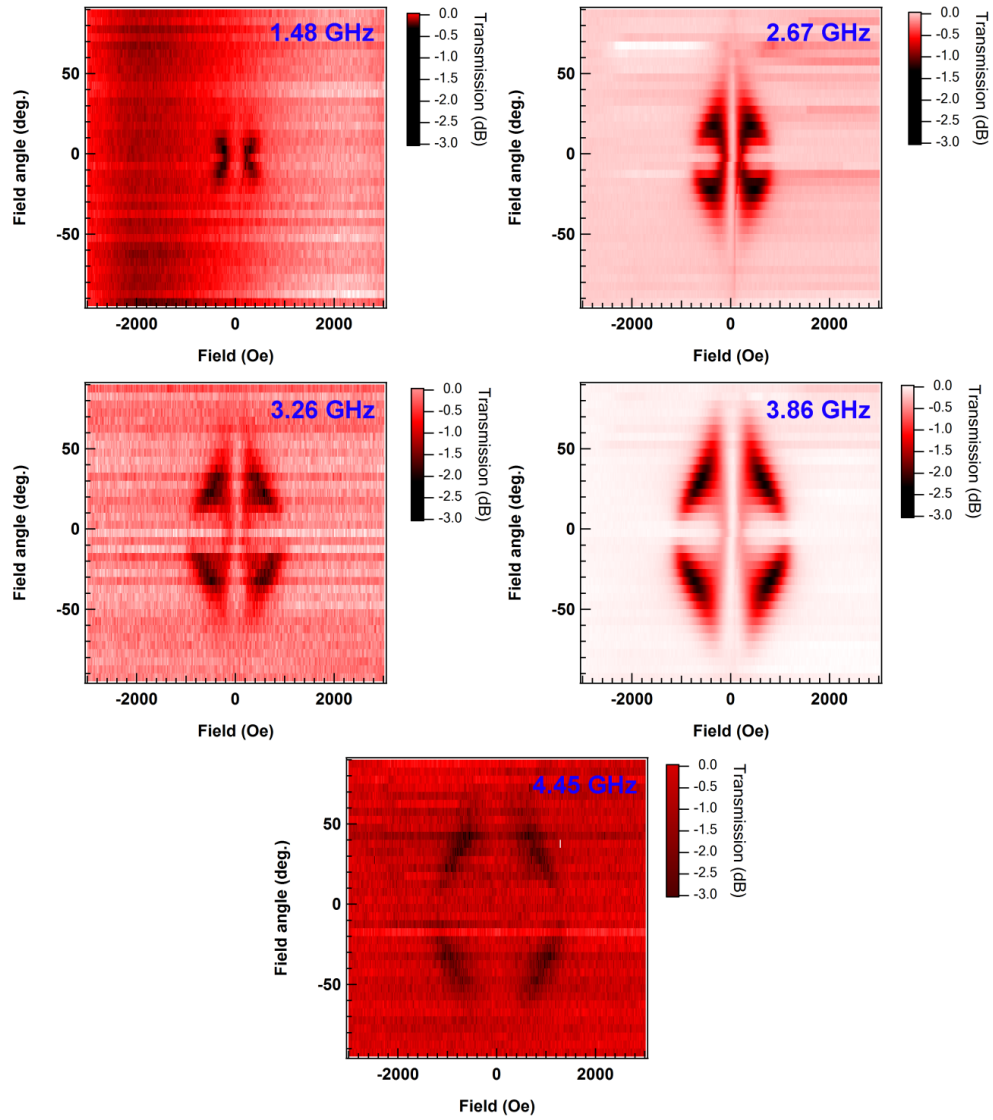


Figure 4.8 VNA $|S_{21}|$ SAW absorption measurement at the center frequency of the bandpasses of a $f_0=300$ MHz SAW delay line with $m = 0.4$.

The S_{21} measurements show SAW absorption lobes that we infer are associated with magnetoelastic resonance. We conclude this from several observations. First, the absorption lobes move to higher field as the SAW pump frequency increases. At high pump frequencies ($f_0 = 4.45$ GHz), the absorption lobes start to approach a four-fold

angular symmetry that is consistent with a resonant excitation from a magnetoelastic tickle field. At lower pump frequencies, the absorption is evidently not four-fold symmetric in the field angle but possesses a lower symmetry that is mirror symmetric about the η axis. For example, the absorption lobes for 1.46 GHz extend to a field angle of $<10^\circ$. For $f_{\text{SAW}} = 2.67$ GHz, the maximum absorption lobes occur at $\sim 20^\circ$. When $f_{\text{SAW}} = 3.86$ GHz the maximum absorption occurs along $\sim 35^\circ$. The fact that the maximum absorption lobes occur at a field angle less than 45° and that this angle increases with pump frequency can be largely explained by the existence of strong in-plane anisotropy in the Ni film.

We conducted AMR measurements of the magnetization along the SAW wave-vector direction and perpendicular to it. The AMR curves show a hard axis AMR curve when the field is swept along the η axis. By mapping the AMR curve to an m-H loop and then integrating we extract an in-plane anisotropy $H_k \sim 380$ Oe with the easy axis along the ζ -axis orthogonal to η -axis. We can rule out any deposition-field effects due to the fact that the Lesker magnet was lifted away from the substrate platen during the deposition such that the growth field on the sample was negligible. It is likely that our huge in-plane H_k come from substantial anisotropic residual strain in the Ni film. Assuming in-plane isotropy of the magnetoelastic coupling due to the polycrystallinity of the Ni film, we assume that the uniaxial magnetoelastic coupling of our 10 nm-thick Ni film is $B_{\text{eff}} = +6 \times 10^7$ ergs/cm³ [9]. Using the relation

$$H_k = \frac{2B_{\text{eff}} (\epsilon_{\eta\eta} - \epsilon_{\zeta\zeta})}{M_s}$$

and a measured $M_s \sim 485$ emu/cm³ we estimate an in-plane

anisotropic strain ($\varepsilon_{\eta\eta} - \varepsilon_{\zeta\zeta}$) $\sim 0.15\%$. The stress must be tensile along the η direction and compressive along the ζ direction thus yielding an easy axis along the ζ direction. Such anisotropic strain is possible due to the fact that the LiNbO₃ lattice constants along the η and ζ direction are very different – with $c = 13.86$ Å in the η direction and $a = 5.15$ Å in the ζ direction.

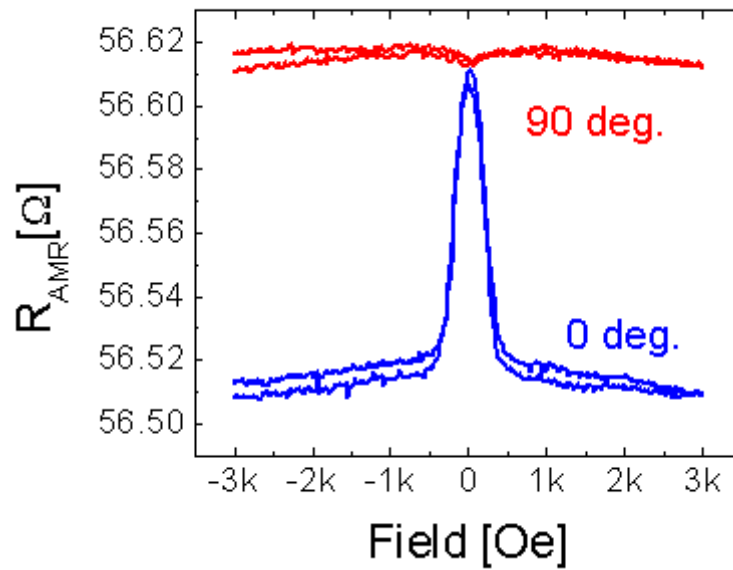


Figure 4.9 AMR resistance curves for 0° (blue) and 90° (red) field angle with respect to the SAW propagation direction show that the Ni has a substantial in-plane anisotropy field H_k with 90° (i.e. the ζ axis) being the easy axis direction.

The very large in-plane H_k means that the equilibrium magnetization angle ϕ_0 is not collinear with ϕ_H . Note that ϕ_H from the calculations is the azimuthal angle with respect to the ζ axis while the field angle in our density plots is with respect to the η axis. Thus the field angle in our density plots is equal to $90^\circ - \phi_H$. With a large H_k , a

sweep along $\phi_H = \pi / 2$ (or 0° in our plot) implies that when H_{app} is in a field region about $\sim H_k / \sqrt{2}$ ϕ_0 is about 45° , and the magnetoelastic tickle field is appreciable. The resonant frequency $\omega_{res}(H)$ also becomes smaller with increasing applied field until $H = H_k$. Thus both the condition for a large tickle field and resonance frequency can be met for lower frequency pumps when the field is swept at or close to the hard axis direction and only for field strengths lower than or on the order of H_k . As the SAW pump frequencies become higher the possibility of absorption in this field and angle regime disappears and one expects the resonance lobes to move to higher applied fields and larger field angles off the hard axis. The angular condition for maximum absorption at very high SAW pump frequency should approach $\phi_H = 45^\circ$.

We can now try to see if the Damon-Eschbach spin wave theory that we introduced in Section 4.4 fits well to the SAW absorption measurements in Figure 4.8. We have used the independently measured values of $M_s = 485 \text{ emu/cm}^3$, $H_k = 380 \text{ Oe}$, and $M_{eff} \sim 115 \text{ emu/cm}^3$ to generate our absorption density plots. We have measured M_{eff} where $M_{eff} = M_s - \frac{H_k^\perp}{4\pi}$ by conducting an out-of-plane field scan on a Ni(10)/Pt(15) bilayer with a buffer layer of Al(10)/AlO_x(2) deposited on our LiNbO₃ substrate.

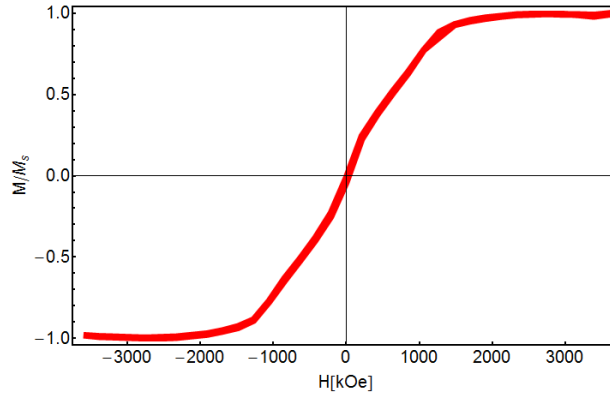


Figure 4.10 Out-of-plane field scan of Al(10)/AlO_x(2)/Ni(10)/Pt(15) bilayer on YZ-cut LiNbO₃.

The M_{eff} we have measured is quite low and implies that the Ni film has a perpendicular anisotropy of 1.13×10^6 ergs/cm³ opposing but not enough to completely overcome the demagnetization energy. We believe that this perpendicular anisotropy is due to magnetoelastic interactions and the existence of a sizeable residual strain in the film. Large in-plane strains, particularly in a low M_s magnetoelastic material such as Ni can lead to substantial contributions to the perpendicular anisotropy field and thereby substantially reduce M_{eff} . With all the quantities that we have measured, the only free parameter left is the spin-wave damping. We set it to $\Gamma = .14$ as this provides a reasonable fit to the data. We have used the same value regardless of pump frequency. We plot the results of the spin-wave absorption [Equation (4.29)] as a function of field angle and H_{app} .

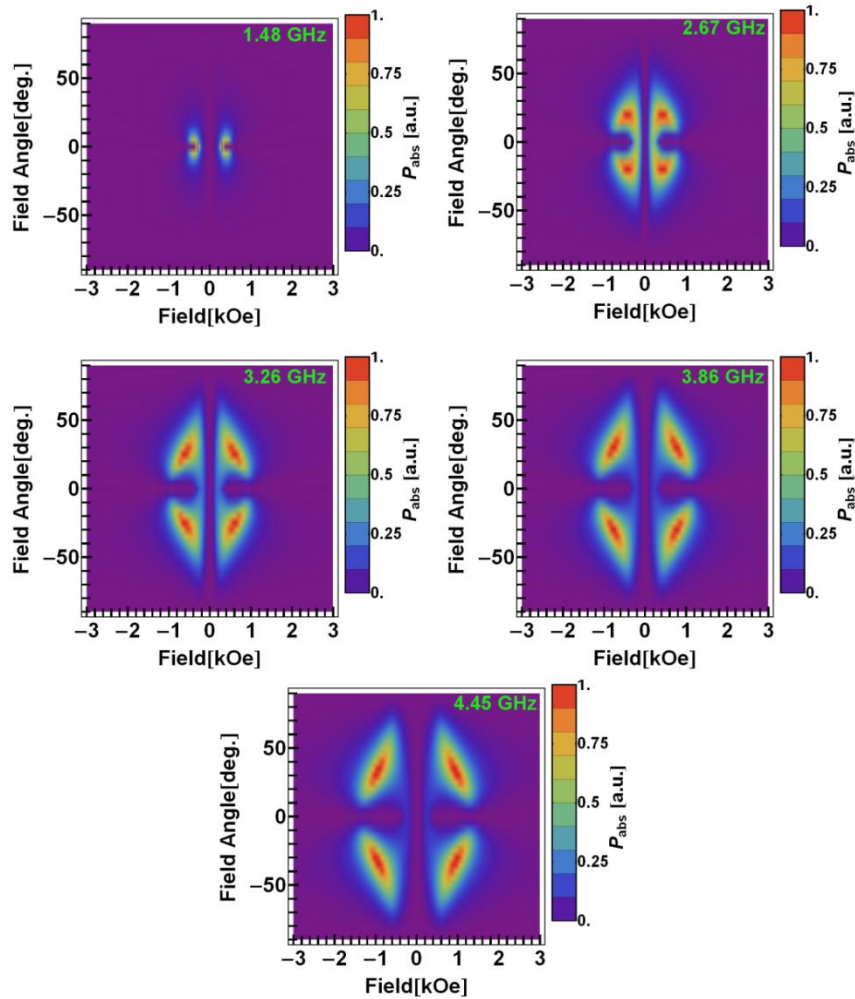


Figure 4.11 Calculations of the field strength and field angle dependence of SAW power resonantly absorbed by a ferromagnetic film through the magnetoelastic interaction using the Damon-Eschbach theory.

These absorption plots when compared with Figure 4.8 shows rather close qualitative and quantitative agreement with the S_{21} absorption data. Next we convert the S_{21} loss to linear power and rescale each S_{21} vs H curve to lie between -1 and 0. We plot field sweeps at various field angles and at a few of the SAW pump frequencies to explicitly show the good quantitative agreement between the

calculations including magnetostatic spin-wave contributions and the data. For each plot we have also shown the results of a simple exchange wave theory.

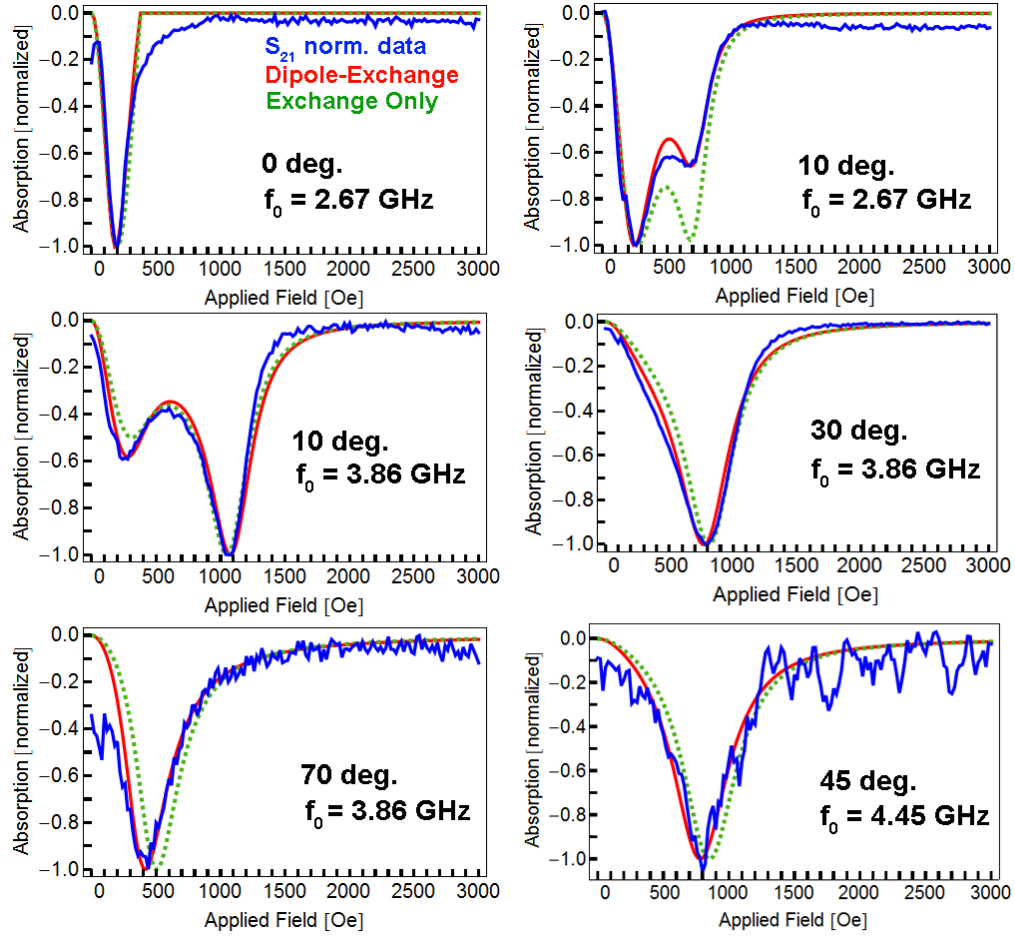


Figure 4.12 Calculations of the absorbed power for dipole-exchange and exchangespin-wave resonance compared to S₂₁ data. The field is swept at a different field angle with respect to the SAW propagation direction and different SAW pump frequencies are examined. Deviations at low-field for high angle sweeps are likely due to domain wall dynamics and non-uniform switching.

We stress that the absorption maxima in a given field angle line cut does not generally occur at the Damon-Eschbach resonance field. This is largely due to the fact that the pump field itself is sensitive to the equilibrium angle ϕ_0 . As the field is swept

(in any direction except for the easy axis) the equilibrium angle ϕ_0 changes and thus there may be portions of the curve where the pump field amplitude is considerably larger than other parts. The absorption peaks will occur where the product of the imaginary part of the susceptibility and the pump amplitude are maximized. At certain field angles this can lead to double absorption peaks as there may be one field where the influence of the pump dominates and another where the susceptibility dominates the absorption. This was a major source of confusion for us in our initial attempts to fit the absorption peak frequencies to spin wave resonance frequencies. We plot the peak absorption fields for the SAW at different pump frequencies for a field angle of 45 degrees off the η -axis (Figure 4.13). The spectrum for the pump frequencies plotted has a single absorption peak and we compare the peak absorption field to the results of our calculations with and without spin-wave dipolar contributions included.

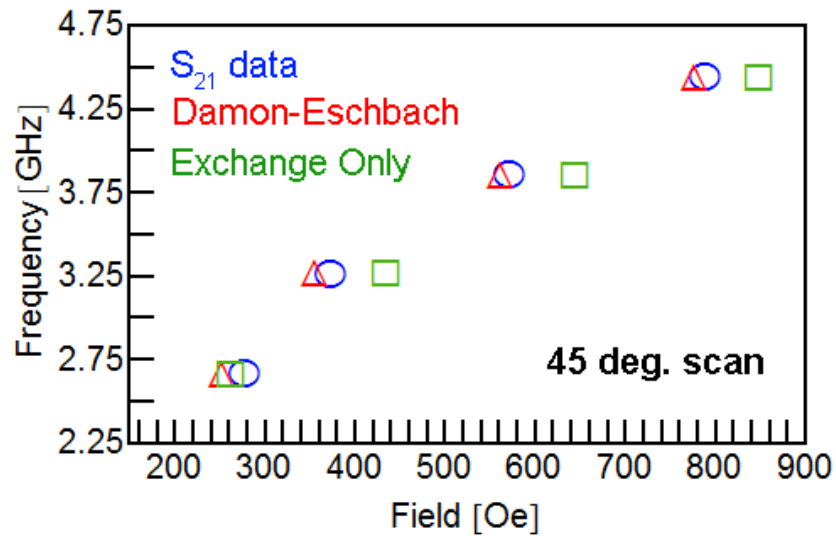


Figure 4.13 Pump frequency vs. applied field magnitude at which maximum absorption occurs at a field angle of 45 degrees off the η -axis.

The line cuts of Figure 4.12 and the pump frequency vs. peak absorption field plot of Figure 4.13 clearly demonstrate that the dipolar spin-wave corrections are important in the angular and field dependence of the absorption. They both show that the corrections from dipolar spin-wave theory are important at higher wave-vectors (or SAW pump frequencies) which makes a good deal of sense. In addition, it seems that the discrepancy between a pure exchange vs. a dipolar theory is often larger at higher field angles with respect to the SAW propagation direction. This corresponds to when the equilibrium angle ϕ_0 gets closer to the ζ axis and where we expect dipolar corrections to be the strongest. The corrections can also be very strong for field sweeps at shallow field angle (i.e. close to the hard axis) and at certain pump frequencies where the absorption peak can correspond to a situation where ϕ_0 is small and the magnetization is not too far from the easy axis. We expect this scenario to occur typically at higher pump frequencies. Such a situation is seen in the lower-field peak of the 10 degree field sweep at $f_0 = 3.855$ GHz (in Figure 4.12) where the discrepancy between the dipolar theory and exchange theory is large. The higher field absorption peak is virtually identical for both cases and corresponds to a scenario where the magnetization is rather close to the hard axis.

We can alternatively visualize the effects of the dipolar interactions on the absorption by plotting the difference of the normalized absorption maps for $f_0 = 3.855$ GHz with and without dipolar interactions included.

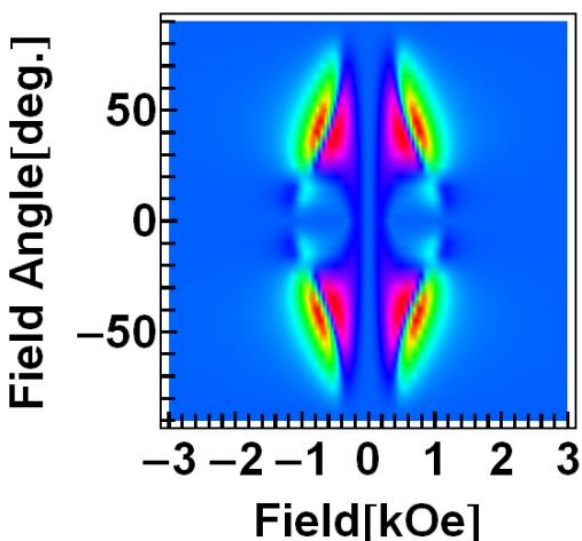


Figure 4.14 Difference map $P_{\text{abs}}[\text{with dipolar correction}] - P_{\text{abs}}[\text{without dipolar correction}]$ of calculated absorption spectrum at 3.86 GHz. Purple is positive and red is negative in the difference map.

Clearly, there is a difference in the predicted absorption spectra for the case where we include dipolar interactions as opposed to when we neglect them.

These corrections become much more substantial in high M_s ferromagnet systems like Co, Fe, and alloys thereof. To illustrate our point we calculate the absorption in a Co(10)|Pt system where $M_s = 1420 \text{ emu/cm}^3$, and where we assume that there is no in-plane anisotropy and no surface anisotropy opposing the out-of-plane demagnetization energy. We take the spin-wave damping $\Gamma = .03$. We have plotted the absorption with and without dynamic magnetostatic corrections. The differences in the fields at which resonant absorption occurs and the field angular dependence are rather striking (Figure 4.15).

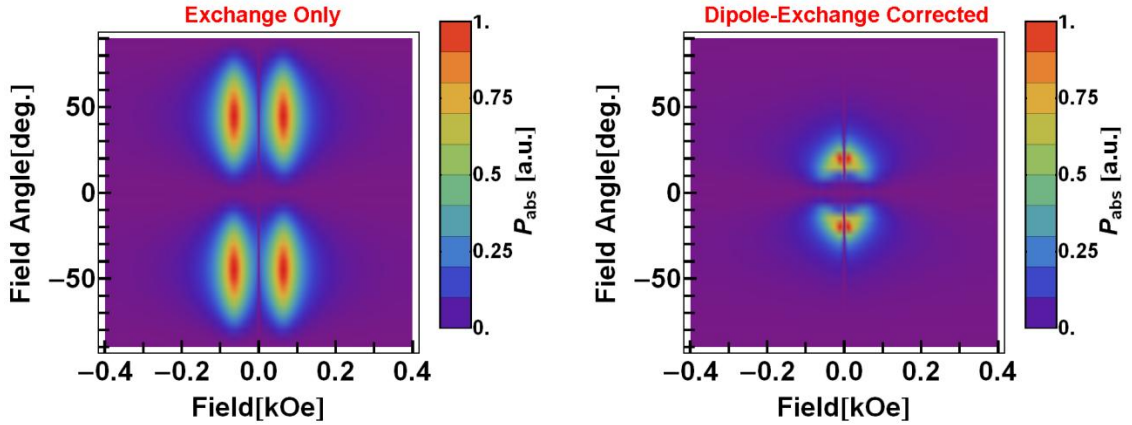


Figure 4.15 Power absorption for SAW-induced resonance for Co ($M_s = 1420$ emu/cm³) with $d = 10$ nm, $H_k = 0$ Oe, $f_{\text{SAW}} = 3$ GHz with and without the dynamic dipolar field correction arising from the spin wave.

The strong change in the angular dependence comes from the anisotropic dipolar field contribution associated with the Damon-Eschbach wave. This magnetostatic spin wave interaction not only radically alters the fields but also the field angles at which maximal absorption of the SAW occurs. The relative importance of the dipolar contribution of course will depend on the SAW wave-vector and pump-frequency as well as the thickness of the ferromagnetic film. For example, if one uses a SAW pump frequency of 1 GHz the angular dependence coming from dipolar corrections becomes much less noticeable. It is fairly clear, however, that SAW-induced spin wave resonance fundamentally derives its absorption properties from the angular dependence of the pump field *and* dipolar interactions arising from the spatial dependence of the spin-wave.

4.8 Resonance Quantification using the Inverse Spin Hall Effect

The dipolar spin wave in the Ni film will also pump a spin current into the Pt layer and then generate an ISHE voltage. Recent papers [2], [10] have proposed SAW driven-magnetic excitations as a way to create phonon-driven spin batteries or as a way to study the Spin Seebeck effect (which has been proposed to arise from nonequilibrium thermal phonon-magnon interactions [11]). In the former case, we see no obvious advantage over other spin-current generation techniques. In the latter case, any spin-thermal effect is broad-band and is likely dominated by acoustic phonons where the D.O.S. and occupation number are appreciable. This occurs in the 10-20 THz frequency range. In this higher frequency regime, we expect that the SAW is not a good description of the physics and we expect that thermal phonons from all three acoustic phonon branches will contribute to magnon generation. Incidentally, the time-scales involved (less than .1 ps) are on the order of electronic relaxation times and so an accurate quantification of these finite life-times with respect to the magnetization precession time should be taken into account.

Our goal here is a bit more modest. The ISHE voltage can be used to extract certain quantities associated with the spin wave resonance. Among these are the spin-wave cone angle and the effective RF pump field created by the magnetoelastic interaction. The effective RF field h_{rf} is relatively easy to extract by a spin-pumping + ISHE measurement. Combined with S_{11} reflection measurements, which give us knowledge of the acoustical power flow and associated strain wave amplitudes, we

can extract the in-plane magnetoelastic constant B_{eff} . The equations governing the spin current pumped into the Pt by the dipolar spin wave in the Ni can be written as:

$$j_s^0 \hat{s} = \frac{g_{r,\text{eff}}^{\uparrow\downarrow}}{4\pi} \left[-\frac{dm_y}{dt} \hat{x} + \frac{dm_x}{dt} \hat{y} + \left(m_x \frac{dm_y}{dt} - m_y \frac{dm_x}{dt} \right) \hat{z} \right] \quad (4.30)$$

We will be interested in any non-zero DC component of the spin-current that is pumped into the Pt layer. This will only occur for the component of the spin current along the magnetization direction (the \hat{z} direction). The transverse parts which are oscillatory can and have been measured but they contribute nothing to a DC spin current in the Pt.

Thus we write the DC spin current as:

$$j_s^0 \hat{z} = \frac{\hbar}{4\pi} g_{r,\text{eff}}^{\uparrow\downarrow} \left(m_x \frac{dm_y}{dt} - m_y \frac{dm_x}{dt} \right) \hat{z} \quad (4.31)$$

The value of m_x and m_y need to be solved for in terms of h_{rf} . We have already solved this problem by having an expression for dynamic susceptibility tensor χ .

Explicit expressions for the complex amplitudes m_x and m_y are given in terms of h_{rf} .

$$\begin{aligned}
\tilde{m}_x &= \left[\frac{\left\{ \left[AB - \left(\frac{\omega}{\gamma} \right)^2 \right] B + \left(\frac{\Gamma \omega}{\gamma} \right)^2 (A+B) \right\} + i \left\{ \frac{\Gamma \omega}{\gamma} \left(B^2 + \left(\frac{\omega}{\gamma} \right)^2 \right) \right\}}{\left(AB - \left(\frac{\omega}{\gamma} \right)^2 \right)^2 + \left(\frac{\Gamma \omega (A+B)}{\gamma} \right)^2} \right] \tilde{h}_{rf} \\
\tilde{m}_y &= \left[\frac{\left\{ -\Gamma \left(\frac{\omega}{\gamma} \right)^2 (A+B) \right\} + i \left\{ \frac{\omega}{\gamma} \left(AB - \left(\frac{\omega}{\gamma} \right)^2 \right) \right\}}{\left(AB - \left(\frac{\omega}{\gamma} \right)^2 \right)^2 + \left(\frac{\Gamma \omega (A+B)}{\gamma} \right)^2} \right] \tilde{h}_{rf}
\end{aligned} \tag{4.32}$$

For simplicity we regroup these rather long expressions in the coefficients so that the equations look a little simpler:

$$\begin{aligned}
\tilde{m}_x &= (C + iD) \tilde{h}_{rf} \\
\tilde{m}_y &= (F + iG) \tilde{h}_{rf}
\end{aligned} \tag{4.33}$$

The expressions for the coefficients C, D, F, and G are given:

$$\begin{aligned}
C &= \frac{\left[AB - \left(\frac{\omega}{\gamma} \right)^2 \right] B + \left(\frac{\Gamma \omega}{\gamma} \right)^2 (A+B)}{\left[AB - \left(\frac{\omega}{\gamma} \right)^2 \right]^2 + \left(\frac{\Gamma \omega (A+B)}{\gamma} \right)^2} \\
D &= \frac{\frac{\omega \Gamma}{\gamma} \left(B^2 + \left(\frac{\omega}{\gamma} \right)^2 \right)}{\left[AB - \left(\frac{\omega}{\gamma} \right)^2 \right]^2 + \left(\frac{\Gamma \omega (A+B)}{\gamma} \right)^2} \\
F &= \frac{-\Gamma \left(\frac{\omega}{\gamma} \right)^2 (A+B)}{\left[AB - \left(\frac{\omega}{\gamma} \right)^2 \right]^2 + \left(\frac{\Gamma \omega (A+B)}{\gamma} \right)^2} \\
G &= \frac{\frac{\omega}{\gamma} \left(AB - \left(\frac{\omega}{\gamma} \right)^2 \right)}{\left[AB - \left(\frac{\omega}{\gamma} \right)^2 \right]^2 + \left(\frac{\Gamma \omega (A+B)}{\gamma} \right)^2}
\end{aligned} \tag{4.34}$$

With the phase of m_x and m_y reference with respect to the oscillating traveling wave pump field $h_{rf}(\vec{r}, t) = h_{rf}^x \cos(\vec{q} \cdot \vec{r} - \omega t)$, the expression for real components of the magnetization precession are:

$$\begin{aligned}
\delta m_x(\vec{r}, t) &= Ch_{rf}^x \cos(\vec{q} \cdot \vec{r} - \omega t) - Dh_{rf}^x \sin(\vec{q} \cdot \vec{r} - \omega t) \\
\delta m_y(\vec{r}, t) &= Fh_{rf}^x \cos(\vec{q} \cdot \vec{r} - \omega t) - Gh_{rf}^x \sin(\vec{q} \cdot \vec{r} - \omega t)
\end{aligned} \tag{4.35}$$

The expression for the z-component of the instantaneous pumped spin current becomes exceptionally simple and is purely DC:

$$\begin{aligned}
j_s^0 \hat{z} &= \frac{\hbar \omega}{4\pi} g_{r,eff}^{\uparrow\downarrow} (-FD + GC) h_{rf}^2 \hat{z} \\
&= \frac{\hbar \omega}{4\pi} g_{r,eff}^{\uparrow\downarrow} \left(\frac{B(\omega/\gamma)}{\left[AB - \left(\frac{\omega}{\gamma} \right)^2 \right]^2 + \left[\frac{\Gamma \omega (A+B)}{\gamma} \right]^2} \right) h_{rf}^2 \hat{z}
\end{aligned} \tag{4.36}$$

This spin current is pumped into the platinum and generates an electric field by the ISHE. We are concerned with the electric field component in the ζ direction (i.e. the long axis of the wire orthogonal to the SAW power flow).

$$E_\zeta = \frac{\left(\frac{2e}{\hbar} \right) j_{s,dc}^0 \lambda_{SD}^{Pt} \tanh \left(\frac{d_{Pt}}{2\lambda_{SD}^{Pt}} \right)}{\sigma_{Ni} d_{Ni} + \sigma_{Pt} d_{Pt}} \sin \phi_0 \tag{4.37}$$

The expression is a solution to the drift-diffusion equations in the limit that the backflow is negligible and where the shorting effect that the Ni film has on the ISHE generated E-field in the Pt is taken into account [12]. The voltage at the terminals of our micro-wire can then be written as:

$$V_{ISHE} = \frac{-e\theta_{SH} \lambda_{SD}^{Pt} \tanh \left(\frac{d_{Pt}}{2\lambda_{SD}^{Pt}} \right) \omega L}{2\pi(\sigma_{Ni} d_{Ni} + \sigma_{Pt} d_{Pt})} \sin \phi_0 \times g_{r,eff}^{\uparrow\downarrow} \left(\frac{B(\omega/\gamma)}{\left[AB - \left(\frac{\omega}{\gamma} \right)^2 \right]^2 + \left[\frac{\Gamma \omega (A+B)}{\gamma} \right]^2} \right) h_{rf}^2 \tag{4.38}$$

Equation (4.38) for V_{ISHE} with the expressions for A and B evaluated in Equation (4.26) provides the correct quantitative connection between V_{ISHE} and h_{rf} in

the limit that $qd \ll 1$. With H_k , M_{eff} , M_s , and the equilibrium angle ϕ_0 at a specific H_{app} and ϕ_H all known, one can extract h_{rf} (at a specific angle ϕ_0) from the measured V_{ISHE} exactly once one knows the Pt spin hall angle θ_{SH}^{Pt} , the film conductivities σ_{Ni} and σ_{Pt} , and the real part of the spin-mixing conductance at the Ni|Pt interface.

Before going further, however, we need to first confirm that the voltages are dominated by the ISHE associated with pumped spin current during SAW-driven resonance and not due to signals arising from AMR rectification effects or AMR/ST-FMR effects. AMR and ST-FMR effects would occur if the potential wave of the SAW dumped a large RF current into the Ni and the Pt by capacitive coupling. If the resulting DC voltage signal, on resonance, is large enough it will produce a significant distortion of the line-shape of the DC voltage with respect to applied field away from that expected by a pure spin-pumping/ISHE signal induced by the magnetoelastic interaction. We have taken DC voltage data for the entire (ϕ_H, H_{app}) space in Figure 4.16. The angular and field dependence, as expected, is quite similar to that of the VNA S_{21} absorption measurements.

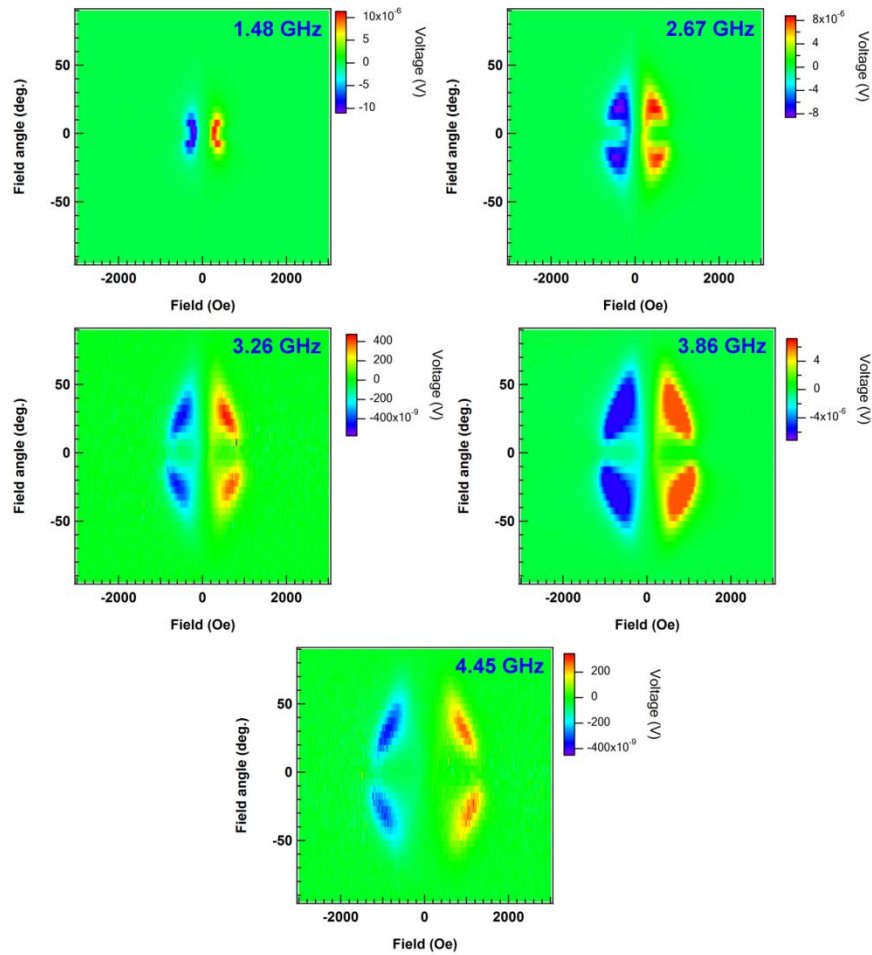


Figure 4.16 Measurement of V_{ISHE} voltage vs. field and angle. The lobes in the V_{ISHE} at each frequency correspond to the absorption lobes in the S_{21} transmission measurement. This confirms that the absorption lobes of the SAW are due to magnetoelastic resonance which drives the magnetization into precession and pumps a pure spin current into the Pt.

We can check for significant AMR contributions by checking whether normalized V_{dc} vs H_{app} curves from field sweeps at fixed angle (i.e. line cuts of the 2D data in Figure 4.17) match the line-shape of our expression for spin-pumping/ISHE in Equation (4.38). As can be seen in Figure 4.17, the line-shape of our V_{dc} vs H_{app}

curves closely follows that predicted from spin pumping + ISHE arising from a dipolar surface spin wave.

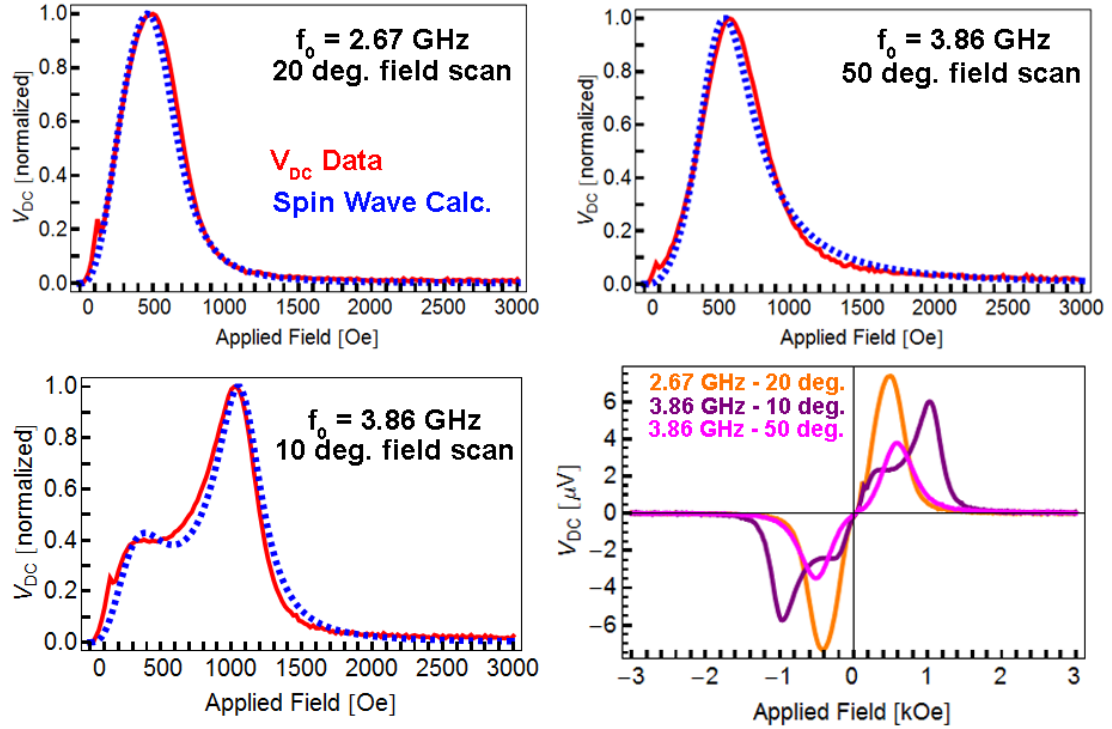


Figure 4.17 Normalized V_{DC} curves plotted against the results of our spin wave calculation from Equation (4.38) at a few frequencies and field angles. The last plot shows the the V_{DC} vs. H_{app} data for these sweeps without normalization. Data for $f_0 = 2.67$ GHz taken was taken at a VNA input power of +16 dBm. For $f_0 = 3.86$ GHz, the data was taken at an RF VNA input power of +24 dBm.

There are small deviations of our calculated V_{ISHE} line-shape from the data which could be due to a small AMR/ST-FMR contribution but it could just as well be from experimental error in our input parameters (M_s , H_k , M_{eff}). Whatever the case, it is pretty clear that the spin-pumping/ISHE voltage process from magnetoelastic pumping dominates the DC voltage signal. The lack of a significant AMR contribution to the

linewidth is probably due to the fact that most of the RF current is shunted through the Al (10 nm) and Pt (15 nm). The thin AlO_x layer will effectively act as a capacitive short in the GHz frequency range. We should, of course, have to also worry about shorting out of the DC ISHE electric field by the Al. However, the 2 nm AlO_x layer should prevent this from occurring in DC.

We can thus assume that the DC charge voltage is captured by Equation (4.38).

We use previously extracted parameters $H_k = 380$ Oe, $M_s = 485$ emu/cm³, $M_{\text{eff}} = 115$ emu/cm³, and an assumed spin-wave damping $\Gamma = .14$. For the transport parameters, we have not independently extracted the spin hall angle and the spin diffusion length of Pt in our Ni|Pt bilayers on LiNbO₃. We therefore assume an upper

bound $\theta_{SH}^{Pt} = .12$, $\lambda_s^{Pt} = 1.4$ nm [13],

$g_{r,\text{eff}}^{\uparrow\downarrow} = 2 \cdot 10^{19} m^{-2}$ [14], $\sigma_{Ni} = 3.4 \times 10^6 (\Omega m)^{-1}$ and $\sigma_{Pt} \sim 4.2 \times 10^6 (\Omega m)^{-1}$. The

conductivities have been extracted by four-point measurements. The length of our micro-wire is $L = 500 \mu m$. We calculate the r.f. field amplitude at the V_{ISHE} peak for a SAW pump frequency of 3.86 GHz with the DC field swept at a field angle of 50 degrees off the η axis. This corresponds to the magenta curve in Figure 4.17. The peak occurs at $H_{\text{app}} = 582$ Oe at a $V_{\text{DC}} = 3.7 \mu V$. The equilibrium magnetization angle at this field is $\phi_0 = 25.4$ degrees. We calculate the rf field at the input RF pump power of +24 dBm (= 250 mW). The rf field strength that we extract with the assumed parameters turns out to be large at $h_{rf} = 12$ Oe (although much smaller than any other

field in the problem). The product $B\varepsilon_{\eta\eta}$ can be determined by $h_{rf} = \frac{2B}{M_s} \sin \phi_0 \cos \phi_0$

and so $B\varepsilon_{\eta\eta} = 7.51 \times 10^3$ ergs/cm³. We can extract the magnetoelastic coupling if we know the longitudinal strain wave amplitude $|\varepsilon_{\eta\eta}|$. For our 3.86 GHz bandpass we have measured $|S_{11}^{rest}|^2 - |S_{11}^{rest+SAW}|^2 \sim 5.8 \times 10^{-3}$ (in linear scale). Plugging this into Equation (4.13) with our input RF power of 250 mW and the parameters for our SAW electrodes and the material characteristics of LiNbO₃, we get a strain wave amplitude $|\varepsilon_{\eta\eta}| = 9.3 \times 10^{-5}$. We can then extract the in-plane magnetoelastic coupling $B_{\text{eff}} = 8.1 \times 10^7$ ergs/cm³. We assumed a $B_{\text{eff}} = 6 \times 10^7$ ergs/cm³ in Section 4.7 to extract values for the residual strain in the film. Thus our B_{eff} extracted by the SAW resonance/spin-pumping method is in the same ball park as our assumed values which were adopted from the literature. As a side note, we admit that we prefer the method of extracting the magnetoelastic coupling employed in the previous chapter. We can also solve for the maximum in-plane and out-of-plane angle during the precession. The in-plane angle $\delta\phi \sim \delta m_x$ and its maximum amplitude is given by $\delta\phi_{\text{max}} = \sqrt{C^2 + D^2} h_{rf}$. The out-of-plane angle goes as $\delta\theta_{\text{max}} = \sqrt{F^2 + G^2} h_{rf}$. Plugging in all the necessary parameters for C, D, F, and G and an $h_{rf} = 12$ Oe, we extract $\delta\phi_{\text{max}} = 2.1^\circ$ and $\delta\theta_{\text{max}} = 1.2^\circ$. This procedure can be applied at any arbitrary field angle, field value, and pump amplitude to extract out the characteristics of the SAW induced magnetostatic spin-wave excitation and the effective internal r.f. field that is generated by the SAW.

We note that we have not characterized the contribution of inhomogeneous broadening to the line-shape. This can produce some error in our spin-wave amplitude and RF field quantification. We do not believe that this error is too large as the phenomenological spin-wave damping parameter $\Gamma = .14$ provides a reasonably close match to the data across a fairly large SAW pump frequency range ($\sim 1.5 - 4.5$ GHz) and at many different field angles. It is also possible that Γ changes as a function of the pump wave-vector and frequency and in a way that is dependent on the in-plane angle. This would alter the extracted amplitudes as well. However, we believe that our estimates here for various numbers for the SAW-induced spin-wave excitation are reasonable and that the analytical method we have used to extract these parameters constitutes the correct physical description of the problem.

4.9 Conclusion

We have quantified and understood the structure of spin-waves excited by SAWs. Now the main question is: Why should we care? SAWs provide a way of exciting magnetization dynamics with nano-to-micron scale spatial control in a way that no other pump can (at least that we are aware of). The SAW pump *enforces* the wave-vector of the magnetic excitation. In a frequency range commensurate with FMR excitations ranging from 2 - 12 GHz, SAW wavelengths (depending on choice of substrate and orientation) are on the order of a few microns down to ~ 150 nm. With a low SAW velocity, the wavelength at a fixed frequency can be pushed down. (001)-cut $\text{Bi}_{12}\text{GeO}_{20}$ (BGO20) with propagation along (110) has a SAW velocity of 1681 m/s. [15], [16] This implies a SAW wavelength of ~ 150 nm at a frequency of 11 GHz.

The piezoelectric coupling coefficient is also reasonably high at $k^2 = .46\%$. A 1.2 GHz fundamental SAW with an electrode pitch of 700 nm (implying a finger width/gap of 350 nm at $\eta = .5$) operating at the 9th overtone bandpass can achieve such a wavelength at FMR frequencies. The IDT electrode gaps and finger width requirements can be readily achieved by deep-UV photolithography. There are also a whole host of other slow SAW wave materials which could be used including Ti_3VS_4 , Ti_3TaSe_4 , GaPO_4 , and $\text{La}_3\text{Ga}_5\text{SiO}_{14}$. [16], [17] Of these others we find 001-cut Ti_3VS_4 to be extremely attractive (although less easily procured than BGO20) as SAWs propagating along (110) have a $k^2 = 1.4\%$ and a SAW velocity of 870 m/s. At a frequency of 9 GHz the SAW wavelength on Ti_3VS_4 is 97 nm.

Ultrasonic excitation of ferromagnets on these low SAW speed materials can lead to a whole host of interesting new ways to probe and control magnetization dynamics. One could imagine making SAW Bragg resonators with standing wave acoustic modes between two reflectors. Nanoscale magnets placed at particular positions in this resonator will experience fields of different spatial symmetries. A 50x150 nm ellipse placed at an acoustical node in a BGO20 SAW Bragg resonator operating at a wavelength of 150 nm will experience an effective RF pump field that is spatially antisymmetric along the major axis of the ellipse (with respect to the magnet center). A nanomagnet placed at a maximum of the standing strain wave pattern will experience an RF pump field of even spatial symmetry. One can pump modes of different spatial symmetry by selecting frequency and nanomagnet position in the Bragg cavity. This could prove very useful for accessing various magnetic

normal modes of a nanomagnet [18] in ways that might be hard to access by spatially uniform field pumping.

It would also be interesting to see what happens in a nanomagnet driven into steady state oscillation by the spin-transfer torque. One can have two modes of different spatial symmetry exhibiting bistability that are excited by the spin-torque. The existence of such a scenario has been inferred from a combination of experimental measurements and micromagnetic simulations. In-plane free layer oscillations in elliptical multilayer structures can exhibit bistability between micromagnetic edge modes (odd spatial symmetry) and quasi-uniform/leaf micromagnetic modes or localized center modes (even spatial symmetry) [19]. One could pump into one of the modes with the SAW, then turn the SAW off and look at the decay/telegraph hopping and energy transfer into the other mode. In this way one could back out mode coupling strength. In a hypothetical case where the mode frequencies get very close to each other, the SAW pump excitation could (in a way that RF current injection-locking could not) allow one to injection lock to one of the modes by spatial symmetry alone.

Even more can be potentially accomplished with SAW or coherent phonon based magnetic resonance excitations. SAW wave diffraction from double slits can be used to pump at diffraction maxima on a magnetic nanowire that is some distance from the slits. SAW-beam collimation could lead to pump fields with resolution on the order of <100 nm focused on a spot in a magnetic nanowire. The point is that Fourier optics of slow ultrasonic excitations in the GHz frequency range could be used to generate non-trivial spatial pump patterns, highly localized excitations, etc. These in

turn could be used to study novel spin-wave physics and potentially even excitations of topological spin textures such as vortices and skyrmions both in extended and confined structures. We do not however claim that this endeavor is trivial. While a lot of time and thinking has been spent on the time-domain and frequency-domain response of SAWs, we can safely say that there is a lot of room for research in tailoring the spatial profile of SAWs on piezoelectric anisotropic substrates by acoustical optics. Thus we believe that the development of SAWs and coherent ultrasonic waves for spatially resolved magnetic excitations could potentially lead to interesting research both in SAW physics/engineering and in the fundamentals of magnetization dynamics.

\

REFERENCES

- [1] M. Weiler, L. Dreher, C. Heeg, H. Huebl, R. Gross, M. S. Brandt, and S. T. B. Goennenwein, “Elastically Driven Ferromagnetic Resonance in Nickel Thin Films,” *Phys. Rev. Lett.*, vol. 106, no. 11, p. 117601, Mar. 2011.
- [2] M. Weiler, H. Huebl, F. S. Goerg, F. D. Czeschka, R. Gross, and S. T. B. Goennenwein, “Spin Pumping with Coherent Elastic Waves,” *Phys. Rev. Lett.*, vol. 108, no. 17, p. 176601, Apr. 2012.
- [3] L. Thevenard, C. Gourdon, J. Y. Prieur, H. J. von Bardeleben, S. Vincent, L. Becerra, L. Largeau, and J.-Y. Duquesne, “Surface-acoustic-wave-driven ferromagnetic resonance in (Ga,Mn)(As,P) epilayers,” *Phys. Rev. B*, vol. 90, no. 9, p. 094401, Sep. 2014.
- [4] L. Dreher, M. Weiler, M. Pernpeintner, H. Huebl, R. Gross, M. S. Brandt, and S. T. B. Goennenwein, “Surface acoustic wave driven ferromagnetic resonance in nickel thin films: Theory and experiment,” *Phys. Rev. B*, vol. 86, no. 13, p. 134415, Oct. 2012.
- [5] L. D. Landau and E. M. Lifshitz, *Theory of Elasticity*. London: Pergamon Press Ltd., 1959.
- [6] S. Datta, *Surface Acoustic Wave Devices*, no. 001. University of Michigan: Prentice Hall, 1986.
- [7] C. K. Campbell, *Surface Acoustic Wave Devices for Mobile and Wireless Communications*, vol. I. Academic Press, Inc., 1998.
- [8] R. L. Stamps and B. Hillebrands, “Dipolar interactions and the magnetic behavior of two-dimensional ferromagnetic systems,” *Phys. Rev. B*, vol. 44, no. 22, pp. 417–423, 1991.
- [9] O. Song, C. A. Ballentine, and R. C. O’Handley, “Giant surface magnetostriction in polycrystalline Ni and NiFe films,” *Appl. Phys. Lett.*, vol. 64, no. 19, p. 2593, 1994.

- [10] K. Uchida, H. Adachi, T. An, T. Ota, M. Toda, B. Hillebrands, S. Maekawa, and E. Saitoh, "Long-range spin Seebeck effect and acoustic spin pumping," *Nat. Mater.*, vol. 10, no. 10, pp. 737–41, Oct. 2011.
- [11] J. Xiao, G. E. W. Bauer, K. Uchida, E. Saitoh, and S. Maekawa, "Theory of magnon-driven spin Seebeck effect," *Phys. Rev. B*, vol. 81, no. 21, p. 214418, Jun. 2010.
- [12] H. Jiao and G. E. W. Bauer, "Spin Backflow and ac Voltage Generation by Spin Pumping and the Inverse Spin Hall Effect," *Phys. Rev. Lett.*, vol. 110, no. 21, p. 217602, May 2013.
- [13] L. Liu, T. Moriyama, D. C. Ralph, and R. A. Buhrman, "Spin-Torque Ferromagnetic Resonance Induced by the Spin Hall Effect," *Phys. Rev. Lett.*, vol. 106, no. 3, p. 036601, Jan. 2011.
- [14] F. D. Czeschka, L. Dreher, M. S. Brandt, M. Weiler, M. Althammer, I.-M. Imort, G. Reiss, A. Thomas, W. Schoch, W. Limmer, H. Huebl, R. Gross, and S. T. B. Goennenwein, "Scaling Behavior of the Spin Pumping Effect in Ferromagnet-Platinum Bilayers," *Phys. Rev. Lett.*, vol. 107, no. 4, p. 046601, Jul. 2011.
- [15] A. J. Slobodnik, "Surface Acoustic Waves and SAW Materials," *Proc. IEEE*, vol. 64, no. 5, 1976.
- [16] R. M. O'Connell and P. H. Carr, "New Materials for Surface Acoustic Wave," *Opt. Eng.*, vol. 16, no. 5, p. 440, 1977.
- [17] T. J. Issacs, M. Gottlieb, M. R. Daniel, and J. D. Feichtner, "Ti3VS4 as an Acousto-Optic and Surface Wave Material," *J. Electron. Mater.*, vol. 4, no. 1, pp. 67–75, 1975.
- [18] R. D. McMichael and M. D. Stiles, "Magnetic normal modes of nanoelements," *J. Appl. Phys.*, vol. 97, no. 10, p. 10J901, 2005.
- [19] I. Krivorotov, D. Berkov, N. Gorn, N. Emley, J. Sankey, D. Ralph, and R. Buhrman, "Large-amplitude coherent spin waves excited by spin-polarized current in nanoscale spin valves," *Phys. Rev. B*, vol. 76, no. 2, p. 024418, Jul. 2007.

CHAPTER 5

MODELING OF STRAIN-INDUCED REVERSAL DYNAMICS IN GIANT MAGNETOSTRICTIVE NANOMAGNETS

5.1 Introduction/Motivation

In recent years pure electric-field based control of magnetization has become a subject of very active research. It has been demonstrated and studied in a variety of systems ranging from multiferroic single phase materials, gated dilute ferromagnetic semiconductors [1]–[3], ultra-thin metallic ferromagnet/oxide interfaces [4]–[10] and piezoelectric/magnetoelastic composites [11]–[15]. Beyond the goal of establishing a understanding of the physics involved in each of these systems, this work has been strongly motivated by the fact that electrical-field based manipulation of magnetization could form the basis for a new generation of ultra-low power, non-volatile memories. Electric-field based magnetic devices are not necessarily limited by Ohmic losses during the write cycle (as can be the case in current based memories such as spin-torque magnetic random access memory (ST-MRAM) but rather by the capacitive charging/discharging energies incurred per write cycle. As the capacitance of these devices scale with area the write energies have the potential to be as low as 1 aJ per write cycle or less.

One general approach to the electrical control of magnetism utilizes a magnetostrictive magnet/piezoelectric transducer hybrid as the active component of a nanoscale memory element. In this approach a mechanical strain is generated by an electric field within the piezoelectric substrate or film and is then transferred to a thin,

nanoscale magnetostrictive magnet that is formed on top of the piezoelectric. The physical interaction driving the write cycle of these devices is the magnetoelastic interaction which describes the coupling between strain in a magnetic body and the magnetic anisotropy energy. The strain imposed upon the magnet creates an internal effective magnetic field via the magnetoelastic interaction that can exert a direct torque on the magnetization. If successfully implemented this torque can switch the magnet from one stable configuration to another, but whether imposed stresses and strains can be used to switch a magnetic element between two bi-stable states will depend on the strength of the magnetoelastic coupling (or the magnetostriction). Typical values of the magnetostriction ($\lambda_s = 0.5\text{-}60$ ppm) in most ferromagnets yield strain and stress scales that make the process of strain-induced switching inefficient or impossible. However, considerable advances have been made in synthesizing materials both in bulk and in thin film form that have magnetostrictions that are one to two orders of magnitude larger than standard transition metal ferromagnets. These giant magnetostrictive materials allow the efficient conversion of strains into torque on the magnetization. However it is important to note that a large magnetostrictive (or magnetoelastic) effect tends to also translate into very large magnetic damping by virtue of the high coupling between magnons and the phonon thermal bath, which has important implications, both positive and negative, for piezoelectric based magnetic devices.

In this chapter we provide an analysis of the switching modes of several different implementations of piezoelectric/magnetostrictive devices. We discuss how

the high damping that is generally associated with giant magnetoelasticity affects the feasibility of different approaches, and we also take other key material properties into consideration, including the saturation magnetization of the magnetostrictive element, and the form and magnitude of its magnetic anisotropy. This work excludes device concepts and physics circumscribed by magneto-elastic manipulation of domain walls in magnetic films, wires, and nanoparticle arrays [11], [12], [16]. Instead we focus on analyzing various magnetoelastic reversal modes, principally within the single domain approximation, but we do extend this work to micromagnetic modeling in cases where it is not clear that the macrospin approximation provides a fully successful description of the essential physics. We enumerate potential material candidates for each of the modes evaluated and discuss the various challenges inherent in constructing reliable memory cells based on each of the reversal modes that we consider.

5.2 Toggle Mode Switching

Stress pulsing of a magnetoelastic element can be used to construct a toggle mode memory. The toggling mechanism between two stable states relies on transient dynamics of the magnetization that are initiated by an abrupt change in the anisotropy energy that is of fixed and short duration. This change in the anisotropy is created by the stress pulse and under the right conditions can generate precessional dynamics about a new effective field. This effective field can take the magnetization on a path such that when the pulse is turned off the magnetization will relax to the other stable state. This type of switching mode is referred to as toggle switching because the same sign of the stress pulse will take the magnetization from one state to the other

irrespective of the initial state. We can divide the consideration of the toggle switching modes into two cases; one that utilizes a high M_s in-plane magnetized element, and the other that employs perpendicular magnetic anisotropy (PMA) materials with a lower M_s . We make this distinction largely because of differences in the structure of the torques and stress fields required to induce a switch in these two classes of systems. The switching of in-plane giant magnetostrictive nanomagnets with sizeable out-of-plane demagnetization fields relies on the use of in-plane uniaxial stress-induced effective fields that overcome the in-plane anisotropy ($\sim O(10^2 \text{Oe})$). The moment will experience a torque canting the moment out of plane and causing precession about the large demagnetization field. Thus the precessional time scales for toggling between stable in-plane states will be largely determined by the demagnetization field (and thus M_s). The dynamics of this mode bears striking resemblance to the dynamics in hard-axis field pulse switching of Py nanomagnets [17]. On the other hand, the dominant energy scale in PMA giant magnetostrictive materials is the perpendicular anisotropy energy. This energy scale can vary substantially (anywhere from $K_u \sim 10^5\text{-}10^7$ ergs/cm³) depending on the materials utilized and the details of their growth. The anisotropy energy scale in these materials can be tuned into a region where stress-induced anisotropy energies can be comparable to it. A biaxial stress-induced anisotropy energy, in this geometry, can induce switching by cancelling and/or overcoming the perpendicular anisotropy energy. As we shall see, this fact and the low M_s of these systems imply dynamical time scales that are substantially different from the case where in-plane magnetized materials are employed.

5.2.1 In-Plane Magnetized Magnetostrictive Materials

We first treat the macrospin switching dynamics of an in-plane magnetized magnetostrictive nanomagnet with uniaxial anisotropy under a simple rectangular uniaxial stress pulse. Giant magnetostriction in in-plane magnetized systems have been demonstrated for sputtered polycrystalline $Tb_{.3}Dy_{.7}Fe_2$ (Terfenol-D) [18], and more recently in quenched Co_xFe_{1-x} thin film systems [19]. We assume that the uniaxial anisotropy is defined completely by the shape anisotropy of the elliptical element and that any magneto-crystalline anisotropy in the film is considerably weaker. This is a reasonable assumption for the materials considered here in the limit where the grain size is considerably smaller than the nanomagnet's dimensions. The stress field is applied by voltage pulsing an anisotropic piezoelectric film that is in contact with the nanomagnet. The proper choice of the film orientation of a piezoelectric material such as $\langle 110 \rangle$ Lead Magnesium Niobate-Lead Titanate (PMN-PT) can ensure that an effective uniaxial in-plane strain develops along a particular crystalline axis after poling the piezo in the z -direction. We assume that the nanomagnet major axis lies along such a crystalline direction (the $\langle 110 \rangle$ -direction of PMN-PT) so that the shape anisotropy is coincident with the strain axis. For the analysis below we use material values appropriate to sputtered, nanocrystalline $Tb_{.3}Dy_{.7}Fe_2$ [18] ($M_s=600$ emu/cm³, $\lambda_s= 670$ ppm is the saturation magnetostriction). Nanocrystalline $Tb_{.3}Dy_{.7}Fe_2$ films, with a mean crystalline grain diameter $d_{\text{grain}} < 10$ nm, can have an extremely high magnetostriction while being relatively magnetically soft with coercive fields, $H_c \sim 50-100$ Oe, results which can be achieved by thermal processing during sputter

growth at $T \sim 375$ C [20]. The nanomagnet dimensions were assumed to be 80 nm (minor axis) x 135 nm (major axis) x 5 nm (thickness) yielding a shape anisotropy field $H_k = 4\pi(N_y - N_x)M_s = 323$ Oe and $H_{demag} = 4\pi(N_z - N_y)M_s = 5.97$ kOe. We use demagnetization factors that are correct for an elliptical cylinder [21].

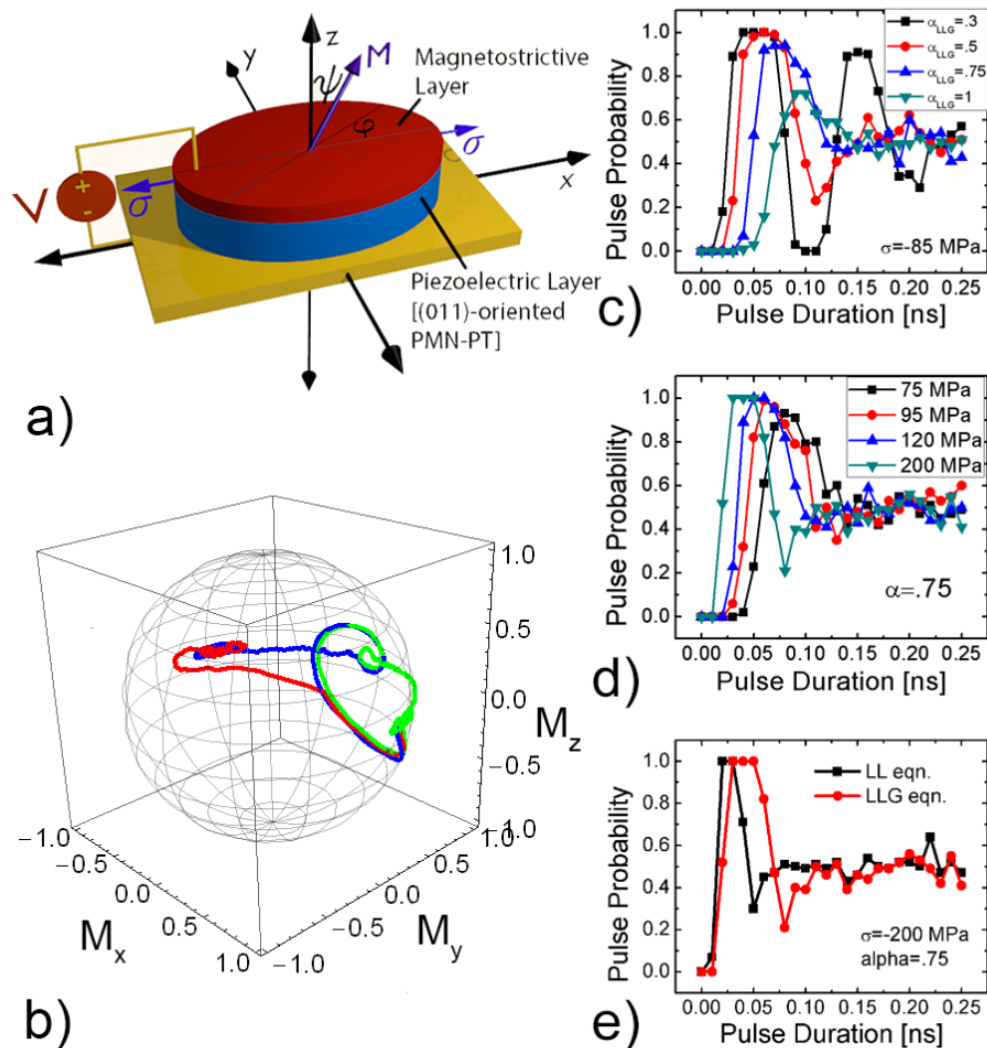


Figure 5.1 a) Magnetoelastic elliptical memory element schematic with associated coordinate system. b) Toggle switching trajectory for an in-plane magnetized

polycrystalline $\text{Tb}_{0.3}\text{Dy}_{0.7}\text{Fe}_2$ element with $\alpha_{\text{LLG}} = 0.3$, $\sigma = -120$ MPa, and $\tau_p = 50$ ps (red) and 125 ps (blue) and 160 ps (green). c) Effect of the Gilbert damping on pulse switching probability statistics for $\sigma = -85$ MPa. d) Effect of increasing stress pulse amplitude for high damping $\alpha_{\text{LLG}} = 0.75$. Very high stress pulses (>200 MPa) required to allow precession to be fast enough to cause a switch before dynamics are damped out. e) Comparison of switching statistics for the LL and LLG dynamics at $\sigma = -200$ MPa, $\alpha = 0.75$. The LL dynamics exhibits faster precession than the LLG for a given torque implying shorter windows of reliability and requirements for faster pulses.

The value of the Gilbert damping parameter α for the magnetostrictive element is quite important in determining its dynamical behavior during in-plane stress-induced toggle switching. Previous simulation results [22]–[24] used a value ($\alpha = 0.1$ for Terfenol-D) that, at least arguably, is considerably lower than is reasonable since that value was extracted from spin pumping in a Ni (2 nm) / Dy (5 nm) bilayer [25]. However, that bilayer material is not a good surrogate for a rare-earth transition-metal alloy (especially for $L \neq 0$ rare earth ions). In the latter case the loss contribution from direct magnon to short wavelength phonon conversion is important, as has been directly confirmed by studies of $L \neq 0$ rare earth ion doping into transition metals [26], [27]. For example in-plane magnetized nanocrystalline 10% Tb-doped Py shows $\alpha \sim 0.8$ when magnetron sputtered at 5 mtorr Ar pressure, even though the magnetostriction is small within this region of Tb doping [27]. We contend that a substantial increase in the magnetoelastic interaction in alloys with higher Tb content is likely to make α even larger. Magnetization rotation in a highly magnetostrictive magnet will efficiently generate longer wavelength acoustic phonons as well and heat

loss will be generated when these phonons thermalize. Unfortunately, measurements of the magnetic damping parameter in polycrystalline $\text{Tb}_{.3}\text{Dy}_{.7}\text{Fe}_2$ do not appear to be available in the literature. However, some results on the amorphous $\text{Tb}_x[\text{FeCo}]_{1-x}$ system, achieved by using recent ultra-fast demagnetization techniques, have extracted $\alpha \sim 0.5$ for compositions ($x \sim .3$) that have high magnetostriction [28]. We can also estimate the scale for the Gilbert damping by using a formalism that only takes into account the effect that magnetoelasticity has on the damping [29]. The damping can be estimated by the following formula:

$$\alpha = \frac{36\rho\gamma}{M_s\tau} \lambda_s^2 \left(\frac{1}{\left(\frac{c_T M}{2\gamma A}\right)^2} + \frac{1}{\left(\frac{c_L M}{2\gamma A}\right)^2} \right) \quad (5.1)$$

Using $M_s=600 \text{ emu/cm}^3$, the exchange stiffness $A=.7 \times 10^{-6} \text{ erg/cm}$, a mass density $\rho = 8.5 \text{ g/cm}^3$, Young's modulus of 65 GPa [30], Poisson ratio $\nu = .3$, and an acoustic damping time $\tau = 0.18 \text{ ps}$ [29] the result is an estimate of $\alpha \sim 1$. Given the uncertainties in the Gilbert damping parameter, we examine the magnetization dynamics for values of α ranging from 0.3 to 1.0.

We simulate the switching dynamics of the magnetic moment of a Terfenol-D nanomagnet at $T=300 \text{ K}$ using the Landau-Lifshitz-Gilbert form of the equation describing the precession of a magnetic moment \vec{m} :

$$\frac{d\vec{m}}{dt} = -\gamma_{\text{eff}} \vec{m} \times \vec{H}_{\text{eff}}(t) - \gamma_{\text{eff}} \vec{m} \times \vec{H}_{\text{Langevin}}(t) + \alpha \vec{m} \times \frac{d\vec{m}}{dt} \quad (5.2)$$

where γ_{eff} is the gyromagnetic ratio. As $Tb_{.3}Dy_{.7}Fe_2$ is a rare earth – transition metal (RE-TM) ferrimagnet (or more accurately a speromagnet), the gyromagnetic ratio cannot simply be assumed to be the free electron value. Instead we use the value $\gamma_{eff} = 1.78 \times 10^7$ Hz/Oe as extracted from a spin wave resonance study in the $TbFe_2$ system [31] which appears appropriate since Dy and Tb are similar in magnetic moment/atom ($10 \mu_B$ and $9 \mu_B$ respectively) and g factor ($\sim 4/3$ and $\sim 3/2$ respectively).

The first term in Equation (5.2) represents the torque on the magnetization from any applied fields, the effective stress field, and any anisotropy and demagnetization fields that might be present. The third term in the LLG represents the damping torque that acts to relax the magnetization towards the direction of the effective field and hence damp out precessional dynamics. The second term is the Gaussian-distributed Langevin field that takes into account the effect thermal fluctuations on the magnetization dynamics. From the fluctuation-dissipation theorem,

$$H_{Langevin}^{RMS} = \sqrt{\frac{2\alpha k_B T}{\gamma_{eff} M_s V \Delta t}}$$

where Δt is the simulation time-step [32]. Thermal

fluctuations are also accounted for in our modeling by assuming that the equilibrium azimuthal and polar starting angles (φ_0 and $\psi_0 = \pi/2$ respectively) have a random mean fluctuation given by equipartition

$$\text{as } \varphi_0^{RMS} = \sqrt{\frac{k_B T}{\left. \frac{\partial^2 E}{\partial \varphi^2} \right|_{\varphi_0} V}} \text{ and } \delta\psi_0^{RMS} = \sqrt{\frac{k_B T}{4\pi(N_z - N_y)M_s^2 V}} .$$

A H_{bias} of 100 Oe was used

for our simulations which creates two stable energy minima

at $\varphi_0 = \arcsin\left(\frac{H_{bias}}{H_k}\right) \sim 18^\circ$ and $\varphi_1 = 162^\circ$ symmetric about $\varphi = \pi/2$. This non-zero starting angle ensures that $\delta\varphi_0^{RMS} \ll \varphi_0$. This field bias is essential as the initial torque from a stress pulse depends on the initial starting angle. This angular dependence generates much larger thermally-induced fluctuations in the initial torque than a hard-axis field pulse. The hard axis bias field also reduces the energy barrier between the two stable states. For $H_{bias}=100$ Oe the energy barrier between the two states is $E_b=1.22$ eV yielding a room temperature $\Delta = E_b / k_B T = 49$. This ensures the long term thermal stability required for a magnetic memory.

To incorporate the effect of a stress pulse in Equation (5.2) we employ a free energy form for the effective field, $\vec{H}_{eff}(t) \equiv -\partial E / \partial \vec{m}$ that expresses the effect of a stress pulse along the x-direction of our in-plane nanomagnet with a uniaxial shape anisotropy in the x-direction. The stress enters the energy as an effective in-plane anisotropy term that adds to the shape anisotropy of the magnet (first term in Equation (5.3) below). The sign convention here is such that $\sigma > 0$ implies a tensile stress on the x-axis while $\sigma < 0$ implies a compressive strain. We also include the possibility of a bias field applied along the hard axis in the final term in Equation (5.3).

$$\begin{aligned}
E(m_x, m_y, m_z) = & -[2\pi(N_y - N_x)M_s^2 + \frac{3}{2}\lambda_s\sigma(t)]m_x^2 \\
& + 2\pi(N_z - N_y)M_s^2 m_z^2 - H_{bias}M_s m_y
\end{aligned} \tag{5.3}$$

The geometry that we have assumed allows only for fast compressive-stress pulse based toggle mode switching. The application of a DC compressive stress along

the x-axis only reduces the magnitude of the anisotropy and changes the position of the equilibrium magnetic angles φ_0 and $\varphi_1 = 180^\circ - \varphi_0$ while keeping the potential wells associated with these states symmetric as well. Adiabatically increasing the value of the compressive stress moves the angles toward $\varphi = \pi / 2$ until $\frac{3}{2} \lambda_s \sigma(t) \geq K_u$ but obviously can never induce a magnetic switch.

Thus the magnetoelastic memory in this geometry must make use of the transient behavior of the magnetization under a stress pulse as opposed to relying on quasistatic changes to the energy landscape. A compressive stress pulse where

$\frac{3}{2} \lambda_s \sigma(t) \gg K_u$ creates a sudden change in the effective field. The resultant effective

field $\vec{H}_{eff} = \left[\frac{3\lambda_s |\sigma| - 2K_u}{M_s} m_y + H_{bias} \right] \hat{y}$ points in the y-direction and causes a torque

that brings the magnetization out of plane. At this point the magnetization rotates rapidly about the very large perpendicular demagnetization

field $H_{demag}^\perp = -4\pi M_s m_z \hat{z}$ and if the pulse is turned off at the right time will relax down

to the opposite state at $\varphi_1 = 163$. Such a switching trajectory for our simulated

nanomagnet is shown in the red curve in Figure 5.1b. This mode of switching is set by

a minimum characteristic time scale $\tau_{sw} = \frac{1}{\gamma 4\pi M_s} \sim 7.5 ps$, but the precession time

will in general be longer than τ_{sw} for moderate stress pulse

amplitudes, $\sigma(t) > 2K_u / 3\lambda_s$, as the magnetization then cants out of plane enough to

see only a fraction of the maximum possible H_{demag} . Larger stress pulse amplitudes

result in shorter pulse durations being required as the magnetization has a larger initial excursion out of plane. For pulse durations that are longer than required for a 180° rotation (blue and green curves in Figure 5.1b) \vec{m} will exhibit damped elliptical precession about $\varphi = \pi / 2$. If the stress is released during the correct portion of any of these subsequent precessional cycles the magnetization should relax down to the φ_1 state [blue curve in Figure 5.1b], but otherwise it will relax down to the original state [green curve in Figure 5.1b].

The prospect of a practical device working reliably in the long pulse regime appears to be rather poor. The high damping of giant magnetostrictive magnets and the large field scale of the demagnetization field yield very stringent pulse timing requirements and fast damping times for equilibration to $\varphi = \pi / 2$. The natural time scale for magnetization damping in the in-plane magnetized thin film case

is $\tau_{damp} = \frac{1}{2\pi\gamma M_s \alpha}$, which ranges from 50 ps down to 15 ps for $\alpha = 0.3-1$ with $M_s=600$

emu/cm³. This high damping also results in the influence of thermal noise on the magnetization dynamics being quite strong since $H_{Langevin} \propto \sqrt{\alpha}$. Thus large stress levels with extremely short pulse durations are required in order to rotate the magnetization around the $\varphi = \pi / 2$ minimum within the damping time, and to keep the precession amplitude large enough that the magnetization will deterministically relax to the reversed φ_1 state. Our simulation results for polycrystalline Tb₃Dy₇Fe₂ show that a high stress pulse amplitude of $\sigma = -85$ MPa with a pulse duration ~ 65 ps is required if $\alpha = 0.5$ (Figure 5.1c). However, the pulse duration window for which the

magnetization will deterministically switch is extremely small in this case (<5 ps). This is due to the fact that the precession amplitude about the $\pi/2$ minimum at this damping gets small enough that thermal fluctuations allow only a very small window for which switching is reliable. For the lowest damping that we consider reasonable to assume, $\alpha = 0.3$, reliable switching is possible between $\tau_{duration} \sim 30-60$ ps at $\sigma = -85$ MPa. At a larger damping $\alpha = 0.75$ we find that the switching is non-deterministic for all pulse widths as the magnetization damps too quickly; instead larger stresses of $\sigma = -200$ MPa are required to generate deterministic switching of the magnetization with a pulse duration window $\tau_{duration} \sim 25-45$ ps (Figure 5.1d).

Given the high value of the expected damping we have also simulated the magnetization dynamics in the Landau Lifshitz (LL) form:

$$\frac{d\vec{m}}{dt} = -\gamma_{LL}(1 + \alpha^2)\vec{m} \times (\vec{H}_{eff}(t) + \vec{H}_{Langevin}(t)) + \alpha\vec{m} \times \frac{d\vec{m}}{dt} \quad (5.4)$$

The LL form and the LLG form are equivalent in low damping limit ($\alpha \ll 1$) but they predict different dynamics at higher damping values. Which of these norm-preserving forms for the dynamics has the right damping form is still a subject of debate [33]–[37]. As one increases α in the LL form the precessional speed is kept the same while the damping is assumed to affect only the rate of decay of the precession amplitude. The damping in the LLG dynamics, on the other hand, is a viscosity term and retards the precessional speed. The effect of this retardation can be seen in the LLG dynamics as the precessional cycles move to longer times as a function of

increasing damping. Our simulations show that the LL form (for fixed α) predicts higher precessional speeds than the LLG and hence an even shorter pulse duration window for which switching is deterministic than the LLG, ~ 12 ps for LL as opposed to ~ 30 ps for LLG (Figure 5.1e).

The damping clearly plays a crucial role in the stress amplitude scale and pulse duration windows for which deterministic switching is possible, regardless of the form used to describe the dynamics. Even though the magnetostriction of $\text{Tb}_{0.3}\text{Dy}_{0.7}\text{Fe}_2$ is high and the stress required to entirely overcome the anisotropy energy is only 9.6 MPa, the fast damping time scale and increased thermal noise (set by the large damping and the out-of-plane demagnetization) means that the stress-amplitude that is required to achieve deterministic toggle switching is 10-20 times larger. In addition, the pulse duration for in-plane toggling must be extremely short, with typical pulse durations of 10-50ps with tight time windows of 20-30 ps within which the acoustic pulse must be turned off. Considering acoustic ringing and inertial terms in the lattice dynamics of the structure this may be difficult to achieve. In addition, the stress scales required to successfully toggle switch the giant magnetostrictive nanomagnet in this geometry are nearly as high or even higher than that for transition metal ferromagnets such as Ni ($\lambda_s \sim -38$ ppm with $\alpha = .045$). For example, with a 70 nm x 130 nm elliptical Ni nanomagnet with a thickness of 6 nm and a hard axis bias field of 120 Oe we get switching at stress values $\sigma = +95$ MPa and $t_{\text{pulse}} = 0.75$ ns. Therefore the use of giant magnetostrictive nanomagnets with high damping in this toggle mode scheme confers no clear advantage over the use of a more conventional transition metal

ferromagnet, and in neither case does this approach appear particularly viable for technological implementation.

5.2.2 Magneto-Elastic Materials with PMA: Toggle Mode Switching

On the other hand, certain amorphous sputtered RE/TM alloy films with perpendicular magnetic anisotropy such as a-TbFe₂ [38]–[41] and a-Tb₃Dy₇Fe₂ [42] have properties that make them attractive candidate materials for stress-pulse toggle switching. In certain composition ranges they exhibit large magnetostriction ($\lambda_s > 270$ ppm for a-TbFe₂ and both λ_s and the effective out of plane anisotropy can be tuned over fairly wide ranges by varying the process gas pressure during sputter deposition, the target atom-substrate incidence angle, and the substrate temperature.

We consider the energy of such an out-of-plane magnetostrictive material under the influence of a magnetic field H_{bias} applied in the \hat{x} direction and a pulsed biaxial stress:

$$E(m_x, m_y, m_z) = -[K_{\perp}^u - 2\pi M_s^2 - \frac{3}{2} \lambda_s \sigma_{biaxial}(t)] m_z^2 - M_s H_{bias} m_x \quad (5.5)$$

Such a biaxial stress could be applied to the magnet if it is part of a patterned [001]-poled PZT thin film/ferromagnet bilayer. A schematic of this device geometry is depicted in Figure 5.2a. When $H_{bias} = 0$, it is straightforward to see the stress pulse will not result in reliable switching since, when the tensile biaxial stress is large enough,

the out of plane anisotropy becomes an easy-plane anisotropy and the equator presents a zero-torque condition on the magnetization, resulting in a 50%, or random, probability of reversal when the pulse is removed. However, reliable switching is possible for $H_{bias} > 0$ since that results in a finite canting of \vec{m} towards the x-axis. This canting is required for the same reasons a hard-axis bias field was needed for the toggle switching of an in-plane magnetized element as discussed previously.

For our simulation study of stress-pulse toggle switching of a PMA magnet, we considered a $Tb_{33}Fe_{67}$ nanomagnet with an $M_s = 300 \text{ emu/cm}^3$, $K_{eff} = 4 \times 10^5 \text{ ergs/cm}^3$ and $\lambda_s = 270 \text{ ppm}$. To estimate the appropriate value for the damping parameter we noted that ultrafast demagnetization measurements on $Tb_{18}Fe_{82}$ have yielded $\alpha = 0.27$. This 18-82 composition lies in a region where the magnetostriction is moderate ($\lambda_s \sim 50 \text{ ppm}$) [42] so we assumed that the damping will be higher for a- $TbFe_2$ due to its higher magnetostriction. Therefore we ran simulations for the range of $\alpha \sim 0.3-1$. For the gyromagnetic ratio we used $\gamma_{eff} = 1.78 \times 10^7$ which is appropriate for a- $TbFe_2$ [31]. We assumed an effective exchange constant $A_{eff} = 1 \times 10^{-6} \text{ erg} \cdot \text{cm}^{-1}$ [43] implying an

exchange length $l_{ex}^{no-stress} = \sqrt{\frac{A_{eff}}{K_{\perp}^{eff}}} = 15.8 \text{ nm}$ (in the absence of an applied stress) and

$l_{ex}^{pulse} = \sqrt{\frac{A_{eff}}{2\pi M_s^2}} = 13.3 \text{ nm}$ (assuming that the stress pulse amplitude is just enough to

cancel the out of plane anisotropy). A monodomain crossover criterion of $d_c \sim$

$\sqrt{\frac{4\pi A_{ex}}{K_u}} \sim 56 \text{ nm}$ (with the pulse off) and $d_c \sim \sqrt{\frac{2A_{ex}}{M_s^2}} \sim 47 \text{ nm}$ (with the pulse on) can

be calculated by considering the minimum length-scale associated with supporting thermal $\lambda/2$ confined spin wave modes [44]. The important point here is that the low M_s of these systems ensures that the exchange length is still fairly long even during the switching process, which suggests that the macrospin approximation should be valid for describing the switching dynamics of this system for reasonably sized nanomagnets.

We simulated a circular element with a diameter of 60 nm and a thickness of 10 nm, under an x-axis bias field, H_{bias} which creates an initial canting angle of 11 degrees from the vertical(z-axis). This starting angle is sufficient to enable deterministic toggle switching between the +z and -z minima via biaxial stress pulsing. The assumed device geometry, anisotropy energy density and bias field corresponded to an energy barrier $E_b = 4.6\text{eV}$ for thermally activated reversal, and hence a room temperature thermal stability factor $\Delta = 185$.

In Figure 5.2 b-f we show selected results of the macrospin simulations of stress-pulse toggle switching of this modeled TbFe₂PMA nanomagnet.

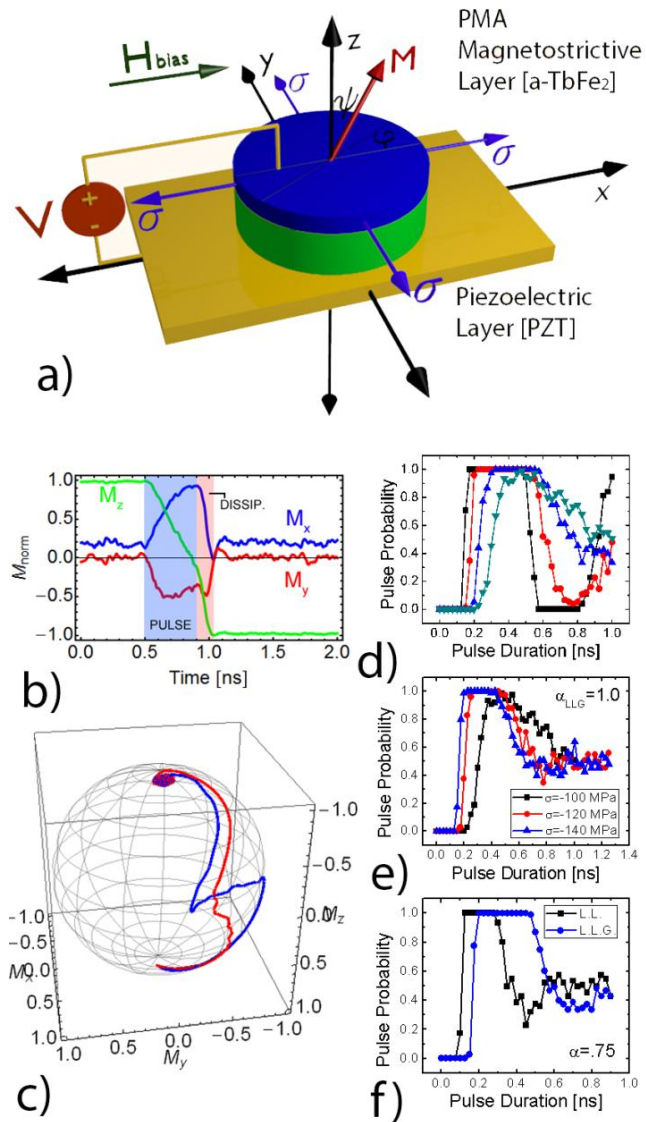


Figure 5.2 a) Schematic of TbFe2 magnetic element under biaxial stress generated by a PZT layer. b) Switching trajectory time trace for $\{m_x, m_y, m_z\}$ for $\sigma = -85$ MPa . The pulse is initiated at $t = 500$ ps. The blue region denotes when precession about H_{bias} dominates (i.e. while the pulse is on) and the red when the dissipative dynamics rapidly damp the system down to the other equilibrium point. c) $\sigma = -85$ MPa, $\tau_p = 400$ ps (red) and $\sigma = -120$ MPa and $\tau_p = 300$ ps (blue). d) Dependence of the simulated pulse switching probability on α for $\sigma = -85$ MPa; α (black) = 0.3, α (red) = 0.5, α (blue) = 0.75, and α (teal) = 1.0. e) Dependence of pulse switching probability on stress amplitude. Stress-induced switching is possible even for $\alpha = 1.0$. f) Comparison of pulse switching probability for LL and LLG dynamics for $\sigma = -85$ MPa and $\alpha = 0.75$. Here the difference between the LL and LLG dynamics has a significant effect on the

width of the pulse window where reliable switching is predicted by the simulations ($\Delta\tau_{LL}=200$ ps and $\Delta\tau_{LLG}=320$ ps.)

The switching transition can be divided into two stages (see Figure 5.2b): the precessional stage that occurs when the stress field is applied, during which the dynamics of the magnetization are dominated by precession about the effective field that arises from the sum of the bias field and the easy-plane anisotropy field

$\frac{3\lambda_s\sigma(t) + 2K_{\perp}^{eff}}{M_s} m_z$, and the dissipative stage that begins when the pulse is turned off

and where the large K_{\perp}^{eff} and the large α result in a comparatively quick relaxation to the other energy minimum. Thus most of the switching process is spent in the precessional phase and the entire switching process is not much longer than the actual stress pulse duration. For pulse amplitudes at or not too far above the critical stress for reversal, $\sigma \approx -2K_{\perp}^{eff} / 3\lambda_s$ the two relevant timescales for the dynamics are set approximately by the precessional period $\tau_{sw} \approx 1 / \gamma H_{bias} \approx 100$ ps of the nanomagnet and the damping time $\tau_d \sim 2 / \alpha \gamma H_{bias}$. Both of these timescales are much longer than the timescales set by precession and damping about the demagnetization field in the in-plane magnetized toggle switching case. The result is that even with quite high damping one can have reliable switching over much broader pulse width windows, 200-450 ps, for stress amplitudes that are readily attainable with piezoelectric transduction (Figure 5.2d). The relatively large pulse duration windows within which reliable switching is possible (as compared to the in-plane toggle mode) hold for both the LL and LLG damping. However, the difference between the two forms is evident

in the PMA case (Figure 5.2f). At fixed α , the LLG damping predicts a larger pulse duration window than the LL damping. Also the effective viscosity implicit within the LLG equation ensures that the switching time scales are slower than in the LL case as can also be seen in Figure 5.2f.

An additional and important point concerns the factors that determine the critical switching amplitude. In the in-plane toggle mode switching of the previous section, it was found that the in-plane anisotropy field was not the dominant factor in determining the stress scale required to transduce a deterministic toggle switch. Instead, we found that the stress scale was almost exclusively dependent on the need to generate a high enough precession amplitude/precession speed during the switching trajectory so as to not be damped out to the temporary equilibrium at $\varphi = \pi / 2$ (at least within the damping range considered). This means that the critical stress scale to transduce a deterministic switch is essentially determined by the damping. We find that the situation is fundamentally different for the PMA based toggle memories. The critical amplitude σ_c is nearly independent of the damping from a range of $\alpha = .3 - .75$ up until $\alpha \sim 1$ where the damping is sufficiently high (i.e. damping times equaling and/or exceeding the precessional time scale) that at $\sigma = -85$ MPa the magnetization traverses too close to the minimum at $\theta = \pi / 2, \phi = 0$. The main reason for this difference between the PMA toggle based memories and the in-plane toggle based memory lies in the role that the application of stress plays in the dynamics. First, in the in-plane case, the initial elliptical amplitude and the initial out of plane excursion of the magnetization is set by the stress pulse magnitude. Therefore the

stress has to be high to generate a large enough amplitude such that the damping does not take the trajectory too close to the minimum at which point Langevin fluctuations become an appreciable part of the total effective field. This is not true in the PMA case where the initial precession amplitude about the bias field is large and the effective stress scale for initiating this precession about the bias field is the full cancellation of the perpendicular anisotropy.

Since the minimum stress-pulse amplitude required to initiate a magnetic reversal in out-of-plane toggle switching scales with K_{\perp}^{eff} in the range of damping values considered, lowering the PMA of the nanomagnet is a straightforward way to reduce the stress and write energy requirements for this type of memory cell. Such reductions can be achieved by strain engineering through the choice of substrate, base electrode and transducer layers, by the choice of deposition parameters, and/or by post-growth annealing protocols. For example growing a TbFe₂ film with a strong tensile biaxial strain can substantially lower K_{\perp}^{eff} . If the PMA of such a nanomagnet can be reduced to $K_{\perp}^{eff} = 2 \times 10^5 \text{ ergs/cm}^3$ our simulations indicate that this would result in reliable pulse toggle switching at $\sigma = -50 \text{ MPa}$ with $t_{\text{pulse}} \approx 400 \text{ ps}$, for $0.3 \leq \alpha \leq 0.75$ and $H_{\text{bias}} = 250 \text{ Oe}$. If we again assume $M_s = 300 \text{ emu/cm}^3$, a diameter of 60 nm and a thickness of 10 nm, this low PMA nanomagnet would still have a high thermal stability with $\Delta = 92$. The challenge, of course, is to consistently and uniformly control the stress in the magnetostrictive layer. It is important to note that no such tailoring (short of systematically lowering the damping) can exist in the in-plane toggle mode case.

5.3 Two State Non-Toggle Switching

So far we have discussed toggle mode switching where the same polarity strain pulse is applied to reverse the magnetization between two bi-stable states. In this case the strain pulse acts to create a temporary field around which the magnetization precesses and the pulse is timed so that the energy landscape and magnetization relax the magnetization to the new state with the termination of the pulse. Non-toggle mode magneto-elastic switching differs fundamentally from the precessional dynamics of toggle-mode switching, being an example of dissipative magnetization dynamics where a strain pulse of one sign destabilizes the original state (A) and creates a global energy minimum for the other state (B). The energy landscape and the damping torque completely determine the trajectory of the magnetization and the magnetization effectively “rolls” down to its new global energy minimum. Reversing the sign of the strain pulse destabilizes state B and makes state A the global energy minimum – thus ensuring a switch back to state A. There are some major advantages to this class of switching for magneto-elastic memories over toggle mode memories. Precise acoustic pulse timing is no longer an issue. The switching time scales, for reasonable stress values, scale from quasi-static to nanoseconds. In addition, the large damping typical of magnetoelastic materials does not present a challenge for achieving robust switching trajectories in deterministic switching as it does in toggle-mode memories. Below we will discuss deterministic switching for magneto-elastic materials that have two different types of magnetic anisotropy.

5.3.1 The Case of Cubic Anisotropy

We first consider magneto-elastic materials with cubic anisotropy under the influence of a uniaxial stress field pulse. There are many epitaxial Fe-based magnetostrictive materials that exhibit a dominant cubic anisotropy when magnetron-sputter grown on oriented Cu underlayers on Si or on MgO or GaAs substrates. For example, Fe₈₁Ga₁₉ grown on MgO [100] or on GaAs exhibit a cubic anisotropy [45]–[47]. Given the low cost of these Fe-based materials compared to rare-earth alloys, it is worth investigating whether such films can be used to construct a two state memory. Fe₈₁Ga₁₉ on MgO exhibits easy axes along <100>. In addition, epitaxial Fe₈₁Ga₁₉ films have been found to have a reasonably high magnetostriction $\lambda_{100}=180$ ppm making them suitable for stress induced switching. If we assume that the stress field is applied by a transducer along the [100] direction and that we have the possibility of applying a bias field at $\varphi = \frac{\pi}{4}$ degrees, the free energy expression for this system is:

$$E(m_x, m_y) = K_1 m_x^2 m_y^2 + K_1 m_z (1 - m_z^2) + 2\pi(N_z - N_{\parallel})M_s^2 m_z^2 - \frac{M_s H_{bias}}{\sqrt{2}}(m_x + m_y) - \frac{3}{2}\lambda_s \sigma(t) m_x^2 \quad (5.6)$$

Equation (5.6) shows that, in the absence of a bias field, the anisotropy energy is 4-fold symmetric in the film-plane. It is rather easy to see that it is impossible to make a two-state non-toggle switching with a simple cubic anisotropy energy and uniaxial stress field along [100]. Figure 5.3a shows the free energy landscape described by Equation (5.6) without stress applied. To create a two-state deterministic

magnetostrictive device approach, H_{bias} needs to be strong enough to eradicate the energy minima at $\varphi = \pi$ and $3\pi/2$ which strictly requires that $H_{bias} \geq 0.5K_1 / M_s$. Finite temperature considerations can lower this minimum bias field requirement considerably. This is due to the fact that the bias field can make the life-time to escape energy minima in the third quadrant and fourth quadrant small and the energy barrier to return them from the energy minima in the first quadrant extremely large. We arbitrarily set this requirement for the bias field to correspond to a lifetime of 75 μ s. The typical energy barriers to hop from back to the metastable minima in the third and fourth quadrant for device volumes we will consider are on the order of several eV.

The requirement for thermal stability of the two minima in the first quadrant sets an *upper* bound on H_{bias} as we require $\Delta \equiv E_b / k_b T > 40$ at room temperature between the two states [Figure 5.3c]. It is desirable that this upper bound is high enough that there is some degree of tolerance to the value of the bias field at device dimensions that are employed. This sets requirements on the minimum volume of the elliptical nanomagnet that are dependent on K_1 .

For $K_1 = 1.5 \times 10^5$ ergs/cm³, two-state non-toggle switching with the required thermal stability can only occur for H_{bias} between 50 - 56 Oe. This is too small a range of acceptable bias fields. However, by increasing the thickness to 15 nm the bias field range grows to $H_{bias} = 50 - 90$ Oe which is an acceptable range. For $K_1 = 2 \times 10^5$ erg/cm³, there is an appreciable region of bias field (~65-120 Oe) for which $E_{barrier}/k_B T > 42$ for

a cylindrical nanomagnet with $d = 100$ nm and $t = 10$ nm. For $K_1 = 2.5 \times 10^5$ ergs/cm³, the bias range goes from 90 – 190 Oe for the same volume. The values of the anisotropy constants, device lateral dimensions, film thickness, and the exchange bias strength need to be taken under consideration and optimized to ensure device stability.

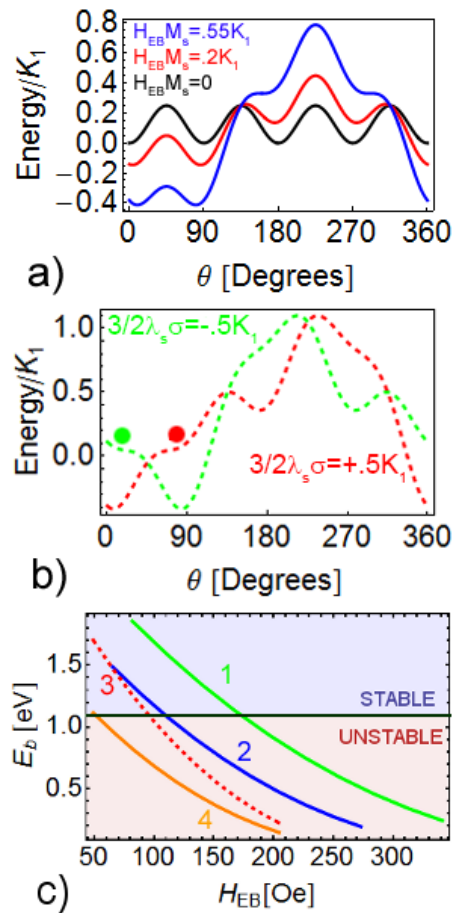


Figure 5.3 . a) Energy (normalized to K_1) landscape as a function of angle for various values of exchange bias energy. b) $\theta=80$ [$\theta=10$] is the only stable equilibrium for compressive [tensile] stress. Dissipative dynamics and the free energy landscape then dictate the non-toggle switching dynamics. c) Shows the energy barrier dependence on

the [110] bias field for a $d=100$ nm, $t=12.5$ nm circular element with (1) $K_1=2.5 \times 10^5$ ergs/cm³, (2) $K_1=2 \times 10^5$ ergs/cm³, and (4) $K_1=1.5 \times 10^5$ ergs/cm³. with $d=100$ nm & $t=15$ nm element with (3) $K_1=1.5 \times 10^5$ ergs/cm³.

We now discuss the dynamics for a simulated case where $K_1=2 \times 10^5$ ergs/cm³, $H_{\text{bias}} = 85$ Oe, and $M_s = 1300$ emu/cm³. Two stable minima exist at $\theta=10^\circ$ and $\theta=80^\circ$. Figure 5.3b shows the effect of the stress pulse on the energy landscape. When a compressive stress $\sigma > \sigma_c$ is applied, the potential minimum at $\theta = 10^\circ$ is rendered unstable and the magnetization follows the free energy gradient to $\theta = 80^\circ$ (green curve). Since the stress field is applied along [100] the magnetization first switches to a minima very close to but greater than $\theta = 80^\circ$ and when the stress is released gently relaxes down to the zero stress minimum at $\theta = 80^\circ$. In order to switch from $\theta = 80^\circ$ to $\theta = 10^\circ$ we need to reverse the sign of the applied stress field to tensile (red curve). A memory constructed on these principles is thus non-toggle.

The magnetization switching trajectory is simple and follows the dissipative dynamics dictated by the free energy landscape (Figure 5.4a). We have assumed a damping of $\alpha = 0.1$ for the Fe₈₁Ga₁₉ system, based on previous measurements [48] and as confirmed by our own. Higher damping only ends up speeding up the switching and ring-down process. Figure 5.4b shows the simulated stress amplitude and pulse switching probability phase diagram at room temperature.

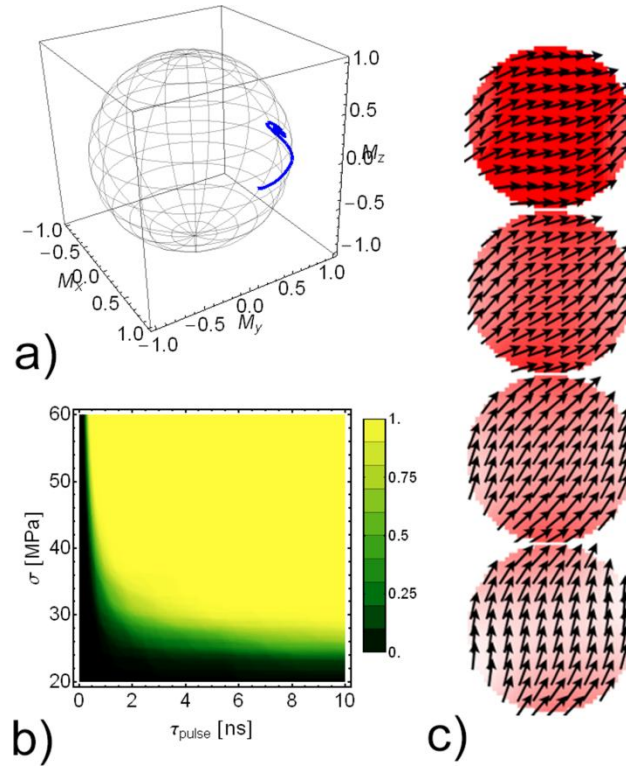


Figure 5.4 a) Magnetoelastic switching trajectory for $\text{Fe}_{81}\text{Ga}_{19}$ with $\sigma = -45$ MPa and $\tau_p = 3$ ns. The main part of the switching occurs within 200 ps. The magnetization relaxes to the equilibrium defined when the pulse is on and then relaxes to the final equilibrium when the pulse is turned off. b) Switching probability phase diagram for $\text{Fe}_{81}\text{Ga}_{19}$ with biaxial anisotropy at $T = 300$ K. c) $T = 0$ K OOMMF simulations showing the equilibrium micromagnetic configuration for $K_1 = 2 \times 10^5$ ergs/cm³ and $M_s = 1300$ emu/cm³. Subsequent shots show the rotational switching mode for a 45 MPa uniaxial compressive stress along [100].

Ultimately, we must take the macrospin estimates for device parameters as a rough guide. The macrospin dynamics approximate the true micromagnetics less and less well as the device diameter gets larger. The main reason for this is the large M_s of $\text{Fe}_{81}\text{Ga}_{19}$ and the tendency of the magnetization to curl at the sample edges. We performed $T = 0$ K micromagnetic simulations in OOMMF. An exchange bias field $H_{\text{bias}} = 85$ Oe was applied at $\varphi = 45$ degrees and we assume $K_1 = 2 \times 10^5$ ergs/cm³,

$M_s=1300 \text{ emu/cm}^3$, and $A= 1.9 \times 10^{-6} \text{ erg/cm}$. Micromagnetics show that the macrospin picture quantitatively captures the switching dynamics, the angular positions of the stable states ($\varphi_0 \rightarrow \sim 10^\circ$ and $\varphi_1 \rightarrow \sim 80^\circ$) and the critical stress amplitude at ($\sigma \sim 30 \text{ MPa}$) when the device diameter $d < 75 \text{ nm}$. The switching is essentially a rigid in-plane rotation of the magnetization from φ_0 to φ_1 . However, we chose to simulate an element with $d=100 \text{ nm}$ because it allowed for thermal stability of the devices in a region of thickness ($t = 12\text{-}15 \text{ nm}$) where $H_{\text{bias}} \sim 50\text{-}100 \text{ Oe}$ at room temperature could be reasonably expected. The initial average magnetization angle is larger ($\varphi_0 \rightarrow \sim 19^\circ$ and $\varphi_1 \rightarrow \sim 71^\circ$) than would be predicted by macrospin for a $d=100 \text{ nm}$ element. We see that this is due to the magnetization curling at the devices edges at $d=100 \text{ nm}$ [Figure 5.4c]. Despite the fact that magnetization profile differs from the macrospin picture we find that there is no appreciable difference between the stress scales required for switching or the basic switching mechanism.

5.3.2 The Case of Uniaxial Anisotropy

Lastly we discuss deterministic (non-toggle) switching of an in-plane giant magnetostrictive magnet with uniaxial anisotropy. In-plane magnetized polycrystalline TbDyFe patterned into elliptical nanomagnets could serve as a potential candidate for such a memory scheme. To implement deterministic switching in this geometry and with such a material a bias field H_{bias} is applied along the hard axis of the nanomagnet. This generates two stable minima at φ_0 and $180 - \varphi_0$ symmetric about the hard axis. The axis of the stress pulse then needs to be non-collinear with respect to the easy axis

in order to break the symmetry of the potential wells and drive the transition to the selected equilibrium position. Figure 5.5a below shows a schematic of the situation. When a stress pulse is applied in the direction that makes an angle β with respect to the easy axis of the nanomagnet, $0^\circ < \beta < 90^\circ$, the free energy within the macrospin approximation becomes:

$$E(m_x, m_y, m_z) = -[2\pi(N_y - N_x)M_s^2 m_x^2 + 2\pi(N_z - N_y)M_s^2 m_z^2 - H_{bias}M_s m_y + \frac{3}{2M_s} \lambda_s \sigma(t) \cdot (\cos(\beta)m_y - \sin(\beta)m_x)^2] \quad (5.7)$$

From Equation (5.7) it can be seen that a sufficiently strong compressive stress pulse can switch the magnetization between φ_0 and $180^\circ - \varphi_0$, but only if φ_0 is between β and 90° . To see why this condition is necessary, we look at the magnetization dynamics in the high stress limit when $0 < \varphi_0 < \beta$. During such a strong pulse the magnetization will see a hard axis appear at $\varphi \approx \beta$ and hence will rotate towards the new easy axis at $\varphi = \beta - 90^\circ$, but when the stress pulse is turned off the magnetization will equilibrate back to φ_0 . This situation is represented by the green trajectory shown in Figure 5.5e.

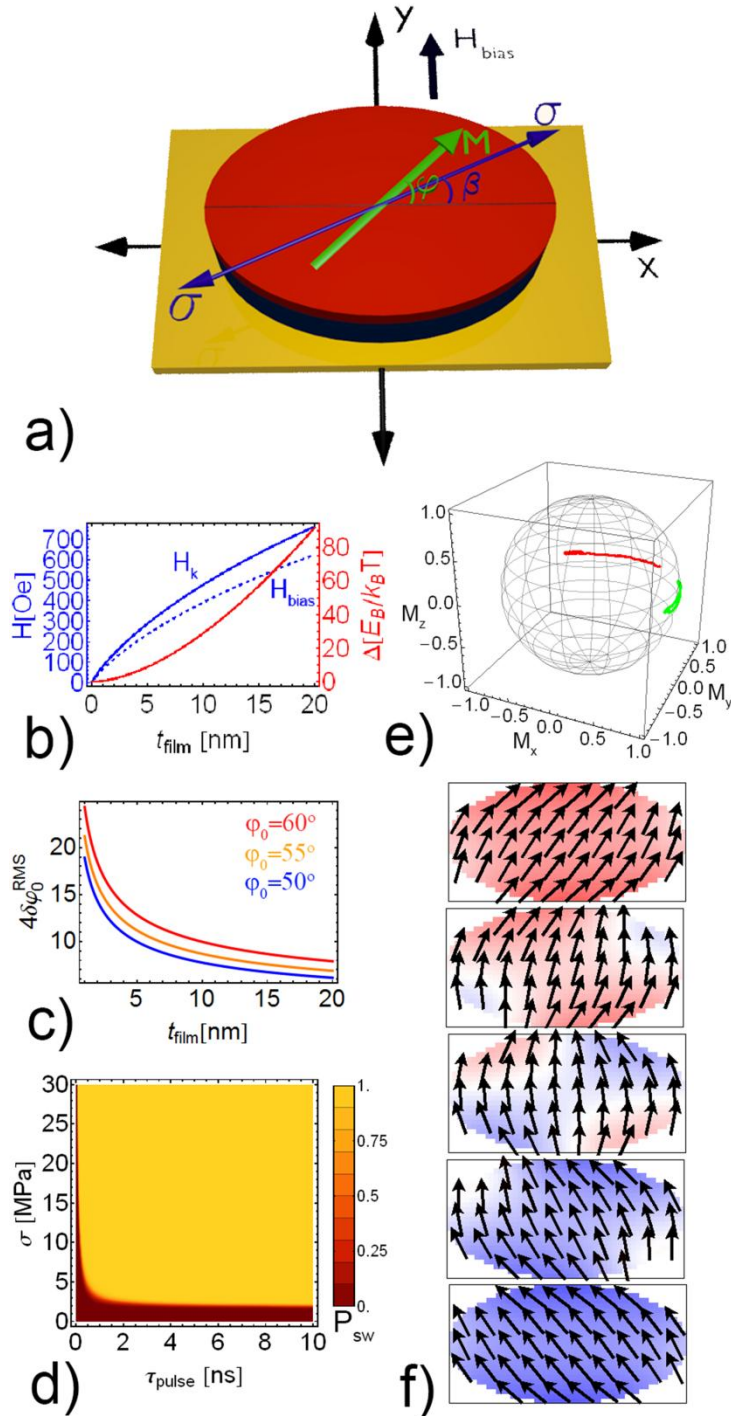


Figure 5.5 a) Schematic of magnetostrictive device geometry that utilizes uniaxial anisotropy to achieve deterministic switching. Polycrystalline $Tb_3Dy_7Fe_2$ on PMN-PT with 1 axis oriented at angle β with respect to the easy axis. b) In-plane shape anisotropy field (H_k) and hard axis bias field (H_{bias}) for a $125 \times 250 \text{ nm}^2$ ellipse as a

function of film thickness required to ensure $\varphi_0 = 55^\circ$. Thermal stability parameter Δ plotted versus film thickness with H_k , H_{bias} such that $\varphi_0 = 55^\circ$. c) Four times the RMS angle fluctuation about three different $\varphi_0 > 45^\circ$ versus film thickness for a 125×250 nm² ellipse at $T = 300$ K. d) $T = 300$ K stress pulse (compressive) switching probability phase diagram for a 125×250 nm² ellipse with $t_{film} = 12.5$ nm $\beta = 45^\circ$, $\varphi_0 = 55^\circ$. e) Magnetization trajectories for $\beta = 45^\circ$, $\sigma = -5$ MPa, $\tau_{pulse} = 3$ ns, with $H_{bias} = 457.6$ Oe yielding $\varphi_0 = 55^\circ$ (red) and $\beta = 45^\circ$, $\sigma = -20$ MPa with $H_{bias} = 225$ Oe yielding a $\varphi_0 = 24^\circ$ (green). f) Micromagnetic switching trajectory of a 125×250 nm² ellipse under a DC compressive stress of -3 MPa transduced along 45 degrees.

But when $\beta < \varphi_0 < 90^\circ$, a sufficiently strong compressive stress pulse defines a new easy axis close to $\varphi = 90^\circ + \beta$ and when the pulse is turned off the magnetization will relax to $\varphi = 180 - \varphi_0$. Similarly the possibility of switching from $180^\circ - \varphi$ to φ with a *tensile* strain depends on whether $90^\circ < 180^\circ - \varphi < 90^\circ + \beta$. Thus $\beta = 45^\circ$ is the optimal situation as then the energy landscape becomes mirror symmetric about the hard axis and the amplitude of the required switching stress (voltage) are equal. This scheme is quite similar to the case of deterministic switching in biaxial anisotropy systems (with the coordinate system rotated by 45°). We note that a set of papers [49]–[51] have previously proposed this particular case as a candidate for non-toggle magnetoelectric memory. However for a nanoscale memory cell the effect of thermal fluctuations has a substantial impact on the biasing conditions that required in this approach for successful performance. In particular, previously we have noted that the

requirement on H_{bias} is that it be strong enough that $45^\circ < \varphi_0$, but this is sufficient only at $T = 0$. The presence of thermal fluctuations implies a thermal, Gaussian distribution of the initial orientation of the magnetization direction φ about φ_0 . If a significant part of this angular distribution falls below 45 degrees there will be a high write error rate. Thus we must ensure that H_{bias} is high enough that the probability of $\varphi < 45^\circ$ is extremely low. We have selected the requirement that $\varphi < 45^\circ$ is a 4σ event. We acknowledge that this constraint may need to be more stringent for realistic memory applications at perhaps $\sim 12\sigma$. We have not yet done the calculations for this more stringent case. The minimum value of H_{bias} needed to satisfy our error rate requirement must be low enough that one does not make the nanomagnet thermally unstable and that one allows for some tolerance in the value of the bias field. This requirement on H_{bias} puts significant constraints on the minimum size of the nanomagnet that can be used in this device approach. It also sets some rather tight requirements on the hard axis bias field, as we shall see.

To illustrate those constraints we now discuss the energetics of a magnetostrictive polycrystalline TbDyFe element having $M_s = 600 \text{ emu/cm}^3$ and an elliptical cross section of $125 \times 250 \text{ nm}^2$. At this cross section we find that an initial angle $\varphi_0^{avg} \sim 55^\circ$ with a TbDyFe cylinder thickness of $t_{film} \geq 12.5 \text{ nm}$ satisfies both the requirement that $\varphi_0 - 4\delta\varphi_0^{RMS} > 45^\circ$ [Figure 5.5c] and the requirement that the nanomagnet is thermally stable with a $\Delta > 42$ [Figure 5.5d]. As the anisotropy field

$H_k = 558.6$ Oe for these dimensions, then $H_{bias} = 457.6$ Oe in order that $\varphi_0^{avg} \sim 55^\circ$.

The required hard axis bias field is rather high and fairly close to the anisotropy field.

Scaling down the lateral area of the nanomagnet lower than these dimensions increases the thickness required to keep the nanomagnet thermally stable. This makes the problem of high hard axis bias fields even worse. For a fixed elliptical aspect ratio with a 80×160 nm² ellipse requires $t = 18.25$ nm in order that $\Delta \geq 42$. This results in $H_k = 841.5$ Oe and an $H_{bias} = 775.5$ Oe. The hard axis bias field is even closer to the anisotropy field value (which is rather undesirable from the point of view of device tolerance). One could lower the aspect ratio of the ellipse while scaling the lateral area down which has the effect of reducing the in-plane anisotropy field. However, in order to maintain thermal stability one must increase the thickness of the nanomagnet which again increases the anisotropy field. An 80×120 nm ellipse requires $t_{film} = 30$ nm to maintain thermal stability. This implies an $H_k = 792$ Oe and $H_{bias} = 697$ Oe.

In this thick limit, the anisotropy field becomes increasingly sensitive to small fluctuations in the lateral shape. An 85×115 nm² ellipse at $t_{film} = 30$ nm yields an $H_k = 590$ Oe and $H_{bias} = 483$ Oe. This extreme sensitivity to the nanomagnet dimensions makes this memory scheme unfeasible to implement at small dimensions. The requirements for the initial in-plane angle and the energy barrier must be satisfied while keeping the nanomagnet cross sectional area as low as possible. But this in turn introduces issues with the scale for the hard axis bias field and the thickness of the nanomagnet as well as concerns arising from the instability of device reliability to

small fluctuations in the shape. This non-toggle magnetoelastic switching geometry is thus not a good candidate for patterned ultra-high density storage.

Despite the constraint of a minimum cell size for viability, this memory does have one advantage that the stress scale required to switch the memory is quite low. We have simulated $T=300$ K macrospin switching dynamics for a 125×250 nm² ellipse with thickness $t=12.5$ nm with $H_{bias}=450$ Oe such that $\varphi_0 \approx 55^\circ$. The Gilbert damping parameter was set to $\alpha = .5$ and magnetostriction $\lambda_s = 670$ ppm. The magnetization switches by simple rotation from $\varphi_0 = 55^\circ$ to $\varphi_1 = 125^\circ$ that is driven by the stress pulse induced change in the energy landscape (see Figure 5.5d). Some results are provided in Figure 5.5c where the switching from $\varphi_0 = 55^\circ$ to $\varphi_1 = 125^\circ$ shows a 100% switching probability for stresses as low as - 5 MPa for pulse widths as short as 1 ns. This stress scale for switching is substantially lower than any of the switching mode schemes discussed before.

5.4 Conclusion

The only conclusion that one can draw from this chapter is that making memories out of giant magnetostrictive nanomagnets is not as easy as it might appear at first glance. For pulsed toggle switching, there is a fundamental tension between giant magnetostriction and large damping. This can lead to unexpectedly large stresses and demanding acoustical pulse control requirements for switching the nanomagnet. For two-state non-toggle switching, the need for substantial hard axis bias fields (both in the biaxial and uniaxial non-toggle nanoscale magnets) makes maintaining thermal

stability of these memories a real concern. Despite all the problems with magnetoelastic based nano-scale memories that we have enumerated and treated exhaustively in the previous section, we do not think all is doom and gloom.

PMA based giant magnetostrictive nanomagnets can be made extremely small ($d < 50$ nm) while still maintaining thermal stability. Given the switching mechanism, the stress fields required are, for large ranges of the damping, essentially set by the out-of-plane anisotropy energy density. We think that it might be possible to engineer giant magnetostrictive RE-TM multilayers in order to tune the magnetostriction, K_{\perp} , and M_s for our application. It is conceivable with the right stack structure and design that one could have nanomagnet switching with a pulse amplitude of 20-50 MPa, with pulse times in the sub-ns regime and with reasonable acoustic pulse timing requirements. The appropriate tailoring of M_s and K_{\perp} might also make it possible to significantly reduce the required in-plane bias field. The small diameter and low cross-sectional area of these PMA giant magnetostrictive devices could lead to very low capacitive write energies.

In addition, there may be a place for two-state non toggle memories such as we described in Section 5.3.2. Despite the fact that these memories are not scalable down into the 100-200 nm size regime, there may be a place for larger footprint (i.e. 500-600 nm size regime) memories with very low write stress pulse amplitudes. We think that with careful thought and engineering, it might be possible to use these sorts of two-state non-toggle devices for ultra-low power EEPROM applications.

REFERENCES

- [1] H. Ohno, D. Chiba, F. Matsukura, T. Omiya, E. Abe, T. Dietl, Y. Ohno, and K. Ohtani, "Electric-field control of ferromagnetism.," *Nature*, vol. 408, no. 6815, pp. 944–6, 2000.
- [2] D. Chiba, M. Sawicki, Y. Nishitani, Y. Nakatani, F. Matsukura, and H. Ohno, "Magnetization vector manipulation by electric fields.," *Nature*, vol. 455, no. 7212, pp. 515–8, Sep. 2008.
- [3] D. Chiba, M. Yamanouchi, F. Matsukura, and H. Ohno, "Electrical manipulation of magnetization reversal in a ferromagnetic semiconductor.," *Science*, vol. 301, no. 5635, pp. 943–5, Aug. 2003.
- [4] M. Weisheit, S. Fähler, A. Marty, Y. Souche, C. Poinson, and D. Givord, "Electric field-induced modification of magnetism in thin-film ferromagnets.," *Science*, vol. 315, no. 5810, pp. 349–51, Jan. 2007.
- [5] T. Maruyama, Y. Shiota, T. Nozaki, K. Ohta, N. Toda, M. Mizuguchi, A. A. Tulapurkar, T. Shinjo, M. Shiraishi, S. Mizukami, Y. Ando, and Y. Suzuki, "Large voltage-induced magnetic anisotropy change in a few atomic layers of iron," *Nat. Nanotechnol.*, vol. 4, no. March, pp. 158–161, 2009.
- [6] M. Endo, S. Kanai, S. Ikeda, F. Matsukura, and H. Ohno, "Electric-field effects on thickness dependent magnetic anisotropy of sputtered MgO/Co[₄₀]Fe[₄₀]B[₂₀]/Ta structures," *Appl. Phys. Lett.*, vol. 96, no. 21, p. 212503, 2010.
- [7] W.-G. Wang, M. Li, S. Hageman, and C. L. Chien, "Electric-field-assisted switching in magnetic tunnel junctions.," *Nat. Mater.*, vol. 11, no. 1, pp. 64–8, Jan. 2012.
- [8] Y. Shiota, T. Nozaki, F. Bonell, S. Murakami, T. Shinjo, and Y. Suzuki, "Induction of coherent magnetization switching in a few atomic layers of FeCo using voltage pulses.," *Nat. Mater.*, vol. 11, no. 1, pp. 39–43, Jan. 2012.
- [9] T. Nozaki, Y. Shiota, S. Miwa, S. Murakami, F. Bonell, S. Ishibashi, H. Kubota, K. Yakushiji, T. Saruya, A. Fukushima, S. Yuasa, T. Shinjo, and Y. Suzuki, "Electric-field-induced ferromagnetic resonance excitation in an ultrathin ferromagnetic metal layer," *Nat. Phys.*, vol. 8, no. 6, pp. 492–497, Apr. 2012.
- [10] P. Khalili Amiri, P. Upadhyaya, J. G. Alzate, and K. L. Wang, "Electric-field-induced thermally assisted switching of monodomain magnetic bits," *J. Appl. Phys.*, vol. 113, no. 1, p. 013912, 2013.

- [11] T. Brintlinger, S.-H. Lim, K. H. Baloch, P. Alexander, Y. Qi, J. Barry, J. Melngailis, L. Salamanca-Riba, I. Takeuchi, and J. Cumings, “In situ observation of reversible nanomagnetic switching induced by electric fields.,” *Nano Lett.*, vol. 10, no. 4, pp. 1219–23, Apr. 2010.
- [12] D. E. Parkes, S. A. Cavill, A. T. Hindmarch, P. Wadley, F. McGee, C. R. Staddon, K. W. Edmonds, R. P. Campion, B. L. Gallagher, and A. W. Rushforth, “Non-volatile voltage control of magnetization and magnetic domain walls in magnetostrictive epitaxial thin films,” *Appl. Phys. Lett.*, vol. 101, no. 7, p. 072402, 2012.
- [13] M. Weiler, A. Brandlmaier, S. Geprägs, M. Althammer, M. Opel, C. Bihler, H. Huebl, M. S. Brandt, R. Gross, and S. T. B. Goennenwein, “Voltage controlled inversion of magnetic anisotropy in a ferromagnetic thin film at room temperature,” *New J. Phys.*, vol. 11, no. 1, p. 013021, Jan. 2009.
- [14] M. Weiler, L. Dreher, C. Heeg, H. Huebl, R. Gross, M. S. Brandt, and S. T. B. Goennenwein, “Elastically Driven Ferromagnetic Resonance in Nickel Thin Films,” *Phys. Rev. Lett.*, vol. 106, no. 11, p. 117601, Mar. 2011.
- [15] M. Weiler, H. Huebl, F. S. Goerg, F. D. Czeschka, R. Gross, and S. T. B. Goennenwein, “Spin Pumping with Coherent Elastic Waves,” *Phys. Rev. Lett.*, vol. 108, no. 17, p. 176601, Apr. 2012.
- [16] V. Novosad, Y. Otani, A. Ohsawa, S. G. Kim, K. Fukamichi, J. Koike, K. Maruyama, O. Kitakami, and Y. Shimada, “Novel magnetostrictive memory device,” *J. Appl. Phys.*, vol. 87, no. 9, p. 6400, 2000.
- [17] H. Schumacher, C. Chappert, P. Crozat, R. Sousa, P. Freitas, J. Miltat, J. Fassbender, and B. Hillebrands, “Phase Coherent Precessional Magnetization Reversal in Microscopic Spin Valve Elements,” *Phys. Rev. Lett.*, vol. 90, no. 1, p. 017201, Jan. 2003.
- [18] P. I. Williams, D. G. Lord, and P. J. Grundy, “Magnetostriction in polycrystalline sputter-deposited TbDyFe films,” *J. Appl. Phys.*, vol. 75, no. 10, p. 5257, 1994.
- [19] D. Hunter, W. Osborn, K. Wang, N. Kazantseva, J. Hattrick-Simpers, R. Suchoski, R. Takahashi, M. L. Young, A. Mehta, L. A. Bendersky, S. E. Lofland, M. Wuttig, and I. Takeuchi, “Giant magnetostriction in annealed Co(1-x)Fe(x) thin-films.,” *Nat. Commun.*, vol. 2, no. May, p. 518, Jan. 2011.
- [20] K. Ried, M. Schnell, F. Schatz, M. Hirscher, B. Ludescher, W. Sigle, and H. Kronmüller, “Crystallization Behaviour and Magnetic Properties of

- Magnetostrictive TbDyFe Films,” *Phys. Status Solidi*, vol. 167, no. 1, pp. 195–208, May 1998.
- [21] M. Beleggia, M. De Graef, Y. T. Millev, D. A. Goode, and G. Rowlands, “Demagnetization factors for elliptic cylinders,” *J. Phys. D. Appl. Phys.*, vol. 38, no. 18, pp. 3333–3342, Sep. 2005.
- [22] K. Roy, S. Bandyopadhyay, and J. Atulasimha, “Switching dynamics of a magnetostrictive single-domain nanomagnet subjected to stress,” *Phys. Rev. B*, vol. 83, no. 22, p. 224412, Jun. 2011.
- [23] K. Roy, S. Bandyopadhyay, and J. Atulasimha, “Energy dissipation and switching delay in stress-induced switching of multiferroic nanomagnets in the presence of thermal fluctuations,” *J. Appl. Phys.*, vol. 112, no. 2, p. 023914, 2012.
- [24] M. Salehi Fashami, K. Roy, J. Atulasimha, and S. Bandyopadhyay, “Magnetization dynamics, Bennett clocking and associated energy dissipation in multiferroic logic,” *Nanotechnology*, vol. 22, no. 30, p. 309501, Jul. 2011.
- [25] J. Walowski, M. D. Kaufmann, B. Lenk, C. Hamann, J. McCord, and M. Münzenberg, “Intrinsic and non-local Gilbert damping in polycrystalline nickel studied by Ti : sapphire laser fs spectroscopy,” *J. Phys. D. Appl. Phys.*, vol. 41, no. 16, p. 164016, Aug. 2008.
- [26] W. Bailey, P. Kabos, F. Mancoff, and S. Russek, “Control of magnetization dynamics in Ni/sub 81/Fe/sub 19/ thin films through the use of rare-earth dopants,” *IEEE Trans. Magn.*, vol. 37, no. 4, pp. 1749–1754, Jul. 2001.
- [27] S. E. Russek, P. Kabos, R. D. McMichael, C. G. Lee, W. E. Bailey, R. Ewasko, and S. C. Sanders, “Magnetostriction and angular dependence of ferromagnetic resonance linewidth in Tb-doped Ni[sub 0.8]Fe[sub 0.2] thin films,” *J. Appl. Phys.*, vol. 91, no. 10, p. 8659, 2002.
- [28] Y. Ren, Y. L. Zuo, M. S. Si, Z. Z. Zhang, Q. Y. Jin, and S. M. Zhou, “Correlation Between Ultrafast Demagnetization Process and Gilbert Damping in Amorphous TbFeCo Films,” *IEEE Trans. Magn.*, vol. 49, no. 7, pp. 3159–3162, Jul. 2013.
- [29] C. Vittoria, S. D. Yoon, and A. Widom, “Relaxation mechanism for ordered magnetic materials,” *Phys. Rev. B*, vol. 81, no. 1, p. 014412, Jan. 2010.
- [30] Q. Su, J. Morillo, Y. Wen, and M. Wuttig, “Young’s modulus of amorphous Terfenol-D thin films,” *J. Appl. Phys.*, vol. 80, no. 6, p. 3604, 1996.

- [31] S. M. Bhagat and D. K. Paul, "Magnetic resonances in a-TbFe₂, a-GdFe₂ and a-YFe₂," *AIP Conf. Proc.*, vol. 29, pp. 176–177, 1976.
- [32] W. F. Brown, "Thermal Fluctuations of a Single-Domain Particle," *Phys. Rev.*, vol. 130, no. 1677, 1963.
- [33] W. M. Saslow, "Landau–Lifshitz or Gilbert damping? That is the question," *J. Appl. Phys.*, vol. 105, no. 7, p. 07D315, 2009.
- [34] M. Stiles, W. Saslow, M. Donahue, and A. Zangwill, "Adiabatic domain wall motion and Landau-Lifshitz damping," *Phys. Rev. B*, vol. 75, no. 21, p. 214423, Jun. 2007.
- [35] N. Smith, "Comment on 'Adiabatic domain wall motion and Landau-Lifshitz damping,'" *Phys. Rev. B*, vol. 78, no. 21, p. 216401, Dec. 2008.
- [36] S. Iida, "The difference between gilbert's and landau-lifshitz's equations," *J. Phys. Chem. Solids*, vol. 24, no. 5, pp. 625–630, May 1963.
- [37] T. L. Gilbert, "Classics in Magnetism A Phenomenological Theory of Damping in Ferromagnetic Materials," *IEEE Trans. Magn.*, vol. 40, no. 6, pp. 3443–3449, Nov. 2004.
- [38] R. B. van Dover, M. Hong, E. M. Gyorgy, J. F. Dillon, and S. D. Albon, "Intrinsic anisotropy of Tb-Fe films prepared by magnetron Co sputtering," *J. Appl. Phys.*, vol. 57, no. 8, p. 3897, 1985.
- [39] F. Hellman, "Surface-induced ordering: A model for vapor-deposition growth of amorphous materials," *Appl. Phys. Lett.*, vol. 64, no. 15, p. 1947, 1994.
- [40] F. Hellman, R. B. van Dover, and E. M. Gyorgy, "Unexpected unidirectional anisotropy in amorphous Tb-Fe/Ni-Fe-Mo bilayer films," *Appl. Phys. Lett.*, vol. 50, no. 5, p. 296, 1987.
- [41] T. Niihara, S. Takayama, and Y. Sugita, "Perpendicular Anisotropy in Tb-Fe and Tb-Co Amorphous Films Sputtered in H₂-Added Ar Gas," *IEEE Trans. Magn.*, vol. 21, no. 5, pp. 1638–1640, 1985.
- [42] P. I. Williams and P. J. Grundy, "Magnetic and magnetostrictive properties of amorphous rare earth-transition metal alloy films," *J. Phys. D Appl. Phys.*, vol. 27, pp. 897–901, 1994.
- [43] F. Hellman, A. L. Shapiro, E. N. Abarra, R. A. Robinson, R. P. Hjelm, P. A. Seeger, J. J. Rhyne, and J. I. Suzuki, "∞ Long Magnetic Correlation Length in Amorphous TbFe₂," *Phys. Rev. B*, vol. 59, no. 17, pp. 408–417, 1999.

- [44] J. Z. Sun, R. P. Robertazzi, J. Nowak, P. L. Trouilloud, G. Hu, D. W. Abraham, M. C. Gaidis, S. L. Brown, E. J. O'Sullivan, W. J. Gallagher, and D. C. Worledge, "Effect of subvolume excitation and spin-torque efficiency on magnetic switching," *Phys. Rev. B*, vol. 84, no. 6, p. 064413, Aug. 2011.
- [45] A. Butera, J. Gómez, J. L. Weston, and J. A. Barnard, "Growth and magnetic characterization of epitaxial Fe₈₁Ga₁₉/MgO (100) thin films," *J. Appl. Phys.*, vol. 98, no. 3, p. 033901, 2005.
- [46] A. Butera, J. Gómez, J. A. Barnard, and J. L. Weston, "Magnetic anisotropy in Fe₈₁Ga₁₉/MgO (100) films sputtered at different powers," *Phys. B Condens. Matter*, vol. 384, no. 1–2, pp. 262–264, Oct. 2006.
- [47] A. Butera, J. L. Weston, and J. A. Barnard, "Ferromagnetic resonance of epitaxial thin films," *J. Magn. Magn. Mater.*, vol. 284, no. d, pp. 17–25, Dec. 2004.
- [48] J. V. Jäger, A. V. Scherbakov, T. L. Linnik, D. R. Yakovlev, M. Wang, P. Wadley, V. Holy, S. A. Cavill, A. V. Akimov, A. W. Rushforth, and M. Bayer, "Picosecond inverse magnetostriction in galfenol thin films," *Appl. Phys. Lett.*, vol. 103, no. 3, p. 032409, 2013.
- [49] N. Tiercelin, Y. Dusch, V. Preobrazhensky, and P. Pernod, "Magnetoelectric memory using orthogonal magnetization states and magnetoelastic switching," *J. Appl. Phys.*, vol. 109, no. 7, p. 07D726, 2011.
- [50] Y. Dusch, N. Tiercelin, A. Klimov, S. Giordano, V. Preobrazhensky, and P. Pernod, "Stress-mediated magnetoelectric memory effect with uni-axial TbCo₂/FeCo multilayer on 011-cut PMN-PT ferroelectric relaxor," *J. Appl. Phys.*, vol. 113, no. 17, p. 17C719, 2013.
- [51] S. Giordano, Y. Dusch, N. Tiercelin, P. Pernod, and V. Preobrazhensky, "Thermal effects in magnetoelectric memories with stress-mediated switching," *J. Phys. D: Appl. Phys.*, vol. 46, no. 32, p. 325002, Aug. 2013.

CHAPTER 6

THE EFFECT OF MAGNETIC NANOCONTACT FORMATION ON SPIN-TRANSFER DYNAMICS IN MgO MTJs

6.1 Introduction

The advent of ultra-thin MgO barriers and a growing understanding of the structure and chemistry of magnetic electrode-MgO interfaces have allowed for the fabrication of high TMR and low resistance area (R.A.) product magnetic tunnel junctions (MTJs) [1]–[6]. The high spin polarization of the tunnel-current [7], [8] in these low R.A. MgO MTJs have allowed for the observation of both spin-transfer switching [9]–[11] and DC driven steady-state magnetization dynamics [12]–[17]. The latter type of excitation bears promise for compact voltage-tunable microwave sources. It has been found by our group and others that typical microwave powers generated are in the 20-100 nW range and show frequency tuning ranges of about 1-2 GHz. Unfortunately, the room temperature linewidths accompanying the high bias, high power peaks are in excess of 300 MHz. The origin of broad linewidths in these tunnel junction structures is still a subject of debate. Noise sources arising from thermal fields, magnon-assisted tunneling, non-uniform spatial distribution of the current due to barrier inhomogeneity, and spin-torque shot noise have all been proposed as physical mechanisms for linewidth broadening. Whatever the case might be, the severe phase noise of these oscillators undermines their potential for many timing or communications circuit applications where source coherence is of utmost importance.

Here we report on the effect that repeated high voltage stress on an MTJ has on its microwave response to DC voltage. The stress-conditioning process leads to a significant reduction in the threshold for dynamic excitation compared to the unstressed samples (e.g from ~250 mV to ~120 mV), a drastic reduction of single peak linewidths down to ~ 10 MHz and with integrated powers (10–50 nW) comparable to unconditioned devices. Similar effects have been reported by other groups as well [14], [15]. They have attributed these changes in the spin-transfer driven dynamics to high current densities localized at hot-spots formed during the stressing of the junction. However, our study suggests that the creation of localized spots of increased current density cannot by itself account for the change in the dynamical behavior of the devices. Rather the data points to the formation of magnetic nano-bridges within the barrier region. These magnetic contacts have significant consequences for both the MTJ's quasi-static field-switching properties as well as its high frequency response to bias and field.

6.2 Experimental Procedure

The studies were conducted on MgO MTJs grown and patterned at HGST. The thin film stack structure for the devices under study were Bottom Lead/IrMn (61 Å)/CoFeB (18 Å)/Ru (4 Å)/CoFeB (20 Å)/MgO (7.6 Å)/CoFe (5 Å)/CoFeB (34 Å)/Ru (60 Å)/Ta (30 Å)/Ru (40 Å) which corresponds to an exchange-biased Synthetic Antiferromagnet (SyAF) fixed layer and simple free layer structure. The exchange bias of the SyAF was set along the easy axis of the ellipse. The devices under study were then patterned into 50x100 nm² ellipses by a combination of e-beam lithography

and Ar ion milling. Our field and voltage convention are such that $H > 0$ favors parallel alignment of the top SyAF and free electrodes and $V < 0$ means that electrons flow from the fixed to the free layer. First the junction was saturated with field into the P state ($H > 0$) and we ramped up the voltage ($V < 0$) on the junction until we observed a discontinuous drop in the parallel resistance. We then quickly ramped down the voltage. Many of the samples remained intact under the stressing until ~ 475 - 500 mV after which the junction resistance dropped abruptly to a complete short. However, approximately 40% of the samples exhibited a soft junction breakdown where the P resistance and the TMR dropped incrementally upon ramping the voltage bias up. The typical soft breakdown voltages varied quite considerably from sample to sample with a range of $V_b = 275$ -400 mV. We took magnetoresistance data (V/I vs. H) on these samples after the initial soft breakdown to see what effects stressing had on the zero bias TMR and the magnetics of the junction. We would then try to drive dynamics with a DC voltage and look at the microwave power spectrum. We would check if the resultant spectra showed signatures of a drastic drop in peak linewidths. The stressing process was repeated until the device showed these microwave characteristics at which point we deemed the device fully conditioned.

For the spectral measurements, we used a bias-tee to separate the DC and AC parts of the circuit. Through the DC port we applied a constant bias to the junction to excite the microwave dynamics. The AC port was connected to an Agilent E4408B Spectrum Analyzer using a total of +32 dB of amplification. Spectral measurements were then taken from 0.46-18 GHz with a RBW of 3 MHz. All spectral data, unless stated otherwise, has been calibrated by the frequency-dependent gain of the network

and represents the power delivered by the MTJ to a 50Ω termination. The calibration was performed by making an S_{21} measurement of the network without the device using an Agilent 8722ES Network Analyzer.

6.3 Quasistatics: Experiment and Simulations

The TMR of the MTJs drops during the conditioning process. (Figure 6.1a). The zero bias TMR of sample decreases from 82% to 31% which is not atypical for the TMR degradation between the conditioned and unconditioned states. The parallel resistance R_P of the conditioned junction is typically 50-120 Ω lower than its unconditioned value. For Sample 1, the drop in R_P is $\sim 100 \Omega$. This corresponds to increase of the MTJ zero-bias parallel conductance G_P of ~ 1 mmho between the unconditioned and fully conditioned device. These changes in the conductance and TMR reflect deformation and thinning of the barrier in localized weak spots and/or the formation of pinholes which serve as parallel lower MR channels for electron flow. But the far more interesting detail lies in the evolution of the hysteresis loops during the conditioning process.

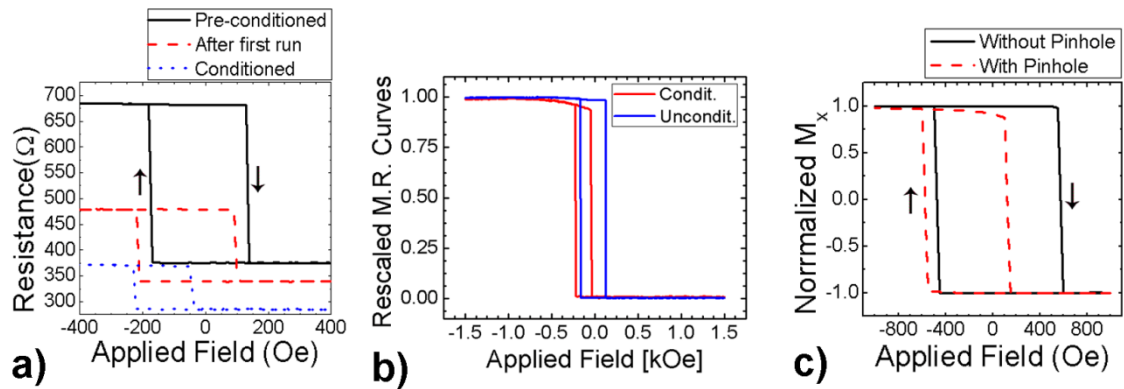


Figure 6.1 a) Room temperature field switching magnetoresistance curves taken during the conditioning procedure for Sample 1. b) Normalized M.R. minor field loops before and after conditioning for Sample 1. c) Zero-temperature OOMMF simulated field-switching curves of 4 nm free layer MTJ with and without pinhole.

Before conditioning, the AP \rightarrow P and P \rightarrow AP switching fields are comparable. After the first conditioning run, the AP \rightarrow P and P \rightarrow AP switching fields shift together towards ferromagnetic alignment. This indicates a simple shift of the center of the hysteresis loop. A shift of the hysteresis loop might arise from a strengthening of the Néel orange peel coupling due to a local roughening and thinning of the barrier. At this point, we do not observe the signatures of the conditioned state in the dynamical spectra. This would seem to suggest that the drop in resistance and TMR after the first conditioning is due to local barrier thinning. After further conditioning, the AP \rightarrow P and P \rightarrow AP switching fields again move in the negative field direction. But the irreversible changes in the switching fields no longer suggest a simple shifting of the loop. It is plain that now the AP \rightarrow P switching field has moved more than the P \rightarrow AP switching field in the negative field direction. The apparent coercivity of the loop has been reduced by nearly a half from its pre-conditioned state. In addition, the gradual

saturation of AP state with increasing negative field might signify non-uniform rotation and some kind of pinning mechanism acting on the free layer. The significant kinking before the AP→P reversal (seen clearly in Figure 6.1b) as the field goes from negative to positive fields corroborates this picture. This behavior indicates that the AP→P and P→AP switching mechanisms have become different during the stressing process.

Our hypothesis is that the differences in the AP→P and P→AP switching mechanisms arise from ferromagnetic electrode material present in pinholes that open up during the conditioning process. These magnetic pinholes can serve to locally exchange couple the free and fixed layers. This coupling would generate an asymmetry between the AP and P states of the free layer. One might expect that the AP state would feature a domain wall localized in the contact region [18] while exchange would force the magnetization of the P state to be fairly uniform. This morphological distinction between the states could be the origin of the observed field switching asymmetries as well as the dragging/pinning behavior in the AP state. We used the zero-temperature OOMMF micromagnetic package to test our hypothesis. We modeled the P and AP equilibrium configurations and the field switching of the Bottom SyAF (2 nm)/Ru (.5 nm)/Top SyAF (2 nm)/Barrier (1 nm)/Free Layer (4 nm) with and without a magnetic pinhole. The cross-sectional area of the simulated device was 50x100 nm². We used a lateral mesh resolution of 2.5 nm, a depth resolution of .5 nm, a saturation magnetization $M_s = 1160 \text{ emu/cm}^3$ for the magnetic layers, and an exchange stiffness $A_{\text{CoFeB}} = 28 \times 10^{-12} \text{ J/m}$ for the whole structure including the pinhole region and its coupling to the free and fixed layers. The pinhole diameter was set at 5

nm for simulating the switching curves, although the estimated upper-bound on the pinhole diameter is a little bit lower. The larger diameter was used for calculational convenience in generating the simulated field switching curves. We calculated the nanocontact resistance by assuming that it was parallel to the MTJ resistance and using the parallel resistance of the junction before and after conditioning. We then employed a Maxwell-Sharvin calculation to place an upper bound estimate of 3 nm on the nanocontact diameter provided that it is metallic (which it may not be) [19]. We observe no qualitative difference in the equilibrium configuration of the P and AP state for a 5 nm and 3 nm diameter pinhole (not shown).

The micromagnetic simulations show that a domain wall is present in the AP state centered near the pinhole region (Figure 6.2a). The free-layer magnetization in the region above and around the contact deviates strongly from the free layer easy axis as can be seen in Figure 6.2b. The resultant AP state generated by contact-mediated exchange between the free layer and top SyAF is one of non-uniform magnetization and the free layer magnetization deviates strongly from collinearity with the polarizer layer in the vicinity of the contact. On the other hand, the P state (Figure 6.2e) is magnetically uniform through the top SyAF layer/pinhole/free layer system and laterally in the free layer as dictated by the exchange interaction.

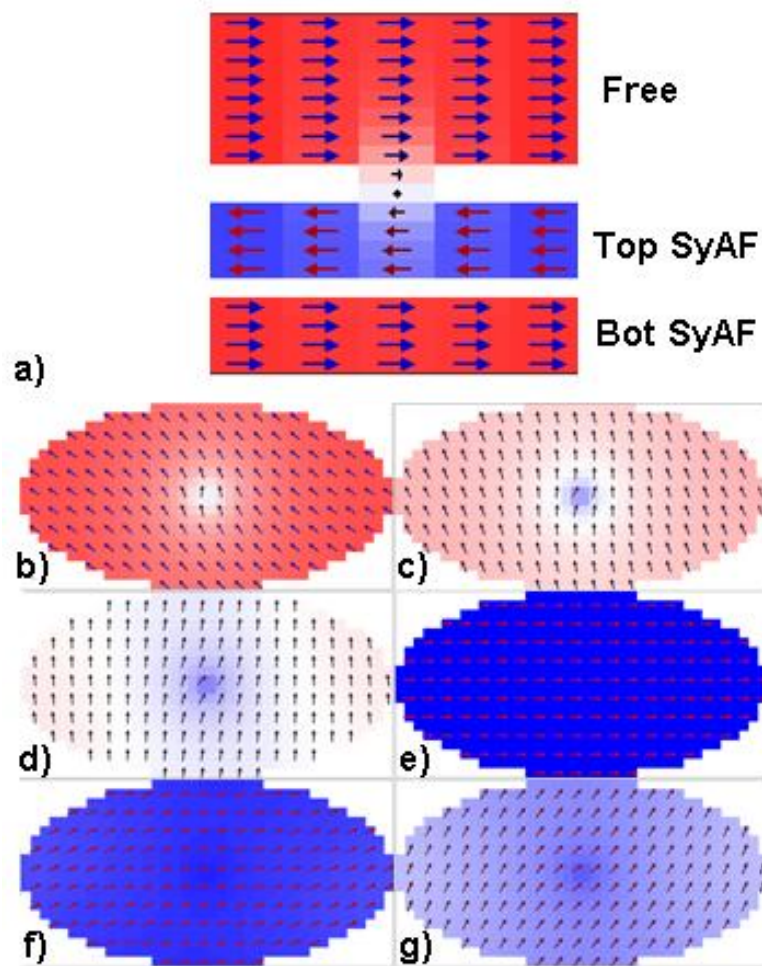


Figure 6.2 a) Simulation results for the equilibrium magnetization of the AP state at $H = -400$ Oe with a simulated pinhole diameter of 3 nm. The magnetization in the pinhole shows the existence of Bloch-type domain wall localized in the constriction. b), c), d) show the AP \rightarrow P switching process. e) P state configuration f), g) show P \rightarrow AP switching process. The switching snapshots were taken with a pinhole diameter of 5 nm.

A quick comparison of the simulated field switching curves for a device with the pinhole and one without the magnetic nanocontact show that the simulations qualitatively reproduce the evolution of the switching fields as the samples goes from the unconditioned to the conditioned state (Figure 6.1c). For the simulation with the

nanocontact the $P \rightarrow AP$ free layer switching field is 100 Oe larger than for the simulation without the nanocontact. This reflects the fact that the exchange coupling through the contact prefers the free layer to be aligned with the top layer of the SyAF. On the other hand, the $AP \rightarrow P$ switching field has shifted by nearly 450 Oe towards negative fields. The apparent coercivity of the loop has decreased by 350 Oe. The sizeable asymmetry in the shifting of the switching fields upon introduction of a magnetic nanocontact can now be readily explained by looking at the switching kinetics. The simulations also capture the saturation behavior of the M.R. loop in the AP state and the kneeing of the AP branch near the $AP \rightarrow P$ switching field for conditioned samples. . The $AP \rightarrow P$ switching is inherently a spatially nonuniform process aided and actuated by ferromagnetic exchange in the nanocontact region. The non-uniform magnetization near the pin-hole initiates the switching process and drags the rest of the magnetization over the hard axis. The kneeing is likely a signature of this constriction mediated exchange on the rest of the free layer. The magnetic contact severely reduces the $AP \rightarrow P$ transition by creating an interaction which tries to make the free layer spring back into the P state. The $P \rightarrow AP$ reversal can be approximately thought of as coherent rotation in its initial stages. The effect of the pinhole in the $P \rightarrow AP$ switching thus can be approximately thought of as an effective average coupling field in the Stoner-Wohlfarth reversal of the free layer. After the $P \rightarrow AP$ reversal, the ferromagnetic coupling between the pinned top SyAF and the free layer generates a pinning/exchange spring effect on the free layer. Application of higher field is thus required to saturate the free layer.

We conducted Scanning Transmission Electron Microscopy (STEM) on micron junctions coming from the same chip as the nanojunctions we measured in order to test whether weak-links in the MgO barrier and/or magnetic contacts existed in the film stacks that were grown, what the typical size for them were, etc. These pre-existing weak links would serve as seeds for nanocontact formation under current stress and would also account for the fact that we measured some devices which exhibited conditioned behavior before any voltage stressing. The samples were prepared by lift-out using an FEI Nova 600 Dual Beam FIB and then transferred to the NION Ultra-STEM 100 for imaging. The cross-sectional images show evidence of small areas where the MgO tunnel barrier is very thin or even disconnected throughout the film. Figure 6.3 shows a close-up of one of these nano-holes both in ADF-STEM as well as with an Electron Energy Loss Spectroscopy (EELS) Co and O composition map.

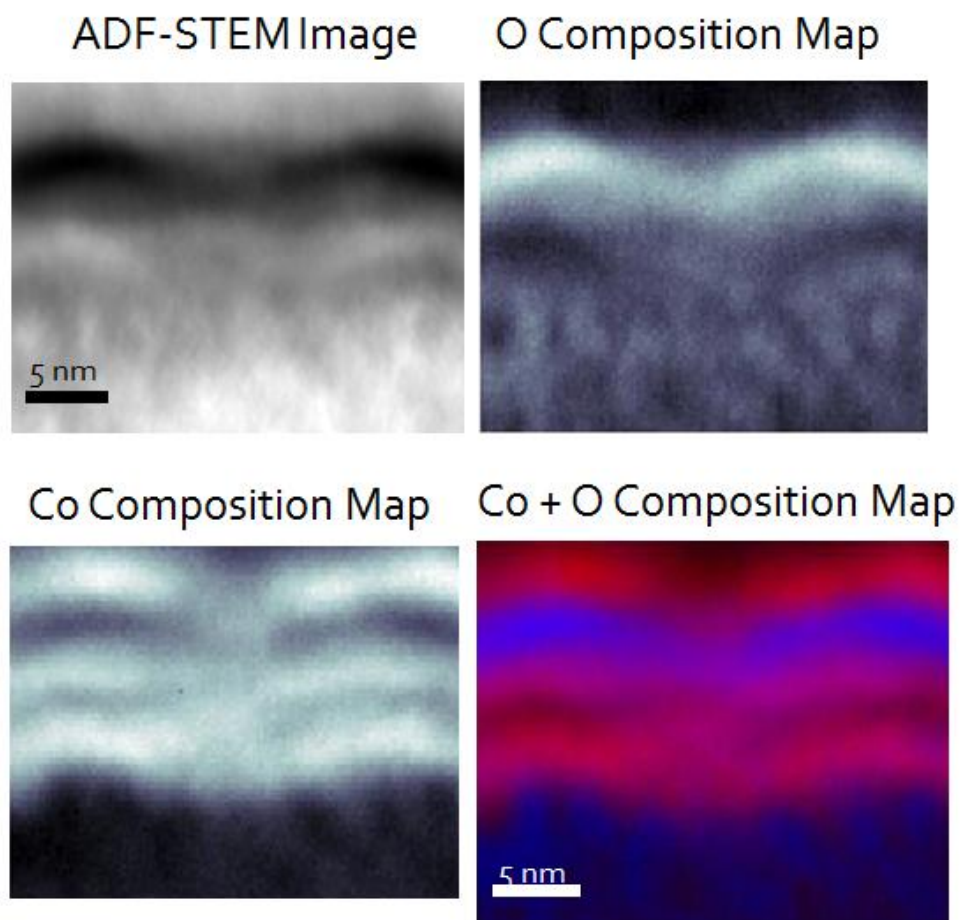
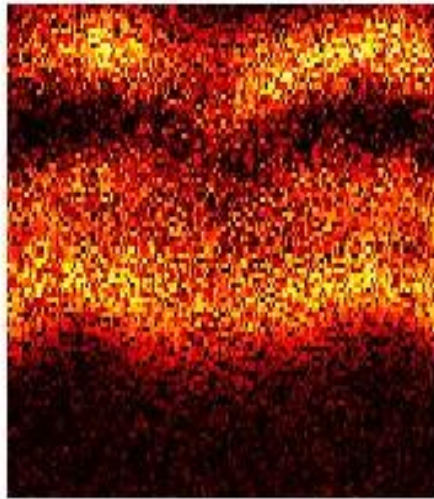


Figure 6.3 Annular dark-field (ADF) STEM and EELS spatial mapping for Co and Oxygen near a magnetic pinhole. The approximate diameter of the nanocontact is ~ 3 - 4 nm. Images taken by P.Y. Huang.

The typical diameter for these nanoscale pinholes are on the order of $d \sim 3 - 4$ nm. As can be seen from the above EELS map, Co (and presumably Fe) appears within this pinhole region. It is not clear from this image whether the Co and Fe in pinhole region is predominantly metallic or oxidic. We conducted a Multivariate Curve Resolution (MCR) fitting of the EELS peaks corresponding to Co in order to determine whether the Co was metallic within the pinhole region. The result of the spatial mapping for metallic type Co is presented in Figure 6.4.



MCR
Fitting:
Co Metal

Figure 6.4 Spatial mapping of the MCR fitting for metallic-type Co EELS signal. Courtesy of P.Y. Huang.

The MCR fitting clearly shows that the Co is not necessarily metallic within the pinhole region (although more metallic Co may enter the pinhole region through electromigration under repeated voltage/current stress). It is thus likely that the region where magnetic coupling between the layers emerges during conditioning is not necessarily metallic and, where it is metallic, the contact is rather dirty (i.e. full of oxidized components). The magnetic coupling thus might emerge as direct CoFeB-CoFeB electrode contact in the pinhole or via exchange by CoFe oxides and sub-oxides – many of which are ferrimagnetic (e.g. CoFe_2O_4). In addition, there are regions near the magnetic contact where the MgO barrier is intact but considerably thinner than in other parts. The Maxwell-Sharvin calculation (under the Wexler interpolation) that we employed for estimating the contact diameter thus likely provides an underestimate for the actual magnetic nanocontact area. Our model of

magnetic contacts opening up under voltage stressing and coupling the free and SyAF layers is thus supported both by TEM and changes in the field switching behavior of the devices. Next, we look to see what the consequences of magnetic nano-contact formation and the conditioning process has on spin-transfer induced GHz dynamics of these structures.

6.4 Dynamical Properties

Microwave emissions for the post-stressed samples were studied as a function of bias voltage and fields applied along the easy axis of the free-layer ellipse. The range of bias voltages explored changed from sample to sample depending on what biases were deemed safe to operate at without risking further barrier degradation. We mapped out the combined power phase diagram of the first and second harmonics for the conditioned samples. The data were taken by starting at negative field and sweeping to positive field. For each field the voltage was stepped from positive to negative voltages in 10 mV steps. As a point of comparison, we also took the phase diagram of a representative pre-stressed MTJ (Figure 6.5a). The dynamical phase diagram of the pre-stressed samples is fairly symmetric between the P with $V > 0$ and the AP state for $V < 0$ and the minimum linewidth case for high bias is fairly incoherent with a linewidth of about 400 MHz (Figure 6.5c). This situation is markedly different for the post-stressed samples (Figure 6.5b). We see large microwave power output when the sample is in the AP state ($H < 0$) with $V < 0$. This

area of the phase diagram corresponds to the highly coherent oscillations characteristic of the conditioned samples (Figure 6.5d).

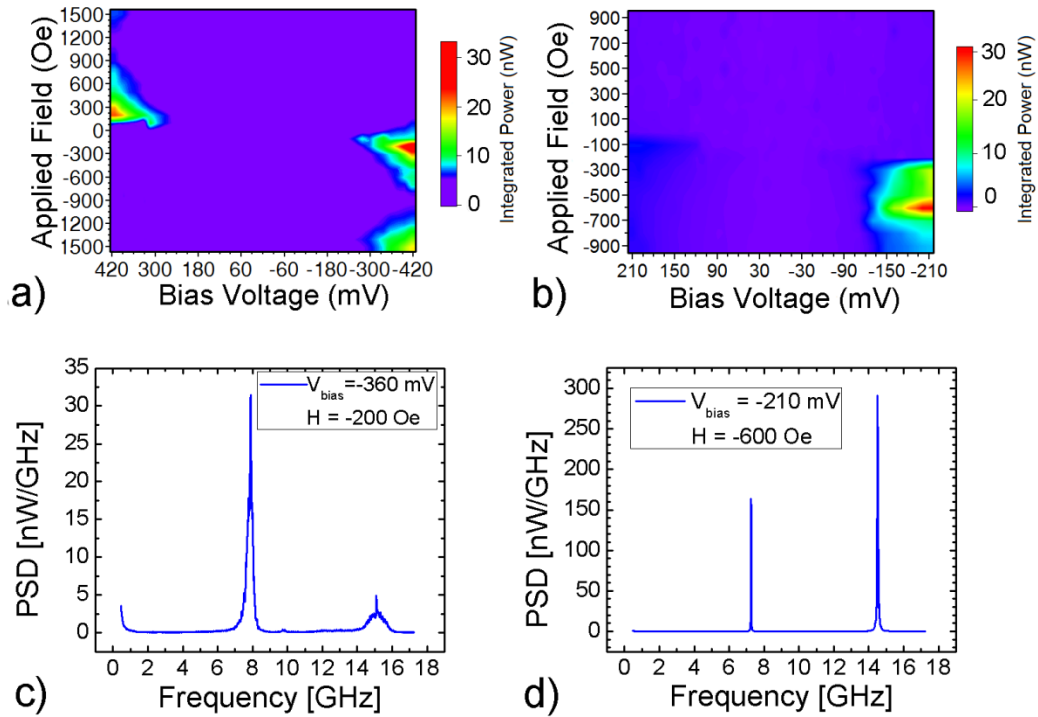


Figure 6.5 a) Power of first and second harmonics generated by an unstressed MTJ as a function of field and bias voltage. b) Power of first and second harmonic for conditioned MTJ. c) Typical Power spectral density (PSD) of unconditioned sample. d) Typical PSD after stressing procedure.

We can see that the dynamics continue with high power out to fields of >900 Oe and the critical voltages for these coherent excitations do not change much from their low field value of $V_c = -120$ mV. While not seen in this sample (due to voltage constraints), many samples display high frequency excitations in the AP state for high $V > 0$. The oscillations redshift with increasing applied field. Given the voltage polarity and the frequency vs. H behavior of this mode we conclude that it arises from

excitation of the SyAF acoustic mode [20]. The most obvious feature of the dynamical phase diagram is seen when the sample is in the P state with $V > 0$. The large power, coherent microwave emissions present in the AP state are absent in this region of the phase diagram. We tested a few samples which could handle higher voltages without further breakdown out to a voltage of $V^+ > 2.5V_c^-$ and we still do not observe coherent high power oscillations. We see peaks on the P side but they are barely above the Johnson/shot-noise floor and correspond to thermally-excited FMR (TE-FMR) noise signals [21].

The asymmetry between the P and AP states in the dynamical phase diagram of conditioned samples is not consistent with a simple thinning of the barrier. Assuming that the tunneling still largely governed by elastic tunneling processes, the Slonczewski torque in MTJs would lead to symmetric critical voltages for dynamical excitation in the P and AP state (assuming symmetric electrode materials) [22]. We argue that the dynamical asymmetry emerges as a consequence of the difference in the magnetic configurations of the P and AP state. The P state contains no domain wall and the exchange coupling enforces a relatively uniform magnetization profile in the free layer and collinearity of the free layer with the polarizer. Thus the initial spin-torque in the P state is relatively small. The magnetic nanocontacts, on the other hand, enforce the AP state to be non-uniform and in particular push the free layer and top SyAF moments away from 180 degree collinearity. This deviation between from electrode collinearity can greatly enhance the spin torque on the free layer in the AP state. Due to the fact that the junction resistance is still quite high after conditioning

we suspect that an appreciable portion of this spin torque is exerted through thinned/intact parts of the barrier surrounding the magnetic nanocontact areas.

The low-bias peaks of conditioned MTJ devices in the AP state are consistent with TE-FMR noise. However, unlike the unstressed samples, the spin-transfer induced excitations do not evolve smoothly with bias from the TE-FMR mode and we observe that the spin-torque at onset stabilizes a mode whose frequency is not directly related to the FMR modes excited by thermal noise (Figure 6.6a). We conclude from the frequency vs. field-dependence (Figure 6.6c) that the oscillations for $V < 0$ are consistent with predominantly free-layer excitations and do not exhibit $df/dH < 0$ typical of SyAF excitations.

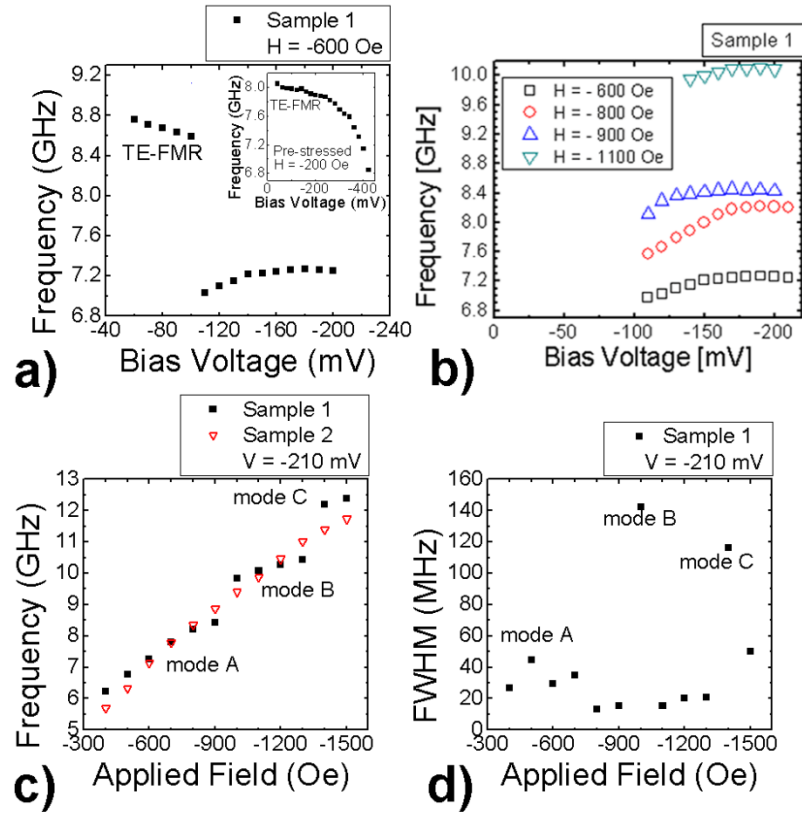


Figure 6.6. a) Frequency vs. V_{bias} for a sample exhibiting weak blue-shifting. Inset shows smooth evolution of TE-FMR modes into STT-driven modes in a different unconditioned device with red-shifting vs. V_{bias} behavior. b) Frequency vs. V_{bias} for Sample 1 at different field values. The frequency vs. V_{bias} does not have an obvious dependence on in-plane applied field. c) Frequency vs. field for oscillations at high bias. Different samples show different type of field behavior in their dynamics after conditioning. d) FWHM of the 1st harmonic vs field at high bias. Shows sharp increase in the linewidth associated with the frequency jumps indicating mode bi-stability.

We have observed that some samples exhibit frequency jumps between different modes at a fixed bias as the field is increased. This can be seen in Figure 6.6c. We found that the critical voltage and the onset of these frequency jumps exhibited no voltage hysteresis [23]. This fact rules out the possibility that the frequency jumps are due to current-induced generation of different metastable magnetic configurations.

This sort of hysteresis is observed in cases where the Oersted field can change the metastable configuration of the magnetization near spots of high current density. The lack of voltage hysteresis is in line with the increase of the linewidths near the onset of each frequency jump and indicates mode bistability at the onset of each mode (Figure 6.6d).

The weak blue-shifting spectrum as seen in Figure 6.6 a) and b) has been previously interpreted as evidence for out-of-plane character oscillations in the free layer induced by the current hot-spots [14]. However, the relatively weak shifting of the frequency vs V_{bias} and the in-plane field dependence of the oscillator frequency makes this scenario unlikely. The origin of the blue-shifting is potentially due to a strong tilting of the free layer magnetization equilibrium angle away from the easy axis during oscillations combined with an increasing average effective field on the magnetization as the oscillation increases associated with SyAF-FL exchange coupling and the free layer anisotropy field. This tilting could be partly due to the spin torque but we also think that the ferromagnetic exchange between the top SyAF layer and the free layer through the magnetic nanocontacts are also important in determining this tilting. This SyAF-FL exchange coupling could force the free and fixed layer configuration to deviate substantially from collinearity near the magnetic nanoconstrictions as can be seen in Figure 6.2b.

The existence of large effective misalignment angles is consistent with the 1f and 2f peak structure. Even at the critical voltage, the integrated power in the 1f peak

as compared to the power in the 2f peak is rather substantial. We plot the integrated power delivered to our 50Ω load.

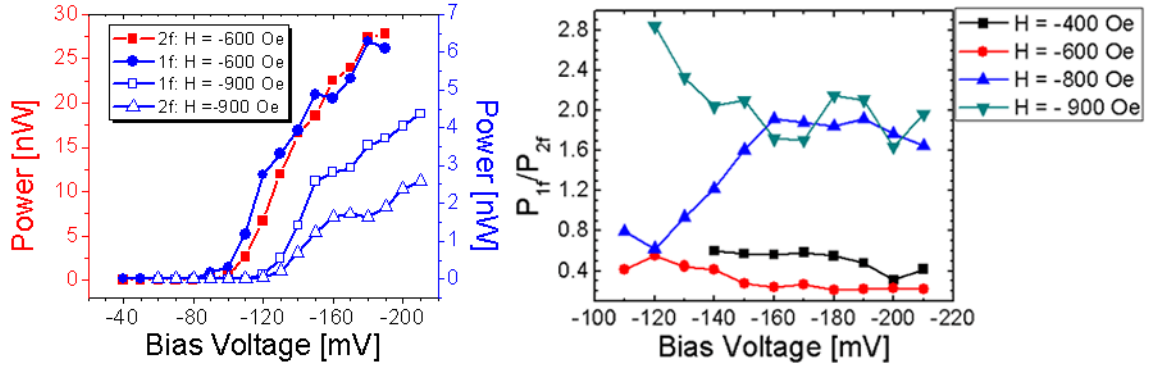


Figure 6.7 a) 1f and 2f integrated power delivered to a 50 load as a function of DC voltage bias for a lower field $H = -600$ Oe and a higher field $H = -900$ Oe. b) Ratio of first to second harmonic integrated power at different fields.

As can be seen the power in the 1f peak relative to the 2f peak is not negligible even close to onset. At many applied field strengths, the power in 1f is considerably larger than in 2f. With the applied field along the easy axis we would expect a very small signal at 1f and that most of the power is at 2f. The presence of an appreciable power at 1f means that there is a substantial effective equilibrium misalignment angle (away from 180 degrees) between the polarizer and free layer. This can be seen by deriving expressions for the oscillatory part of the conductance. The conductance of an MTJ can be expressed as:

$$G(\varphi) = \left(\frac{G_{AP} + G_P}{2} \right) \cdot \left(1 + \left[\frac{G_P - G_{AP}}{G_P + G_{AP}} \right] \cos(\varphi) \right) \quad (6.1)$$

Under the assumption that the in-plane part of the oscillation can be approximated as $\varphi(t) = \varphi_{mis} + \varphi_{prec} \sin(\omega t)$, the time-dependent part of the conductance can easily be shown to be:

$$\Delta G_{RF}(t) = \frac{G_P - G_{AP}}{2} \left[2J_2(\varphi_p) \cos(\varphi_{mis}) \cos(2\omega t) - 2J_1(\varphi_p) \sin(\varphi_{mis}) \sin(\omega t) \right] \quad (6.2)$$

J_1 and J_2 are Bessel functions of the first kind. We have terminated the Bessel-function expansion at terms that include only the ω and 2ω terms. We have ignored higher order terms as they are smaller. An MTJ under a DC voltage bias that is undergoing an auto-oscillation will produce a RF voltage:

$$V_{RF}^{source} = -V_{DC} \langle R_{MTJ} \rangle \cdot \Delta G_{RF}(t) \quad (6.3)$$

Equation (6.3) is only valid when $\Delta R_{RF}(t) \ll \langle R_{MTJ} \rangle$. The measured RF voltage and power will only have components at ω when φ_{mis} deviates substantially from either 0 or 180 degrees. Thus this analysis shows that the average equilibrium angle between the free and fixed layer for our conditioned junctions has substantial deviations from collinearity even close to the critical voltage for spin-transfer dynamics.

The increase in P_{1f}/P_{2f} for larger applied field $H < 0$ (seen in Figure 6.7b) indicates that the effective in-plane misalignment angle is large for larger fields along the easy axis. This does not make too much sense from the point of view of a magnetically uncoupled free and fixed layer system. In such a case, we would expect that the ratio of P_{1f}/P_{2f} would decrease as a function of in-plane field as the free layer

was enforced to be closer to 180 degrees with respect to the top SyAF layer. However, the observed behavior might be possible in a system where the free layer and top SyAF layer are ferromagnetically coupled. In that case, the ferromagnetic coupling between the top and free layer, the antiferromagnetic RKKY coupling between the top and bottom SyAF layers and the exchange bias on the bottom SyAF and the influence of the spin-torque all need to be taken into account. It may be possible that, given the right layer thicknesses, interlayer coupling strengths and spin-torque that an increasing in-plane bias field favoring AP alignment actually counter-intuitively serves to increase the misalignment angle. This is something that we have not yet tested but could be verified with micromagnetics.

In order to make meaningful comparisons between magnetic oscillation powers at different bias voltages, the measured integrated power in 1f and 2f needs to be normalized by V_{bias} and should take into account changes in $\langle R_{MTJ}^{AP} \rangle$. Changes in $\langle R_{MTJ}^{AP} \rangle$ can come from the bias dependence of the TMR as well as changes in the misalignment and precessional amplitude associated with the dynamics. The bias dependence of the average resistance as well as the average conductance relative to the conductance in the P state is plotted in Figure 6.8. We note that the maximum difference in the conductance $G_P - G_{AP}$ will also depend on V_{bias} and that this should be taken into account to truly normalize the oscillation power. Unfortunately, this cannot be done for high biases in the AP state as the measured conductance will include contributions from the dynamics and misalignment as well as the TMR bias dependence.

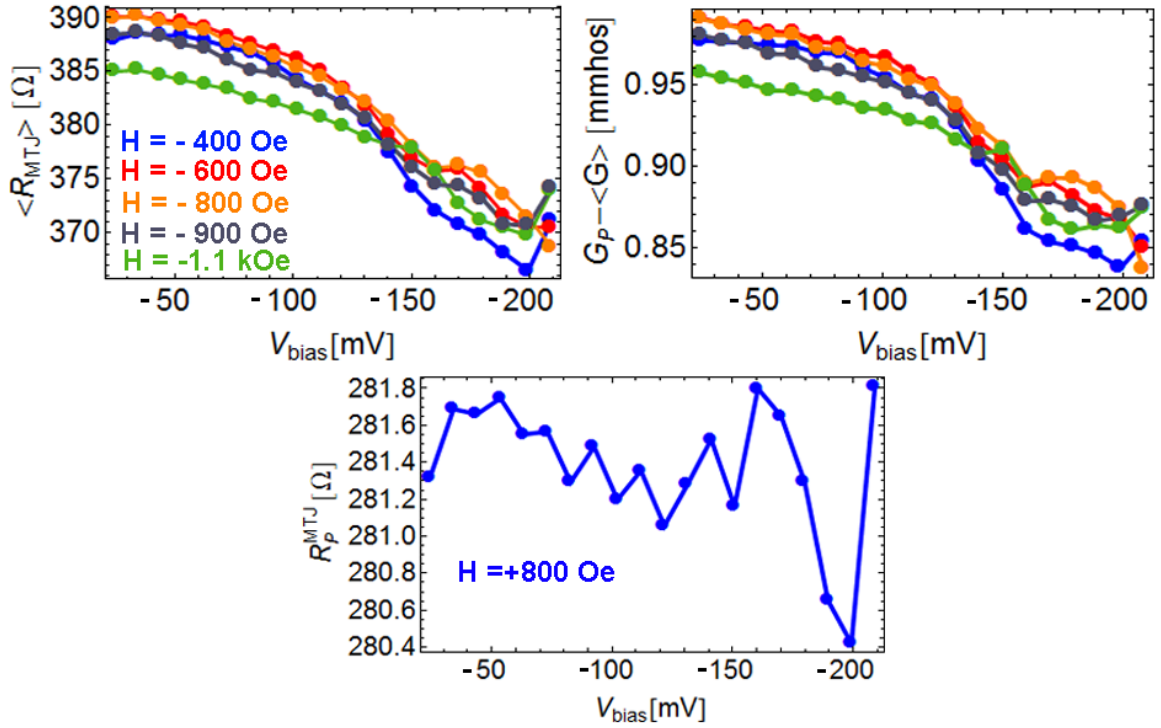


Figure 6.8 Average DC Resistance, average DC conductance with respect to the parallel conductance, and the parallel resistance as a function of V_{bias} across the MTJ for different field values. All data shown here was for Sample 1.

If we ignore the renormalization of the oscillation power by the TMR bias dependence, the normalization procedure is rather simple. We treat the MTJ as an RF voltage source outputting $-V_{DC} \langle R_{MTJ} \rangle \cdot \Delta G_{RF}(t)$ with an internal resistance $\langle R_{MTJ} \rangle$. A large part of the voltage is dropped across the internal source resistance and a fraction is delivered to $Z_0 = 50\Omega$ load in the spectrum analyzer. The measured voltage at the 50Ω termination is simply:

$$V_{RF}^{meas} = -V_{DC} \langle R_{MTJ} \rangle \cdot \Delta G_{RF}(t) \left(\frac{Z_0}{\langle R_{MTJ} \rangle + Z_0} \right) \quad (6.4)$$

Equation (6.4) is only correct when parasitic capacitances between the pads and Si substrate can be neglected. The shunting to the Si substrate, however, is quite negligible as the UHF-compatible devices supplied by HGST were fabricated on high-resistivity substrates. Equation (6.4) can be recast into a relation between the conductance oscillation power and the power delivered to the 50Ω load.

$$\langle (\Delta G_{RF})^2 \rangle = \left(\frac{\langle R_{MTJ} \rangle + Z_0}{\langle R_{MTJ} \rangle Z_0} \right)^2 \cdot \left(\frac{2Z_0 (P_{RF}^{meas} / A(\omega))}{V_{DC}^2} \right) \quad (6.5)$$

We have also included the frequency dependent power gain factor $A(\omega)$ associated with our amplifiers and any RF losses in the line. This simple division by the gain as expressed in Equation (6.5) is only valid when the amplifier input impedances are Z_0 . We plot the normalized conductance PSD calculated by Equation (6.5) vs. frequency at $H = -600$ Oe.

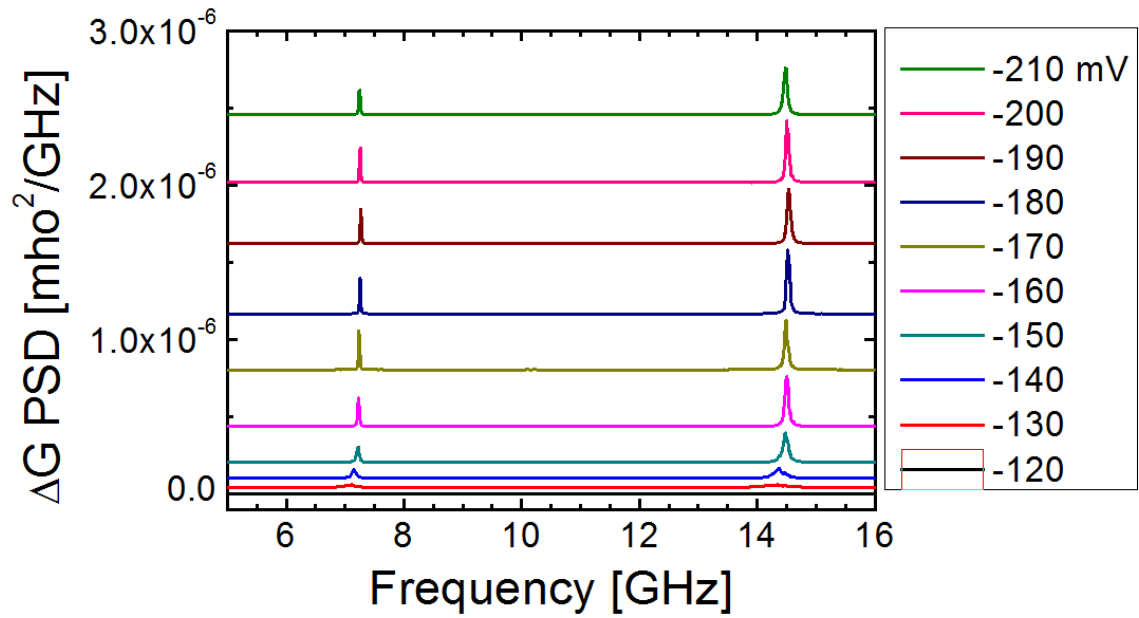


Figure 6.9 Conductance power spectral density of Sample 1 as a function of frequency for $H = -600$. This field and sign of voltage corresponds to configuration for the highest integrated microwave power emissions observed from Sample 1.

We plot the integrated conductance power in $1f$ and $2f$ across a wide range of field values for Sample 1 in Figure 6.10. The integrated power conductance power shows saturation after a particular voltage bias. This has been observed at all the fields we have measured and across all the conditioned samples we looked at.

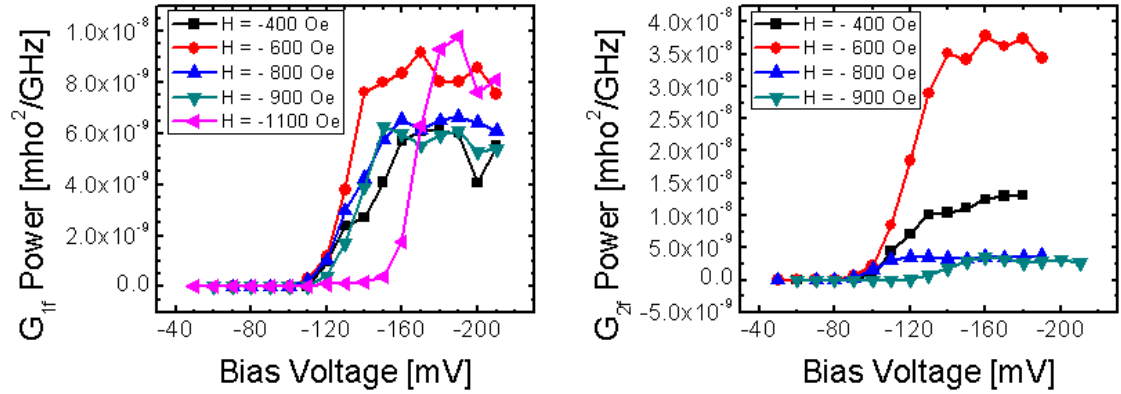


Figure 6.10 Integrated conductance power for 1f and 2f peaks. Note that after the initial increase in the conductance power, the power saturates for both 1f and 2f (i.e. $d\langle(\Delta G)^2\rangle/dV_{bias}$ becomes small).

This saturation phenomenon of the conductance power is not due to large amplitude saturation (i.e. $\Delta G_{prec} \rightarrow \Delta G_{max}$). In fact, we argue that the oscillation amplitude is, in general, quite small. We plot the oscillation conductance amplitude ΔG_{prec} in Figure 6.11 for 1f and 2f at $H = -900$ Oe which corresponds to the field at where the oscillation linewidths are quite low. The oscillation conductance amplitude scales are small compared to the scale set by $G_p - \langle G \rangle$ (see Figure 6.8). Note that $G_p - \langle G \rangle$ will be smaller than the full ΔG_{max} so that the oscillation conductance scale is even smaller when compared to ΔG_{max} .

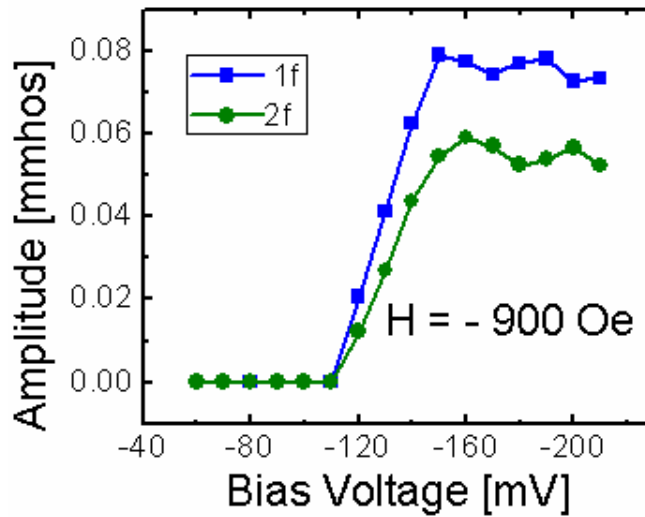


Figure 6.11 Conductance oscillation amplitude at 1f and 2f for Sample 1 at $H = -900$ Oe. Amplitude was obtained by taking the square root of the conductance power.

This power saturation behavior implies that, as the bias increases, the oscillation reaches a portion of the effective energy surface such that a slight increase in the oscillator energy does not increase the amplitude by very much. Thus increasing V_{bias} serves to increase the amplitude and oscillator power by a small amount. This is tantamount to a dynamic amplitude dependent stiffening of the oscillation. Lee et al. [24] have pointed out that this sort of power saturation can be thought of as an enhanced dynamical damping of the oscillations in the framework of the nonlinear auto-oscillator theory. In their experiment, the dynamical damping occurred due to negative micromagnetic feedback between the left and right sides of the elliptical free layer and the spin-torque. In our case, we think that the exchange coupling between the top SyAF layer and the free layer generated by the magnetic nanocontacts is likely responsible for this power saturation.

We have plotted the oscillation linewidth vs V_{bias} for Sample 1 at few different applied fields (Figure 6.12). We have observed no general trend in the coherence as a function of applied in-plane easy axis field up until one goes below fields of ~ 300 Oe and above 1.5 kOe –where the minimum linewidths become larger than 100 MHz. In the former case, the decrease in oscillator coherence is probably associated with thermally activated hopping between a metastable static state and the dynamical state. In the latter case, the field is close to the SyAF spin-flop field (inferred from the fact that for $H_{\text{app}} > 1.5$ kOe R_{AP} starts to decrease gradually signifying SyAF scissoring) and likely SyAF dynamics will start to play a role in the coherence of the oscillator.

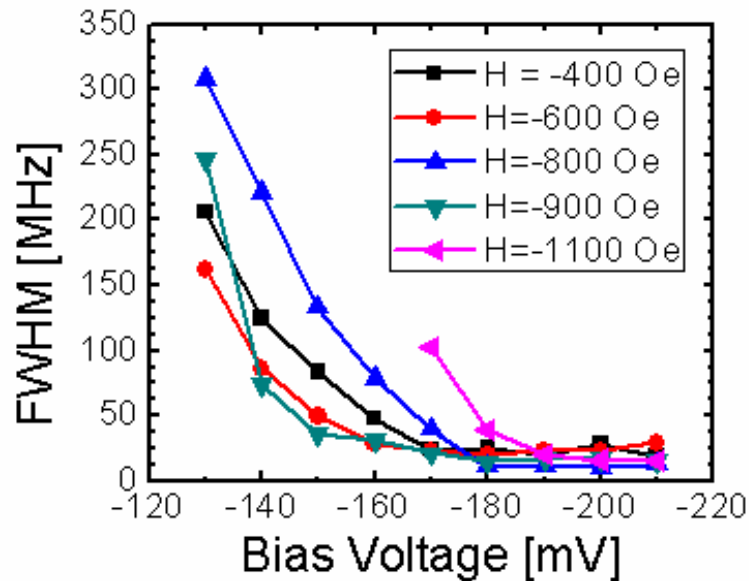


Figure 6.12 FWHM of 1f peak vs V_{bias} for Sample 1 at $H = -600$ Oe and $H = -900$ Oe.

The lowest linewidths that we observe for Sample 1 occur at $H = -800$ Oe with a minimum linewidth of $\Delta f = 11$ MHz for the 1f peak at $V_{\text{bias}} = -180$ mV. Low

linewidths < 50 MHz can be seen for a V_{bias} region of $160 - 210$ mV for $H = -400$ Oe, $150 - 210$ mV at $H = -600$ Oe, $170 - 210$ mV for $H = -800$ Oe, $150 - 210$ mV for $H = -900$ Oe, $180 - 210$ mV for $H = -1100$ Oe. These regions of low linewidth tend to be correlated with the region where the normalized power saturates. For example, when $H = -1100$ Oe, the normalized power saturates at $V_{\text{bias}} = -180$ mV which corresponds to the bias region where the linewidth starts to tighten. The same is true for $H = -900$ where the linewidths start to tighten substantially at $V_{\text{bias}} = -160$ mV corresponding to the region where the normalized power starts to saturate. This correspondence holds true for $H = -400$ ($V_{\text{bias}} > 160$ mV for 1f peak) and $H = -600$ Oe for V_{bias} . There is a slight deviation at $H = -800$ Oe where the 1f peak starts power saturation at $V_{\text{bias}} = -160$ mV whereas the low linewidth region starts at $V_{\text{bias}} > -170$ mV. That being said, the correspondence between conductance power saturation and the low linewidth region is quite strong.

The key point emerges when one sees that the low linewidth region is also in a bias range where df/dV_{bias} becomes very small. For $H = -600$ Oe and $H = -800$ Oe we plot the normalized power, the oscillation frequency vs V_{bias} and the linewidth.

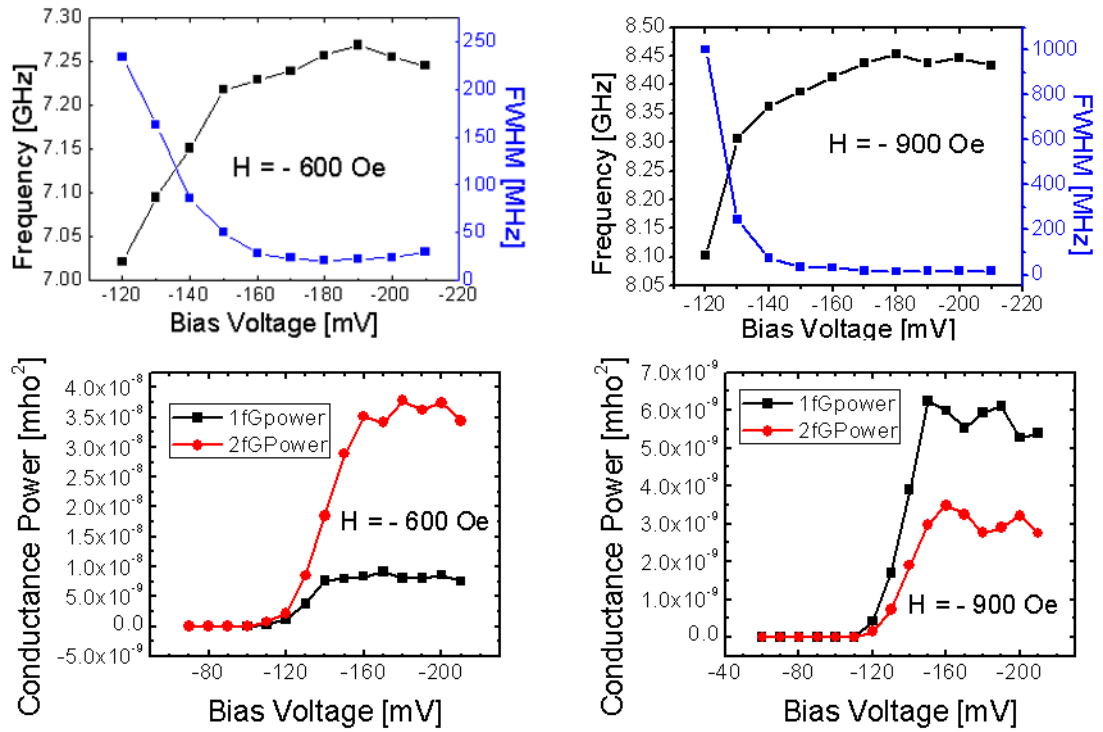


Figure 6.13 Frequency, 1f peak FWHM, and 1f and 2f conductance plotted as a function of V_{bias} at $H = -600$ Oe and $H = -900$ Oe for Sample 1.

It is easy to see that the region where the linewidth is lowest is precisely where df/dV becomes close to zero *and* the normalized power saturates. This phenomenon occurs for all conditioned samples and at all fields where highly coherent oscillations are observed. The saturation of the oscillation frequency with bias voltage makes sense in this picture. As $\omega(p) = \omega_0 + Np$ ($N = d\omega/dp$ being the nonlinear frequency shift), when the normalized power p (which is proportional by a simple constant to the conductance power) saturates we expect that the oscillation frequency should also saturate regardless of what N is.

This gets to the central point that it is the saturation of the oscillation power which predominantly determines the coherence of these oscillators. The dimensionless frequency shift parameter is $\nu = N / \Gamma_{eff}$ and the STNO linewidth can be written as:

$$\Delta\omega = (1 + \nu^2)\Gamma_+(p_0) \frac{k_B T}{\mathcal{E}(p_0)} \quad (6.6)$$

Much work has focused on reducing N by tailoring magnetic anisotropies, equilibrium magnetization angle, polarizer direction, etc. It is very clear from our data of the normalized conductance power, frequency vs. bias, and linewidth behavior that N is probably not negligible as the region where the normalized power increases as a function of bias corresponds roughly to a region where the frequency shift is non-negligible and where the linewidths are larger (generally >75 MHz and usually considerably larger than that). The denominator of ν (i.e. Γ_{eff}) on the other hand will be very large in the normalized power saturation region. This is easy to see as the expression for Γ_{eff} , as pointed out by Lee et al., can be written as:

$$\Gamma_{eff} = \Gamma_0 \left(V_{bias} \frac{dp}{dV_{bias}} \right)^{-1} \quad (6.7)$$

Here Γ_0 is simply proportional to the Gilbert damping. When the normalized power vs. voltage saturates and dp/dV becomes zero, Γ_{eff} diverges and the dimensionless nonlinear frequency shift ν vanishes. From Equation (6.6) this means

that the contribution to phase noise arising from non-linear amplitude-frequency coupling disappears and the linewidth in this saturated power region is correspondingly very low. Cast into physical terms: when the system is stiff, it will be less susceptible to Gaussian-noise driven amplitude fluctuations and the noise arising from the nonlinear frequency-amplitude coupling will become small.

At this point, it would be nice to quantify the dimensionless power p (instead of our conductance power) and use this to put numbers on N and Γ_{eff} . We have not done this yet, but we can and will in the near future. This would be essentially done by mapping the 1f and 2f peaks to effective misalignment and precessional angles. However, despite the lack of quantification, we think we have hit upon the physical reasons why these conditioned junctions have such coherent microwave generation.

The origin for the low linewidths in conditioned samples that we have just discussed provides a description of the physics on one level. It does not explain the rather remarkable fact that blowing pinholes randomly in an MTJ improves the linewidth. The actual magnetic structure of the conditioned junction is unknown. Where are the magnetic nanocontacts? How many of them are there? What is the precise spin-torque distribution near the contacts? It seems to us that there are too many things that are universal across conditioned devices (blue-shifting and frequency saturation vs. V_{bias} , power saturation vs V_{bias} , ultra-coherent oscillations in the saturated regime, AP/P dynamical phase diagram asymmetry, and the emergence of strong FL-SyAF coupling via magnetic nanocontacts as evidenced by the M.R. loop behavior) for these finer details to matter *too* much. Whatever is going on, it is quite

robust. We would like to hazard a guess and introduce a hypothesis for what might be going on.

Our guess is that the ferromagnetic coupling between the free and the fixed layer generated at the nanocontacts is largely responsible for the blue-shifting and eventual frequency/power saturation. Our simple physical description is that the nanocontact exchange coupling, anisotropy field, and applied field creates a finite effective φ_{mis} about which the magnetization precesses. As the spin torque increases, the oscillation amplitude starts to increase. When the amplitude is sufficiently low, the exchange between the SyAF and the free-layer serves to keep the free layer spins stiff at the nanocontact. Since this is also the region where the barrier has been degraded, we expect the spin-torque to be negligible at the nanocontact. The spin-torque in regions adjacent to the nanocontacts, however, are not negligible and cause the magnetization to precess. This precession creates a lateral gradient in the free layer magnetization away from the stiff magnetization near the nanocontact region. As the effective oscillation amplitude increases, this lateral magnetization gradient grows. The magnetization gradient generates an exchange field which must also grow with the oscillation amplitude. The increasing exchange field increases the spin precessional frequency. Thus the frequency blue shifts as the effective oscillation power increases.

As the oscillation power increases further, the increasing lateral exchange in the free layer and the stiff spins near the nanocontacts act to limit the oscillation power. Further increases in the oscillator amplitude by the spin torque are effectively

counteracted by the exchange interaction and the oscillation power saturates. The power saturation generates the observed frequency saturation and the high oscillator coherence in this high bias regime. This, of course, is a working hypothesis that probably needs to be tested numerically.

6.5 Micromagnetic Simulations: Dynamics

Before we start this section, we would like to note that we did much of the micromagnetic work before we had a clear understanding of where to direct our efforts in modeling. We include it in the thesis to document what we did, and as homage to the very long time we spent on it. We think that the physics that we inputted into these simulations was incorrect.

The micromagnetic study was conducted in collaboration with researchers at the University of Messina using their finite-temperature micromagnetic GPMagnet package. The package is a finite difference code computed on a fixed size rectangular mesh. We simulated a $50 \times 100 \text{ nm}^2$ elliptical cross-section stack. The cell size was $1 \text{ nm} \times 1 \text{ nm} \times .5 \text{ nm}$. We used a layer structure of CoFeB(2 nm)/Ru(.5)/CoFeB(2)/MgO(1)/CoFeB(4). As a first approximation, we kept the SyAF spins fixed. This may be incorrect and that the dynamics of the SyAF excitations probably play an important role in the dynamics, but our goal was to see what elements in the problem are necessary to reproduce general trends and characteristics of the dynamics (such as frequency vs V_{bias} behavior, power saturation, and linewidth reduction) and so we wanted to start with the minimum amount of variables/factors

and build up. We assume a two channel current model consisting of the MTJ channel and the nanoconstriction. We found that the MTJ channel was essential as there is a non-negligible tunnel current in parallel with the current going through the constriction. Attempts to model the dynamics without a parallel tunnel junction channel (i.e. just nanoconstrictions) lead to an unrealistic situation where the magnetization would execute dynamics only at very high currents $I \sim 3$ mA. We calculated effective resistances for the tunneling channel and the nanoconstriction by assuming that the reduction of the resistance during conditioning was due exclusively to parallel resistances generated by newly formed localized hotspots/nanoconstrictions. We have made the simplifying assumption that the conditioning process only damages the barrier in the hotspot regions and does not alter the structure of the barrier on a larger scale. The resistance of the tunneling channel was set such that the $RA = 1.5 \Omega \mu\text{m}^2$. The resultant parallel resistance per $1\text{nm} \times 1\text{nm}$ cell was $R_{cell}^P = 1.5 \text{ M}\Omega$. The TMR was taken to be 80%.

We used an $RA = .055 \Omega \mu\text{m}^2$ for the nanocontact regions. This means a resistance $R = 1.33 \text{ k}\Omega$ for a 4 nm^2 contact. This corresponds roughly to the parallel resistance required to reduce R_p from its unconditioned value (375Ω) to its final conditioned value ($\sim 280 \Omega$) in Figure 6.1 and pinhole area from a Maxwell-Sharvin calculation. Since the actual nature of the contacts (including the number of contacts) is not well known these estimates could be an underestimate of the single nanocontact resistance. The magnetoresistance was assumed to be negligible in the nanocontact regions. The spin polarization P in the tunneling channels was assumed to be $P_{\text{MTJ}} =$

0.66. For any non-magnetic nanocontacts used we set the polarization there to be $P = 0.38$ and assumed that the spin-torque between the free and top SyAF layer was well described by the Slonczewski torque (with the spin accumulation $\Lambda = 1$). For magnetic nanocontacts, the spin polarization was taken to be $P = 0.38$ and the non-adiabatic parameter $\beta = 0.04$. We simply guessed the polarization at the contacts and a more thorough study would need to vary the polarization of the contacts with respect to the MTJ to see what effect that would have. The time duration of the micromagnetic simulations were 100 ns resulting in a frequency resolution of ~ 10 MHz.

We ran simulations for a variety of scenarios. We first tried unconditioned junctions where the barrier was considered intact and the tunnel current was uniform. The dynamics in this case was strongly red shifting with a change of frequency $f \sim 2.75$ GHz with $\Delta I \sim 0.14$ mA of current. The linewidths of these simulated unconditioned oscillators were large and ranged from $\Delta f \sim 700$ MHz – 1.5 GHz.

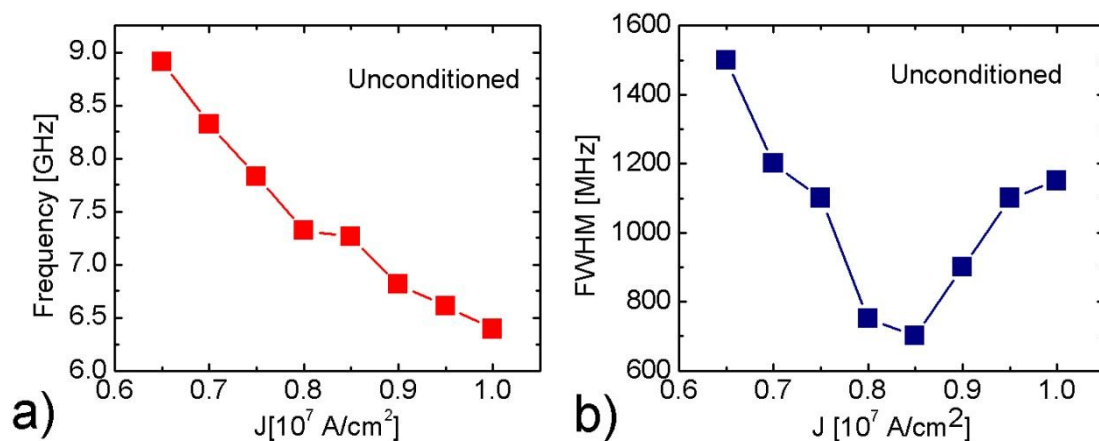


Figure 6.14 a) Micromagnetic results for frequency vs current density for unconditioned junctions b) Oscillator linewidth vs current density for unconditioned MTJ.

The reason for the incoherent dynamics in the unconditioned MTJ structure is in and of itself not entirely clear. Spin-torque non uniformities due to current non-uniformities arising from random variation in the barrier thickness could be an issue (although our simulations do not take this into account). Spin-torque spatial non-uniformities in the field/electrode geometry we chose (P/AP collinear electrode arrangement) due to local thermal fluctuations of the magnetization could also be an issue. Also, edge dipolar fields coming from the SyAF may be another source of linewidth broadening. This source of broadening was also not modeled accurately when we chose the SyAF layers to be fixed. However, explaining the origin of the linewidth in unconditioned samples was not the focus of our study.

We restrict ourselves to the question of how dynamical behavior exhibited by the conditioned devices might emerge. First we asked whether the nature of the dynamics (i.e. small linewidths, etc) in the conditioned MTJs depend on magnetic coupling between the free and fixed layer or whether they are simply a consequence of the emergence of areas of increased current density (hotspots) where the tunnel barrier is thin. We thus considered junctions with current hotspots in a variety of geometries. First, we considered a hotspot in the center, then one at the ellipse long axis edge at $y=0$ nm, $x = +40$ nm, then two hotspots at $y = 0$ nm, $x = \pm 25$ nm, and finally three hotspots located at $(y = 0$ nm, $x = \pm 25$ nm) and $(x=0$, $y=0)$. We use a coordinate system where $(x = 0$ nm, $y = 0$ nm) corresponds to the center of the ellipse. We ran simulations for nanocontacts of two different cross-sectional areas $A_{\text{pinhole}} = 12$ nm²

and $A_{\text{pinhole}} = 4 \text{ nm}^2$. We have included Oersted fields derived from the current flowing through the junction in these simulations. In all the cases that we simulated, the dynamics were both spatially and temporally incoherent. The dynamics also exhibited strong frequency red shifting as a function of increasing current density. The situations we simulated for junctions with simple current hotspots do not correspond to the experimentally observed behavior of STT-induced dynamics in the conditioned MTJs. This suggests that magnetic coupling between the free and fixed layers that we have argued occur upon conditioning are important for understanding the nature of dynamics in the conditioned MTJs.

We thus simulated the dynamics including magnetic pinholes in a variety of locations and numbers to see whether we could reproduce the behavior of the conditioned junctions. We tried one magnetic pinhole in various locations, two pinholes in various locations and finally we tried the case of three magnetic pinholes. We found temporally and spatially incoherent dynamics and strong frequency red-shifting for the one-pinhole regardless of the location of the pinhole. Simulations with two pinholes placed at $y=0$, $x = \pm 25 \text{ nm}$ (not shown) showed flat frequency spectra with virtually no frequency shift but incoherent dynamics ($\Delta f > 500 \text{ MHz}$) for all current densities and fields ($H=40 \text{ mT}$ to 100 mT) applied to the junction. We then simulated the situation with three pinholes placed at $(y=0, x=0)$ and $(y=0, x = \pm 25 \text{ nm})$. We found that the dynamics in this case seemed have a frequency vs. V_{bias} behavior that is not too dissimilar to what was observed experimentally (Figure 6.15). We ran the simulations with and without the Oersted field but this did not seem to make a big

difference in the frequency and linewidth vs V . The oscillations show a weak blue shift and then a turn over and eventual red-shift as the bias is increased.

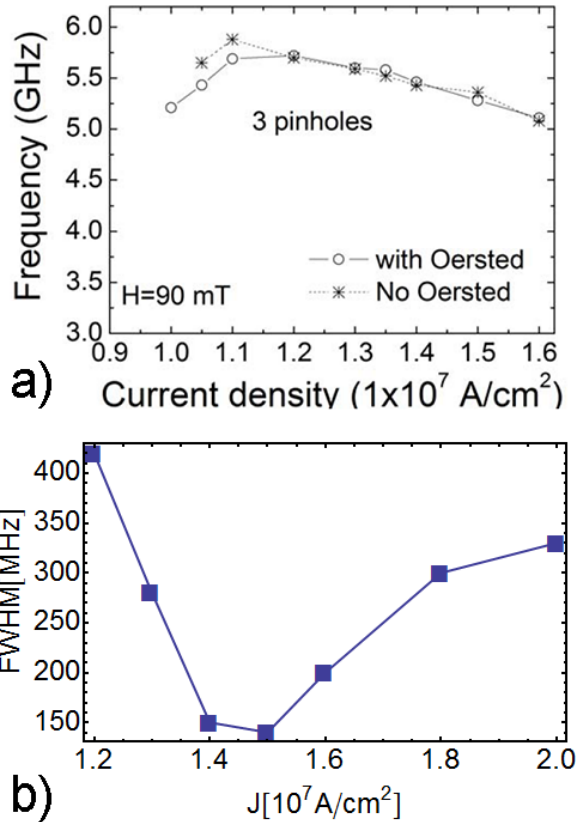


Figure 6.15 a) 1st Harmonic frequency dependence in the resistance signal vs. average current density with and without Oersted field for three pinhole case. Note that the spectra have the weak blue shift and red shift observed in the experiment. b) Linewidth vs. current density for three pinhole case.

The minimum linewidth is lower than that observed in the room temperature simulations of junctions without pinholes. The linewidth vs current density shows a minimum linewidth of $\sim 150 \text{ MHz}$ (Figure 2.9b). Clearly the oscillator has regions of bias where it operates far more coherently than when no nano-contacts exists.

However, the linewidth is still a bit larger than the type of linewidths (<50 MHz) seen experimentally for conditioned devices.

We then reduced the pinhole size down to an effective area $A_{\text{pinhole}} = 4 \text{ nm}^2$. The behavior of the frequency shifting did not change too much but the linewidth decreased considerably. We observed a $T=300$ K linewidth as low as $\Delta f \sim 50$ MHz. This linewidth is close to the coherent linewidths observed in the experiment and is substantially lower than observed for the simulations with no pinholes. We checked whether the highly coherent dynamics and weak blue-shifting had anything to do with an increase in the average z component of the magnetization oscillation. The average z -component of the magnetization $\langle m_z \rangle$ is extremely small and shows that the weak blue shifting is not due to an increased average out-of-plane character of the oscillation (as we have previously said).

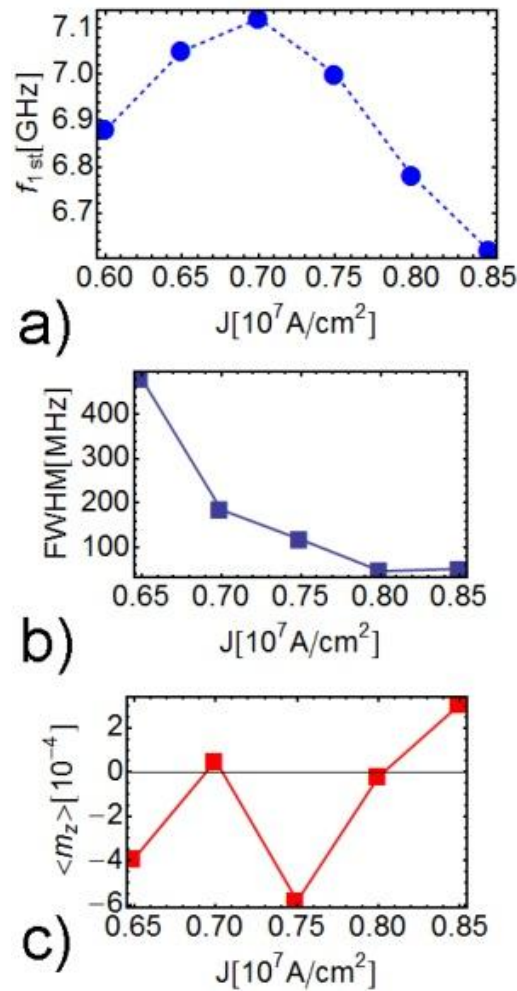


Figure 6.16 a) f vs J (average current density) for first harmonic in the resistance oscillations of the three pinhole $A = 4 \text{ nm}^2$ scenario. b) Oscillation linewidth vs. current density of first harmonic. c) Spatially averaged m_z component time averaged over an oscillation cycle as a function of current density.

The trajectories are not simple in the case of this three-pinhole case and are certainly not spatially uniform. A look at a few snapshots of the dynamics shows that the magnetization executes rather large angle dynamics and that the dynamics are largely in-plane.

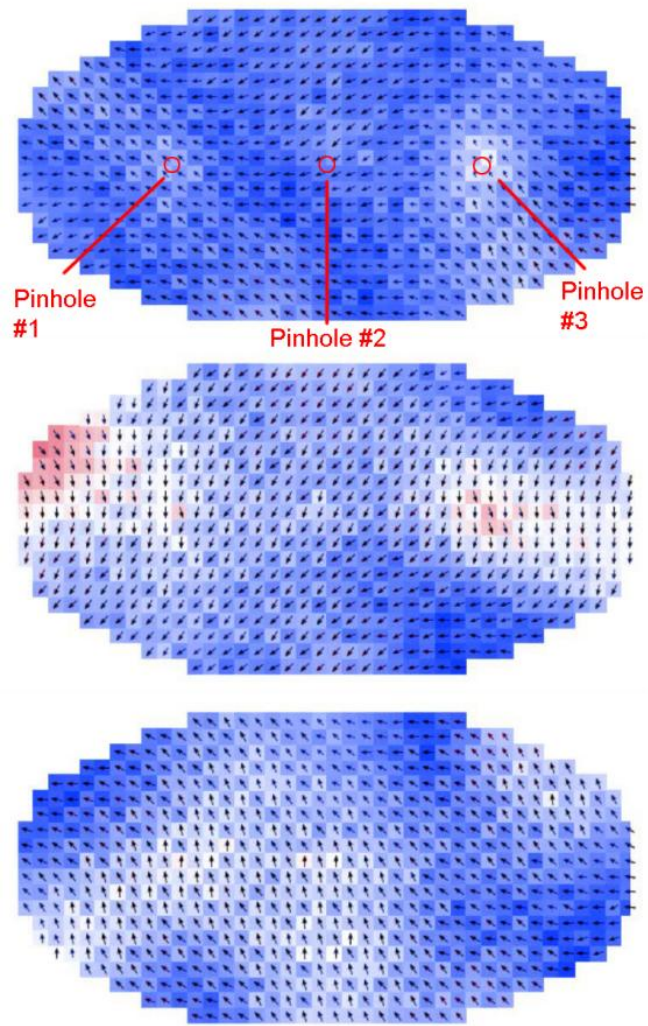


Figure 6.17 Snapshots of magnetization dynamics in three magnetic pinhole case. Location of the three pinholes are shown in the first snapshot. The dynamics were for $H = 90$ mT and $J = 8 \times 10^6$ A/cm².

These large-angle dynamics (and no observed power saturation) do not match well with the picture that we have gained from the normalized conductance power data. The frequency red-shifting in the region where the linewidth is low also does not agree with our experimental observations of flattening of the frequency vs V_{bias} behavior in

the minimum linewidth region. We do not think that these simulated dynamics represent the real dynamics of the system.

The fact that three correctly-sized magnetic nanocontacts placed in a high symmetry arrangement are required to produce coherent dynamics and weak frequency blue-shifting are also somewhat concerning. In principle, the two pinhole case with larger magnetic coupling area and/or higher polarization and lower resistance should be able to reproduce the frequency behavior and oscillation coherence observed experimentally. We do not discount the possibility of four highly resistive magnetic nanocontacts. The main problem is that based off our data we feel that the general mechanism for conditioned behavior should be fairly robust. The lack of robustness in the micromagnetic simulations, as evidenced by the large difference in the linewidths induced by changing the size of the three magnetic nanocontacts or by having two pinholes instead of three pinholes, points to the fact that we have missed some key physics in our micromagnetic modeling and/or there are numerical artifacts/effects that need to be taken into account.

6.6 Future Directions and Conclusion

The basics physics that we think we missed in our micromagnetic simulations are that the spin-torque at the nanoconstriction is negligible and that the spins there are stiff and act to generate a restoring force on the oscillation. Our inclusion of significant spin-torque at the nanoconstriction gets the physics wrong. In addition, we think that there may be finite size artifacts associated with the small number of cells

we used to simulate the nanocontacts as well as artifacts associated with sharp, discontinuous changes in the current distribution that were used in the simulations. In order to simulate further we think that switching to a finite element package would be beneficial. The mesh resolution near and farther away from the nanocontacts can then be set appropriately. For further simulations, we would ignore any spin torque in the contact region and assume the full MgO spin-filtered spin torque outside the nanocontact region.

Our hypothesis, if correct, would prove an interesting and general point. By providing local spots in the free layer of an STNO where the free layer is locally tethered and where the spin torque is negligible in the tethering regions and high everywhere else, one can actually create an STNO which has highly coherent microwave emissions. It would be interesting to try and purposefully engineer a high TMR system with this sort of tethering/spin-torque distribution (as opposed to haphazardly blowing holes into a tunnel barrier by voltage stressing). We like a recent idea sparked during a conversation with our esteemed and illustrious colleague Dr. Sriharsha Aradhya. One could use sharp conductive AFM tips to apply biases in certain spots and break the barrier locally in order to generate a magnetic nanocontact. It would then be possible to control where the magnetic nanocontacts are, how many of them there are, etc. This would open up the path towards reliable engineering of highly coherent MTJ spin-torque oscillators based off the mechanism we have discussed in this chapter.

REFERENCES

- [1] T. Linn and D. Mauri, "U.S. Patent 6841395 B2," 2013.
- [2] J. J. Cha, J. C. Read, W. F. Egelhoff, P. Y. Huang, H. W. Tseng, Y. Li, R. A. Buhrman, and D. A. Muller, "Atomic-scale spectroscopic imaging of CoFeB/Mg–B–O/CoFeB magnetic tunnel junctions," *Appl. Phys. Lett.*, vol. 95, no. 3, p. 032506, 2009.
- [3] J. C. Read, P. G. Mather, and R. A. Buhrman, "X-ray photoemission study of CoFeB/MgO thin film bilayers," *Appl. Phys. Lett.*, vol. 90, no. 13, p. 132503, 2007.
- [4] S. Yuasa, Y. Suzuki, T. Katayama, and K. Ando, "Characterization of growth and crystallization processes in CoFeB/MgO/CoFeB magnetic tunnel junction structure by reflective high-energy electron diffraction," *Appl. Phys. Lett.*, vol. 87, no. 24, p. 242503, 2005.
- [5] K. Tsunekawa, D. D. Djayaprawira, M. Nagai, H. Maehara, S. Yamagata, N. Watanabe, S. Yuasa, Y. Suzuki, and K. Ando, "Giant tunneling magnetoresistance effect in low-resistance CoFeB/MgO(001)/CoFeB magnetic tunnel junctions for read-head applications," *Appl. Phys. Lett.*, vol. 87, no. 7, p. 072503, 2005.
- [6] Y. Nagamine, H. Maehara, K. Tsunekawa, D. D. Djayaprawira, N. Watanabe, S. Yuasa, and K. Ando, "Ultralow resistance-area product of $0.4 \text{ } \Omega(\mu\text{m})^2$ and high magnetoresistance above 50% in CoFeB/MgO/CoFeB magnetic tunnel junctions," *Appl. Phys. Lett.*, vol. 89, no. 16, p. 162507, 2006.
- [7] W. Butler, X.-G. Zhang, T. Schulthess, and J. MacLaren, "Spin-dependent tunneling conductance of Fe|MgO|Fe sandwiches," *Phys. Rev. B*, vol. 63, no. 5, p. 054416, Jan. 2001.
- [8] J. Mathon and A. Umerski, "Theory of tunneling magnetoresistance of an epitaxial Fe/MgO/Fe(001) junction," *Phys. Rev. B*, vol. 63, no. 22, p. 220403, May 2001.
- [9] H. Kubota, A. Fukushima, Y. Ootani, S. Yuasa, K. Ando, H. Maehara, K. Tsunekawa, D. D. Djayaprawira, N. Watanabe, and Y. Suzuki, "Evaluation of Spin-Transfer Switching in CoFeB/MgO/CoFeB Magnetic Tunnel Junctions," *Jpn. J. Appl. Phys.*, vol. 44, no. No. 40, pp. L1237–L1240, Sep. 2005.
- [10] Y. Huai, M. Pakala, Z. Diao, D. Apalkov, Y. Ding, and A. Panchula, "Spin-transfer switching in MgO magnetic tunnel junction nanostructures," *J. Magn. Mater.*, vol. 304, no. 1, pp. 88–92, Sep. 2006.

- [11] G. Fuchs, J. Katine, S. Kiselev, D. Mauri, K. Wooley, D. Ralph, and R. Buhrman, “Spin Torque, Tunnel-Current Spin Polarization, and Magnetoresistance in MgO Magnetic Tunnel Junctions,” *Phys. Rev. Lett.*, vol. 96, no. 18, p. 186603, May 2006.
- [12] A. M. Deac, A. Fukushima, H. Kubota, H. Maehara, Y. Suzuki, S. Yuasa, Y. Nagamine, K. Tsunekawa, D. D. Djayaprawira, and N. Watanabe, “Bias-driven high-power microwave emission from MgO-based tunnel magnetoresistance devices,” *Nat. Phys.*, vol. 4, no. 10, pp. 803–809, Aug. 2008.
- [13] S. Cornelissen, L. Bianchini, G. Hrkac, M. Op de Beeck, L. Lagae, J.-V. Kim, T. Devolder, P. Crozat, C. Chappert, and T. Schrefl, “Auto-oscillation threshold and line narrowing in MgO-based spin-torque oscillators,” *EPL (Europhysics Lett.)*, vol. 87, no. 5, p. 57001, Sep. 2009.
- [14] D. Houssameddine, S. H. Florez, J. A. Katine, J.-P. Michel, U. Ebels, D. Mauri, O. Ozatay, B. Delaet, B. Viala, L. Folks, B. D. Terris, and M.-C. Cyrille, “Spin transfer induced coherent microwave emission with large power from nanoscale MgO tunnel junctions,” *Appl. Phys. Lett.*, vol. 93, no. 2, p. 022505, 2008.
- [15] T. Devolder, L. Bianchini, J.-V. Kim, P. Crozat, C. Chappert, S. Cornelissen, M. Op de Beeck, and L. Lagae, “Auto-oscillation and narrow spectral lines in spin-torque oscillators based on MgO magnetic tunnel junctions,” *J. Appl. Phys.*, vol. 106, no. 10, p. 103921, 2009.
- [16] D. Houssameddine, U. Ebels, B. Dieny, K. Garello, J.-P. Michel, B. Delaet, B. Viala, M.-C. Cyrille, J. Katine, and D. Mauri, “Temporal Coherence of MgO Based Magnetic Tunnel Junction Spin Torque Oscillators,” *Phys. Rev. Lett.*, vol. 102, no. 25, p. 257202, Jun. 2009.
- [17] B. Georges, J. Grollier, V. Cros, A. Fert, A. Fukushima, H. Kubota, K. Yakushijin, S. Yuasa, and K. Ando, “Origin of the spectral linewidth in nonlinear spin-transfer oscillators based on MgO tunnel junctions,” *Phys. Rev. B*, vol. 80, no. 6, p. 060404, Aug. 2009.
- [18] P. Bruno, “Geometrically Constrained Magnetic Wall,” *Phys. Rev. Lett.*, vol. 83, no. 12, pp. 2425–2428, Sep. 1999.
- [19] G. Wexler, “The size effect and the non-local Boltzmann transport equation in orifice and disk geometry,” *Proc. Phys. Soc.*, vol. 89, p. 927, 1966.
- [20] D. Houssameddine, J. F. Sierra, D. Gusakova, B. Delaet, U. Ebels, L. D. Buda-Prejbeanu, M.-C. Cyrille, B. Dieny, B. Ocker, J. Langer, and W. Maas, “Spin torque driven excitations in a synthetic antiferromagnet,” *Appl. Phys. Lett.*, vol. 96, no. 7, p. 072511, 2010.

- [21] S. Petit, N. de Mestier, C. Baraduc, C. Thirion, Y. Liu, M. Li, P. Wang, and B. Dieny, "Influence of spin-transfer torque on thermally activated ferromagnetic resonance excitations in magnetic tunnel junctions," *Phys. Rev. B*, vol. 78, no. 18, p. 184420, Nov. 2008.
- [22] J. Slonczewski, "Currents, torques, and polarization factors in magnetic tunnel junctions," *Phys. Rev. B*, vol. 71, no. 2, p. 024411, Jan. 2005.
- [23] M. Pufall, W. Rippard, M. Schneider, and S. Russek, "Low-field current-hysteretic oscillations in spin-transfer nanocontacts," *Phys. Rev. B*, vol. 75, no. 14, p. 140404, Apr. 2007.
- [24] O. Lee, P. Braganca, V. Pribiag, D. Ralph, and R. Buhrman, "Quasilinear spin-torque nano-oscillator via enhanced negative feedback of power fluctuations," *Phys. Rev. B*, vol. 88, no. 22, p. 224411, Dec. 2013.

CHAPTER 7

CONCLUSION/SUMMARY

We will now provide a quick summary of the work we did. In Chapter 3 we measured surface magnetoelastic interactions in the Ta|CoFeB|MgO system and discussed how these surface magnetoelastic interactions could be important in the thickness dependence of the PMA. In particular, we showed that thickness dependent magnetoelastic effects could be used to extend beyond the simplistic Neel model in the Ta|CoFeB|MgO system and suggested that these magnetoelastic effects could be employed to tailor and optimize the behavior of the PMA. In addition, we suggested that strain could be an important knob in understanding the underlying mechanisms at work behind the VCMA.

In Chapter 4, we used GHz frequency surface acoustic waves (SAWs) and the magnetoelastic interaction to induce spin-wave resonance in Ni|Pt bilayers. We determined that the excitation was a Damon-Eschbach magnetostatic surface spin wave whose wave-vector was set by the SAW propagation wave-vector and not by boundary conditions of the magnetic film. We then studied the in-plane angular structure of the resonant coupling between this Damon-Eschbach wave and the SAW and found that the anisotropy associated with dynamic dipolar interactions arising from the spin-wave was crucial in quantitatively matching the field angle and field strength dependence of the SAW absorption that was observed. Using spin pumping into the Pt and the inverse spin Hall effect (ISHE), we were able to quantify the

thickness-averaged precessional amplitude of the Damon-Eschbach spin wave, and the magnetoelastic interaction B_{eff} of the Ni film. We finished the chapter by arguing that ultrasonics and in particular SAWs could be used to probe and manipulate magnetism in a novel and interesting way.

In Chapter 5, we performed macrospin and micromagnetic simulations (where appropriate) evaluating various magnetoelastic switching schemes and their strengths and disadvantages. We showed that the damping can be an extremely important consideration in designing toggle-mode devices based off of giant magnetostrictive magnets. We found that devices constructed on in-plane magnetized, higher moment giant magnetostrictive nanomagnets will suffer greatly from the high damping – both in terms of acoustical pulse shaping/timing requirements and the pulse amplitude required in overcoming the damping. We demonstrated that the penalty may be so severe that magnetoelastic switching with a transition metal ferromagnet like Ni might be more effective. We then showed that PMA giant magnetostrictive magnets could, with the right engineering, be more attractive for memory applications both in terms of storage density and minimum bit size but also pulse amplitude and timing requirements. In addition, we argued that the small size of the devices would ensure that the energy dissipated per write cycle due to capacitive charging/de-charging energies would be low. Finally we discussed various non-toggle magnetoelastic switching schemes where damping aids the switching process. We investigated in-plane magnetized systems (in particular epitaxial $\text{Fe}_{81}\text{Ga}_{19}$) with biaxial magneto-crystalline anisotropy and discussed ways in which one could make a deterministic two state memory out of such a system without compromising long-term bit thermal

stability. We finally evaluated a non-toggle switching scheme involving an in-plane magnetized giant magnetostrictive magnet with uniaxial anisotropy (defined by shape anisotropy) and an acoustical strain pulse direction 45 degrees with respect to the anisotropy axis. We discussed the hard-axis bias field requirements in order to make switching deterministic and show that these considerations place severe limitations on the scalability of this type of memory. That being said, we also showed that the stress amplitudes required for a write operation are the lowest of any of the other switching schemes/geometries discussed in the rest of the chapter.

In Chapter 6, we reported and provided a plausible explanation for the rather odd observation that the soft-breakdown of low-RA MTJs under high voltage stressing can cause the dynamics of such MTJs to become highly coherent. We showed that magnetic coupling between the free and fixed layer induced by ferromagnetic exchange through nanocontacts created during the stressing process are responsible for the dramatic rise in oscillator coherence over unconditioned MTJs. We also argued that the existence of magnetic nanocontact coupling, along with the guess that the spin-torque exerted at the nanocontacts is low, can explain many other aspects of the data – including changes in the M.R. field minor loop behavior, the AP vs. P asymmetry in the dynamical phase diagram, the blue shifting of the oscillator frequency with bias, and the normalized power saturation as a function of bias regardless of the applied field strength. We pointed out that the mechanism for coherent linewidth is fairly general, robust, and quite novel. It might be possible to either directly design MTJ oscillators with engineered magnetic nanocontacts or use a different geometry/interaction to tether the magnetization and allow for oscillation

self-limiting and high oscillator coherence over a large range of external field and voltage bias conditions.

We conclude this thesis by noting that the last three to four years or so have been a remarkably exciting time to be in spintronics. A lot has happened and a lot is going on: PMA and VCMA in CoFeB|MgO systems, pure spin-current generation in metals via spin-orbit mechanisms and the physics of torques induced by such spin current at FM|NM interfaces, the discovery of Dzyaloshinskii-Moriya anisotropic exchange at FM|NM interfaces [1]–[4], the physics of ferrimagnetic insulator|NM bilayers (i.e. spin-pumping/ISHE measurements [5]–[10], spin Hall magnetoresistance effects [11]–[14], and the potential for spin-torque manipulation of magnetic insulators [15]–[17]), recent measurements of spin-pumping/ISHE voltages measured through and in antiferromagnets [18], [19], and the list goes on.

We think that the elastic/crystal strain degrees of freedom can be an important knob to tune and manipulate many of these systems. We have already argued for the potential that strain manipulation has in tuning and understanding the fundamental mechanisms behind the PMA and the VCMA. We have also discussed the possibility of using GHz strain waves to manipulate magnetization dynamics with a certain degree of spatial control. We think that strain could also be a powerful tool for manipulating oxide antiferromagnets, where magnetoelastic effects can be very large, in order to study the physics of oxide antiferromagnet|NM interfaces. More specifically, we think that ultra-high frequency ultrasonics might prove a much better technique than classic mm-wave electromagnetic techniques for resonantly exciting

these oxide antiferromagnets and performing spin-pumping measurements on antiferromagnet|NM bilayers. Recent work by the Robinson group here at Cornell on creating sub-THz phonon spectrometers on Si using Al|AlO_x|Al STJs give us hope that these experiments could be done on chip [20], [21]. Strain could also be used as a new knob to study the physics of spin Hall effects and interfacial torques in FM|NM systems (and potentially tune/increase the spin Hall angle of certain heavy metals). There clearly is a lot that can be done with strain/stressed-based techniques in spintronics and nanoscale magnet manipulation and we sincerely hope to see development along these lines in the years to come.

REFERENCES

- [1] M. Bode, M. Heide, K. von Bergmann, P. Ferriani, S. Heinze, G. Bihlmayer, A. Kubetzka, O. Pietzsch, S. Blügel, and R. Wiesendanger, “Chiral magnetic order at surfaces driven by inversion asymmetry,” *Nature*, vol. 447, no. 7141, pp. 190–3, May 2007.
- [2] M. Heide, G. Bihlmayer, and S. Blügel, “Dzyaloshinskii-Moriya interaction accounting for the orientation of magnetic domains in ultrathin films: Fe/W(110),” *Phys. Rev. B*, vol. 78, no. 14, p. 140403, Oct. 2008.
- [3] A. Thiaville, S. Rohart, É. Jué, V. Cros, and A. Fert, “Dynamics of Dzyaloshinskii domain walls in ultrathin magnetic films,” *EPL (Europhysics Lett.)*, vol. 100, no. 5, p. 57002, Dec. 2012.
- [4] S. Emori, U. Bauer, S.-M. Ahn, E. Martinez, and G. S. D. Beach, “Current-driven dynamics of chiral ferromagnetic domain walls,” *Nat. Mater.*, vol. 12, no. 7, pp. 611–6, Jul. 2013.
- [5] Y. Kajiwara, K. Harii, S. Takahashi, J. Ohe, K. Uchida, M. Mizuguchi, H. Umezawa, H. Kawai, K. Ando, K. Takanashi, S. Maekawa, and E. Saitoh, “Transmission of electrical signals by spin-wave interconversion in a magnetic insulator,” *Nature*, vol. 464, no. 7286, pp. 262–6, Mar. 2010.
- [6] B. Heinrich, C. Burrowes, E. Montoya, B. Kardasz, E. Girt, Y.-Y. Song, Y. Sun, and M. Wu, “Spin Pumping at the Magnetic Insulator (YIG)/Normal Metal (Au) Interfaces,” *Phys. Rev. Lett.*, vol. 107, no. 6, p. 066604, Aug. 2011.
- [7] V. Castel, N. Vlietstra, B. J. van Wees, and J. Ben Youssef, “Frequency and power dependence of spin-current emission by spin pumping in a thin-film YIG/Pt system,” *Phys. Rev. B*, vol. 86, no. 13, p. 134419, Oct. 2012.
- [8] C. Hahn, G. de Loubens, O. Klein, M. Viret, V. V. Naletov, and J. Ben Youssef, “Comparative measurements of inverse spin Hall effects and magnetoresistance in YIG/Pt and YIG/Ta,” *Phys. Rev. B*, vol. 87, no. 17, p. 174417, May 2013.
- [9] S. M. Rezende, R. L. Rodríguez-Suárez, M. M. Soares, L. H. Vilela-Leão, D. Ley Domínguez, and a. Azevedo, “Enhanced spin pumping damping in yttrium iron garnet/Pt bilayers,” *Appl. Phys. Lett.*, vol. 102, no. 1, p. 012402, 2013.
- [10] H. L. Wang, C. H. Du, Y. Pu, R. Adur, P. C. Hammel, and F. Y. Yang, “Large spin pumping from epitaxial $\text{Y}_3\text{Fe}_5\text{O}_{12}$ thin films to Pt and W layers,” *Phys. Rev. B*, vol. 88, no. 10, p. 100406, Sep. 2013.

- [11] H. Nakayama, M. Althammer, Y.-T. Chen, K. Uchida, Y. Kajiwara, D. Kikuchi, T. Ohtani, S. Geprägs, M. Opel, S. Takahashi, R. Gross, G. E. W. Bauer, S. T. B. Goennenwein, and E. Saitoh, “Spin Hall Magnetoresistance Induced by a Nonequilibrium Proximity Effect,” *Phys. Rev. Lett.*, vol. 110, no. 20, p. 206601, May 2013.
- [12] M. Althammer, S. Meyer, H. Nakayama, M. Schreier, S. Altmannshofer, M. Weiler, H. Huebl, S. Geprägs, M. Opel, R. Gross, D. Meier, C. Klewe, T. Kuschel, J.-M. Schmalhorst, G. Reiss, L. Shen, A. Gupta, Y.-T. Chen, G. E. W. Bauer, E. Saitoh, and S. T. B. Goennenwein, “Quantitative study of the spin Hall magnetoresistance in ferromagnetic insulator/normal metal hybrids,” *Phys. Rev. B*, vol. 87, no. 22, p. 224401, Jun. 2013.
- [13] N. Vlietstra, J. Shan, V. Castel, J. Ben Youssef, G. E. W. Bauer, and B. J. Van Wees, “Exchange magnetic field torques in YIG/Pt bilayers observed by the spin-Hall magnetoresistance,” pp. 3–6, 2013.
- [14] Y.-T. Chen, S. Takahashi, H. Nakayama, M. Althammer, S. Goennenwein, E. Saitoh, and G. Bauer, “Theory of spin Hall magnetoresistance,” *Phys. Rev. B*, vol. 87, no. 14, p. 144411, Apr. 2013.
- [15] X. Jia, K. Liu, K. Xia, and G. E. W. Bauer, “Spin transfer torque on magnetic insulators,” *EPL (Europhysics Lett.)*, vol. 96, no. 1, p. 17005, Oct. 2011.
- [16] J. Xiao and G. E. W. Bauer, “Spin-Wave Excitation in Magnetic Insulators by Spin-Transfer Torque,” *Phys. Rev. Lett.*, vol. 108, no. 21, p. 217204, May 2012.
- [17] T. Chiba, G. E. W. Bauer, and S. Takahashi, “Current-Induced Spin-Torque Resonance of Magnetic Insulators,” *Phys. Rev. Appl.*, vol. 2, no. 3, p. 034003, Sep. 2014.
- [18] J. B. S. Mendes, R. O. Cunha, O. Alves Santos, P. R. T. Ribeiro, F. L. a. Machado, R. L. Rodríguez-Suárez, A. Azevedo, and S. M. Rezende, “Large inverse spin Hall effect in the antiferromagnetic metal Ir₂₀Mn₈₀,” *Phys. Rev. B*, vol. 89, no. 14, p. 140406, Apr. 2014.
- [19] C. Hahn, D. Loubens, O. Klein, M. Viret, and J. Ben Youssef, “Conduction of spin currents through insulating oxides,” pp. 1–9.
- [20] O. O. Otelaja, J. B. Hertzberg, M. Aksit, and R. D. Robinson, “Design and operation of a microfabricated phonon spectrometer utilizing superconducting tunnel junctions as phonon transducers,” *New J. Phys.*, vol. 15, no. 4, p. 043018, Apr. 2013.

- [21] J. B. Hertzberg, M. Aksit, O. O. Otelaja, D. A. Stewart, and R. D. Robinson, “Direct measurements of surface scattering in Si nanosheets using a microscale phonon spectrometer: implications for Casimir-limit predicted by Ziman theory,” *Nano Lett.*, vol. 14, no. 2, pp. 403–15, Feb. 2014.